

Structure-activity investigations of mixed Ni-Fe oxides as catalysts for electrochemical water splitting

vorgelegt von

M.Sc.

Eva Mikaela Charlotte Görlin

St. Tuna, Schweden

von der Fakultät II – Mathematik und Naturwissenschaften

der Technischen Universität Berlin

zur Erlangung des akademischen Grades

Doktorin der Naturwissenschaften

Dr. rer. nat

Promotionsausschuss:

Vorsitzender: Prof. Dr. Maria Andrea Mroginski, Technische Universität Berlin

Gutachter: Prof. Dr. Peter Strasser, Technische Universität Berlin

Gutachter: Prof. Dr. Holger Dau, Freie Universität Berlin

Gutachter: Prof. Dr. Karl Mayrhofer, Max-Planck-Institut/Forschungszentrum Jülich

Tag der wissenschaftlichen Aussprache: 9th June 2016

Berlin 2017

To the free spirit

To decisions not confined by boundaries

Let not knowledge limit our choices

ABSTRACT

Structure-activity investigations of mixed Ni-Fe oxides as catalysts for electrochemical water splitting

A balanced utilization of energy requires new approaches in catalysis, to reach sufficient levels of production of renewable energy. Specifically, there is a need of efficient catalysts for energy utilization, conversion, and storage.

Research concerning electrochemical water splitting has attracted attention due to the possibility to utilize water in integrated solar-to-water splitting devices. One challenge in utilizing these devices is catalyzing the sluggish oxygen evolution reaction (OER). Of recent interest have been non-precious metal catalysts, which at high pH have shown competitive activities in comparison to noble metal based catalysts. Specifically, Ni-Fe based catalysts show superior OER activity to a variety of both non-precious and noble metal catalysts. The origin of this high activity is not completely understood, and elucidating this is one of the goals of the present work. This dissertation focuses on establishing a structure-activity correlation of mixed Ni-Fe oxide based materials for the oxygen evolution reaction.

In *Chapter 3*, we present a study of mixed Ni-Fe oxyhydroxides (OOH) in attempt to establish a structure-activity correlation between catalyst composition, OER activity, local atomic structure, and catalyst redox states. Ni-Fe oxides - specifically oxyhydroxides - show catalytic activity extending to the bulk of the catalytic film, meaning there is no passive oxide core. This enables all metal sites to participate in the reaction, which facilitate the use of X-ray methods that are sensitive to the bulk. The catalysts we investigated were prepared by a solvothermal method, which is up to date less investigated than electrodeposited Ni-Fe catalysts. We established activity-composition trends, following the Sabatier principle, with optimal activity around 50 % Fe. We identified the catalytically active state using quasi-*in situ* X-ray absorption spectroscopy (XAS), and combined the study using differential electrochemical mass spectrometry (DEMS) to evaluate the faradaic charge efficiencies toward O₂ formation. With this approach, we could determine how much of the faradaic current that was directed into products and how much that was used to change oxidation states of the catalyst. Our results in addition revealed that Fe stabilizes Ni atoms in its low-valent +2 state, which is so far in contrast to earlier studies. We justified this by proposing a mechanistic hypothesis that a kinetic competition between the metal oxidation step

(i) and the rate of OER catalysis leading to O₂ formation (ii) prevail. Subsequently, if process (ii) outweighs that of process (i), Ni atoms will not accumulate in its high-valent +4 state. This would justify why discrepancies regarding the oxidation states of Ni and Fe have been reported in literature.

In *Chapter 4*, we extended the OER activity measurements to a wider range of pH (pH 7-13), where we focused on a carbon supported Ni-Fe/C oxyhydroxide catalysts. We could establish a pH dependent activity trend, where we confirmed an extensive corrosion (leaching) of Ni at pH 7. In addition, we could show on morphological changes occurring after exposure to catalytic potential, proposed as the result of a leaching-recrystallization process during potential cycling.

In *Chapter 5*, we investigated a series of physical mixtures of Ni+Fe(OOH) catalysts, prepared by mixing the parental Ni(OH)₂ and Fe(OOH) catalysts. The physical mixtures showed as high OER activity as the pre-synthesized catalysts. To estimate the degree of mixing, XAS measurements were correlated to electrochemical measurements and EDX elemental mapping.

In *Chapter 6*, we focused on a comparison of OER activities of unsupported and carbon supported Ni-Fe/C oxyhydroxide catalysts, where the focus was to investigate the origins of the enhanced catalytic activity observed on carbon support. We used XAS and DEMS to deduce the local atomic structure and metal redox state contribution. We also looked at the influence of varying the catalyst loading and the electrolyte pH.

In *Chapter 7*, we investigated shape selected Ni-Fe oxide nanocatalysts and looked into how to obtain a narrow size distribution in the range of 10 nm. We compared OER activities at different oxide surfaces in order to relate the activity at a confined oxide surface to the activity of a Ni-Fe oxyhydroxide catalyst with catalysis extending to the bulk. We extend the discussions to the importance of electrocatalytically active area surface area, the influence of the oxide phase, size, and surface composition.

The vast number of investigations of Ni-Fe OER catalysts continue to contribute to knowledge regarding the origin of the high catalytic activity, which will eventually help to establish a complete understanding of these catalysts. However, many areas remain unexplored up to date. With this work, we aim to contribute to a deeper insight into some aspects.

ZUSAMMENFASSUNG

Struktur-Aktivitätsuntersuchungen von gemischten Ni-Fe-Oxiden als Katalysator zur elektrochemischen Wasserspaltung

Die Nutzung erneuerbarer Energien erfordert neue Katalysekonzepte, mit dem Ziel, eine nachhaltige Energieproduktion zu nutzen. Effiziente Katalysatoren sind dabei von größter Wichtigkeit, um die Umwandlung der Energie und Energieproduktion in ihre vorgesehene Form optimieren zu können.

Die elektrochemische Wasserspaltung erlangte viel Aufmerksamkeit vor dem Hintergrund, Wasser als eine Energiequelle in integrierten solaren Wasser spaltenden Anlagen nutzen zu können. Die Sauerstoffevolutionsreaktion (OER) weist dabei ein hohes Überpotential (η) auf und erfordert demnach hocheffiziente Katalysatoren. Der Fokus liegt mittlerweile auf Katalysatoren, welche aus unedlen Metallen hergestellt werden. Diese haben gezeigt, dass sie mit den Aktivitäten edler Metalle konkurrieren können. Allerdings erfordern unedle Metalle hohe pH Werte des Elektrolyten. Speziell Ni-Fe basierte Katalysatoren zeigen eine überlegene Aktivität für die OER gegenüber einem breiten Spektrum von Metallkatalysatoren, wobei der Ursprung dieser hohen Aktivität bis heute weitestgehend unbekannt ist. Dies wiederum wäre von großer Bedeutung, um neue, hochaktive Anodenmaterialien herstellen zu können.

Die vorliegende Arbeit hat sich gezielt mit dem Aufstellen von Struktur-Aktivitätsbeziehung Ni-Fe Oxid und der Sauerstoffevolutionsreaktion beschäftigt, um ein neues Grundverständnis dieser Materialien zu gewinnen.

Kapitel 3 beschäftigt sich mit einer Studie bezüglich gemischter Ni-Fe Oxyhydroxide (OOH), um eine Struktur-Aktivitätsbeziehung in Bezug auf die Katalysatorkomposition, OER Aktivität und der lokalen Struktur aufstellen zu können. Ni-Fe-OOH wurden bereits umfassend untersucht, da in diesen Materialien die Katalyse in einem großen Volumen stattfindet und sie somit keinen passiven Kern besitzen. Folglich können sich alle Metallzentren des gesamten Volumens an der katalysierten Reaktion beteiligen. Dadurch können hohe intrinsische OER Aktivitäten beobachtet werden. Die hier verwendeten Katalysatoren wurden über eine solvothermale Methode hergestellt, da diese Methode eine ideale Möglichkeit des „scale-up“ bietet. Die OER Aktivitäten der Katalysatoren wurden, dem „Sabatier“ Aktivitätstrend folgend, als Funktion des Eisengehaltes abgebildet. Mit Hilfe einer quasi in-situ Röntgen-

Absorptionsspektroskopie (XAS) konnte der katalytisch aktive Zustand identifiziert werden. Ferner wurde die differenzielle elektrochemische Massenspektrometrie (DEMS) verwendet, um Ladungstransferverhalten zu erforschen. Dazu wurde der Ladungstransfer in das Produkt Molekül gegen den Ladungstransfer in den Katalysator, was zu einer Oxidationszustandsänderung des Metalls führt, bestimmt. Resultierend zeigte sich, dass es zur Stabilisierung des Ni-Atoms in einer niedrigen Oxidationsstufe durch das Fe kommt. Dies wird durch einen kinetischen Wettbewerb zwischen der Oxidation des Metalls (i) und der katalytischen OER (ii) begründet. Zeigt sich in (ii) eine erhöhte Geschwindigkeit des Prozesses im Vergleich zu (i), sollte Ni nicht in der oxidierten Form akkumulieren. Das würde auch die in der Literatur beschriebenen Abweichungen der Oxidationsstufen der Ni-Fe Katalysatoren erklären.

In *Kapitel 4* befasst sich mit der untersuchten OER Aktivität in einem weiten pH Bereich (pH 7-13) von auf Kohlenstoff geträgerten NiFe-OOH/C Katalysatoren. Zusätzlich wurde dafür ein pH-Aktivitätstrend aufgestellt. Zudem wurde auch die Korrosion des Metalls von den aktiven Zentren als Funktion des pH Wertes und dessen Aktivitätsverlust sowie dessen strukturell morphologische Veränderung während katalytischer Bedingungen behandelt.

In *Kapitel 5* wurde die Wechselwirkung zwischen Ni und Fe in Ni+Fe Katalysatoren untersucht. Diese Ni+Fe Katalysatoren wurden durch einfaches physisches Mischen von separat synthetisierten Ni(OH)₂ und Fe(OOH) Materialien hergestellt. Die physische Mischung zeigte die gleiche OER Aktivität wie der „Misch-Katalysator“. Mit Hilfe dessen wurde der Grad der Inkorporation diskutiert, um den Ursprung dieser Aktivitätssteigerung zu verstehen.

In *Kapitel 6* werden die geträgerten Ni-Fe-OOH/C mit den ungeträgerten NiFe Katalysatoren verglichen, um den Ursprung der hohen Aktivitätssteigerung durch das Kohlenstoffträgermaterial verstehen zu können. Hierfür wurden XAS Messungen verwendet, um dessen lokale atomare Strukturen und den Redoxzustand des Metalls zu bestimmen.

In *Kapitel 7* wurden Ni-Fe Oxid Nanokristalle Katalysatoren mit einer geringen Größenverteilung und in unterschiedlichen Formen hergestellt, um diese als „Model“ Materialien nutzen zu können. Resultierend daraus konnten die OER Aktivitäten von unterschiedlichen Oxidoberflächen untersucht werden, um diese mit einer „spezifischen“ Oberfläche in Verbindung zu setzen und mit den ursprünglichen Katalysatoren, welche eine große Volumenaktivität aufzeigen, zu vergleichen. Anschließend wird die Relevanz von elektrochemischen aktiven Arealen sowie der Einfluss des Oxidkerns und dessen Oberfläche diskutiert.

ACKNOWLEDGEMENT

First of all, I would like to thank the Unifying Concepts in Catalysis (UniCat) and the Berlin International Graduate School of Sciences & Engineering (BIG-NSE) for giving me this great opportunity to carry out my Dissertation work in Berlin. Many thanks to Dr. Dr. Jean-Philippe Lonjaret for the excellent organization. It has been a very nice time both scientifically and socially.

Second, thanks to my first supervisor, Prof. Dr. Peter Strasser, for excellent supervision and for a great time in the group. We had many valuable discussions that brought this work forward.

Then I would like to give a special thanks to Prof. Dr. Holger Dau, both as the main collaborator and as the second supervisor. Thanks for the assistance with the X-ray absorption spectroscopy and the valuable scientific discussions. The depth of this work would not have been achievable without your great support.

Gratitude to Prof. Dr. Karl Mayrhofer from Max Planck Institute (now Forschungszentrum Jülich) for the contribution as an external evaluator of this work.

Many thanks to Prof. Dr. Maria Andrea Mroginski for the contribution as a chairman in the evaluation process of this work.

Thanks to Dr. Petko Chernev, who has been one of the most valuable resources for this work. The customized software for data evaluation and the assistance with the XAS measurements have made it possible to achieve results and reach the goals within the given time frame.

Big time thanks to Jorge Ferreira de Araújo (we made a good team, didn't we) for the DEMS measurements!

I would also like to give a special thanks to Dr. Zenonas Jusys for the great collaboration and the work on DEMS. Thanks for the contributions to Chapter 6.

Another big time thanks to Manuel Gliech for many long night hours at the TEM microscope.

Thanks to Sören Dresch for volunteering as a Master thesis student and contributions to Chapter 3, 4, and 6.

Many thanks to Henrike Schmies for contributions to Chapter 6.

Thanks to Tobias Reier for SEM characterization.

Thanks to Dr. Chunhua Cui and Prof. Dr. Lin Gang for TEM characterization at the initial work-up stage.

Thanks to Prof. Dr. Raffaella Buonsanti and to Anna Loiudice for TEM characterization of materials in Chapter 7.

Thanks to Dr. Ralph Krähnert and Benjamin Paul for SEM characterization, and to Denis Bernsmeier for BET measurements. I hope you got you many nice long hours in the lab because of me.

Thanks to Dr. Arno Bergmann for excellent XRD support.

Thanks to Fang Luo for chemisorption measurements.

I would also like to thank the rest of the work group (no names forgotten) who made the time in Berlin worth all hard work. Thank you all, both present and past, you have all made the day's brighter, well the evenings as well...

Also gratitude to all people at TU Berlin who made a significant contribution to the construction work and made the daily practical things flow. Thanks also to the workshop and the glass blower for all your bright ideas and improvements.

Lastly but not forgotten, I would like to thank all of my family and friends who have been a great support. Without you, this would not have been an experience at all.

TABLE OF CONTENTS

Chapter 1. Motivation: *Prospects on Renewable Energy &*

<i>Electrochemical Water Splitting</i>	1
1.1. Current status on renewable energy	1
1.2. From natural to artificial photosynthesis	4
1.3. Oxygen evolution electrocatalysts – metal oxides to oxyhydroxides	6
1.4. Ni-Fe electrocatalysts	7
1.5. Theoretical considerations on electrochemical water splitting	9
1.6. Reactions mechanisms, OER intermediates, and scaling relations	10
1.7. Electrode kinetics	12
1.8. Motivation	14
1.9. Chapter overview	15

Chapter 2. Experimental

2.1. Synthesis of amorphous oxyhydroxides	18
2.1.1. Ni-Fe oxyhydroxide catalysts	18
2.2. Synthesis of Ni-Fe nanoparticles	20
2.2.1. Preparation of metal-oleate-complex (MOC)	21
2.2.2. Spherical Ni-Fe nanoparticles	21
2.2.3. Shape-selected Ni-Fe nanoparticles	21
2.2.4. Immobilization of Ni-Fe nanoparticles on carbon support	22
2.2.5. Annealing step	22
2.3. Physical characterization and elemental analysis	22
2.3.1. Inductively coupled plasma-optical emission spectroscopy (ICP-OES)	22
2.3.2. Total Reflection X-Ray Fluorescence (TXRF)	24
2.3.3. Transmission Electron Microscopy (TEM) and Energy Dispersive X-rays (EDX)	23
2.3.4. Scanning electron microscopy (SEM) and EDX elemental mapping	23
2.3.5. Powder X-ray diffraction (XRD)	23
2.3.6. Brunauer Emmet Teller (BET)	24

2.4. Electrochemical characterization	25
2.4.1. Rotating disk electrode (RDE) setup.....	25
2.4.2. Catalyst inks	26
2.4.3. Turnover frequency (TOF) calculations	26
2.4.4. Determination of redox electrons	26
2.5. Mass Spectrometry.....	27
2.5.1. Differential electrochemical mass spectrometry (DEMS).....	27
2.5.2. Online headspace Mass Spectrometry and Gas Chromatography	28
2.6. X-ray absorption spectroscopy (XAS).....	29
2.6.1. Sample preparation for quasi- in situ XAS	30

Chapter 3. Oxygen evolution reaction dynamics, faradaic charge efficiency, and the active metal redox states of Ni-Fe oxide water splitting electrocatalysts.....	31
Abstract.....	32
3.1. Introduction	33
3.2. Experimental	35
3.2.1. Synthesis of mixed Ni-Fe catalysts	35
3.2.2. Elemental analysis	35
3.2.3. Scanning electron microscopy (SEM) and energy dispersive X-ray (EDX) analysis.....	36
3.2.4. Powder X-ray diffraction (XRD)	36
3.2.5. Electrochemical characterization	36
3.2.5.1 Turnover frequency (TOF) and Ni redox charge calculations	37
3.2.6. Differential Electrochemical Mass Spectrometry	37
3.2.7. X-ray absorption spectroscopy (XAS)	38
3.3. Results & Discussion	40
3.3.1 Electrochemical activity, turnover frequency, voltammetric metal redox behavior	40
3.3.2. Faradaic charge efficiency derived from in-situ electrochemical mass spectrometry (DEMS).....	43
3.3.3 Compositional analysis, long-range order and SEM-EDX elemental mapping	46
3.3.4. Quasi-in situ X-ray absorption spectroscopy (XAS)	48
3.3.5. Correlation of activity, faradaic efficiency, and metal redox states	53
3.4. Conclusions	55

Supporting Information	58
------------------------------	----

Chapter 4. Dynamical changes of a Ni-Fe oxide water splitting catalyst

investigated at different pH	91
Abstract	92
4.1. Introduction	93
4.2. Experimental	94
4.2.1. Catalyst preparation	94
4.2.2. Physical characterization	94
4.2.3. Electrochemical characterization	95
4.2.4. Calculation of turnover frequency (TOF) and redox charge (Q)	96
4.2.5. Differential electrochemical mass spectrometry (DEMS)	96
4.3. Results & Discussion	98
4.3.1. Catalytic OER activity in pH 13, 9.2, and 7	98
4.3.2. Transmission electron microscopy (TEM) and selected area electron diffraction (SAED)	101
4.3.3. Catalyst composition at different pH	104
4.3.4. Differential Electrochemical Mass Spectrometry (DEMS)	107
4.4 Conclusions	109
Supplementary Information	111

Chapter 5. Formation of a highly active Ni-Fe water oxidation catalysts

by physically mixing Ni and Fe oxyhydroxides	120
Abstract	121
5.1. Introduction	122
5.2. Results and Discussion	124
5.2.1 Formation of a highly active Ni+Fe catalysts	124
5.2.2. SEM and EDX elemental composition	126
5.2.3. Quasi- in situ X-ray absorption spectroscopy (XAS)	128
5.3. Conclusions	132
Supporting Information	134

Chapter 6. The influence of carbon support on the oxygen evolution activity in amorphous Ni-Fe electrocatalysts	141
Abstract	142
6.1. Introduction	143
6.2. Results & Discussion	145
6.2.1. A comparison of different supports	145
6.2.2. The influence of carbon support	147
6.2.3. The effect of electrolyte pH	150
6.2.4. BET surface area	151
6.2.5. Short-term stability up to 1000 c	152
6.2.6. Mass spectrometric detection of oxygen	154
6.2.7. The catalytically active state	156
6.3. Conclusions	158
Supporting Information	160
Chapter 7. Electrochemical water oxidation on shape-selected Ni-Fe oxide nanocatalysts	172
Abstract	173
7.1. Introduction	174
7.2. Results & Discussion	176
7.2.1. Spherical Ni-Fe nanoparticles	176
7.2.2. Shape selected Ni-Fe nanoparticles	179
7.2.3. Optimization of annealing conditions	181
7.2.4. OER activity on shaped oxides	185
7.2.5. Stability test up to 1000 cycles	187
7.2.6. TEM and elemental composition after 1000 cycles	190
7.3. Conclusions	192
Supporting Information	193
Chapter 8. Summary & Outlook	197
8.1. Summary of Chapters 3-7	197

8.2. Outlook	201
List of Figures	202
List of Tables	217
APPENDIX I	219
List of publications	227
References	228

LIST OF ABBREVIATIONS

EIS	Electrochemical Impedance Spectroscopy
B _i	Borate buffer pH 9.2
CV	Cyclic voltammetry
DEMS	Differential Electrochemical Mass Spectrometry
EDX	Energy dispersive X-ray
EXAFS	Extended X-ray Absorption Fine Structure
FE	Faradaic efficiency
FT-EXAFS	Fourier Transformed Extended Absorption Fine Structure
GC	Glassy carbon
HC-MS	Head-space Mass Spectrometry
ICP-OES	Inductively coupled plasma atomic emission spectroscopy
MOC	Metal-oleate-complex
NP	Nanoparticle
OCP	Open circuit potential
OER	Oxygen Evolution Reaction
OL	Oleate
PCET	Proton coupled electron transfer
PCTFE	Polychlorotrifluoroethene
PDF	powder diffraction file
PEEK	polyether ether ketone
(K)P _i	Phosphate buffer pH 7
PS II	Photosystem II
PV	Photovoltaics
Q	Charge
RDE	rotating disk electrode
RHE	Reversible hydrogen electrode
rpm	revolutions per minute
SAED	Selected area electron diffraction
SEM	Scanning electron microscopy
STP	Standard temperature and pressure
TEM	Transmission electron microscopy
TOF	Turnover frequency
TPR	Temperature programmed reduction
TXRF	Total Reflection X-ray Fluorescence
XANES	X-ray absorption near-edge structure
XAS	X-ray absorption spectroscopy
XRD	X-ray diffraction
ICP-OES	Inductively coupled plasma atomic emission spectroscopy

Chapter 1

MOTIVATION

Prospects on Renewable Energy & Electrochemical Water Splitting

1.1. Current status on renewable energy

The increasing demand of energy requires development of alternative methods for energy production, utilization, conversion, and storage.¹ To make this process sustainable, a carbon-neutral cycle needs to be taken into use. This requires highly efficient catalysts for electrochemical water splitting and CO₂ electroreduction processes, which require technologically advanced materials that need to be optimized in terms of energy efficiency and production costs.²⁻¹⁸

The interplay between increasing levels of atmospheric greenhouse gases such as CO₂, CH₄, and N₂O, and the steadily increasing global temperatures is a rising concern.¹⁹⁻²³ The global energy consumption reported in 2013 was as high as 18 TW worldwide²⁰ with an annual increase of 2.6% driven by improving global economy, growing population and industrialization.²¹ The largest fraction of that energy currently comes from non-renewables such as oil and coal sources.²⁰ These are defined by sources with a long carbon cycle lifetime – Carbon sources that takes longer time to transform back to their original values than it takes for the atmosphere and oceans to heat up as a cause of accumulation of the combustion products in the atmosphere.

The correlation between atmospheric emissions and increased temperatures has been under debate. At the same time, scientific data and trends determined from gases trapped in the Antarctic ice cores from the past 800,000 yr consistently show a strong correlation between temperature and atmospheric levels of CO₂ and CH₄. Despite natural variation cycles of about 100,000 yr of increasing and decreasing levels as an effect of glacial-interglacial transition periods,^{22,23} the current atmospheric CO₂ and CH₄ levels far exceed past normal variation levels.^{22,23} The correlated global increasing global temperature hence is a matter of fact.

If the current CO₂ emissions proceed to increase with the current rate, the predicted increase in global temperature is estimated to 6 °C by 2050.²⁴ To limit this increase, a higher share of renewables would need to be introduced to the energy market. The renewables currently account for ~13 % of the total

energy supply which includes biomass (10 %), hydro (2.3%), direct solar (0.1%), geothermal (0.1%), wind (0.2%), and ocean energy (0.002%).²⁰ The contribution of renewables might appear low however is accounted for 21% of the total electricity generation in 2015,²⁰ yet not sufficient to slow down the emissions accumulating from the usage of carbon based resources.

A “closed energy cycle” where the consumption process results in regeneration of the original resource would cause net zero excess of carbon emissions. There are two scenarios to achieve such carbon-neutral cycle, either via the *hydrogen cycle* - or via the *carbon cycle*, where it is desirable to go through energy-conversion-storage pathways depicted in Figure 1.1. This scheme includes the hydrogen evolution reaction (HER) and carbon dioxide reduction (CO₂RR). In the *left hand cycle*, water (H₂O) is oxidized to protons (H⁺) and electrons (e⁻), which are combined (reduced) to hydrogen (H₂). In the *right hand cycle*, CO₂ is recaptured from the atmosphere and reduced via CO₂ electroreduction into hydrocarbons or oxygenates (*OR, where R can be H, OH, CH₃, CH₂CH₃).²⁵⁻²⁷ In both cases to achieve a closed cycle, water would act as the source of energy to drive the electroreduction processes into storable fuels. Therefore, the key process is the oxygen evolution reaction (OER) where water is oxidized to release the reducing equivalents (e⁻) needed for both the CO₂ and H₂ reduction processes.

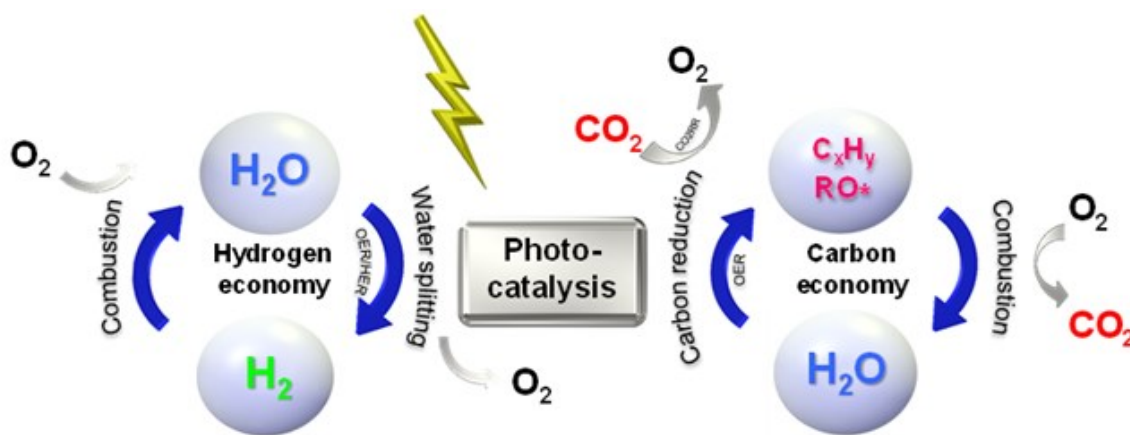


Figure 1.1. The hydrogen cycle versus the short-lifetime carbon cycle to produce carbon fuels. Water (H₂O) acts as the “key” source to provide the energy in the form of electrons (e⁻), and carbon dioxide (CO₂) is recaptured from the atmosphere, necessary to achieve net zero emissions. Integrated photovoltaics or photocatalysts could be used to drive the energy conversion at lowest possible overpotential, powered by solar energy.

Both cycles results in carbon neutrality, based on that the carbon source for the CO₂RR cycle is atmospheric CO₂. For other cycles such as consumption of biomass from plants, a carbon-neutral cycle is achieved though the principle that CO₂ is recaptured from the atmosphere on a short enough time scale according to the criteria for accounting as a renewable energy process.

In the energy scheme depicted in Figure 1.1 there are three key reactions; OER, HER, and CO₂RR. Each of these reactions require a certain energy to make the reactions thermodynamically downhill (will be further discussed in next section). This requires the development of efficient electrocatalysts that can make each of the reactions proceed at lowest possible minimal energy input above the thermodynamic equilibrium potential (denoted as overpotential, η). Due to thermodynamic limitations, we cannot escape a certain amount of excess energy required to break and form chemical bonds, despite utilization of efficient catalysts. For this purpose the optimal energy source would be solar energy, where the electrochemical water splitting process could be integrated with either photovoltaics (PV) or with “photocatalysts”, both which harvest solar energy to catalyze the reactions^{16,17,26,28-30}. Solar energy is our major source of energy which covers our yearly total energy demand within two hours of illumination (~12 TW per h reaches Earth)²⁴ assuming 100 % solar-to-energy conversion efficiency of a photovoltaic device. In the real case, the conversion efficiency of PVs are in the order of ~15 % today.^{16,29} To make the technology compatible on the market, the energy conversion needs to run with small energy-conversion losses and at low production costs. This would require cheap and preferably abundant materials and efficient catalysts optimally designed for both anodic and cathodic reactions. Hence, the key to a sustainable global economy lies in the understanding of how to harvest the energy of already existing energy resources and direct these into fuels in a way that the result is zero excess carbon emissions.

1.2. From natural to artificial photosynthesis

The oxygen (O_2) levels in the atmosphere are generated through water oxidation in plants, which takes place in Photosystem II, a large oxidoreductase enzymatic complex composed of more than twenty subunits. The active site for water splitting is a $3d$ transition metal complex, a manganese cluster (Mn_4CaO_5) with a cubane moiety, see Figure 1.2. The electrons released from water are transported to the acceptor side, and together with the protons further shuttled to participate in CO_2 reduction process. Molecular oxygen is released as a byproduct to the atmosphere. High resolution crystal structures have provided detailed information of the structure of the active site for water oxidation³¹⁻³⁵, the latest structure at 1.95 Å resolution obtained using a free electron laser by Suga et al.³⁶

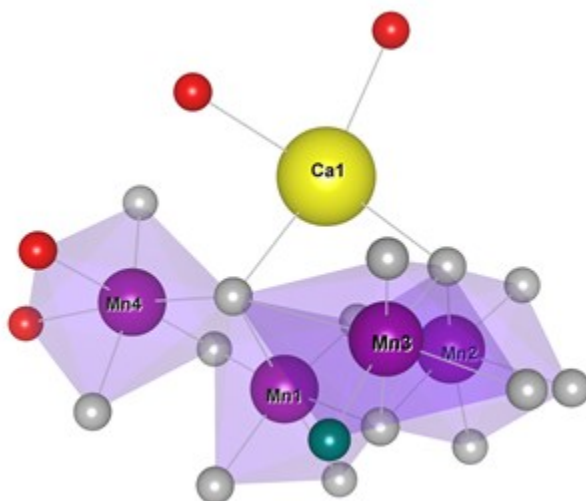


Figure 1.2. The catalytic water oxidation complex in photosystem II, a Mn_4O_5Ca cluster. Shown are Mn atoms labeled Mn 1-4 (purple), ligand-bound oxygen (O) (gray), water-bound O (red), Ca (yellow), and N (green). The atomic coordinates are taken from the structure provided by Suga et al.³⁶

The process of water splitting in Photosystem II takes place through four consecutive proton-coupled electron transfer (PCET) steps, denoted the S-state cycle. This includes a series of steps labelled S_n ($n = 0-4$), where O_2 release takes place on the $S_4^+ \rightarrow S_0^n$ transition. Briefly, light is absorbed and channeled to a special chlorophyll pair, P680, which is further oxidized to $P680^{++}$ as a redox potential of > 1.0 V.³⁷ This induces a series of charge transfer steps; the $P680^{++}$ oxidizes a closely located tyrosine amino acid (Y_z) to Y_z^* , which in turn extracts electrons from the Mn_4CaO_5 cluster. The Mn atoms are consecutively oxidized in PCET steps from Mn^{+3} to Mn^{+4} , which compensates for the charges of extracting electrons from H_2O .⁵ Two water molecules are oxidized in one complete cycle, after four electrons have been extracted from the Mn cluster, and in turn releases O_2 and $4 H^+$.

The key principle of artificial photosynthesis is to mimic the photocatalytic water splitting process, ideally coupled to harvesting solar energy. Challenges reside in achieving multistep accumulative electron transfer and charge separation, long-lived excited states, and minimal charge recombination. Many systems have been studied based on the “donor-sensitizer-acceptor” triad concept (see Figure 1.3)^{30,38-42}, including Ru^{II}(bpy)₃ sensitizers coupled to dinuclear Mn complexes studied by Borgström et al.⁴³ Other systems include porphyrin derivatives as sensitizers with linked co-catalysts⁴⁴. In case the system is not integrated with a co-catalyst, different electron acceptors are used for accumulation of the built up charges, such as fullerenes or secondary electron acceptors. Recent advances include a molecular synthetic analogue of the Mn₄CaO₅ cluster.⁴⁵

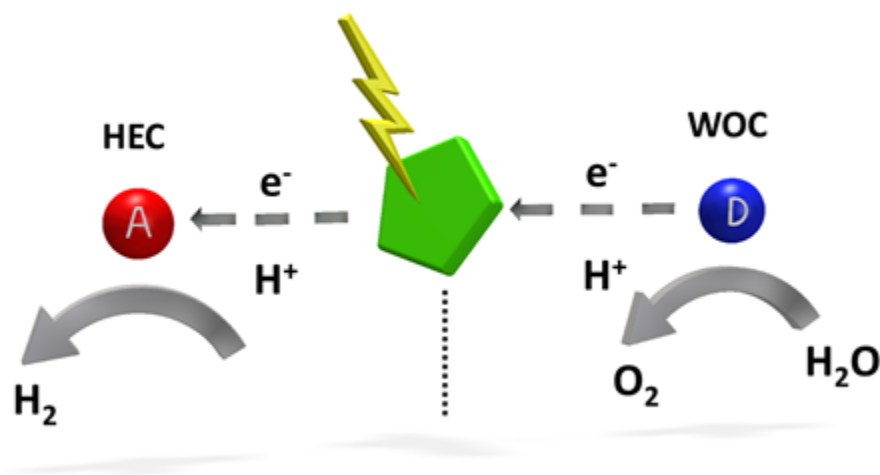


Figure 1.3. “Donor-sensitizer-acceptor” triad concept where the donor (D) represents an integrated oxygen evolution reaction (OER) catalyst and the acceptor (A) an integrated hydrogen evolution reaction (HER) catalyst. The OER releases protons (H⁺) and electrons (e⁻) which are directed via covalently linked π ligands to the HER acceptor side. The protons are there reduced to H₂, which should ideally be separated from the O₂ for instance via a membrane. The image is based on the concept presented in reference³⁰.

Today the concept of a photoelectrochemical cell is rapidly evolving, where semiconductor materials achieve both the light harvesting process, charge separation and water splitting, however more efficient integrated anode and cathode catalysts can be tuned towards a specific catalytic reaction.^{4,25} Honda-Fujishima presented a simple concept in 1972 of water splitting, where semiconducting TiO₂ was used to achieve water oxidation and coupled to a Pt cathode to generate H₂.⁴⁶ Grätzel and coworkers further developed the dye-sensitized solar cell (DSSC), where a dye is integrated at the semiconductor interface

which allows tuning of the optical properties.⁴⁷ However, water splitting using “conventional” solar cells (Si, CIGS, CdTe) is associated with high overpotentials. Recently, a perovskite based water-splitting PEC cell with an integrated Ni-Fe based bifunctional catalyst showed 12.3 % solar-to-hydrogen efficiency.¹⁶ A DSSC utilizing porphyrin dye and a Co^{III}(bpy)₃ redox couple also showed 13 % power conversion efficiency (PCE).²⁹

1.3. Oxygen evolution electrocatalysts

Fundamental understanding of reaction mechanisms of catalytic water splitting do in principle not require full coupling of the solar energy to the final product. The first studies on OER date back to 1947 when Hickling and Hill methodically investigated a series of metal based electrodes (Ag, Pt, Pd, Pb, Cd, Fe, Co, Ni, Cu) in alkaline electrolyte.⁴⁸ Work by Beer and coworkers resulted in the development of the dimensionally stable anode (DSA[®])⁴⁹ which utilized Ti based catalysts, the prototype of the electrolyzers used today. The development of smaller and more compact polymer electrolyte membrane (PEM) electrolyzers came as a result of Aerospace programs, which allowed for the use of membrane materials such as perfluorosulfonic acid (Nafion[®]) in proton exchange membrane fuel cells (PEMFC).^{50,51} Bockris⁵², Trasatti^{53,54} and Matsumoto⁵⁵ carried out work on oxides as OER catalysts. Trasatti also presented early work on the Sabatier principle where “volcano” activity trends were presented on a series of oxide surfaces (RuO₂, TiO₂).² The use of oxides as OER catalysts was a great success, however main work focused on expensive or scarce noble metals such as Ru, Ir, and Pt in acidic conditions, which also today remain actively used in commercialized fuel cells and electrolyzers.⁵⁶ Recent work has focused on reducing the noble metal content. Strasser and coworkers have demonstrated a series of effective methods to optimize catalytic activity and minimize material costs by mixing noble metals with non-noble metals such as IrNi, PtNi, IrNi, PtCu, PtCo, achieved by dealloying to form a noble metal rich surface and a non-noble richer inner core.⁵⁷⁻⁶⁰

In 2008, Kanan and Nocera presented an electrodeposited Co catalyst (CoCat) for the oxygen evolution reaction.³ The catalyst attracted a great deal of attention because it operated at neutral pH and showed “self-repair” abilities. Reports on similar materials dates back to the 1950s however were so far not as heavily investigated as water oxidation catalysts.⁶¹ The local atomic structure of the Co catalyst was determined soon after using X-ray absorption spectroscopy (XAS).^{62,63} This revealed that the Co centers were linked mainly via octahedrally coordinated oxygen atoms (edge-sharing CoO₆ octahedra), hence revealing similarities to the Mn₄CaO₅ cluster in PSII. Electrodeposited catalysts with similar local atomic structure consisting of mostly di- μ -oxo bridged metals have been reported also for Mn⁶⁴ and Ni⁶⁵.

Recently, Dau and coworkers introduced the concept of “volume activity”, demonstrating that the catalysis extends to the bulk in Co hydroxides.⁶⁶ Currently there are ongoing discussions regarding the importance of the amorphicity and the true nature of the active site. Meanwhile it has also been shown that spinel-type oxides convert into a hydrated state upon operation at catalytic potential. Bergmann et al. showed that a “reversible amorphization” takes place in Co_3O_4 , which transforms into a hydrated state during catalysis and converts back to its original state upon relaxation.⁶⁷ Reier et al. recently showed that the coverage of hydroxyl groups on the surface is a good descriptor for the OER activity in Ir-Ni oxide thin films.⁶⁸ Thin films of NiO electrodes have also been shown to convert into Ni oxyhydroxide under electrochemical conditioning.⁶⁹ The active state may be controlled by thermodynamic phase equilibrium, since oxides hypothetically should not be stable under alkaline conditions. Since determination of the amount and contribution of the amorphous material in oxides is more challenging compared to oxyhydroxides due to a larger amount of inactive bulk material, the fraction of electrochemically accessible sites might be below detection limits of many X-ray based techniques that are not enough surface sensitive. Therefore more advanced atomic structure techniques such as *operando* ambient pressure X-ray photoelectron spectroscopy (XPS) needs to be more easy available to extend the discussion to the atomic level of the oxide materials.⁷⁰

1.4. Ni-Fe electrocatalysts

The investigations of mixed Ni-Fe oxides as efficient electrocatalysts for electrochemical water oxidation started with the work of Corrigan in 1987, which showed that Fe impurities in NiOOH electrodeposited films increased the activity towards OER significantly.⁷¹ A great deal of important work that followed was carried out by Boettcher and coworkers, first nearly three decades later. Trotochaud et al. presented a method where all Fe impurities had been eliminated and thus the activity trends could be revised.⁷² This also showed that the original work of Bode⁷³ on Ni electrodes most likely was influenced by Fe impurities in the electrolyte, including the α/γ and β/β phase transformations included in the Bode scheme.^{74,75} However, work by Klaus et al. showed that despite removal of Fe impurities, formation of a β -NiOOH phase occurred under potential cycling, however was partly inhibited by the presence of Fe.⁷⁶

During recent years, several research groups have present a vast number of studies on the enhanced catalytic OER activity in mixed Ni-Fe catalysts.^{3,18,69,71,77-100} The activity has been clearly shown to follow the Sabatier principle showing a "volcano" activity trend as a function of Fe-content, where catalysts with a Fe content between 25-50 % Fe have showed most optimal OER activity. Discussions was raised concerning the solubility of Fe in the NiOOH phase, after indications that Fe was nucleating as a separate

phase in electrodeposited Ni-Fe(OOH) catalysts.⁸⁰ Previous attempts to determine the local atomic structure using X-ray synchrotron based techniques have been larger in number for electrodeposited Ni-Fe catalysts^{80,85,101-104} in comparison to chemically precipitated Ni-Fe catalysts.^{77,100,105-107} Worth to mention is the recent operando X-ray absorption spectroscopic study by Friebe et al., which identified the active state in electrodeposited Ni-Fe(OOH) as a function of Fe-content, and presented theoretical calculations showing that Fe is most likely to be the active site of catalysis.⁸⁰ This was closely followed by an X-ray absorption spectroscopic study on solvothermally synthesized Ni-Fe(OOH) catalysts presented in this work.¹⁰⁸ A recently study presented a first *operando* Mössbauer spectroscopy study successfully applied to Ni-Fe electrocatalysts.¹⁰³ Recent studies also provided through-film conductivity measurements of a series of 1st row transition metals.^{72,109} These measurements revealed a correlation between OER activity and conductivity.

Since this thesis mainly concerns work on the Ni-Fe electrocatalysts system, I will not go into further details here. Instead, I suggest that you read each scientific Chapter, which will guide you through the most important and recent aspects in the discussion of Ni-Fe as OER electrocatalysts.

What makes the Ni-Fe catalytic system so interesting. In principle, the local atomic environment is similar to that of other oxide based catalysts (Co, Ni, Mn) discussed in previous section (see Figure 1.4).

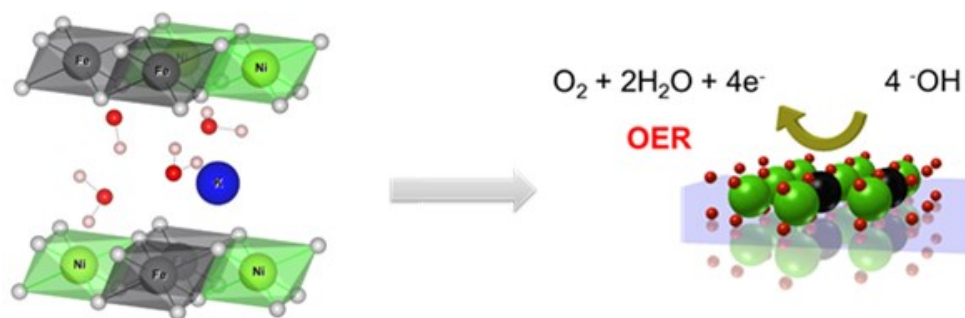


Figure 1.4. The structure of a layered Ni-Fe(OOH). The *left hand* image represent a small fragment demonstrating the interlayer spacing separating two sheets, with intercalated H₂O and K⁺. The *right hand* image demonstrate oxygen evolution reaction on a layer of Ni-Fe(OOH). Atomic coordinates are taken from α-Ni(OH)₂ (cif 9012316).

What appears to differentiate the Ni-Fe based oxyhydroxides is their superior OER activity in alkaline electrolyte. A glimpse into the metal oxidation states and local atomic structure in search for descriptors that regulates the OER activity is still at an early stage. Past studies on mixed Ni-Fe catalysts have also showed a significant number of differences concerning formal oxidation states of the respective metals. This awakes the question whether the family of related Ni-Fe catalysts all have a unified catalytic active

state, or does composition, phase, or other external factors such as catalyst support and pH hold important yet up to date, largely unexplored influences on the metal redox states and catalytic activity in mixed Ni-Fe catalysts. In this work, we will present detailed experimental data trying to approach these questions from a structural as well as mechanistic point of view.

1.5. Theoretical considerations on electrochemical water splitting

The first attempt of water electrolysis dates back to 1789 when van Troostwijk and Deiman reported decomposition of water into “combustible air”¹³, followed by the work of Volta and Nicholson and Carlisle^{110,111}. The water splitting reaction can be simply written according to equation (1.1).

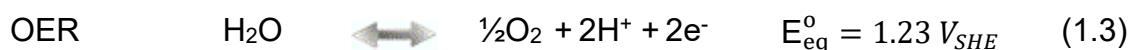


The minimum energy required to split one mole of water at reversible equilibrium can be described by the Gibbs free energy (ΔG_{298}^0) according to equation (1.2)

$$\Delta G_{298}^0 = n F E_{298,\text{eq}}^0 \quad (1.2)$$

where n represents the charge equivalents transferred per moles of water ($n = 2$), F is the Faraday constant, and $E_{298,\text{eq}}^0$ the standard equilibrium potential. The equilibrium potential for electrochemical water splitting is +1.23 V.⁵

The overall reaction can be divided into two half-cell reactions; the oxygen evolution reaction (OER) and the hydrogen evolution reaction (HER) according to equations (1.3) and (1.4)



where the values of E_{eq}^0 refer to the standard hydrogen electrode (SHE) which is defined at pH = 0 and a $\rho = 1$ bar.¹¹²

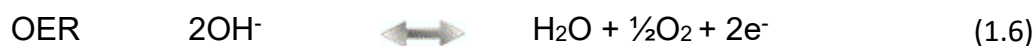
The total energy required to split one mole of water under standard temperature and pressure (STP) can be described according to equation (1.5)

$$\Delta G_{298}^0 = \Delta H_{298}^0 - T \Delta S_{298}^0 \quad (1.5)$$

where the Gibbs free energy change (ΔG_{298}^0) corresponds to +237 kJ mol⁻¹, the molar enthalpy change (ΔH_{298}^0) to +286 kJ mol⁻¹, and the entropy change ($T\Delta S_{298}^0$) to 49 kJ mol⁻¹ associated with heat from the surroundings. The absence of an additional heating term would result in an equilibrium potential of 1.48 V.^{5,112} The electrochemical water splitting process at room temperature between 1.48 and 1.23 V hence would be an endothermic process.⁵

1.6. Reactions mechanisms, OER intermediates, and scaling relations

The half-cell reactions of electrochemical water splitting under acidic conditions were described in equations (1.3)-(1.4), whereas the half-cell reactions in alkaline electrolyte can be written according to equations (1.6)-(1.7)

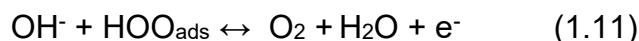
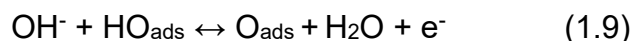
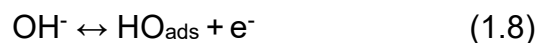


The mechanistic implications of the oxygen evolution reaction on oxide surfaces is assumed to comprise elementary reaction steps with adsorbed intermediates, including four consecutive proton-coupled electron transfer (PCET) steps.^{5,6,113} The considered adsorbed OER intermediates, HO_{ads} , O_{ads} , and HOO_{ads} ⁶, which in acidic electrolyte or alkaline electrolyte can be written according to equations (1.8)-(1.11)

Acidic conditions



Alkaline conditions



Whether these reactions solely include concerted steps or if some of the steps are decoupled have been under discussion, as well as if the adsorbed species include oxygen species of superoxo character.¹¹⁴ Universal scaling relations between chemically adsorbed species, where the binding energies of the adsorbed OER intermediates follow a linear scaling relation, have been reviewed in detail.¹¹⁵⁻¹¹⁷ This allows for determination of the differences in free energies which is achieved through first-principles quantum chemical and density functional theory (DFT) computational methods.¹¹⁸ The Gibbs free energies of each of the involved reaction intermediate can be described as four single-electron elementary steps as shown in Figure 1.5a.

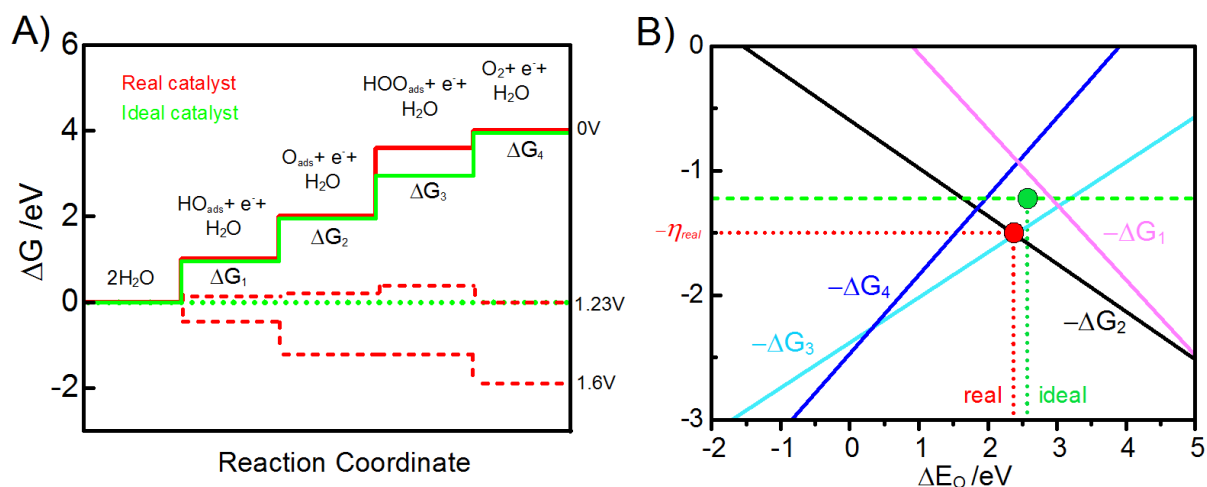


Figure 1.5. (a) Gibbs free energy diagram for electrochemical water oxidation at different electrode potentials¹¹⁹. The associated OER intermediates (HO_{ads} , O_{ads} , HOO_{ads}) shown for alkaline conditions. The solid lines represent the Gibbs Free reaction energies at different electrode potentials indicated on the *right axis* **(b)** Universal scaling relation between the OER intermediates¹¹⁹. The solid lines represented the Gibbs free reaction energies and the dotted lines an example of the ideal and the real case in terms of overpotential.

In Figure 1.5a, the ideal catalyst has equally spaced energy levels (green solid line) which under applied equilibrium potential would result in a theoretically zero energy barrier (green dotted line). The adsorption intermediates however scale to each other, so if one changes the others will also change. This scaling relation will make the ideal catalyst case almost impossible to achieve and as a result, the activity will follow a “Volcano” type activity trend as shown in Figure 1.5b. The key is to understand the origins of the scaling relation to make practical improvements towards optimal catalyst performance. Different oxide surfaces show different scaling relations, meaning that the OER adsorption intermediates have different interactions with the catalyst surface. For this, one would have to find descriptors that is controlling the adsorption energies of different intermediates. The boundaries that appear as the

theoretical top of the volcano may be possible to move further, to “cheat” the scaling relation. This could for instance be visualized by introducing “non-proportionality” to the catalyst surface or subsurface, such as dopants or extending the structure into a 3D framework. However, this is not widely understood and both experimental examples and theoretical calculations would be needed to reach an understanding of what is possible to achieve.

1.7. Electrode kinetics

An electrochemical reaction under equilibration conditions is strongly dependent on the applied electrode potential. A faradaic half-cell reaction can be described according to equation (1.12)



The Butler-Volmer equation relates the current to the electrode potential and can be described according to equation (1.13) ¹²⁰

$$j = j_0 \left[\exp\left(\frac{(1-\beta)nF}{RT}\eta\right) - \exp\left(-\frac{\beta nF}{RT}\eta\right) \right] \quad (1.13)$$

Where j is the sum of the anodic and the cathodic current densities ($j = j_a + j_c$), j_0 = exchange current density, n = number of electrons transferred in the reaction, F is the the Faraday constant, R the universal gas constant, T the temperature, η the overpotential, and β the symmetry factor (commonly assumed as 0.5 for a symmetric reaction).

Assuming that one of the reactions (anodic or cathodic) is neglectible to the electrode potential, the Butler-Volmer equation for the respective processes can be separated and simplified according to equations (1.14)-(1.15).

$$\text{Anodic} \quad j_a = j_0 \left[\exp\left(\frac{(1-\beta)nF}{RT}\eta\right) \right] \quad (1.14)$$

$$\text{Cathodic} \quad j_c = j_0 \left[\exp\left(-\frac{\beta nF}{RT}\eta\right) \right] \quad (1.15)$$

The overpotential can be solved by taking the logarithm to generate the Tafel equation according to equation (1.16)

$$\eta = \left(2.303 \frac{RT}{\beta n F}\right) \cdot \log\left(\frac{j}{j_0}\right) \quad (1.16)$$

The current flux at the electrode surface can be described as in equation (1.17)¹²⁰

$$i = nFAD \left(\frac{\delta C_O}{\delta y} \right)_{y=0} \quad (1.17)$$

In rotating disk electrode(RDE) experiments, a diffusion controlled current under limiting current conditions ($i = i_{l,c}$), the equation can be written as the Levich equation according to equation (1.18).¹²⁰

$$i_{l,c} = 0.62 nFAD^{2/3} \omega^{1/2} \nu^{-1/6} C \quad (1.18)$$

where D = Diffusion coefficient, C = analyte concentration, ω = angular rotation rate of electrode, ν = viscosity, A = electrode area.

As discussed in previous section, the oxygen evolution reaction is considered as four consecutive single-electron transfer steps as shown in equations (1.8)-(1.11). Rossmeisl and coworkers showed based on computational calculations that each of the elementary steps is associated with different adsorption energies between the OER intermediates and the surface, also dependent on the applied electrode potential¹¹⁷. The origin of the thermodynamic overpotential could be described as the elementary step that is the last step to maintain a positive reaction Gibbs free energy, which is the step that is the last to attain a negative Gibbs free energy, the prerequisite for the overall reaction to proceed. However, once the reaction proceeds at a certain potential where all elementary steps have a negative Gibbs free energy, the “potential-limiting step” may not be the step that is determining the overall rate of the reaction.⁵ That is, once all elementary steps are negative, other processes such as “kinetic overpotential” could instead limit the overall rate. Hence, it should be kept in mind that the definition of a kinetically rate-determining step in terms of the “slowest step” may not necessarily equal the thermodynamic concept “potential determining step”.

1.8. Motivation

The overall goal of this work is to establish structure-activity trends in mixed Ni-Fe oxides as catalysts for the electrochemical oxygen evolution reaction. Throughout, we are methodically searching for factors that are controlling the catalytic activity.

What makes the Ni-Fe catalyst actually interesting is that in addition to its high oxygen evolution activity, it shows a quite complex redox chemistry with natural phase changes occurring under catalytic potential. The Ni-Fe oxyhydroxide is an intercalation compound that host both electrolyte and ions in between stacked layers. The structure can show different degree of stacking faults, which makes the structural characterization challenging. The local atomic structure is octahedrally coordinated $[MO_6]$ units. This is similar to Nature's own water oxidation catalyst, the $MnCaO_4$ cluster in the catalytic oxygen evolving complex in Photosystem II. The binary combination of Ni-Fe, in comparison to other studied non-noble metal OER catalysts (Mn, Co) is the exceptional catalytic activity in alkaline electrolyte. The Ni-Fe catalyst hence appear as one of the most prominent non-precious solid-state electrocatalysts.

In this work, we have mainly studied the Ni-Fe oxyhydroxide (OOH) catalyst, which is thought to have catalysis extending to the bulk. This facilitate characterization using bulk methods. A vast scope of studies helped us to establish a fundamental understanding. Yet we found plenty of unexplored areas, all which we tried to approach from our own unique point of view. In the later part, we also widened our investigations to more well-defined round and shaped oxide surfaces. With this, we aim to and to provide a new perspective and to complement the scarce number of studies on shape-selected Ni-Fe oxide nanoparticles and its implementation as oxygen evolution electrocatalysts.

1.9. Chapter overview

Below follows a brief summary and overview of each Chapter presented in this work.

- **Chapter 1: Introduction & motivation**

- **Chapter 2: Experimental**

- **Chapter 3**

Title: Oxygen evolution reaction dynamics, faradaic charge efficiency, and the active metal redox states of Ni-Fe oxide water splitting electrocatalysts

This chapter has been reprinted with permission from the American Chemical Society as the latest accepted version of a published Journal article. Copyright (2016) American Chemical Society.

(Görlin, M.; Chernev, P.; Ferreira de Araújo, J.; Reier, T.; Dresch, S.; Paul, B.; Krähnert, R.; Dau, H.; Strasser, P. *Journal of the American Chemical Society*, 2016, 138, 5603. DOI: 10.1021/jacs.6b00332)

URL: <http://dx.doi.org/10.1021/jacs.6b00332>

Contribution: I wrote the manuscript, carried out main parts of the experiments, and made all figures

The overall goal with this Chapter was to achieve fundamental understanding of the structure-activity relationship of solvothermally prepared Ni-Fe(OOH) catalyst with various composition. This included X-ray absorption spectroscopy (XAS) to deduce the local atomic and metal redox states of as-prepared catalysts and under catalytic potential. The chapter also includes electrochemical mass spectrometry to determine faradaic charge injected into catalyst redox states and product formation. The Chapter deals with reaction dynamics and redox state changes.

- **Chapter 4**

Chapter title: Dynamical changes of a Ni-Fe oxide water splitting catalyst investigated at different pH

This chapter has been reprinted with permission from Elsevier as the latest accepted version of a published Journal article. Copyright (2016) Elsevier.

(Görlin, M.; Glied, M.; Ferreira de Araújo, J.; Dresch, S.; Bergmann, A.; Strasser, P. Dynamical changes of a Ni-Fe oxide water splitting catalyst investigated at different pH, *Catalysis Today*, 2015, 262, 65. DOI: 10.1016/j.cattod.2015.10.018)

URL: <https://doi.org/10.1016/j.cattod.2015.10.018>

Contribution: I wrote the manuscript, carried out main parts of the experiments, and made all figures

Here we studied the activity of a carbon supported Ni-Fe/C catalyst in different electrolytes and pH; in KOH pH 13, B_i pH 9.2 and KPi pH 7. Transmission electron microscopy (TEM), selected area electron diffraction (SEAD), elemental analysis was used to track both activity, and compositional-morphological changes associated with the different electrolytes.

- **Chapter 5**

Chapter title: Formation of a highly active Ni-Fe water oxidation catalysts by physically mixing Ni and Fe oxyhydroxides

As manuscript, unpublished

Contribution: I wrote the manuscript, carried out main parts of the experiments, and made all figures

This Chapter includes studies of physical mixtures of Ni(OH)₂ and Ni(OOH) catalysts that were mixed post-synthesis. A high catalytic activity could be achieved solely by mixing two separate Ni and Fe catalysts. There were no earlier methodical reports on physically mixed Ni+Fe catalysts, and therefore it was of high interest both for fundamental understanding of the origins of the high activity at Ni-Fe sites, and for practical applications where a simple preparation method is desirable. X-ray absorption spectroscopy was employed to correlate structural parameters with local atomic structure and the degree of Fe incorporation.

- **Chapter 6**

Chapter title: The influence of carbon support on the oxygen evolution activity in amorphous Ni-Fe electrocatalysts

Parts of this chapter has been reprinted or adapted with permission from the American Chemical Society as a published Journal article. Copyright (2017) American Chemical Society.

(Görlin, M.; Ferreira de Araújo, J.; Schmies, H.; Bernsmeier, D.; Dresp, S.; Gliech, M.; Jusys, Z.; Chernev, P.; Kraehnert, R.; Dau, H.; Strasser, P. Tracking Catalyst Redox States and Reaction Dynamics in Ni–Fe Oxyhydroxide Oxygen Evolution Reaction Electrocatalysts: The Role of Catalyst Support and Electrolyte pH. *Journal of the American Chemical Society*, 2017, 139, 2070. DOI: 10.1021/jacs.6b12250)

URL: <http://dx.doi.org/10.1021/jacs.6b12250>

Contribution: I wrote the manuscript, carried out main parts of the experiments*, and made all figures

** Related work to this Chapter has been published as part of a Master of Science thesis by Sören Dresp, titled "Synthese und Charakterisierung von Metalloxiden zur elektrokatalytischen Wasserspaltung" at Technische Universität Berlin (2013).*

This Chapter relates back to previous investigations in Chapter 3-4. We carried out extended investigations of both unsupported Ni-Fe catalysts and carbon supported Ni-Fe/C catalysts. We also investigated other supports including metal oxide supports. Measurements were carried out at different catalyst composition, catalyst loading, and electrolyte pH. We were striving to relate effects of external influences to properties such as catalyst redox states, local atomic structure, and catalytic activity. We also investigated BET surface area, faradaic efficiency, and evaluated stability up to 1000 potential cycles.

- **Chapter 7**

Title: Electrochemical water oxidation on shape-selected Ni-Fe oxide nanocrystal catalysts

As manuscript, unpublished

Contribution: I wrote the manuscript, carried out main part of the experiments, and made all figures

Here we started to explore the concept of "model oxide surfaces" in order to explore the influence of a different underlying oxide subsurface. We used the metal-oleate-complex route to obtain Ni-Fe nanocrystals with a small size distribution. By varying reaction conditions we could tune the shape. We further investigated oxygen evolution activity in order to deduce what parameters that appeared to control the activity. We also addressed shape stability before and after catalysis using TEM to observe how stable the surfaces were.

Chapter 2

EXPERIMENTAL

2.1. Synthesis of amorphous oxyhydroxides

2.1.1. Ni-Fe oxyhydroxide catalysts

Ni and Fe catalysts were prepared solvothermally using microwave assisted synthesis.¹²¹ The Ni(OH)₂ catalyst was prepared from a solution of 0.1 M Ni(NO₃)₂ x 6H₂O (99.999% trace metals basis, ALDRICH) and the Fe(OOH) catalyst from 0.1 M Fe(acac)₃ (99.5% trace metal basis, ALDRICH) solution, dissolved in benzyl alcohol (Puriss, 99-100.5%). 4.4 mL of the precursor solutions were mixed with 1 mL of 10 mM 1,2-Benzenediol (>99%, ALDRICH) to a total volume of 20 mL. The reaction mixtures were sealed in special autoclave vials (Anton Paar) and heated to 190 °C for 15 min with a ramping step of 16.5 °C/min (see Figure 2.1). The reactions were quenched by cooling to room temperature. The solid products were collected by washing five times with high purity ethanol using with repetitive centrifugation at 7500 rpm. The collected materials were freeze-dried and stored under inert atmosphere.

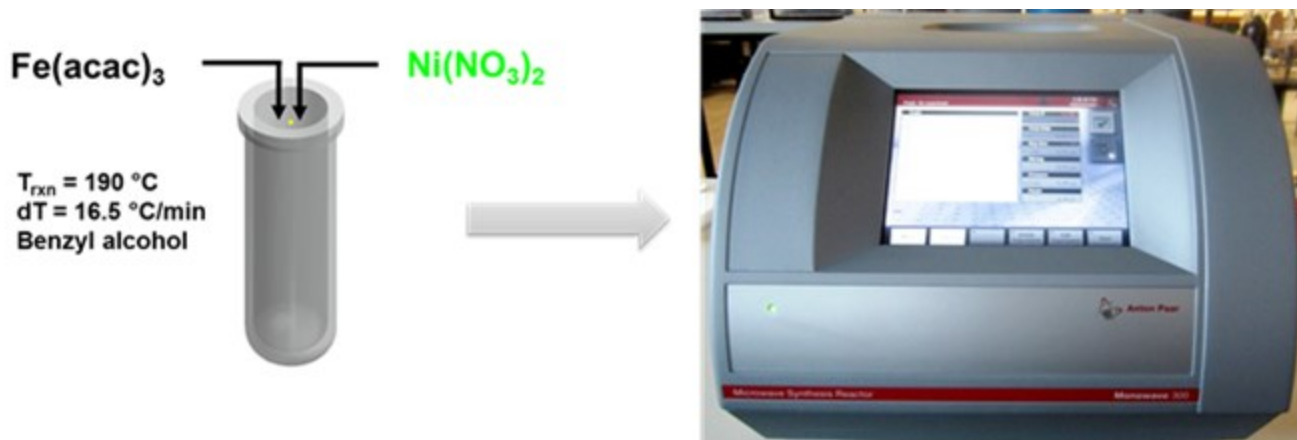


Figure 2.1. Microwave synthesis; *left hand* microwave vial, and *right hand* Anton Paar Monowave 300.

2.1.1.1. Fe-Free Ni catalyst

To minimize the Fe impurities in the Ni(OH)₂ catalyst the chemicals were purified prior to the synthesis according to the method reported by Trotochaud et al.⁷² And additional Fe-Free Ni(OH)₂ catalyst was synthesized without addition of 1,2-Benzenediol using the same conditions.

2.1.1.2. Physically mixed Ni+Fe catalysts

Were prepared by post-mixing inks of the parental Ni and Fe oxyhydroxides prepared as described in section 2.1 above. To form the Ni+Fe catalyst, a catalytic voltage was applied at 1.63 V_{RHE} for 30 min.

Spherical Ni-Fe oxyhydroxide nanoparticles were synthesized using the same reaction conditions and solvent but with additions of 10 mM 1,2-tetradecanediol (Sigma-Aldrich), 10 mmol oleic acid (Ph.Eur., Fluka), and 10 mM citric acid. The reaction mixtures were sealed in autoclave vials (Anton Paar) and heated to 190 °C for 15 min with a ramping step of 16.5 °C/min using a Monowave 300 autoclave (Anton Paar). Carbon supported catalysts were prepared by addition of estimated 80 wt % Vulcan XC-72r post synthesis. The catalysts were slowly added to the carbon mixture dissolved in ethanol (EtOH) under sonication, and left for additional 30 min sonication and then stirring for 24 h. The products were collected and washed several times with high purity EtOH and Milli-Q water (> 18 MΩ cm) using repeatedly centrifugation at 7500 rpm. The samples were freeze dried and stored as powders under inert atmosphere.

2.1.1.3. Microwave conditions

The reaction mixtures were sealed in autoclave vials (Anton Paar) and heated to 190 °C for 120 min with a ramping step of 16.5 °C/min using a Monowave 300 autoclave (Anton Paar).

2.1.1.4. Immobilization on support

Catalysts were immobilized on different supports; Vulcan XC-72r, oxidized carbon nanotubes (oxCNTs), or antimony doped tin oxide (ATI) according to the same method. The catalysts were slowly added to ~ 80 wt % of the support dispersed in EtOH by slowly dropping the catalyst under sonication. Catalyst-support mixtures were left for additional 30 min sonication and then afterwards stirring for 24 h. The products were collected and washed several times with high purity EtOH and Milli-Q (> 18 MΩ cm) using repetitive centrifugation at 7500 rpm. The last step included additions of a few milliliters of Milli-Q water to the ethanol to obtain a more fine powder. The samples were freeze dried and stored as powders under inert atmosphere until use.

Oxidized carbon nanotubes (oxCNTs) were prepared according to a modified version of Hummers method graphitic oxide^{81,122}. Briefly, 308.86 mg of CNTs (Baytube) were calcined at 500 °C for 1 h. The nanotubes were afterwards washed with 70 mL of 10 % HCl. The CNTs were product redispersed in 23 mL of concentrated H₂SO₄ in a 250 mL round bottom flask and stirred at room temperature for ~ 15 h. Following, 2.8 g of KMnO₄ was added to the nanotubes, the temperature raised to 40°C, and stirred for 30 min. Then, 5 mL of Milli-Q water was added two times separated by 5 min. After additional 5 min waiting time, 50 mL of Milli-Q water was added and left for 15 min before the flask was removed from the heat. Additions of the 140 mL of ~ 2 % H₂O₂ were used to quench the reaction. The CNTs were washed 5 times with 5% HCl solution and freeze dried overnight. The oxCNTs were stored under inert atmosphere until use.

2.2. Synthesis of Ni-Fe nanoparticles

The Ni-Fe oxide nanoparticles were prepared via the metal-oleate-complex (MOC) route in a two-step approach described previously.^{123,124} A three-neck bottle setup were used under reflux conditions and protective N₂ atmosphere, see Figure 2.2 below.

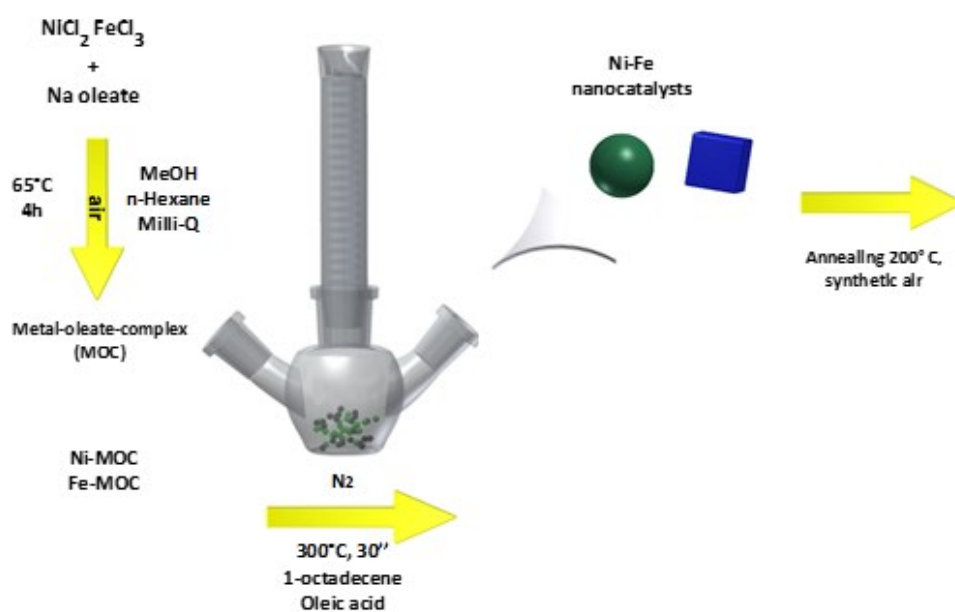


Figure 2.2. The synthesis setup for the metal-oleate-complex (MOC) route to highly crystalline Ni-Fe oxide nanoparticles.

2.2.1. Preparation of metal-oleate-complex (MOC)

Metal oleate complexes (MOCs) were prepared by mixing 5 mmol of $\text{NiCl}_2 \cdot 6\text{H}_2\text{O}$ (99.5% Trace metal basis, Aldrich), 5 mM of FeCl_3 -anhydrous (98%, Alfa Aesar), and 25 mmol of sodium oleate (Na-OL) ($\geq 82\%$ fatty acids, Sigma). The amount of Na-OL was based on the coordination number of the respective metals; two times the molar Ni and three times the molar Fe. The Ni-OL was prepared either as one-pot synthesis or as separate oleate complex precursors. The metal oleate mixtures were dissolved in 15 mL of Milli-Q water ($> 18 \text{ m}\Omega \text{ cm}$), 20 mL of methanol (anhydrous, 99.9%, Alfa Aesar), and 35 mL of n-Hexane (99%, Alfa Aesar) in a 250 mL round bottom flask, and heated to $\sim 65 \text{ }^\circ\text{C}$ for 4h under reflux conditions. After cooled down to room temperature, the colored upper organic phase containing the metal-oleate-complex was collected and washed five times with Milli-Q water to remove excess of salts. The total metal content of the oleate complexes was determined using ICP-OES.

2.2.2. Spherical Ni-Fe nanoparticles

Nanoparticle synthesis followed by pipetting the Ni and Fe metal oleate complexes in a 100 mL three-neck bottle flask. The total amount of metal was $\sim 1.5 \text{ mmol}$ determined by ICP-OES. The hexane phase was evaporated off by heating to $115 \text{ }^\circ\text{C}$ for typically 1h. The dried metal oleate complexes were redispersed in 40 mL of 1-octadecene (Tech. 90%, Alfa Aesar) and additions of 0.25 mL of oleic acid (0.8 mmol) (Ph.Eur., Fluka) under stirring. The reaction mixture was heated to $160 \text{ }^\circ\text{C}$ under N_2 protective atmosphere and held for 20 min to evaporate water. The reaction mixture was then heated to $300 \text{ }^\circ\text{C}$ by ramping $5 \text{ }^\circ/\text{min}$, and kept there for typically 30 min. The reaction usually turned turbid and blackish when the temperature approached $300 \text{ }^\circ\text{C}$. The reaction was subsequently cooled down to room temperature using a water bath.

Catalysts were also prepared using microwave-assisted autoclave synthesis where a faster ramping step ($18\text{-}70^\circ\text{C}/\text{min}$) could be applied. The reaction mixtures were then degassed with N_2 before sealed in the autoclave vial (Anton Paar), and heated to $300 \text{ }^\circ\text{C}$ using a Monowave 300 autoclave (Anton Paar).

2.2.3. Shape-selected Ni-Fe nanoparticles

Shaped Ni-Fe nanoparticles were synthesized according to the same principle as described for spherical nanoparticles in section 2.2.2 above but with additions of tertiary or quaternary ammonium salts or Na-OL to control the nucleation and growth step, as have been described previously to yield shaped Fe nanoparticles.¹²⁵ Cubic Ni-Fe nanoparticles were synthesized by additions of Tetraoctylammonium bromide (TOBr) (98 %, Alfa Aesar) to a ratio of 2:1 of TOBr:MOC in 1-octadecene. Cubic Ni-Fe nanoparticles were also prepared by additions of Na-oleate salt to a molar ratio 2:1 of Na-OL:MOC in

Squalene (98%, Alfa Aesar). Octahedrally shaped nanoparticles were synthesized by additions of 1:1 molar ratio of TOBr:MOC in 1-octadecene. Nanoparticles were also prepared by mixing 1-Hexadecyltrimethyl ammonium bromide (TMBBr) (98 %, Alfa Aesar) with the MOC in squalene to a molar ratio of 2:1 of TMBBr:MOC. The reaction solutions followed the same synthesis procedure as described for the spherical nanoparticles in section 2.2.2. The nanoparticles were supported on Vulcan XC-72r, and washed and freeze-dried as described above.

2.2.4. Immobilization of Ni-Fe nanoparticles on carbon support

Nanoparticles were prepared by slowly pipetting the reaction solution to ~250 mg (~80 wt %) Vulcan XC-72r (Cabot) dispersed in 40 mL n-Hexane and 20 mL ethanol under sonication. The nanoparticle-carbon mixture was left for additional 30 min in the sonication bath and for additional 24h under magnetic stirring. The supported nanoparticles were washed five times in 15 mL of hexane and precipitated by additions of the same amount of high purity ethanol; by repetitive centrifugation at 7500 rpm for 10 min. In the last washing step, the nanoparticles were dissolved in 20 mL of ethanol and ~2 mL of Milli-Q water to make a fine powder. Unsupported nanoparticles followed the same washing procedure. The carbon-supported nanoparticles were cooled in liquid N₂ for 10 min before freeze-dried. The powders were stored under inert atmosphere until use.

2.2.5. Annealing step

To remove the capping ligands from the oleate synthesis, the carbon-supported nanoparticles were heated in a tubular quartz furnace with a controlled atmosphere of synthetic air to 200°C using a ramping step of 10°C/min. An annealing temperature study was carried out between temperatures of 180 to 700°C. The optimal annealing temperature was selected based on the highest catalytic activity for the oxygen evolution reaction (OER).

2.3. Physical Characterization and elemental analysis

2.3.1. Inductively coupled plasma-optical emission spectroscopy (ICP-OES)

ICP-OES was used to determine the metal content of the as-synthesized catalyst powders, used for calculations of total metal loadings in the catalyst inks for the rotating disc electrode measurements. Data was collected using a Varian 715-ES spectrometer coupled to a CCD detector. The samples were digested in an acid mixture of HNO₃:H₂SO₄:HCl to a ratio of 1:1:3 and heated to 180 °C for 15 min using microwave irradiation. The sample probes were diluted with Milli-Q water (< 18 mΩ cm). Standard ICP solutions with known concentrations of Ni and Fe (Sigma-Aldrich) were co-analyzed with the samples.

2.3.2. Total Reflection X-Ray Fluorescence (TXRF)

Total Reflection X-Ray Fluorescence (TXRF) analysis was used to quantify the metal loading dealing with small amounts, example the total amount of metal in the catalyst before and after an electrochemical potential cycling protocol. The catalysts were dissolved by dipping the electrode tip in in 300 μl of HCl (37 %, Merck) under sonication for ~ 10 min. Afterwards, the dissolved catalyst was rested in the HCl for at least ~ 2 h to make sure all metal was dissolved. Additions of the same amount (300 μl) of Ga-standard (Merck) of a concentration of 1 mg/mL, allowed for quantitative determination of the metal content. The analysis was acquired using a PicoTAX spectrometer with a 40 kV using a Si-drift detector (Röntec).

2.3.3. Transmission Electron Microscopy (TEM) and Energy Dispersive X-rays (EDX)

Analysis were measured using a FEI Tecnai G² Microscope 20 S-Twin with a LaB₆-cathode at 200 kV accelerating voltage (ZELMI Centrum, Technical University of Berlin). Catalyst powders were re-dispersed in 2-propanol by ultrasonication and drop-dried on a Cu-grids coated with Lacey carbon. TEM images were analyzed using software packages from ImageJ and GatanMicroscope Inc. Selected area electron diffraction (SAED) and energy dispersive X-ray spectroscopy (EDX) were analyzed at local spots using the build in detector unit. The intensities were estimated from the *K*-lines.

Selected catalysts investigated after potential cycling, were dissolved in 2-propanol under sonication prior to analysis.

2.3.4. Scanning electron microscopy (SEM) and EDX metal mapping

SEM images of samples drop-casted on polished glassy carbon electrodes were acquired in secondary electron mode using a JEOL JSM-7401F high resolution field emission SEM operated at 10 kV or, respectively, 15 kV, if the images were acquired in the context of energy dispersive X-ray (EDX) spectroscopic measurements. EDX analysis (including elemental mapping and line-scans) was measured in the same microscope using the EDX detector unit (Quantax 400, BrukerAXS Microanalysis GmbH, Germany). The working distance was 12 mm for EDX quantifications for elemental mapping and line-scan analysis. Quantifications of the Ni and Fe contents were obtained from the *K* lines.

2.3.5. Powder X-ray diffraction (XRD)

XRD was recorded using Bruker D8 advance powder diffractometer (Bragg-Brentano geometry), with a Cu *K* _{α} source, a variable divergence slit (6mm) and position sensitive detector. Data were recorded between 10° to 80° 2 θ with a step size of 0.038°.

2.3.6. Brunauer Emmet Teller (BET)

N₂ adsorption isotherms to determine Brunauer Emmet Teller (BET) specific surface area was measured in a Quantachrome Autosorb-1-C instrument. The samples were outgased in vacuum at 70 °C for ~22 h prior to the measurement. The adsorption was carried out at 77 K in a relative pressure range of

$$\frac{p}{p^0} = 0.08 - 0.3.$$

2.4. Electrochemical characterization

2.4.1. Rotating disk electrode (RDE) setup

The activity for the oxygen evolution reaction was measured in a rotating disk electrode setup (RDE) in a 3-electrode setup using a glassy carbon working electrode ($\Phi = 5$ mm), a reversible hydrogen reference electrode (RHE), and a Pt-mesh as counter electrode, see Figure 2.3. The measurements were recorded on a GAMRY reference 3000 or 600 potentiostat. The electrolyte concentration was 0.1 M KOH (semiconductor grade, 99.99% trace metals basis, Aldrich), in some cases further purified using the method reported by Trotochaud et al.⁷² The rotation speed was 1600 rpm during CV scans and 1600 or 2200 rpm during quasi-stationary state measurements.

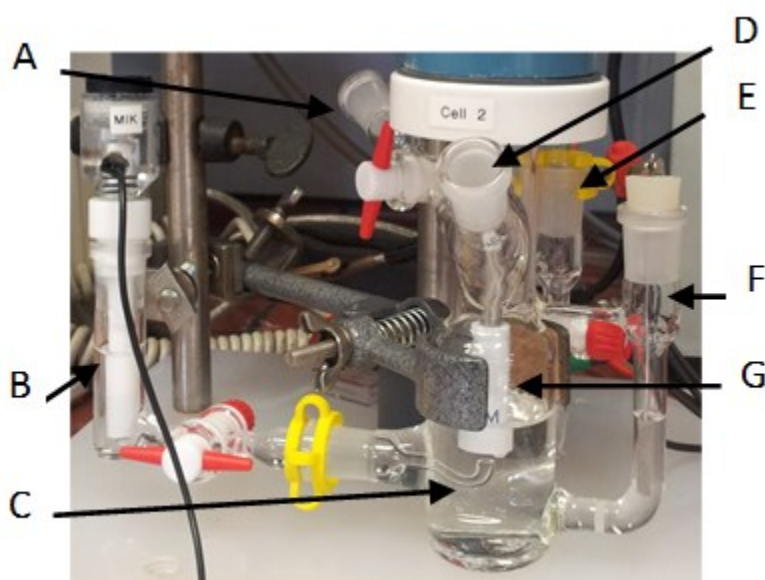


Figure 2.3. Standard 3-compartment electrochemical cell for rotating disk electrode measurements (RDE). Switchable gas inlets/outlets for degassing electrolyte and keep N_2 protective atmosphere (**a**), (**e**) and (**d**). Reference electrode compartment (**b**), working electrode with a Luggin capillary connection (**c**). Counter electrode separated by a glass frit (**f**). Working electrode separated by a glass frit (**g**).

2.4.2. Catalyst inks

An ink containing a solution of re-dispersed catalyst powder was drop-casted onto a glassy carbon working electrode. The ink was typically prepared by mixing 5 mg of catalyst powder, 500 μl of Milli-Q water, 750 μl of 2-propanol, and 20 μl of Nafion (5 wt %, Sigma); dispersed by ultrasonication for ~ 15 min. The amount loaded on the electrode was typically between 5 and 20 μl , however dependent on the desired metal loading.

2.4.3. Turnover frequency (TOF) calculations

TOF is defined as the moles of O_2 evolved per moles of total metal (Ni+Fe) per second (s^{-1}). TOF was normally estimated at 300 mV OER overpotential ($1.53V_{\text{RHE}}$) from quasi-stationary state measurements, or from CVs measured at a low scan-rate in the order of $\sim 5\text{mV/s}$. The geometric current densities were normalized to the total number of moles of total metal on the electrode determined by ICP or TXRF analysis of the catalyst inks according to equation (2.1).

$$TOF = \frac{i}{z \cdot F \cdot n} \quad (2.1)$$

where i is the current density, z the number of electrons (assuming 4 electron reaction for OER), F is the Faraday constant, n is the total moles of metal (typically Ni+Fe).

2.4.4. Determination of redox electrons

The redox electrons were estimated by integrating the area under the anodic $\text{Ni}(\text{OH})_2/\text{Ni}(\text{OOH})$ redox peak from CVs, and normalized to the geometric moles of Ni on the electrode determined by elemental analysis. The amount of redox active Ni atoms (redox electrons) was obtained by integration of the area under the voltammetric pre peaks ascribed to the $\text{Ni}(\text{OH})_2/\text{Ni}(\text{OOH})$ transition. The area associated with the charge was estimated as the area between the experimental curve and a fit line described by the Butler-Volmer equation, $i_a = i_0^{(1-\alpha)F\eta/RT}$. The fit was minimized by the non-linear least squares method using the Levenberg-Marquardt algorithm using in-house software, as demonstrated in Figure 2.4 below.

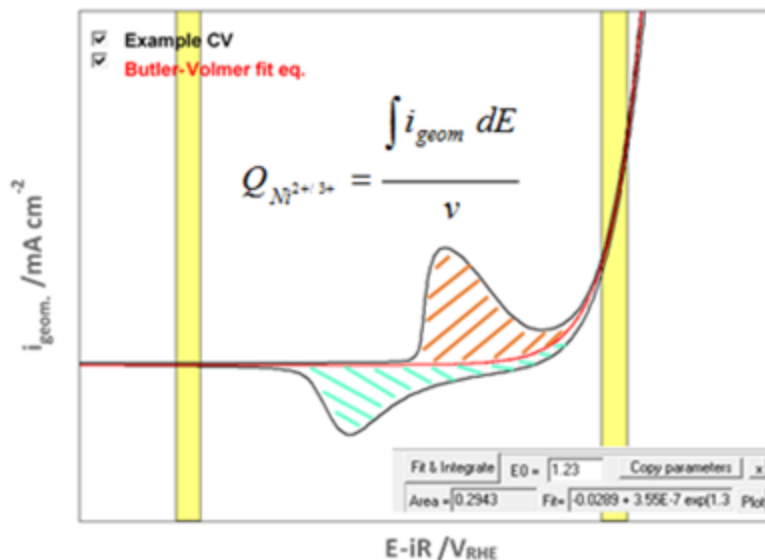


Figure 2.4. Example CV demonstrating how the integrated anodic vs. cathodic charges were determined for calculation of the redox number of the Ni^{+2/+3} redox transition.

To obtain the redox electrons (the electrons transferred per Ni atoms, $e^- \text{ Ni}^{-1}$), the redox charge was normalized to the total moles of Ni on the electrode determined by ICP-OES prior to, or by TXRF analysis after electrochemical conditioning, according to (2.2).

$$e^- \text{ per Ni} = \frac{Q_{\text{Ni}^{2+/3+}}}{z \cdot F \cdot n_{\text{Ni}}} \quad (2.2)$$

where Q is the charge of the Ni^{+2/+3} redox transition, z the number of electrons (assuming 1 electron reaction for the redox reaction), F is the Faraday constant, n is the total moles of Ni.

2.5. Mass Spectrometry

2.5.1. Differential electrochemical mass spectrometry (DEMS)

Measurements in 0.1 M KOH, 0.1 M KPi pH 7.0, and 0.1M Bi pH9.2 was carried out at Technical University of Berlin, using a custom-made dual thin layer flow cell connected to a Prisma™ quadrupole mass spectrometer (QMS 200, Pfeiffer-Vacuum) with a separating hydrophobic PTFE microporous membrane with 20-30 nm pore size (Cobetter®), see Figure 2.5. A typical electrolyte flow of 2-10 $\mu\text{l/s}$ was applied. The electrochemistry was controlled using a BioLogic potentiostat. Catalyst inks were prepared as described in section 2.4.2. above and drop-casted on polished glassy carbon electrodes (Pine Instruments) to a total metal loading of 10 $\mu\text{g Ni+Fe/cm}^2$. To convert the mass spectrometric ion current

(i_{MS}) to faradaic current (i_{F,O_2}^{DEMS}), a sensitivity factor K^* was used, determined from quasi-stationary chronopotentiometric step measurements. This assumes 100 % faradaic efficiency in the steady state. More information on DEMS and faradaic efficiency calculations can be found in section 3.2.6.

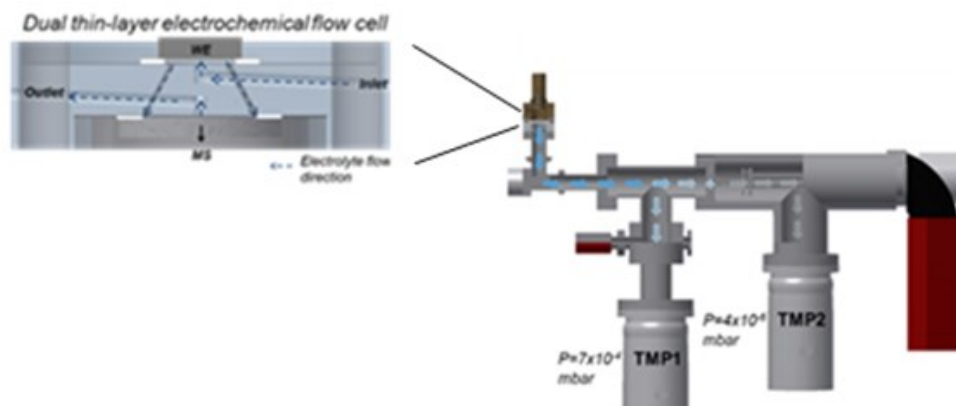


Figure 2.5. Differential electrochemical Mass Spectrometric Dual thin layer flow cell. The drawing demonstrate the real cell and were designed and made by Jorge Ferreira de Araújo, and schematical drawings in Autodesk® Inventor® Professional.

Measurements in 0.5 M NaOH in Chapter 6 was carried out in a similar setup, in collaboration with Ulm University¹²⁶. The electrochemistry was controlled using an AFRDE5 potentiostat (Pine Instruments), a standard calomel reference electrode (-1.0 V vs RHE in 0.5 M NaOH), and a Pt-counter electrode. The cell was connected to a Balzers QMS 112 mass spectrometer via a Teflon+Goretex microporous membrane. CVs were recorded by potential cycling between 0.05-1.5 V_{RHE} at a scan-rate of 10 mVs^{-1} .

2.5.2. Online headspace Mass Spectrometry and Gas Chromatography

Volatile products were detected in the gas-phase in a steady flow of 5 sccm (mL/min) N_2 in a customized-made flow cell (see Figure 2.6). The measurements were carried out in 0.1 M KOH, with a Pt-mesh counter electrode and an RHE reference electrode, separated by a glass frit to avoid H_2 in the gas phase. As working electrode, a 2 cm^2 carbon fiber paper was used (fuelcellstore.com), double sided coated to at a total metal loading of 10-20 $\mu g_{Ni+Fe}/cm^2$. Chronopotentiometric steps were applied between 0.25 and 10 $mA\ cm^{-2}$. Online detection of volatile products released to the headspace of the cell was achieved by mass spectrometric detection (Pfeiffer Omnistar GSD 301) attached to the outlet of the cell. Gas chromatography was carried out by manual sampling of the gas phase using a gas-tight syringe (a volume of 12 mL was taken out) which was injected into a GC-2014 chromatograph (Shimadzu), equipped with a molsiev 13x column and a thermal conductivity detector (TCD). An improved design of the cell was

made, where an anion exchange membrane (Fumasep) was used to separate the Pt-mesh from the working electrode (see more details in Appendix I).

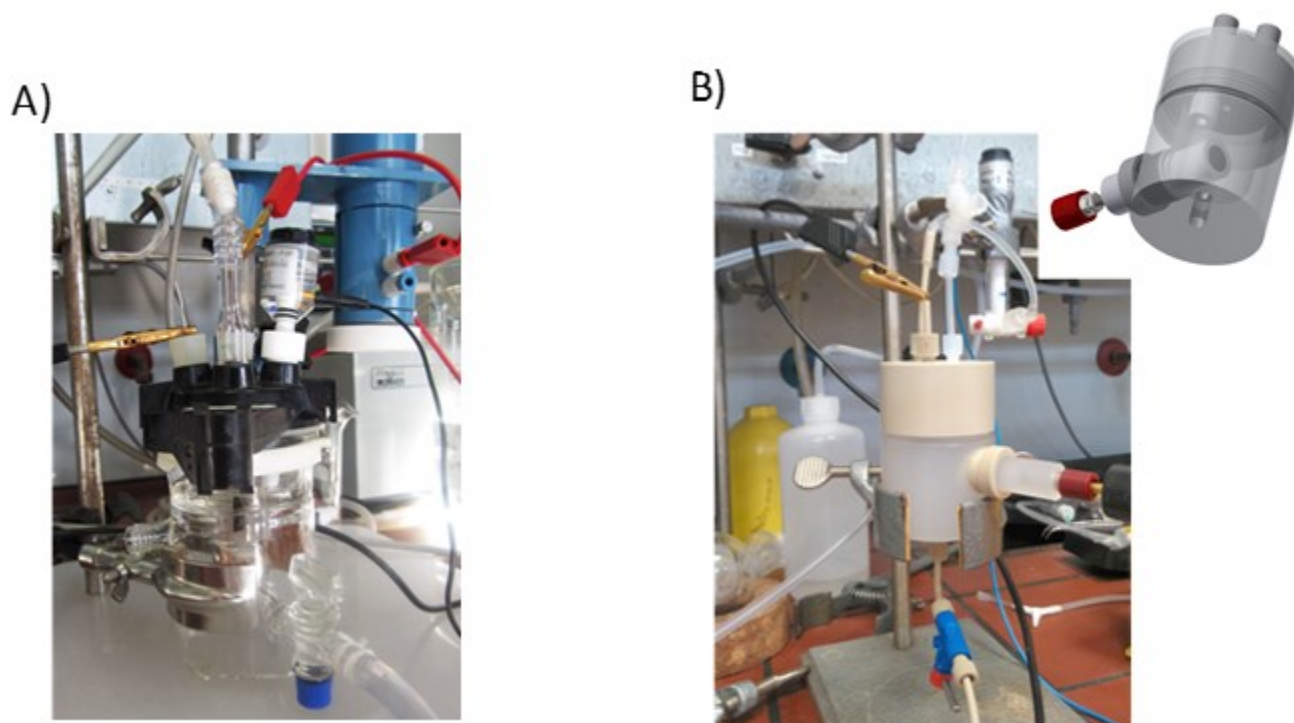


Figure 2.6. Online Mass Spectrometric cells **(a)** initial design in glass **(b)** improved design of in Kel-F (PTCFE). More images of cell (b) are attached in Appendix I. Schematic drawings were prepared in Autodesk Inventor Professional.

2.6. X-ray absorption spectroscopy (XAS)

X-ray absorption spectroscopy was measured at the Ni and Fe *K*-edges, at the KMC-1 and KMC-3 beamlines at the BESSY-II synchrotron facility at Helmholtz-Zentrum Berlin. The liquid-helium cryostat was cooled to 20 K, as described elsewhere ¹²⁷. Absorption spectra were collected in the fluorescence mode for films freeze-quenched under applied catalytic potentials and in absorption and fluorescence mode for as-synthesized catalysts. In the fluorescence mode, a 13-element energy-resolving Ge detector (Canberra) was used at the K_{α} emission line of the respective element. The k^3 weighted extended X-ray absorption fine structure (EXAFS) spectra were extracted using the E_0 value equal to 8333 eV for Ni and to 7117 eV for Fe *K*-edges. The simulations of the EXAFS spectra were carried out using in-house software (SimX lite). Phase functions were generated from atomic structures of layered Ni(OH)₂ and Fe(OOH) using the FEFF software package version 9.1 with self-consistent field option switched on.^{128,129} The

amplitude reduction factor (S_0^2) was set to 0.85 at both Ni and Fe *K*-edges. The data ranges used in the simulations were 25-801 eV above E_0 (corresponding to a k -range of 2.6 -14.5 \AA^{-1}) for the Ni *K* edge and 25-595 eV (2.6 - 12.5 \AA^{-1}) for the Fe *K*-edge. The simulations were optimized in k -space by the least-squares method using the Levenberg-Marquardt algorithm with numerical derivatives. The error ranges of the fit parameters were estimated from the covariance matrix of the fits and correspond to a 68 % confidence intervals as described in by Risch et al.¹³⁰

2.6.1. Sample preparation for quasi- in situ XAS

Samples were prepared as described previously.¹³¹ Catalyst powders were dispersed as a catalyst ink, which was drop-dried onto polished glassy carbon electrodes. Special sample holders were used to hold the working electrode, and a Pt-mesh was used as counter electrode, a reversible hydrogen electrode (RHE) as reference, and a GAMRY 3000 potentiostat. Catalysts were freeze quenched under applied catalytic potential using liquid nitrogen, according to a previously described method,^{132,133} after conditioning for 30 min in 0.1 M KOH at the given potential. The samples were stored in liquid nitrogen until analyzed at the BESSY-II synchrotron facility, Helmholtz-Zentrum Berlin. Images of the freeze quench setup is shown in Figure 2.7 below.

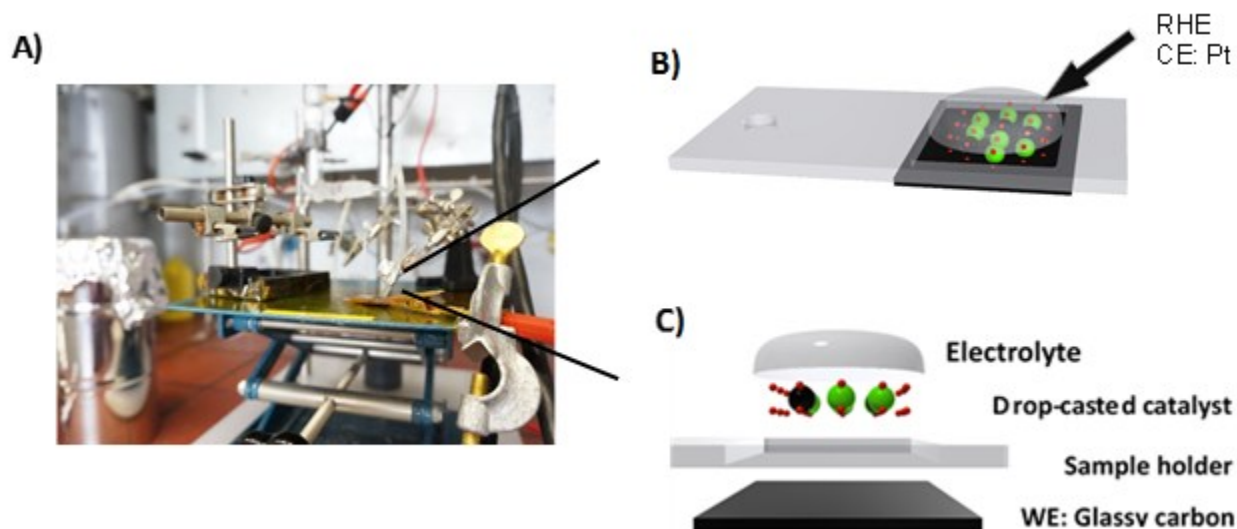


Figure 2. 7. XAS sample preparation for freeze quenching **(a)** Schematic drawing of the working electrode **(b)** and of the assembly **(c)**. Schematic drawings were prepared in Autodesk Inventor Professional.

Chapter 3

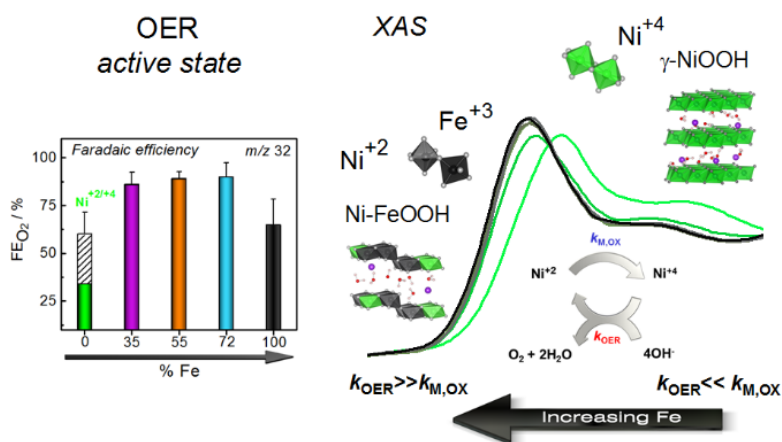
Oxygen evolution reaction dynamics, faradaic charge efficiency, and the active metal redox states of Ni-Fe oxide water splitting electrocatalysts

This Chapter has been reprinted with permission from the American Chemical Society as the latest version of a published Journal article.

(Görlin, M.; Chernev, P.; Ferreira de Araújo, J.; Reier, T.; Dresp, S.; Paul, B.; Krähnert, R.; Dau, H.; Strasser, P. Journal of the American Chemical Society 2016, 138, 5603, DOI: 10.1021/jacs.6b00332)

URL: <http://dx.doi.org/10.1021/jacs.6b00332>

Copyright (2016) American Chemical Society



Mikaela Görlin¹, Petko Chernev², Jorge Ferreira de Araújo¹, Tobias Reier¹, Sören Dresp¹, Benjamin Paul¹, Ralph Krähnert¹, Holger Dau², and Peter Strasser¹

¹Technical University of Berlin, Department of Chemistry, Chemical Engineering Division, Straße des 17. Juni 124, 10623, Berlin, Germany

²Free University of Berlin, Department of Physics, Arnimallee 14, 14195 Berlin, Germany

Abstract

Mixed Ni–Fe oxides are attractive anode catalysts for efficient water splitting in solar fuels reactors. Because of conflicting past reports, the catalytically active metal redox state of the catalyst has remained under debate. Here, we report an in operando quantitative deconvolution of the charge injected into the nanostructured Ni–Fe oxyhydroxide OER catalysts or into reaction product molecules. To achieve this, we explore the oxygen evolution reaction dynamics and the individual faradaic charge efficiencies using operando differential electrochemical mass spectrometry (DEMS). We further use X-ray absorption spectroscopy (XAS) under OER conditions at the Ni and Fe *K*-edges of the electrocatalysts to evaluate oxidation states and local atomic structure motifs. DEMS and XAS data consistently reveal that up to 75% of the Ni centers increase their oxidation state from +2 to +3, while up to 25% arrive in the +4 state for the NiOOH catalyst under OER catalysis. The Fe centers consistently remain in the +3 state, regardless of potential and composition. For mixed Ni_{100-x}Fe_x catalysts, where *x* exceeds 9 atomic %, the faradaic efficiency of O₂ sharply increases from ~30% to 90%, suggesting that Ni atoms largely remain in the oxidation state +2 under catalytic conditions. To reconcile the apparent low level of oxidized Ni in mixed Ni–Fe catalysts, we hypothesize that a kinetic competition between the (i) metal oxidation process and the (ii) metal reduction step during O₂ release may account for an insignificant accumulation of detectable high-valent metal states if the reaction rate of process (ii) outweighs that of (i). We conclude that a discussion of the superior catalytic OER activity of Ni–FeOOH electrocatalysts in terms of surface catalysis and redox-inactive metal sites likely represents an oversimplification that fails to capture essential aspects of the synergisms at highly active Ni–Fe sites.

3.1. Introduction

The increasing global demand of energy calls for the development of alternative, solar-based energy harvesting technologies, involving integrated photoelectrochemical reactors for efficient solar energy conversion and storage of solar fuels in the form of molecular bonds.¹ To achieve this, earth abundant, nonprecious electrocatalyst materials at anode and cathode are critical. Anode electrocatalysts oxidize water in the oxygen evolution reaction (OER),⁵ and cogenerate protons and electrons, while cathode electrocatalysts generate solar fuels.^{2,4,6-12,14,18,109,134} Mixed Ni and Fe oxide electrocatalysts are among the most active nonprecious OER catalysts in alkaline electrolyte and help split water at low overpotentials,^{15,58,69,72,77,80-83,87,88,96,97,99,135,136} and have been shown applicable to photocatalytic applications.^{16,17,94} Mixed Ni–Fe catalysts containing ~10–50 atomic % Fe have been reported to exhibit most favorable intrinsic OER activities.^{87,89,91,95,98}

To achieve structural atomic-level and chemical insight into the origin and the mechanism resulting in the low OER overpotential in mixed Ni–Fe electrocatalysts, previous experimental studies have largely relied on the combination of X-ray absorption spectroscopy (XAS), in situ spectroscopic, and voltammetric techniques. Lattice strain, surface area, and conductivity effects have also been brought to the fore; however a common conclusive picture about the metal redox states is still emerging. A missing piece has been the charge transfer reaction dynamics and its selectivity under reaction conditions, in particular in situ deconvolution of the total faradaic charge transfer which goes into forming molecular products vs catalyst charge processes. This contribution will address this issue.

Synchrotron-based XAS studies of Ni–Fe catalysts including XANES and EXAFS have repeatedly been used successfully to reveal details on the chemical states and the local atomic structure around the metal centers under catalytic potential. These studies have shown conflicting results regarding the formal charges of the Ni and Fe in the catalytically active state.^{77,80,101,102,104,105,137,138} In situ XAS of a mixed Ni–Fe oxides studied by Landon et al.⁷⁷ showed no significant potential-induced changes in local atomic structure or oxidation state under catalytic potential, which was contradicting other studies regarding the oxidation state of Ni atoms during catalysis. The absence of oxidation state changes was attributed to possible electrolyte inaccessible sites which is likely in oxide nanoparticles with a large bulk to surface volume ratio.⁷⁷ Operando XAS by Friebel et al.⁸⁰ of electrodeposited and/or sputtered Ni-FeOOH electrocatalysts with various compositions of Ni and Fe showed that Ni atoms oxidize from Ni²⁺ to Ni⁴⁺ during applied potential regardless Ni–Fe composition, with the catalytically active state described as Ni⁴⁺Fe³⁺OOH. This in agreement with early EXAFS investigations of Ni-based electrodes by Corrigan and

co-workers,¹³⁹ which showed that α -Ni(OH)₂ converts to γ -NiOOH with Ni in oxidation state +4 under oxidizing potentials. A recent in situ XAS study by Wang et al.¹³⁸ of Ni-Fe oxyhydroxide catalysts electrodeposited on carbon paper confirmed Ni atoms in oxidation state +4 and the presence of a highly covalent Fe⁴⁺-O bond under OER potential, and a charge transfer between Ni and Fe atoms was proposed. The presence of Fe⁴⁺ was also proposed in an earlier study by Balasubramanian et al.¹⁰¹ in electrodeposited Ni-Fe oxyhydroxide catalysts. The presence of Fe⁴⁺ species under catalytic potentials in a Ni-FeOOH catalyst was recently confirmed by Chen et al.¹⁰³ using operando Mössbauer spectroscopy. The role of Fe⁴⁺ was discussed to potentially provide important mechanistic implications if generated at an edge, corner, or a “defect” site.¹⁰³ Regarding the synergism between Ni and Fe centers, Bates et al.¹⁰⁶ reported a clear difference in the Ni oxidation state in Ni-catalysts vs. and Ni-Fe catalysts, where the presence of Fe apparently stabilized Ni centers in a lower oxidation state visible at potentials up to 1.45 V.

In the operando XAS study by Friebel et al.,⁸⁰ indications of Fe nucleating as a separate phase was observed above 25% Fe based on diverging Fe-O and Ni-O distances, which could explain why the OER activity did not improve above this Fe content. Moreover, Trotochaud et al.⁷² showed that traces of Fe impurities in the electrolyte readily incorporate into the Ni oxyhydroxide lattice, which increases the OER activity of α -NiOOH due to the presence of Fe and not due to formation of β -NiOOH which was long proposed as the reason for increased activities of NiOOH catalysts after aging in KOH. Klaus et al.⁷⁶ showed that despite removal of Fe impurities, mixed phases of α , β , and γ phases in Ni oxyhydroxides are likely to form; however, Fe impurities resulted in a lower degree of β -Ni(OH)₂ formation upon aging based on in situ spectroscopic Raman measurements. Using DFT calculations, Friebel et al.⁸⁰ showed that OER intermediates have nearly optimal binding energy at Fe sites located in proximity to a Ni site,⁸⁰ thus Fe was proposed as the expected active site. Trzeźniewski et al.¹⁰⁴ observed negatively charged species referred to as “active oxygen” in Ni(Fe)OOH in KOH pH 13 using Raman spectroscopy, which was absent in borate buffer pH 9.2, explaining the strong pH dependence of OER catalysis.

Direct comparison between studies is notoriously demanding due to deviating experimental parameters, catalyst supports, or other variations in electrochemical testing conditions. Despite these difficulties, recurring OER activity trends and structural motifs have been observed in systematic studies across, which are necessary to eventually lend support to the yet incomplete mechanistic picture of the catalytic interface processes.

In this contribution, we provide new insight into the Ni–Fe OER puzzle by combining operando differential electrochemical mass spectrometry (DEMS), quasi-in situ X-ray absorption spectroscopy (XAS)^{64,130} and electrochemical characterization. The DEMS analysis yields reaction product dynamics data that allowed for a quantitative deconvolution of faradaic charge generating molecular oxygen and charge injected into the metal oxide catalyst causing redox state changes. This constitutes a first-of-its-kind cross-check of our XAS-based findings on the metal redox states. A simple but plausible hypothesis is brought forward to reconcile our and previous findings with respect to the redox states of the metal centers under catalytic oxygen evolution conditions.

3.2. Experimental

3.2.1. Synthesis of Mixed Ni-Fe Catalysts

Nanosized Ni–Fe catalysts with varying Ni/Fe ratios were synthesized by a microwave-assisted, surfactant-free solvothermal route.^{121,140} This allowed for high solubility of the Fe³⁺ precursor under these conditions. Desired amounts of solutions of 0.1 M Ni(NO₃)₂·6H₂O (99.999% trace metals basis, Aldrich) and 0.1 M Fe(acac)₃ (99.5% trace metal basis, Aldrich) with additions of 10 mM 1,2-Benzenediol (>99%, Aldrich) were mixed in benzyl alcohol (Puriss, 99–100.5%) to make up a final total concentration of 22 mM of Ni+Fe precursors to a volume of 20 mL. The reaction mixtures were sealed in special autoclave vials (Anton Paar) and heated to 190 °C for 15 min with a ramping step of 16.5 °C/min. After immediate cooling to room temperature the solid products were collected by washing five times with high purity ethanol and recollected by repetitive centrifugation at 7500 rpm for 15 min. The collected nanoparticles were freeze-dried and stored as powders under inert atmosphere until use. An Fe-free Ni-catalyst was prepared according to the same synthesis method but with an additional purification step where the solvent and the ethanol had been cleared of Fe-traces prior to synthesis according to the method reported by Trotochaud et al.⁷² An additional Fe-Free Ni-catalyst was synthesized without addition of 1,2-Benzenediol using the same conditions.

3.2.2. Elemental Analysis

The metal content was determined by inductively coupled plasma–optical emission spectrometry (ICP-OES), using a Varian 715-ES spectrometer with a CCD detector. Prior to analysis, the samples were digested in mixtures of concentrated HNO₃:HCl in a 1:3 ratio for ~2 h and sonicated for 10 min and diluted with appropriate amounts of >20 MΩ cm Milli-Q water.

Total metal content in catalysts after electrochemical conditioning was analyzed using total reflection X-ray fluorescence (TXRF) spectroscopy. Conditioned electrodes were dissolved in 300 μL of HCl (37%, Merck) by sonication for ~ 10 min, and further left in the HCl solutions for at least 2 h. Additions of the same amount of a Ga-standard solution of 1 mg/mL (Merck), allowed for determination of the metal content. The analysis was acquired using a PicoTAX spectrometer with a 40 kV using a Si-drift detector (Röntec).

3.2.3. Scanning Electron Microscopy (SEM) and Energy Dispersive X-ray (EDX) Analysis

SEM images of samples drop-casted on polished glassy carbon electrodes were acquired in secondary electron mode using a JEOL JSM-7401F high resolution field emission SEM operated at 10 kV or, respectively, 15 kV, if the images were acquired in the context of energy dispersive X-ray (EDX) spectroscopic measurements. EDX analysis (including elemental mapping and line-scans) was measured in the same microscope using an EDX detector unit (Quantax 400, BrukerAXS Microanalysis GmbH, Germany). The working distance was 12 mm for EDX elemental mapping and line-scan analysis. Quantifications of the Ni and Fe content were obtained from the *K* lines.

3.2.4. Powder X-ray Diffraction (XRD)

XRD was recorded using a Bruker D8 advance powder diffractometer (Bragg–Brentano geometry), equipped with a Cu $K\alpha$ source, variable divergence slit and position sensitive device as detector. Data were recorded between 10° to 80° 2θ with a step size of 0.038° .

3.2.5. Electrochemical Characterization

The catalytic activity was measured in rotating disk electrode setup (RDE) using a standard 3-electrode electrochemical cell designed to hold the glassy carbon electrode ($\Phi = 5$ mm), a Pt-mesh counter electrode, and a reversible hydrogen reference electrode (RHE). The electrodes were polished with $2 \mu\text{m}$ followed by $0.05 \mu\text{m}$ silica polishing solutions (Buehler), and sequentially washed with Milli-Q - 2-Propanol - Milli-Q water in a sonication bath. Trace metals were removed with HCl and the washing procedure repeated. All measurements were recorded in 0.1 M KOH (semiconductor grade, 99.99% trace metals basis, Aldrich) in electrolyte purged with N_2 for 20 min prior to the experiments (and keeping a protective N_2 atmosphere), using a GAMRY potentiostat 3000 at a rotation speed of 1600 rpm. Catalyst powders were prepared as inks with mixtures of 50:75:1 of Milli-Q water, 2-propanol, and 5 wt % Nafion (SIGMA). The inks were homogeneously dispersed by ultrasonication for ~ 20 min, and drop-casted onto the glassy carbon electrodes to make up a total metal loading of $\sim 5 \mu\text{g}$ of Ni+Fe cm^{-2} (~ 175 nmol of Ni+Fe cm^{-2}), and dried in an oven at 60°C for 10 min. Fe-free KOH was prepared by purification according

to a reported method,⁷² measured in polypropylene beakers (Nalgene) instead of the standard electrochemical cell to avoid contamination from glass etching. The uncompensated series resistance (*iR*-drop) was determined by electrochemical impedance spectroscopy (EIS) in the frequency range between 1 Hz to 100 kHz, with typical values in 0.1 M KOH of 30 Ω. CVs were corrected afterward for *iR*-drop whereas chronoamperometric measurements were carried out at *iR* compensated potentials determined prior to the measurement.

3.2.5.1 Turnover Frequency (TOF) and Ni Redox Charge Calculations

The turnover frequency was defined as moles of O₂ per moles of total metal content (Ni+Fe) evolved per second (s⁻¹). The geometric current densities (*i*) were extracted at 300 mV overpotential (1.53 V_{RHE}, all reported potentials are *iR* corrected) and 400 mV overpotential (1.63 V_{RHE}) from quasi stationary state measurements, based on the total moles of Ni+Fe (*n*_{Ni+Fe}) on the electrode determined by ICP-OES prior to the measurement, assuming a *z* = 4 electron transfer for the overall reaction according to eq (3.1).

$$\text{TOF} = \frac{i}{z \cdot F \cdot n_{\text{Ni+Fe}}} \quad (3.1)$$

Determination of redox charge (*Q*) (equivalent to the number of redox active Ni atoms) was done by integration of the area under the voltammetric prewave ascribed to the Ni(OH)₂/NiOOH redox transition. The redox charge was described as the area between the experimental curve and a fit line described by the Butler–Volmer equation, $i_a = i_0^{(1-\alpha)F\eta/RT}$. The fit was minimized by the nonlinear least-squares method using the Levenberg–Marquardt algorithm using in-house software. To obtain the redox number (electrons transferred per Ni atoms, e⁻ Ni⁻¹), the integrated charge was normalized to the total moles of Ni on the electrode determined by ICP-OES prior to, or by TXRF analysis after electrochemical conditioning, according to eq (3.2).

$$e^- \text{ per Ni} = \frac{Q_{\text{Ni(OH)}_2/\text{NiOOH}}}{z \cdot F \cdot n_{\text{Ni}}} \quad (3.2)$$

3.2.6. Differential Electrochemical Mass Spectrometry

Differential electrochemical mass spectrometry (DEMS) was recorded in a home customized dual thin-layer electrochemical flow cell based on the concept reported elsewhere.¹⁴¹ The volatile products were detected using a Prisma quadrupole mass spectrometer (QMS 200, Pfeiffer-Vacuum) equipped with two turbomolecular pumps (HiPace 80) operating under 10⁻⁶ mbar.

The electrolyte was separated from the chamber by a hydrophobic PTFE membrane with a pore size of 30 nm and thickness of 150 μm (Cobetter, Cat. No. PF-003HS). The catalysts were drop-casted on

polished glassy carbon electrodes ($\Phi = 5$ mm, HTW GmbH) as described in section 3.2.5, to make up a total metal loading of ~ 10 $\mu\text{g Ni+Fe cm}^{-2}$ determined by ICP-OES. Cyclic voltammograms (CVs) were recorded in 0.1 M KOH by cycling the potential between 1.0–1.8 V_{RHE} (prior to iR -compensation) at a scan-rate of 50 mV/s. The electrodes were initially allowed to stabilize in electrolyte solution at 1.1 V_{RHE} , in order to record the ionic current baseline before recording the CVs. The electrolyte was constantly purged with N_2 before entering the flow cell and pumped through the cell at a flow of 8 $\mu\text{L/s}$. Formation of volatile products (m/z 2, 16, 18, 28, 30, 36, 32, 34, 44) was monitored during the CV scan. Quantification of the Faradaic efficiency (FE) of O_2 (m/z 32) was done using a calibration constant (K^*) obtained from quasi-stationary state measurements where chronoamperometric steps were applied in the linear region. The value of K_j^* directly relates the mass spectrometric ion current (i_{MS}) to the faradaic current at the potentiostat (i_{F}) to the volatile product j according to eq (3.3)¹⁴²

$$K_j^* = \frac{i_{\text{MS},j} \cdot z_j}{i_{\text{F}}} \quad (3.3)$$

where z_j represents the number of transferred electrons per molecule of volatile product j . The Faradaic efficiency (charge selectivity) during a CV scan was obtained by integration of the mass spectrometric ion current ($Q_{\text{MS},j}$) and the capacitive current-corrected, faradaic current (Q_{F}), and combining the two integrated charge values according to eq (3.4)¹⁴³

$$\text{FE (\%)} = \frac{Q_{\text{MS},j} \cdot z_j}{Q_{\text{F}} \cdot K_j^*} \cdot 100 = \frac{Q_{\text{F},j}^{\text{DEMS}}}{Q_{\text{F}}} \cdot 100 \quad (3.4)$$

Here $Q_{\text{F},j}^{\text{DEMS}}$ denotes the DEMS-derived, total faradaic charge that is converted into volatile product j . Only anodic faradaic currents were included in the analysis to exclusively account for anodic processes (molecular O_2). The potential/time integration limits of the mass currents were selected from the onset of O_2 formation (m/z 32) until the detected signal had returned to the initial baseline level. The absolute integration limits slightly varied for different Ni:Fe compositions due to different onset potentials for OER.

3.2.7. X-ray Absorption Spectroscopy (XAS)

X-ray absorption spectra were recorded at the K -edges of Ni and Fe at the KMC-1 and KMC-3 beamlines at the BESSY-II synchrotron facility at Helmholtz-Zentrum Berlin, Germany, using a liquid-helium cryostat cooled to 20 K.¹²⁷ Absorption spectra were collected in fluorescence mode of films conditioned at OER potentials and in absorption and fluorescence mode of as-prepared powder samples. The fluorescence was detected using a 13-element energy-resolving Ge detector (Canberra), selecting the K_{α} emission

lines of the respective element. The k^3 weighted extended X-ray absorption fine structure (EXAFS) spectra were extracted using E_0 value equal to 8333 eV at the Ni K -edge and to 7117 eV at the Fe K -edge. Theoretical simulations of the EXAFS spectra were carried out using in-house software (SimX) with phase functions generated from the atomic coordinates of α -Ni(OH)₂, γ -NiOOH, γ -FeOOH, and α -FeOOH, using the FEFF software package^{128,129} version 9.1 with self-consistent field option switched on. The amplitude reduction factor (S_0^2) was set to 0.85 for both Ni and Fe K -edges. The data ranges used for the simulations were 25–750 eV above E_0 (k -range of 2.6–14 Å⁻¹) for the Ni K -edge and 25–600 eV (2.6–12.5 Å⁻¹) for the Fe K -edge. The simulations were optimized in k -space by the least-squares method using a Levenberg–Marquardt algorithm with numerical derivatives. The error ranges of the fit parameters were estimated from the covariance matrix of the fits corresponding to a 68% confidence level as described elsewhere.¹³⁰ More details about selected fit parameters are given in Supporting Information S3.6.

3.2.7.1. Sample preparation For Quasi-In Situ XAS

Catalyst inks were prepared as described above without additions of Nafion, and drop-casted on polished glassy carbon working electrodes with a geometric area of $\sim 1 \text{ cm}^2$, and prepared for quasi-in situ XAS as described previously.^{64,130} Catalysts were assembled in custom-made sample holders designed to hold a small volume of electrolyte on top of the working electrode. A Pt-wire was used as counter electrode and an RHE reference electrode connected to the working electrode via a Luggin capillary to the electrolyte. The iR -drop was determined by EIS prior to the measurement, which showed typical values of 2 Ω . Oxygen evolution potential was applied using a GAMRY 3000 potentiostat and the catalysts were conditioned at 1.0 or 1.63 V_{RHE} for 30 min in 0.1 M KOH (semiconductor grade, 99.99% trace metals basis, Aldrich) without further purification. The catalysts were freeze quenched in liquid N₂ during applied potential. All samples were stored in liquid N₂ until analyzed at the BESSY-II synchrotron facility, Helmholtz-Zentrum, Berlin.

3.3. Results & Discussion

3.3.1 Electrochemical Activity, Turnover Frequency, Voltammetric Metal Redox Behavior

Mixed Ni–Fe oxyhydroxide catalysts with atomic compositions ranging from 0 to 100 at % Fe were prepared using solvothermal synthesis. Consistent with earlier reports they showed high catalytic activity for the oxygen evolution reaction (OER) in a specific compositional range. The highest oxygen evolution activity was observed for the Ni₄₅Fe₅₅ catalyst containing 55 at. % Fe (Figure 3.1a-b and S3.1a-d), demonstrating a synergism between Ni and Fe centers in accordance with previous studies.^{69,77,88,91,107,144,145} The lower limits of the catalytic turnover frequency based on total metal of Ni + Fe determined by ICP-OES (TOF_{Ni+Fe}) at $\eta = 300$ mV was determined to 0.14 s⁻¹ for the Ni₄₅Fe₅₅ catalyst in 0.1 M KOH (Figure 3.1b, see also Figure S3.1c for mass based activity). The upper limit TOF, based on the redox active Ni centers obtained by integration of the Ni(OH)₂/NiOOH redox peak area of the Ni₄₅Fe₅₅ catalyst under the same conditions was estimated to 2 s⁻¹. Direct comparison to other work is rather challenging due to variations in a number of parameters such as catalyst loading^{100,146} and electrochemical conditions as well as the definition of the active site, the approach to evaluate redox active sites, and the contribution of these to the overall activity.^{107,109} The values we observe meet or exceed previous estimations of likely catalytic turnover frequencies of mixed Ni–Fe catalysts.^{69,87,107,147} The redox electrons (e⁻ per Ni atoms) of the Ni(OH)₂/NiOOH redox transition visible in the CVs at ~ 1.4 V_{RHE} was estimated to ~ 1.1 for the Ni-catalyst on the anodic scan, and slightly higher on the cathodic scan (Figure 3.1c), well consistent with previous reports on NiOOH catalysts.^{69,144} In other words, every metal center in our Ni-catalyst appear to undergo an oxidation state change assuming 1 electron transfer. Upon addition of Fe, however, this number is substantially decreased, with an associated anodic peak shift of ~ 70 mV when the Fe content is increased from 0 to 50% Fe (Figure 3.1d). Addition of Fe also had an evident effect on the Tafel slopes, which varied between 35 mV dec⁻¹ for the most active Ni₄₅Fe₅₅ catalyst to 60 mV dec⁻¹ for less active catalysts (Figure 3.1e and S3.1d).

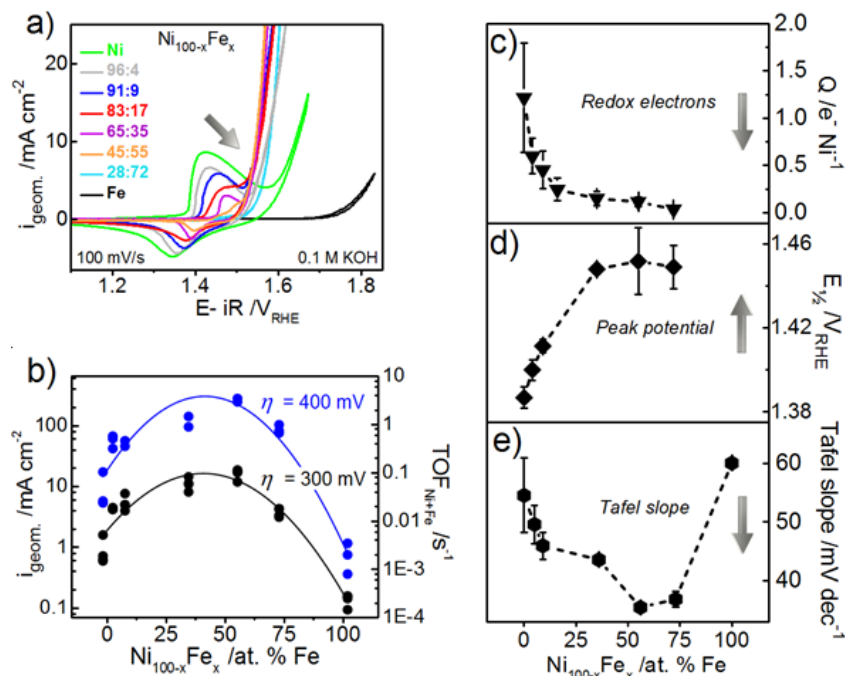


Figure 3.1. Electrochemical characterization of mixed Ni–Fe catalysts with varying catalyst composition ($\text{Ni}_{100-x}\text{Fe}_x$) measured in RDE setup in 0.1 M KOH. **(a)** Cyclic voltammograms (CVs) recorded at a scan-rate of 100 mV/s after conditioning at 1.63 V_{RHE} for 30 min (see also Figure S3.1a for CVs at 10 mV/s). **(b)** Geometric current density (i_{geom}) and turnover frequency (TOF) of Ni–Fe catalysts based on the total metal loading of Ni+Fe (chosen identical for all samples) extracted from stationary measurements at $\eta_{\text{OER}} = 300$ mV (black curve) and 400 mV (blue curve). TOF is defined as moles of O_2 evolved per total moles of metal (Ni+Fe) per second. **(c)** Number of electrons transferred per Ni atoms ($e^- \text{Ni}^{-1}$) obtained by integration of the area under the $\text{Ni}(\text{OH})_2/\text{NiOOH}$ redox peak obtained by integration of the area under the redox peak, obtained from the maximum average value of anodic and cathodic redox wave during the first 150 cycles, $\left(\frac{Q_{p,a} + Q_{p,c}}{2}\right)$ **(d)** Midpeak potential, $\left(\frac{E_{p,a} + E_{p,c}}{2}\right)$ of the $\text{Ni}(\text{OH})_2/\text{NiOOH}$ redox peak. **(e)** Tafel slopes obtained from quasi-stationary state measurements (see also Figure S3.1d). Catalyst loadings were determined by ICP-OES analysis. Additional electrochemical measurements are presented in Supporting Information S3.1. *This figure has been reprinted with permission from ref. 108. Copyright (2016) American Chemical Society.*

Addition of small traces of Fe (4%) resulted in a drastic decrease of the redox electrons to 0.5 e^- per Ni, with a further decrease down to ~ 0.1 for the $\text{Ni}_{45}\text{Fe}_{55}$ catalyst. This effect was previously noted for electrodeposited Ni–Fe catalysts by Louie et al.,⁸⁷ which was referred to as a decrease in the average oxidation state of Ni. Stabilization of the Ni in lower valent states in a mixed Ni–Fe catalyst on Raney-nickel support was observed by Bates et al.,¹⁰⁶ however at relatively low overpotentials (1.45 V). In a

study by Friebel et al.,⁸⁰ Fe incorporation in mixed Ni–Fe oxyhydroxides did not appear to have any effect on the formal oxidation state of Ni. The origin of this discrepancy has not yet been clearly elucidated.

To eliminate the possibility of trapped oxidized Ni⁴⁺ escaping detection due to formation of an insulating layer of nonconductive Ni²⁺(OH)₂ at the electrode interface as was recently discussed by Batchellor et al.,¹⁴⁶ catalysts were investigated before and after application of a reducing potential of 0 V_{RHE} for 20 min. We found, in accordance with the study, that the redox wave in the first CV when starting in the “reduced state” appeared larger than in the steady state CVs, without significant changes in the cathodic redox wave (Figure S3.2). The increase in the anodic wave was clearly dependent on the Ni:Fe stoichiometry, where largest effect was observed for the Ni₉₁Fe₉ catalyst, similar to the composition where a large change was demonstrated by Batchellor et al.¹⁴⁶ Increased catalyst loading has also been shown to result in increased OER activity.^{100,146} Starting in the “reduced state” did not result in an instant increase in the OER activity on the anodic scan for any of the Ni–Fe catalysts, where a larger fraction of Ni centers hypothetically should be exposed to the electrolyte as suggested by the increased redox wave, and thus a direct correlation between the observed effect and increased electrolyte accessibility is not strongly supported by these observations. Other possibilities include processes related to adsorption intermediates or formation of low valent [Ni⁺²–OOH]⁻ species during the first CV scan as was recently discussed by Smith et al.¹⁴⁸

Conditioning of the catalysts by CV cycling or, alternatively, application of a constant electrode potential of +1.63 V showed distinct changes in the OER activity (Figure S3.3) associated with a change in the number of redox electrons transferred during the first 150 cycles (Figure S3.4a-b) accompanied by an anodic peak shift of ~30 mV (Figure S3.4c-d). These changes could be either a consequence of hydration, loss of catalyst,^{100,134} or continuous Fe incorporation.⁷² To address possible losses of catalyst, comparison of metal content of as-prepared catalysts and after the conditioning step determined by TXRF analysis, showed a loss of ~30% total metal, which was similar for both the Ni and Ni–Fe catalysts, thus suggesting that the e⁻ per Ni was slightly underestimated (see Figure S3.5 for reviewed redox electrons). There was also a loss of Ni (not only Fe) during this conditioning step; however, the relative loss of Fe was consistently higher under these conditions resulting in a small, however neglectable fractional change (~6%). A stable CV was achieved after the conditioning step upon further cycling, suggesting that these initial losses could be due to stress under strong oxygen evolution conditions.

Experiments of the Ni-catalyst were repeated in Fe-free electrolyte purified according to the method by Trotochaud et al.⁷² These experiments showed that elimination of Fe impurities from the KOH electrolyte

(case 3 in Figure S3.6a) increased the OER overpotentials at 10 mA cm^{-2} by about 180 mV compared to the unpurified or Fe-Free KOH conditions (cases 1,2), in agreement with previous observations upon removal of Fe-impurities.⁷⁶ An additional redox peak appeared at 1.56 V_{RHE} (Figure S3.6a). The relative activity and Ni redox peak charge evolution during the first 150 cycles under Fe-Free conditions exhibited similar trends as the Ni-catalyst measured in unpurified electrolyte; however, under Fe-free conditions the OER activity was descending (Figure S3.6b,c). Since a proper method was lacking to determine whether Fe-impurities still remained in the catalysts, we cannot claim that trace Fe-impurities did not affect the measured curves. It is on the other hand likely that processes such as phase transformations and coexistence of α , β and γ phases occur even under Fe-Free conditions, recently demonstrated by Klaus et al.⁷⁶

The reaction dynamics analysis has evidenced that application of oxidizing potentials results in pronounced and complex changes in redox properties and catalytic activity extending over a time period of 10 min (maximal OER activity) up to 30 min (approximate equilibration reached). The origin of these changes may be related to trace Fe impurities; however, a partial influence by a loss of catalyst material (~30%) was confirmed. As a conclusion, our analysis shows that the extent of redox-state changes detected in Ni-containing catalysts implies that not only surface exposed metal sites are redox-active, but that a catalytic volume activity of the catalyst material is more likely as previously found for amorphous oxides.^{132,149}

3.3.2. Faradaic Charge Efficiency Derived from In Situ Differential Electrochemical Mass Spectrometry (DEMS)

To learn more about the reaction dynamics of the OER process, volatile product species were detected under catalytic conditions using operando differential electrochemical mass spectrometry (DEMS). The operando DEMS analysis allowed for a separation of the total faradaic anodic charge, Q_F^{tot} , transferred during a cyclic voltammetric OER scan, into two components: (1) the faradic charge Q_{F,O_2}^{DEMS} , which corresponds to the number of oxidizing equivalents consumed for water oxidation (O_2 formation), (2) the oxidation charge, $Q_{F,M}$, which corresponds to the number of redox-equivalents needed for oxidation-state changes of the metal centers.

The voltammetric profiles obtained in the DEMS setup were nearly identical to those previously measured using the RDE setup (see Figure 3.1a and S3.7-S3.8). This lent support to the accuracy of our DEMS-based faradaic charge analysis. No volatile products other than molecular O_2 (e.g., no CO_2) were

detected during anodic polarization of the Ni–Fe oxyhydroxide electrocatalysts over the entire compositional range. Figure 3.2a exemplifies our analysis for the Ni catalyst. The anodic charge under the voltammetric curve (green) represents the total faradaic charge Q_F^{tot} . The charge under the mass spectrometric trace (black) is Q_{MS,O_2} which can be converted into $Q_{\text{F},\text{O}_2}^{\text{DEMS}}$. The quantity Q_F^{tot} splits into a component associated with oxidation of Ni centers, $Q_{\text{F},\text{Ni}}$, and a component associated with the evolution of O_2 , $Q_{\text{F},\text{O}_2}^{\text{DEMS}}$.

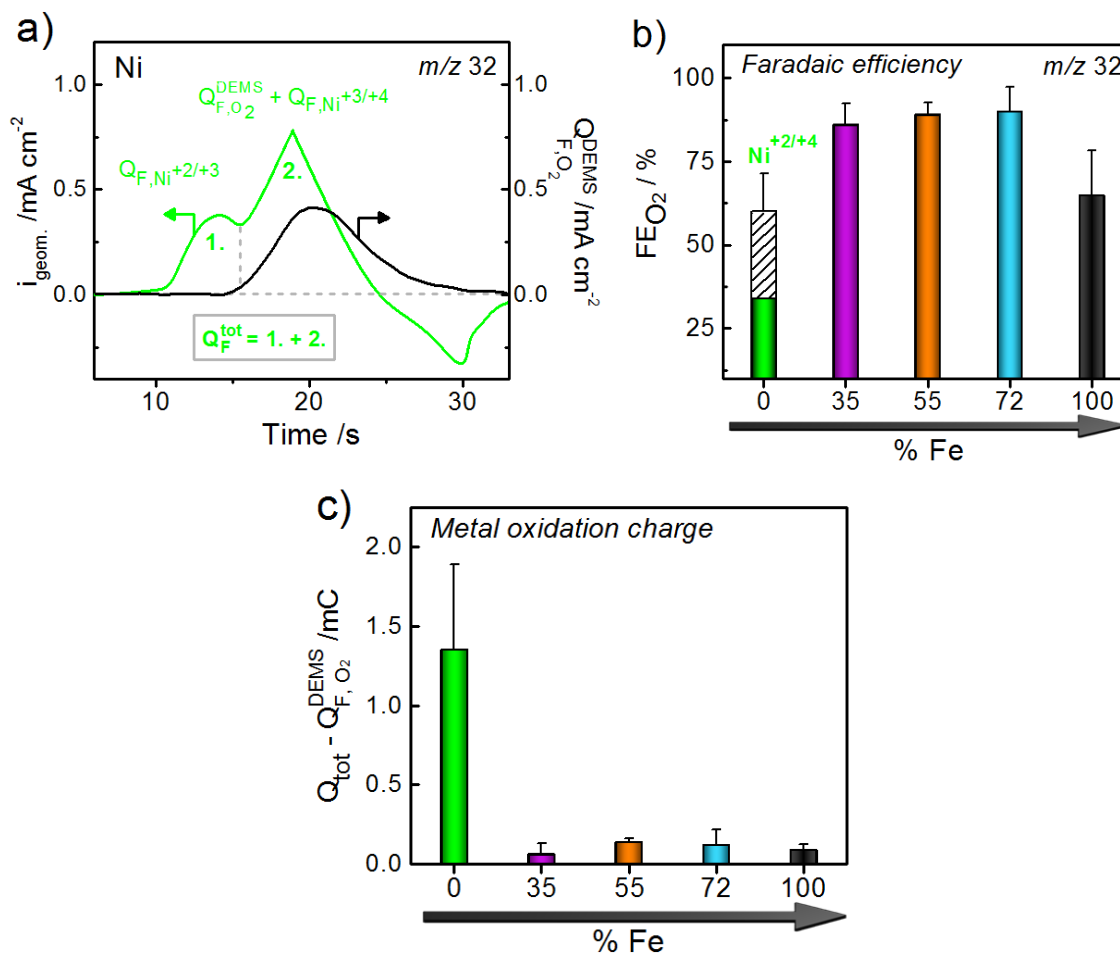


Figure 3.2. Operando DEMS during CVs in the OER region between 1 and 1.8 V_{RHE} (before iR -comp.) in 0.1 M KOH (a) In situ cyclic voltammetric scan (green curve) and the corresponding faradaic ion current of O_2 (m/z 32) (black curve) of the Ni-catalyst. Q_F^{tot} represents the total anodic charge under the green trace, and $Q_{\text{F},\text{O}_2}^{\text{DEMS}}$ is derived from the charge under the black ion current trace. (b) Faradaic O_2 efficiencies of Ni–Fe oxyhydroxide catalysts as a function of Fe-content ($\text{Ni}_{100-x}\text{Fe}_x$) given as atomic %. The hatched bar represent the O_2 efficiency excluding the charge associated with $Q_{\text{F},\text{Ni}^{+2/+3}}$, corresponding to the $\text{Ni}(\text{OH})_2/\text{NiOOH}$ redox process. The Faradaic O_2 efficiency was derived from $\text{FE}_{\text{O}_2} (\%) = Q_{\text{F},\text{O}_2}^{\text{DEMS}} / Q_F^{\text{tot}}$ (c) Absolute faradaic charge ($Q_F^{\text{tot}} - Q_{\text{F},\text{O}_2}^{\text{DEMS}}$) injected into catalyst layer for changing metal oxidation states. The catalyst composition ($\text{Ni}_{100-x}\text{Fe}_x$) is given as atomic % Fe on x-axis. The

catalyst loading was $\sim 10 \mu\text{g}/\text{cm}^2$. Error bars are derived as the standard deviation from 3 independent measurements. Additional measurements are presented in Supporting Information S3.2 (Figure S3.7-S9). *This figure has been reprinted with permission from ref. 108. Copyright (2016) American Chemical Society.*

For the Ni-catalyst, the experimental faradaic efficiency of the O_2 evolution process, FE_{O_2} , can be evaluated according to eq (3.5)

$$\text{FE}_{\text{O}_2} = Q_{\text{F},\text{O}_2}^{\text{DEMS}} / Q_{\text{F}}^{\text{tot}} = Q_{\text{F},\text{O}_2}^{\text{DEMS}} / (Q_{\text{F},\text{O}_2}^{\text{DEMS}} + Q_{\text{F},\text{Ni}}) \quad (3.5)$$

was about 33%, (see green bar in Figure 3.2b). We note that this value of FE_{O_2} was almost identical in nonpurified (Fe-containing) electrolyte and in Fe-free electrolyte. Given the absence of any other volatile product, this result implies that 67% of $Q_{\text{F}}^{\text{tot}}$ constitutes faradaic charge solely used to change the oxidation state of Ni atoms. If the 1-electron $\text{Ni}^{2+}/3+$ redox charge process (see peak area “1.” in Figure 3.2a) was subtracted from $Q_{\text{F}}^{\text{tot}}$, the resulting FE_{O_2} value roughly doubled to 60% (hatched bar in Figure 3.2). This still leaves a significant portion of the experimental anodic charge unaccounted for.

To account for this missing charge, we assume that $Q_{\text{F},\text{Ni}}$, splits into $Q_{\text{F},\text{Ni}^{2+}/3+}$, the contribution from the 1-electron $\text{Ni}^{2+}/3+$ transition, and into $Q_{\text{F},\text{Ni}^{3+}/4+}$, associated with the consecutive 1-electron redox transition from Ni^{3+} to Ni^{4+} , according to eq (3.6)

$$Q_{\text{F},\text{Ni}} = Q_{\text{F},\text{Ni}^{2+}/3+} + Q_{\text{F},\text{Ni}^{3+}/4+}. \quad (3.6)$$

Eq (6) is a plausible assumption given the much more anodic electrode potentials during the OER compared to the $\text{Ni}(\text{OH})_2/\text{NiOOH}$ redox peak potential (Figure 3.1a). Simple algebra yields eq (3.7)

$$Q_{\text{F},\text{Ni}^{3+}/4+} = 0.25 \times Q_{\text{F},\text{Ni}^{2+}/3+} \quad (3.7)$$

for the data of the Ni-catalyst (see derivation eqs S3.1-S3.5).

Considering our earlier conclusion that all Ni centers of the Ni-catalyst reached the Ni^{3+} oxidation state, our DEMS-based charge balance analysis in eq 5 clearly evidence the formation of Ni^{4+} ; in particular a maximum of 25% of all Ni centers had reached the Ni^{4+} state during the scanned OER conditions. Figure 3.2c highlights the absolute charge ($Q_{\text{F}}^{\text{tot}} - Q_{\text{F},\text{O}_2}^{\text{DEMS}}$) that was injected into the Ni redox state changes for the Ni-catalyst.

Figure 3.2b suggests that the faradaic contribution of the evolved O_2 (m/z 32) differed substantially at higher Fe contents. The O_2 faradaic efficiency reached a maximum at intermediate Ni:Fe compositions (35, 55, and 72% Fe) before it dropped again for the pure Fe catalyst. This was quite similar to the OER activity trends discussed before.

For the mixed Ni–Fe oxide catalysts, an evaluation of $Q_{F,Ni^{2+/+3}}$ is no longer possible, because the anodic redox feature vanished or shifted anodically merging with the OER voltammetric profile. The much larger FE_{O_2} values of the $Ni_{65}Fe_{35}$, $Ni_{45}Fe_{55}$ and $Ni_{28}Fe_{72}$ catalysts (Figure 3.2b) evidenced less metal redox charge processes relative to oxygen evolution charge. Thus, the average Ni valence in the mixed Ni–Fe catalysts must have remained lower compared to the Ni-catalyst. In fact, Figure 3.2c confirms how much the metal redox charge dropped in the presence of Fe. Fe appears to have a stabilizing effect on low-valent Ni centers, which largely suppresses the oxidation of Ni to higher oxidation states under OER conditions. This will be further complemented with X-ray absorption studies below.

Unlike the Ni-catalyst, the Fe catalyst showed little charge contribution toward oxidation state changes (Figure 3.2c) suggesting that Fe centers largely remained in their oxidation state even at catalytically active OER electrode potentials. The somewhat lower FE_{O_2} value directly reflects the lower catalytic OER rate compared to the mixed Ni–Fe catalysts, which lowers the relative contribution of Q_{F,O_2}^{DEMS} . Additional measurements were carried out with extended scan-limits in order to reach a similar O_2 -rate for all Ni–Fe catalysts (Figure S3.7f-g and Figure S3.8f-g). These measurements confirmed a higher FE_{O_2} value of the Fe catalyst when cycling to higher current densities (Figure 3.9). However, at such high overpotentials, other processes such as catalyst degradation and carbon corrosion might lower the overall efficiency.

In summary, our DEMS-based faradaic efficiency analysis provided independent evidence for a $Ni^{2+/4+}$ transition for the Ni-catalyst under OER conditions. In contrast, the presence of Fe caused much higher faradaic efficiency, FE_{O_2} , with values of $\sim 90\%$ for the most active mixed Ni–Fe catalysts. This evidence highly O_2 -selective catalytic OER cycles, while Fe appears to reduce the detectable amounts of high-valent Ni.

3.3.3 Compositional Analysis, Long-Range Order and SEM-EDX Elemental Mapping

X-ray diffraction of the mixed Ni–Fe catalysts (Figure 3.3a and Figure S3.10) showed broad diffraction peaks at 15° and 25° , corresponding to the (0 0 3) and (0 0 6) lattice planes associated with the interlayer spacing of the layered $Ni(OH)_2$.¹⁵⁰ Broad diffraction peaks were also visible at $\sim 40^\circ$ and $61^\circ 2\theta$; the peak at 40° could be refined with three peaks at 35° , 38° , and 45° . These all match well with observations of turbostratic α - $Ni(OH)_2$.^{72,150-155} The Fe catalyst showed reflections at similar positions, 14° , 20° , 36° , and $60^\circ 2\theta$, however with lower intensity, which have been reported for highly distorted $FeOOH$ structures. The d -spacings were found between ~ 6 – 8 \AA obtained from the (0 0 3) reflection, with small variations as a function of Fe-content. Changes in turbostratic oxyhydroxide structures are difficult to accurately

interpret due to *c*-axis stacking faults.^{72,88,105,155-158} The relative peak intensities of the (1 0 1) and (1 1 0) reflections continued to decrease at increased Fe content, which is consistent with formation of more distorted phase, in line with earlier observations of the effect of Fe intrusion in Ni lattices.^{87,89}

Scanning electron micrographs (SEM) of the Ni and the Ni₄₅Fe₅₅ catalysts showed a similar layered morphology with stacked, slightly distorted layers with a layer size of ~100 nm (see Figure 3.3b and Figure S3.11a-c). The morphology of the Fe catalyst revealed a much smaller domain size with small particles <10 nm, which partly assembled to form larger round agglomerated particles in the size of ~500 nm (see Figure S3.11d-f). This would suggest that the low XRD amplitudes observed for the Fe catalyst could have been influenced by the small particle size. The Ni-catalyst before and after exposure to catalytic potentials (1.63 V for 30 min in 0.1 M KOH) did not show detectable amounts of Fe impurities; however, traces of Fe could be below the detection limits. Elemental EDX mapping and line-scan analysis of the Ni₄₅Fe₅₅ catalyst showed a homogeneous distribution of Ni and Fe across the analyzed area (Figure 3.3b and S3.12-13), with a significant amount of oxygen distributed in the metal associated regions both of the as-prepared catalyst and after conditioning at catalytic OER potential. The EDX analysis indicated a relative loss of Fe content, resulting in a fractional change of ~9% after OER catalysis (see Figure 3.3b and S3.12), which was also confirmed by TXRF analysis as a ~6% loss (see discussion above). Apparent changes were also visible in the morphology after exposure to 1.0 and 1.63 V (Figure S3.13). The EDX mapping showed that Ni and Fe remained well distributed without visible formation of separate phases.

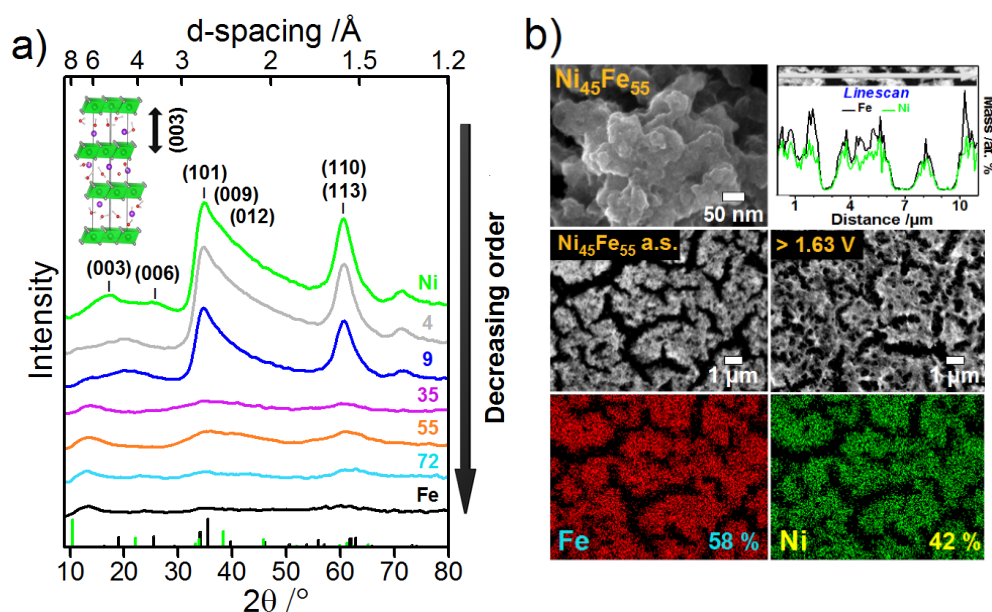


Figure 3.3. (a) Powder XRD diffractograms of as-prepared Ni-Fe(OOH) catalysts with varying Ni:Fe compositions (Ni_{100-x}Fe_x). The inset shows the structural motif of α -Ni(OH)₂ with the arrow indicating the (003) interlayer

spacing. The Fe content is indicated as atomic % Fe determined by ICP-OES. The bottom green vertical lines show the diffraction peaks of α -Ni(OH)₂ (pdf # 00–038–0715) and of FeOOH (0015441¹⁵⁹). **(b)** SEM image (top left and middle) and EDX elemental mapping (bottom) of the Ni₄₅Fe₅₅ catalyst; as-prepared catalyst. A line-scan analysis with the relative change of the Ni and Fe content across a selected path of the as-prepared catalyst is shown in the upper right corner. Atomic compositions are reported as atomic %. See also Figure S3.12 for additional SEM-EDX elemental mapping after exposure to OER catalytic conditions. *This figure has been reprinted with permission from ref. 108. Copyright (2016) American Chemical Society.*

3.3.4. Quasi-In Situ X-ray Absorption Spectroscopy (XAS)

Gaining access into prevalent local structural motifs, atomic coordination number and bond lengths of the mixed Ni–Fe catalysts was achieved using X-ray absorption spectroscopy (XAS) at the Ni and Fe *K*-edges. Catalysts with different compositions of Ni and Fe were drop-casted onto glassy carbon electrodes at a geometric metal loading of ~ 145 nmol/cm². Catalytic voltages of ~ 1.63 V_{RHE} ($\eta_{\text{OER}} = 400$ mV) were applied during 30 min in 0.1 M KOH as the conditioning step. The catalysts were freeze-quenched under applied potential using liquid N₂ according to a previously reported approach.^{132,160} Selected catalysts were also investigated under non catalytic potentials of 1.0 V_{RHE}.

2.3.4.1. Local Structure and Metal Redox States

X-ray absorption near-edge structure (XANES) showed that the Fe centers were consistently in oxidation state +3 both in as-prepared catalysts and catalysts freeze-quenched in the OER-active state (Figure 3.4a and Figure S3.14a), which have been observed in several in situ XAS studies of mixed Ni–Fe catalysts.^{77,80,102,106} Conflicting results regarding the Fe oxidation state of our catalysts compared to other studies, where Fe⁺⁴ has been observed^{138,161} up to a molar fraction of ~ 12 % at similar catalytic potentials,¹⁰³ might be attributed to the sensitivity of the respective methods. The presence of Fe⁺⁴ sites can therefore not be excluded in our study; however, the main fraction is confirmed as Fe⁺³. Distances fitted from the Fe EXAFS showed that the Fe catalyst could be well represented by O coordinated at 1.98 Å and Fe at 3.07 Å (Table 3.1 and Figure S3.15-16); however, the amplitudes of the peaks were lower than expected for a highly crystalline phase, suggesting a high distortion of the oxide motifs around the metal center in accordance with the amorphous XRD nature. The oxidation state of the Fe in our mixed Ni–Fe catalyst based on the Fe–O distances obtained from the EXAFS fitting varied between +3.1–3.4, which is in conflict with Fe in oxidation state 3+ as estimated from the *K*-edge positions (see Figure S3.17 and Table S3.1). A possible explanation for this discrepancy is that a fraction of the Fe centers are not coordinately saturated, and thus either appear as tetrahedral coordination, or the presence of O vacancies, which would explain a relatively low coordination number.

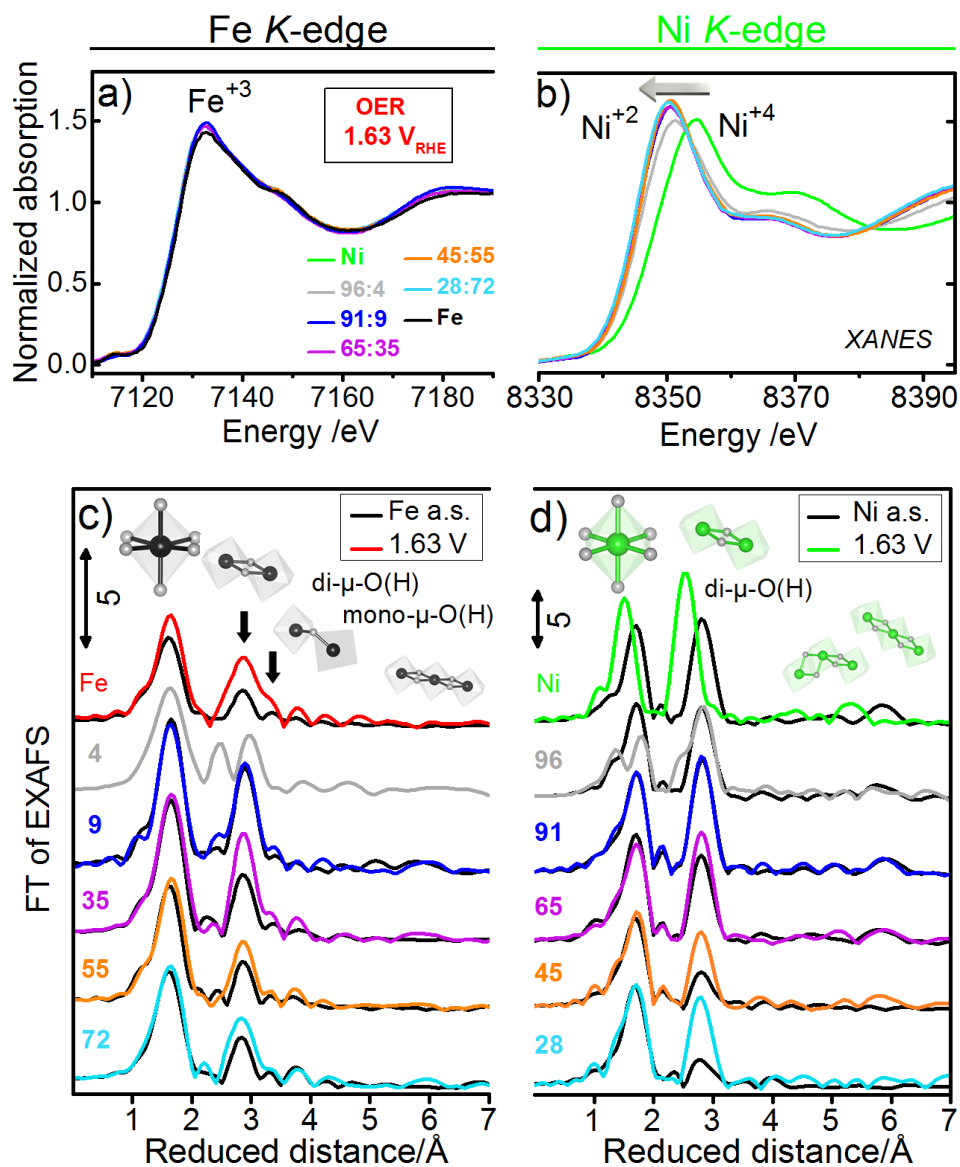


Figure 3.4. X-ray absorption spectra of the Ni–Fe catalysts with varying catalyst composition ($\text{Ni}_{100-x}\text{Fe}_x$) freeze-quenched under application of catalytic potential after conditioning at 1.63 V for 30 min in 0.1 M KOH. **(a)** Fe *K*-edges and **(b)** Ni *K*-edges. Fourier transformed k^3 -weighted EXAFS oscillations (FT-EXAFS) of as-prepared (a.s.) catalysts (black lines) and catalysts frozen under applied catalytic potential after conditioning at 1.63 V_{RHE} for 30 min in 0.1 M KOH (colored lines) measured at the **(c)** Ni *K*-edge and **(d)** Fe *K*-edge. The catalyst composition is indicated as atomic % Fe. Fit parameters are listed in Table 3.1 and Supporting Information S6, Tables S3.1–S3.7. *This figure has been reprinted with permission from ref. 108. Copyright (2016) American Chemical Society.*

Table 3.1. Fit Parameters Obtained from EXAFS Ni and Fe K-Edges of Selected Catalysts Freeze-Quenched under Applied Catalytic Potential of 1.63 V_{RHE}. This table has been reprinted with permission from ref. 108. Copyright (2016) American Chemical Society.

Fe K-edge at 1.63 V _{RHE}						
Ni _{100-x} Fe _x	R(Fe-O) /Å	CN	Ox. state	R(Fe-M) /Å	CN	R _f
Fe	1.98 ± 0.02	5.0 ± 0.9	3.4	3.05 ± 0.02	4.9 ± 1.0	20.1
Ni ₉₆ Fe ₄	1.99 ± 0.03	5.8 ± 1.0	3.4	3.11 ± 0.01 2.88 ± 0.02	3.4* ± 0.3 2.6*	23.0
Ni ₉₁ Fe ₉	2.01 ± 0.01	6.3 ± 0.8	3.1	3.12 ± 0.01	6.7 ± 1.0	15.9
Ni ₆₅ Fe ₃₅	2.01 ± 0.01	6.2 ± 0.8	3.1	3.09 ± 0.01	6.5 ± 0.8	14.4
Ni ₄₅ Fe ₅₅	2.00 ± 0.01	5.2 ± 0.8	3.2	3.08 ± 0.01	3.7 ± 0.5	17.9
Ni ₂₈ Fe ₇₂	1.99 ± 0.01	5.4 ± 0.8	3.4	3.07 ± 0.02	3.5 ± 0.7	19.4

Ni K-edge at 1.63 V _{RHE}						
Ni _{100-x} Fe _x	R(Ni-O) /Å	CN	Ox. state	R(Ni-M) /Å	CN	R _f
Ni	1.88 ± 0.01	4.9 ± 0.3	3.7	2.82 ± 0.01	6.3 ± 0.2	15.2
Ni ₉₆ Fe ₄	1.87 ± 0.02	1.9 ± 0.2	3.7	2.83 ± 0.01	4.0* ± 0.2	24.4
	2.06 ± 0.01	4.1 ± 0.2	2.0	3.07 ± 0.01	2.0*	
Ni ₉₁ Fe ₉	2.04 ± 0.01	6.6 ± 0.5	2.0	3.09 ± 0.01	5.4 ± 0.3	15.5
Ni ₆₅ Fe ₃₅	2.05 ± 0.01	6.6 ± 0.6	2.1	3.08 ± 0.01	4.9 ± 0.2	16.6
Ni ₄₅ Fe ₅₅	2.04 ± 0.01	5.6 ± 0.5	2.1	3.08 ± 0.01	3.3 ± 0.1	24.8
Ni ₂₈ Fe ₇₂	2.05 ± 0.01	6.7 ± 0.5	2.0	3.07 ± 0.01	4.4 ± 0.2	23.5

^a Full fit parameters and errors are given in Tables S3.2-S3.7. Parameters were obtained from fitting in the k-range of 2.6-12.5 Å⁻¹ for the Fe K-edge and 2.6-14 Å⁻¹ for the Ni K-edge. Error values correspond to a 68 % confidence interval. Error values correspond to a 68% confidence interval. Oxidation states were determined from M–O distances (see Figure S3.17a for oxidation states from K-edge positions). Complete fit parameters are given in Supporting Information S6, Tables S3.1-S3.7, structural models used for the Fe and Ni K-edges are shown in Figure S3.20-3.21, and reference compounds in Figure 3.22 and in Tables S3.8-S3.9.

At the Ni *K*-edge, the XANES spectra of the as-prepared catalysts showed consistently Ni atoms oxidation state +2 independent of Ni–Fe composition (Figure S3.14b) also supported by the Ni–O distances (Table 3.1), whereas the Ni-catalyst frozen under catalytic potentials of 1.63 V showed a distinct Ni *K*-edge shift of +2.7 eV (Figure 3.4b). This is consistent with Ni atoms in changing from oxidation +2 to +4 (+3.7), in accordance with previous reports of formation of a γ -NiOOH phase under catalytic OER potential.^{80,101,130,162} The FT-EXAFS of the as-prepared Ni-catalyst showed a nearly perfect match with the layered α -Ni(OH)₂^{80,101,130,139,163} and with oxygen coordinated at a distance of 2.04 Å and a Ni–Ni coordination at 3.08 Å in the as-prepared state, which upon application of 1.63 V contracted to a short Ni–O distance at 1.87 Å and Ni–Ni coordination at 2.82 Å (see also Figure S3.15-S3.16 for EXAFS fits), confirming that Ni atoms oxidized from Ni²⁺(OH)₂ → Ni⁴⁺-oxy(hydroxide) under OER potential. In the Ni₉₆Fe₄ catalyst, the potential-induced Ni *K*-edge shift was reduced to a +~0.8 eV shift (Figure 3.4b). In the Ni FT-EXAFS, this was observed as two split Ni–O distances at 1.87 and 2.06 Å and two split Ni–M distances at 2.83 and 3.07 Å (Figure 3.4d, S3.15d, and S3.17b-c. This indicates that a fraction of the Ni centers remained in oxidation state +2 under applied catalytic potential at 1.63 V. The respective Fe EXAFS of the Ni₉₆Fe₄ at 1.63 V showed two clearly separated Fe–M peaks at 2.88 and 3.11 Å, and a slightly broadened Fe–O peak (Figure 3.4c and Figure S3.15c, and Figure S3.17b-c), which implies that Fe is adapting to the changing Ni lattice without changing its oxidation state. Further addition of Fe resulted in a further decline in the potential-induced Ni *K*-edge shift, which was absent at 9% Fe (Ni₉₁Fe₉). This would suggest that Ni atoms remain in oxidation state +2 in the OER-active state in the presence of Fe atoms in mixed Ni–Fe centers. This supports the observation regarding the Faradaic efficiency of O₂ as presented in the DEMS study in Figure 3.2 above, where a contribution of Ni oxidation in the Ni-catalyst was confirmed, however absent in the mixed Ni–Fe catalysts, which showed low charge contributions and high Faradaic efficiencies of ~90% (see discussion above). Extracted Ni–O and Ni–M trends vs catalyst composition are shown in Figure S3.17. Fit parameters are listed in Table 3.1 and Supporting Information S3.6, Table S3.1-S3.7.

Our results are conflicting previous XAS studies of mixed Ni-Fe catalysts,^{14,80,101,102} however have been partly supported.^{77,106} We speculate that external influences such as measurement conditions and/or electrode material might play a more important role than previously thought. Possible charge-transfer interactions between the catalyst and Au were highlighted in MnO_x by Gorlin et al.¹⁶⁴ and were recently correlated to an increase in OER activity and Mn oxidation state by Seitz et al.¹⁶⁵. Yeo et al.¹⁴⁴ have also discussed possible charge transfer interactions between NiO_x and Au based on a significant increase in the OER activity. Doyle et al.¹⁶⁶ showed clear differences in the redox wave of NiOOH when deposited

on Au, Pt or GC electrodes. Klaus et al.⁷⁶ recently confirmed that Au also enhances the OER activity of Fe atoms. Au has been shown to oxidize already at 1.2 V_{RHE} in alkaline electrolyte,¹⁶⁷ and interactions between the catalyst and electrochemically dissolved Au atoms are therefore plausible however has so far not been thoroughly explored. The impact of external influences as a likely explanation for diverging results regarding the Ni oxidation state during OER catalysis in mixed Ni–Fe oxyhydroxides would require further investigations.

3.3.4.2. Structural Motifs, Amorphicity and Long-range Order

The Fourier-transformed EXAFS spectra showed two main peaks at the Fe and Ni *K*-edges, one at shorter distance corresponding to the nearest oxygen ligands, and a second peak at longer distance reflecting the nearest metal ligands of the X-ray absorbing metal ion (Figure 3.4c-d). The positions of these peaks and the lack of major peaks at higher distances suggest that the dominant structural motifs in the catalysts were octahedrally coordinated [MO₆] units where Ni and Fe atoms were extensively connected via μ-O(H) bridges. Addition of Fe resulted in decreased FT amplitudes, which was significant at Fe contents above 35%, suggesting that addition of Fe leads to a distortion of the ligand environment around the metal center, in accordance with the increasing atomic amorphicity suggested by the XRD data. Weaker Ni–Ni peaks were visible at longer distances, which can be well described by backscattering from the corresponding Ni atoms within the oxide layer. The FT-EXAFS spectra show that nearly identical spectral motifs were present at both Ni and Fe *K*-edges for the same Ni:Fe composition, which imply that the Ni and Fe atoms formed well-mixed centers. This contrasts findings of Friebel et al.,⁸⁰ where it was proposed that Fe nucleates as a separate phase at Fe contents above 25%. In the present study, no detection of metallic Ni or Fe was confirmed. Surprisingly, the Fe atoms contributed to binuclear Ni–Fe motifs at a coordination distance of 3.09 Å (possibly di(μ-OH) bridging) and a shorter distance of 2.86 Å (possibly di(μ-O) bridging), whereas in the Fe catalyst such long or short Fe–Fe distances were not observed. This suggests that Fe was incorporated to form Ni–Fe bonds also at Fe-contents > 25 at %. An increase of the Fe–M amplitudes at 3.45 Å was clearly visible toward high Fe contents under catalytic OER potentials. This distance indicates the presence of corner-sharing octahedra,¹⁶⁸ which have been proved computationally to be thermodynamically feasible in β-Ni(OH)₂.⁸⁹ This may also be explained by aggregation of metal-oxo octahedra undergoing condensation during catalysis, where if hydrated oxyhydroxide layers attaching end-by-end would result in such distance,¹⁶⁸ however this has so far non been extensively discussed in terms of mixed Ni–Fe oxyhydroxides. Presented SEM images (Figure S3.12-S3.13) are supportive of a rearrangement with visible changes in the morphology during applied OER potential in the mixed Ni₄₅Fe₅₅ catalyst.

Catalysts frozen under catalytic OER potential of 1.63 V showed an increase in the FT-EXAFS amplitudes compared to the as-prepared catalysts both at the Ni and Fe *K*-edge clearly revealed in Figure S3.18 (see also Figure S3.19 for XANES and EXAFS). We notice that this increase is not caused specifically by the application of catalytic potential since catalysts frozen under non catalytic potential (1.0 V) showed even higher FT-EXAFS amplitudes than catalysts conditioned at 1.63 V. The Ni₄₅Fe₅₅ catalyst showing highest OER activity also preserved highest distortion around the metal center in the active state (visible in Figure 3.4d). Thus, high catalytic OER activity is correlated with higher distortion around the metal center. This would suggest that high activity is associated with a highly disordered state, which could be ascribed to high amorphicity. This could on the other hand be reflected in the number of highly active Ni–Fe centers, and thus would be most visible in the catalyst with a high turnover.

3.3.5. Correlation of Activity, Faradaic Efficiency, and Metal Redox States

This section establishes a plausible correlation of the voltammetric, XAS, and DEMS results and seeks reconciliation with earlier reports. Key findings of our present study are illustrated in Figure 3.5. The Ni-catalyst with its edge-connected octahedral structural motifs undergoes a pronounced redox state change between +2 and +3/+4 under OER conditions, evidenced by both XAS and DEMS-based faradaic efficiency data. In presence of Fe, however, data suggested a stabilization of low-valent Ni centers, in particular for the most active mixed Ni–Fe catalysts. Pure Fe centers essentially showed no change in their redox state, as well. Our XAS results pointed in the same direction given the absence of any potential-induced Ni or Fe *K*-edge shift of the Fe-containing catalysts under catalytic reaction conditions. At the same time, corner-connected Fe–O octahedra emerge as a prominent structural motif. While these results are in agreement with a number of previous studies,^{80,106,138} they are partially in conflict with others.^{80,103} These conflicting reports on the metal oxidation state bear the question whether the catalytically most active metal centers actually remain in low-valent states, or whether there are other mechanisms or external influences that make the observation of low-valent states under certain experimental and catalytic conditions extremely challenging as discussed above.

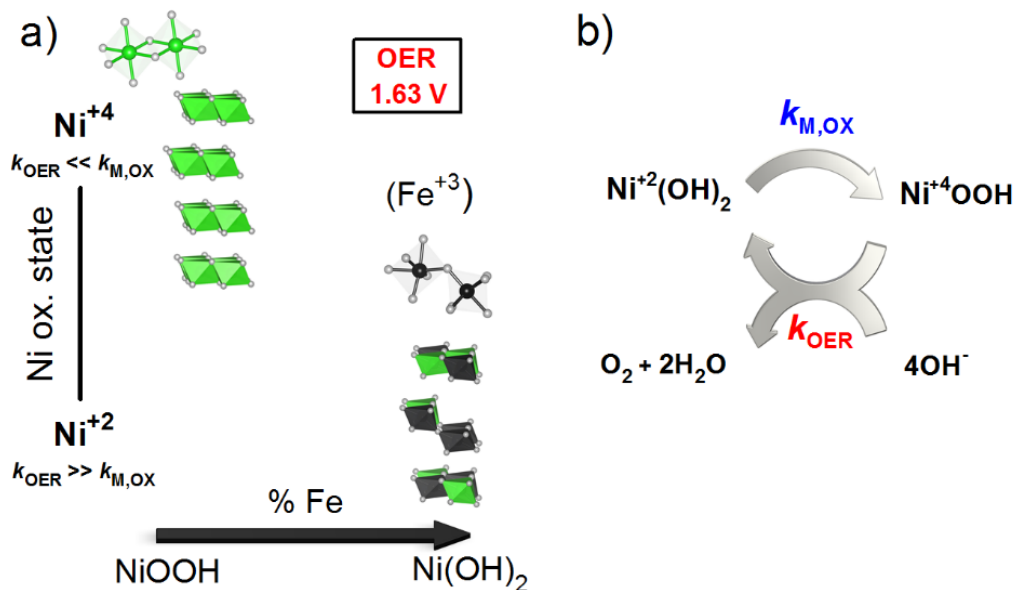


Figure 3.5. a) XAS-derived structural motifs prevalent during OER catalysis at high and intermediate Ni-content. At high Ni-content the dominating host is the layered γ -NiOOH (a “NiO₂” phase) with octahedrally coordinated edge-sharing Ni⁴⁺. In the presence of Fe there is a mixture of edge- and corner sharing octahedra.¹⁶⁸⁻¹⁷⁰ Above 4% Fe, the dominant host is the Ni(OH)₂ with Ni²⁺. (b) Simplified scheme of the electrochemical water splitting cycle with metal oxidation rate constant, $k_{M,OX}$, and the catalytic OER rate constant, k_{OER} . *This figure has been reprinted with permission from ref. 108. Copyright (2016) American Chemical Society.*

Intuitively, one would expect the metal redox centers to build up oxidation equivalents during the catalytic cycles. So, a muted redox activity of the Ni and the suspected active Fe centers appears implausible. A simple argument states that the bulk-sensitive XAS methods may miss the catalytic redox processes near surfaces. However, this can be ruled out based on the fact that the XAS analysis of the pure Ni-catalyst showed indeed strong variations in its redox state. In addition, the DEMS results gave independent evidence for significantly reduced charge injection associated with metal redox processes.

Assuming the muted metal redox processes are real, one may argue that the presence of Fe centers might have shifted the neighboring Ni²⁺ oxidation potential to such positive values that Ni²⁺ oxidation is no longer energetically possible at +1.63 V. The electrochemical data, however, are in conflict with this view. The Ni(OH)₂/NiOOH redox peak does indeed shift by ~70 mV from +1.38 V to +1.45 V (see Figure 3.1) at increasing Fe contents: the midpoint potential, however, is still clearly below the applied potential of +1.63 V. Thus, the population of Ni atoms at catalytic potential should include formation of Ni⁴⁺OOH.

An alternative hypothesis to reconcile conflicting results regarding the actual metal redox state under catalytic conditions is outlined in Figure 3.5b. We represent an individual catalytic OER cycle by a very simplified reaction scheme, where the buildup of oxidation equivalents from Ni²⁺ to Ni⁴⁺ (or Fe³⁺ to Fe⁴⁺) sites is followed by the O–O bond formation with the subsequent release of molecular oxygen. This process restores the metal site back to its reduced state. The full cycle thus can be split into two consecutive processes that are assumed to proceed with the reaction rate constants $k_{M,ox}$ and k_{OER} , respectively (see Figure 3.5.b).

It has been shown for various water-oxidizing oxides of monometallic first-row transition metals that the second water-oxidation–metal-reduction step is slower (rate-limiting) than the metal oxidation ($k_{Mox} \gg k_{OER}$) which results in accumulation of high-valent metal species at catalytic potentials. In our bimetallic Ni–Fe catalysts, however, the presence of Fe enhances the OER rate by 1–2 orders of magnitude. This increase reflects a dramatically increased rate constant, k_{OER} , which may exceed the rate of the metal oxidation, i.e., $k_{OER} \gg k_{Mox}$. The origin of the increased OER activity in terms of faster OER rate constant have been discussed previously as a plausible explanation;^{72,87} however, evidence of low valent Ni could not be confirmed. Under these conditions, a significant accumulation of high-valent metal centers is prevented, even though the reaction cycle does involve formation of high-valent metal ions.

Our hypothesis reconciles voltammetric, DEMS and XAS data consistently. It predicts that the observation of Ni in its high-valent state critically depends on the $k_{M,ox}/k_{OER}$ ratio. Subtle differences between catalyst materials, or external influences, thus could favor or disfavor detection of Ni⁴⁺ ions at OER potentials so that our model offers a simple explanation for conflicting results in previous reports.

3.4. Conclusions

We have characterized and correlated the OER reaction dynamics, the faradaic charge efficiency, and the corresponding metal redox states of Ni–Fe oxyhydroxide electrocatalysts. To achieve this, we combined operando electrochemical mass spectrometry (DEMS) and X-ray absorption spectroscopy (XAS) with electrochemical characterization. Our results and conclusions offer new fundamental insights into the reaction dynamics and the state of the metal centers under reactive conditions. Our critical discussion of the present results in light of previous reports has resulted in a simple mechanistic model hypothesis that is capable to resolve conflicting past reports on the prevailing active metal redox states.

We investigated amorphous Ni–Fe catalysts with various compositions (0–100 at. % Fe). The highest OER activity was observed around a 50% Fe, supported by low Tafel slopes in the order of 35 mV dec⁻¹. Tracking the evolution of the normalized Ni^{2+/3+} redox charge evidenced that the OER catalysis needs to

be recognized as a volume, not as a surface process. The continuous change in the electrochemical properties of the Ni–Fe(OOH) series excludes the formation of separate Ni- and Fe-oxide phases or metallic Ni, instead suggests the formation of a well-mixed bimetallic phase with catalytic properties determined by the Ni:Fe stoichiometry.

The deconvolution of faradaic processes using operando DEMS allowed for relating the evolution of O₂ to the metal redox state changes. For the NiOOH catalyst, there was a large charge contribution process not resulting in product formation and a low faradaic efficiency (max ~60%), which evidenced the presence of Ni⁴⁺. The presence of Fe (while boosting the OER activity) diminished the charge contribution process of Ni⁴⁺, reaching faradaic efficiencies in the order of ~90%.

Quasi-in situ X-ray absorption spectroscopy confirmed the DEMS-based conclusions. They showed that the oxidation state of Ni atoms in the mixed Ni–Fe electrocatalysts under catalytic OER conditions were highly dependent on the Ni:Fe stoichiometry whereas the Fe oxidation state was not. The Fe structure was best described as a highly distorted Fe³⁺OOH with a mixture of edge-sharing and corner-sharing octahedra. The Ni structure was well described as α-Ni(OH)₂ with Ni in oxidation state +2 in the as-prepared state. Under catalytic conditions, Ni atoms were present as Ni⁴⁺ at Fe content below 4%, and above, Ni atoms were stabilized in low-valent oxidation state under catalytic conditions, and thus the OER active state could be described as Ni²⁺Fe³⁺OOH. At the Fe *K*-edge, there was no visible *K*-edge shift for any composition; however, a strong Fe-M bond contraction was observed, well correlated with the lattice contraction in the Ni host.

Finally, a simple mechanistic hypothesis was put forward to explain why the experimental detection of Ni centers predominantly in lower-valent states do not preclude an efficient electrocatalytic water splitting process where redox equivalents are accumulated in the metal centers. The mechanistic hypothesis highlights the fact that the detection of metal centers in high-valent states critically depends on the $k_{M,ox}/k_{OER}$ ratio. High catalytic OER activity of the mixed Ni–Fe catalysts sharply decreases this ratio; the population of high-valent Ni atoms are depressed due to a faster OER rate constant in comparison to the metal oxidation step ($k_{OER} \gg k_{M,ox}$). This hypothesis plausibly explains water oxidation at seemingly low-valent metal centers and reconciles past diverging reports.

Supporting Information

The Supporting Information is available free of charge on the [ACS Publications website](#) at DOI: [10.1021/jacs.6b00332](https://doi.org/10.1021/jacs.6b00332).

Experimental details and additional electrochemical and structural characterization. ([PDF](#))

Contact

pstrasser@tu-berlin.de

holger.dau@fu-berlin.de

Acknowledgement

This project received financial support by the Bundesministerium für Bildung und Forschung (BMBF) under grant 03SF0433A–“MEOKATS”. P.S. acknowledges partial funding by the German Federal Ministry of Education and Research (Bundesministerium für Bildung und Forschung, BMBF) under grant #03SF0523A–“CO2EKAT”. We thank the Helmholtz-Zentrum Berlin (HZB) for allocation of synchrotron radiation beamtime at KMC-1 and KMC-3 (BESSY synchrotron, Berlin Adlershof), and we gratefully acknowledge support by Marcel Mertin, Dr. Franz Schäfers, and Dr. Ivo Zizak (all BESSY/HZB). This project also received financial support by the Berlin cluster of excellence “UniCat”.

Supporting Information

Oxygen evolution reaction dynamics, faradaic charge efficiency, and the active metal redox states of Ni-Fe oxide water splitting electrocatalysts

This material has been reprinted with permission from the American Chemical Society as the Supporting Information of the latest version of a published Journal article

(Görlin, M.; Chernev, P.; Ferreira de Araújo, J.; Reier, T.; Dresp, S.; Paul, B.; Krähnert, R.; Dau, H.; Strasser, P., *Journal of the American Chemical Society*, 2016, 138, 5603. DOI: 10.1021/jacs.6b00332)

URL: <http://dx.doi.org/10.1021/jacs.6b00332>

Copyright (2016) American Chemical Society

Mikaela Görlin¹, Petko Chernev², Jorge Ferreira de Araújo¹, Tobias Reier¹, Sören Dresp¹, Benjamin Paul¹, Ralph Krähnert¹, Holger Dau², and Peter Strasser¹

¹*Technical University of Berlin, Department of Chemistry, Chemical Engineering Division, Straße des 17. Juni 124, 10623, Berlin, Germany*

²*Free University of Berlin, Department of Physics, Arnimallee 14, 14195 Berlin, Germany*

S3.1. Electrochemical characterization

S3.1.1. OER activity

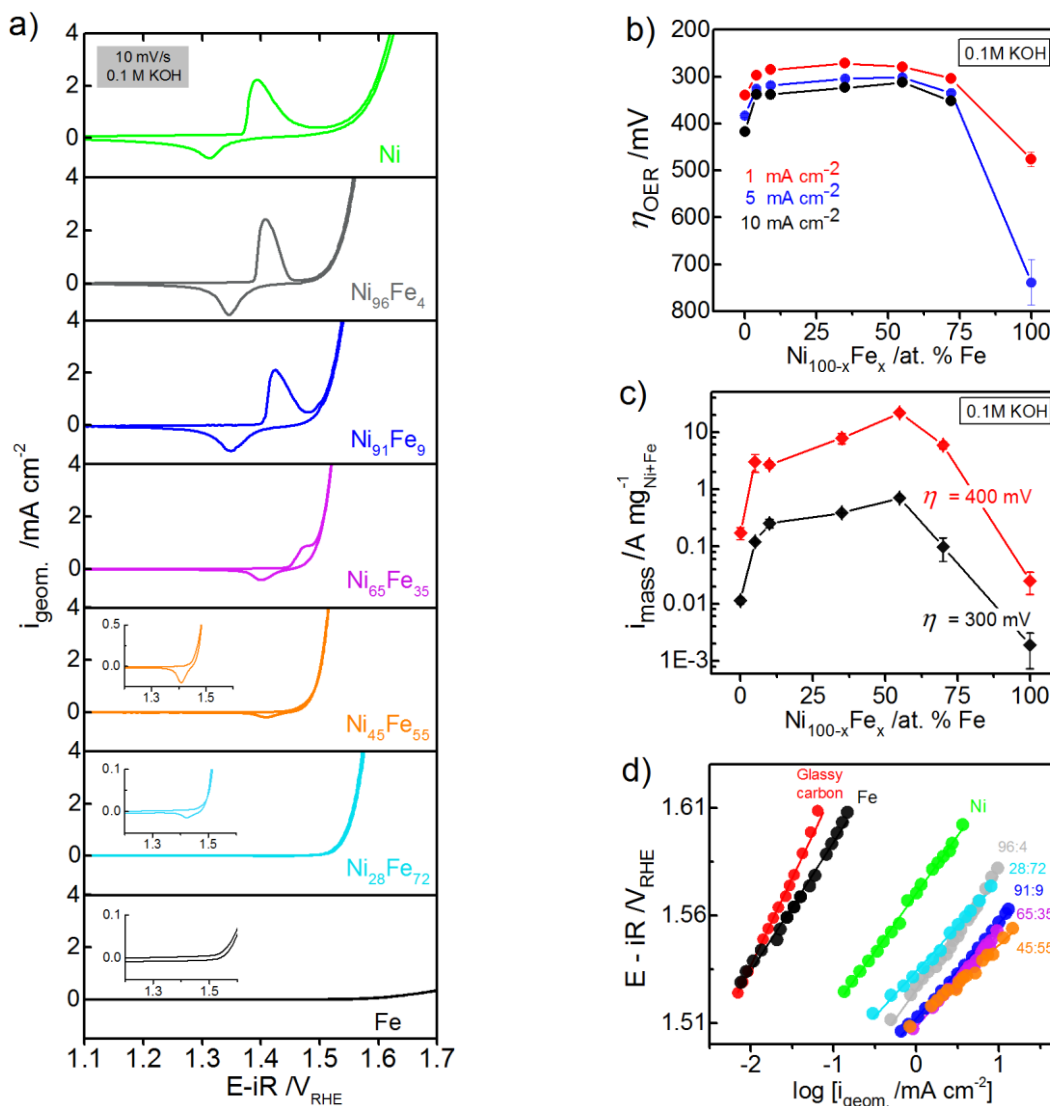


Figure S3.1 (a) CVs measured at 10 mV/s in rotating disk electrode (RDE) setup after an initial pre-conditioning step of 1.63 V_{RHE} for 30 min in 0.1 M KOH. (b) Overpotential (η_{OER}) at 1, 5, and 10 mA cm⁻², extracted from chronopotentiometric measurements. (c) Mass activity (i_{mass}) based on the total metal loading obtained by ICP-OES. (d) Tafel plots obtained from quasi-stationary state measurements by applying a stable potential for 90 s in 0.1 M KOH. The catalyst composition, Ni_{100-x}Fe_x, is indicated as atomic %. The total geometric metal loading was determined by ICP-OES prior to the measurements, kept at $\sim 10 \mu\text{g Ni+Fe cm}^{-2}$ in the presented measurements. The rotation speed was set to 1600 rpm. *This figure has been reprinted with permission from ref. 108. Copyright (2016) American Chemical Society.*

S3.1.2. The effect of applying reducing potential

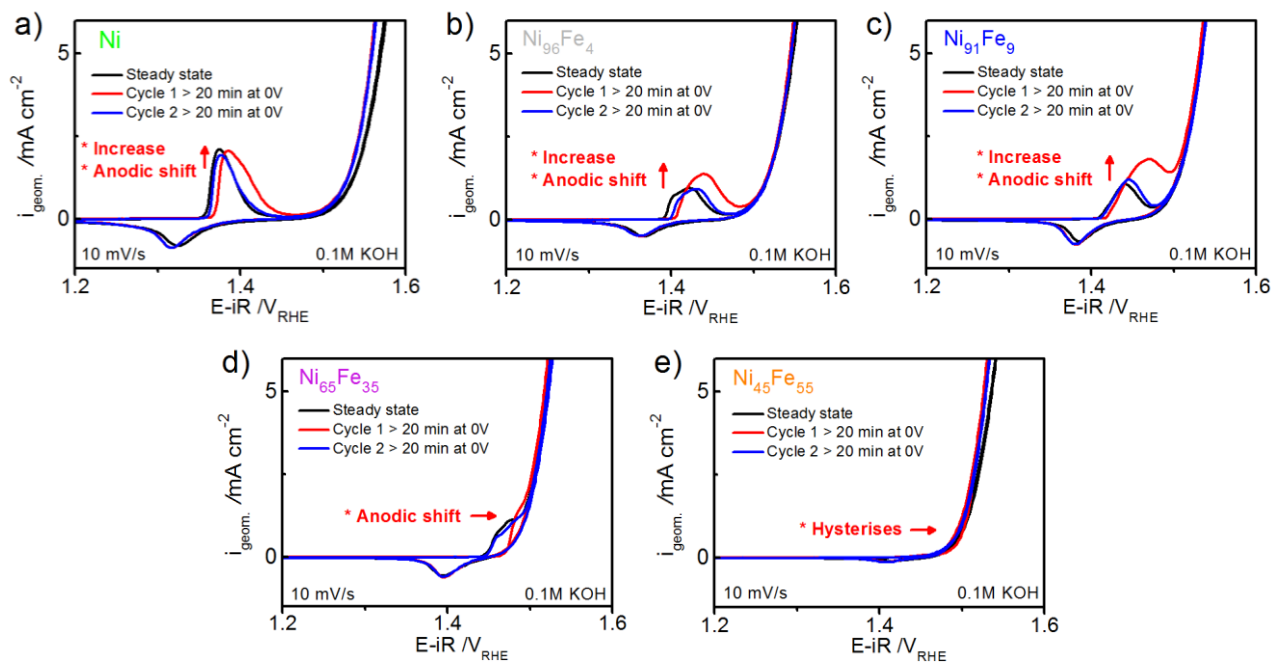


Figure S3.2. CVs measured before and after application of a reducing potential (0 VRHE) for 20 min to make sure all Ni centers were in the reduced state, according to the principle presented by Batchellor et al.¹⁴⁶ (a) The Ni catalyst (b) Ni₉₆Fe₄ (c) Ni₉₁Fe₉ (d) Ni₆₅Fe₃₅ (e) Ni₄₅Fe₅₅. CVs were recorded in RDE setup at a scan-rate of 10 mV/s, a rotation speed of 1600 rpm, and a metal loading of $\sim 6 \mu\text{g Ni+Fe cm}^{-2}$. The catalyst composition (Ni_{100-x}Fe_x) is given as atomic %. This figure has been reprinted with permission from ref. 108. Copyright (2016) American Chemical Society.

S3.1.3. Conditioning of catalysts

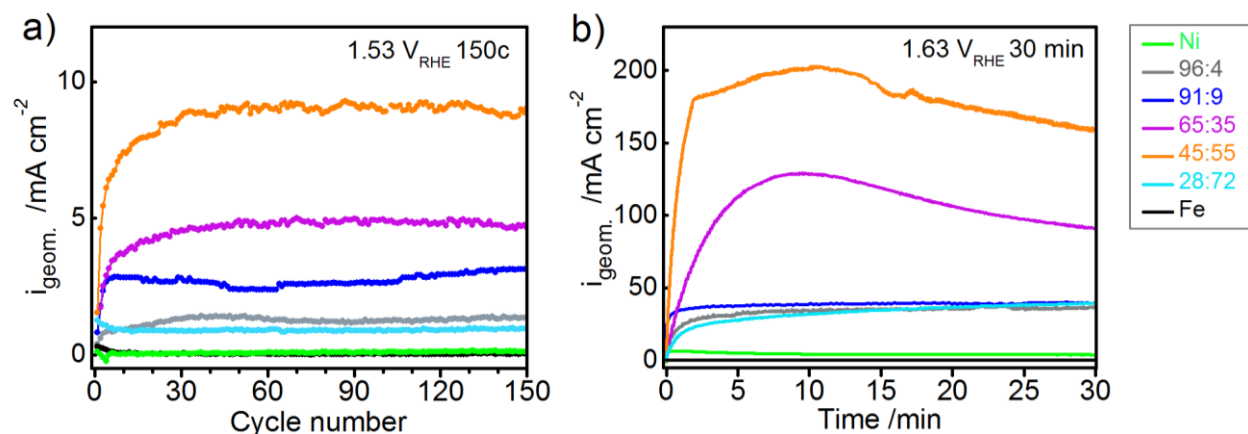


Figure S3.3. Evaluation of the OER activity during potentiodynamic and potentiostatic conditioning. **(a)** Geometric current densities ($i_{\text{geom.}}$) extracted at $1.53 \text{ V}_{\text{RHE}}$ during the first 150 cycles, collected at a scan-rate of 100 mV/s . **(b)** Application of $1.63 \text{ V}_{\text{RHE}}$ for 30 min according to the conditioning protocol for the quasi-in situ XAS measurements. The measurements in (b) were carried out at iR-corrected potentials. Measurements were carried out in RDE setup in 0.1 M KOH . The metal loading was $\sim 10 \mu\text{g Ni+Fe cm}^{-2}$. The catalyst composition ($\text{Ni}_{100-x}\text{Fe}_x$) is given as atomic %. *This figure has been reprinted with permission from ref. 108. Copyright (2016) American Chemical Society.*

S3.1.4. Dynamic redox changes

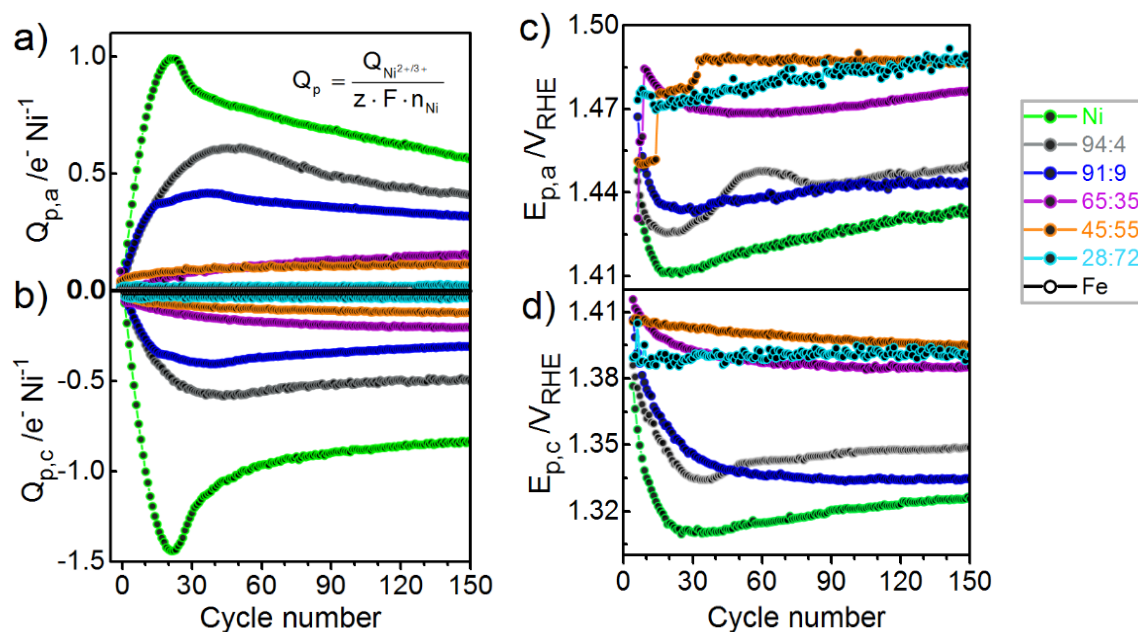


Figure S3.4. Evaluation of the $Ni(OH)_2/NiOOH$ redox peak during the first 150 cycles; **(a)** Anodic redox electrons ($Q_{p,a}$) defined as electrons transferred per Ni atoms ($e^- Ni^{-1}$) **(b)** Cathodic redox electrons ($Q_{p,c}$) **(c)** Anodic peak potential ($E_{p,a}$) **(d)** Cathodic peak potential ($E_{p,c}$). The value of Q was estimated based on the moles of Ni on the electrode determined prior to the measurement using ICP-OES. Measurements were carried out in RDE setup in 0.1 M KOH, at a scan-rate 100 mV/s at a rotation speed of 1600 rpm, and a metal loading of $\sim 10 \mu g Ni+Fe cm^{-2}$. The catalyst composition ($Ni_{100-x}Fe_x$) is indicated as atomic %. *This figure has been reprinted with permission from ref. 108. Copyright (2016) American Chemical Society.*

S3.1.4.1. Mass corrected redox electrons

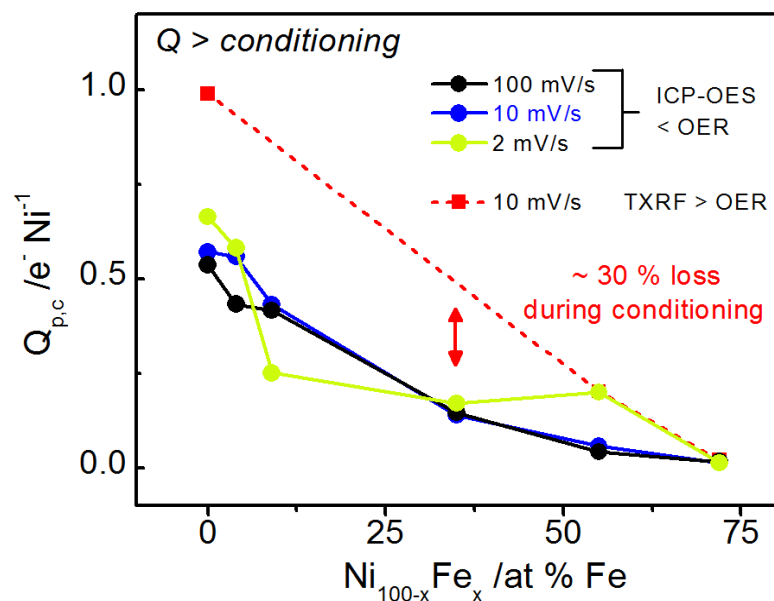


Figure S3.5. Evaluation of redox electrons ($e^- \text{Ni}^{-1}$) for the cathodic $\text{Ni}(\text{OH})_2/\text{NiOOH}$ redox peak estimated after application of $1.63V_{\text{RHE}}$ for 30 min in 0.1 M KOH. The integration was done at different scan-rates (100, 10, and 2 mV/s). The values of Q were estimated based on the total moles of Ni on the electrodes determined of as-prepared catalysts prior to the measurements using ICP-OES (< OER), and based on the total moles of Ni on the electrodes after the conditioning step determined using TXRF analysis (> OER). *This figure has been reprinted with permission from ref. 108. Copyright (2016) American Chemical Society.*

S3.1.5. Impact of Fe impurities

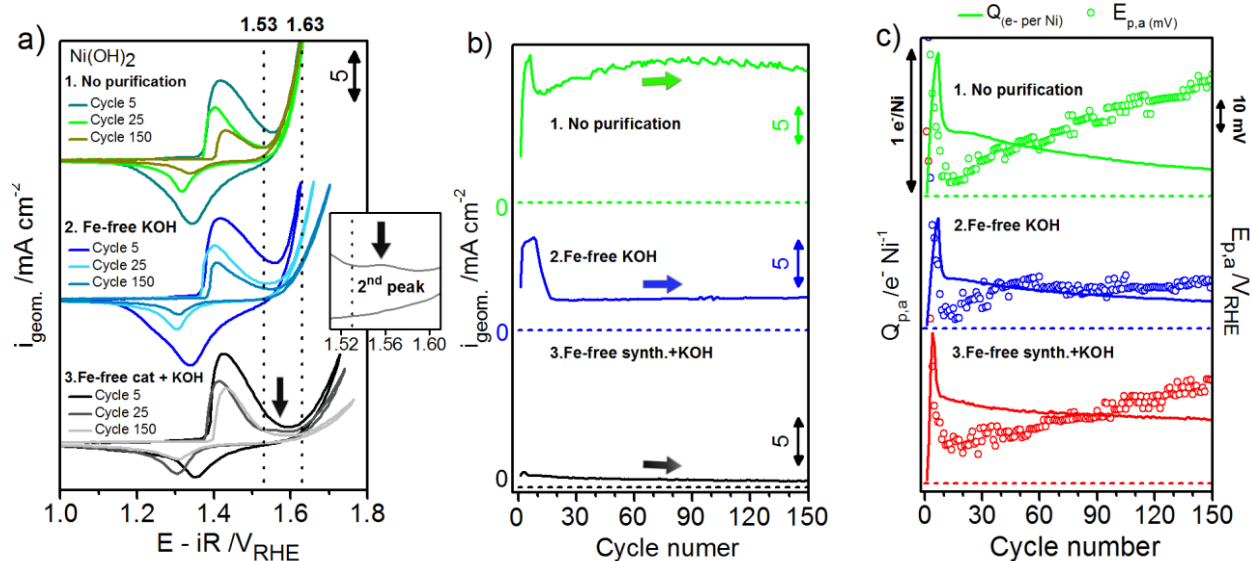


Figure S3.6. The Ni-catalyst (α -Ni(OH)₂) measured in 0.1 M KOH at different levels of Fe-impurities. **(a)** CVs of the Ni catalyst prepared without further purification measured in non-purified KOH **(1.)** Ni catalyst measured in Fe-free 0.1 M KOH **(2.)** Ni-catalyst prepared with purified chemicals measured in Fe-free 0.1 M KOH **(3.)**. Displayed CVs are cycle 5, 25 and 150. The inset shows an additional redox peak visible at ~ 1.56 V at cycle 25 **(b)** Geometric current density at $1.63 V_{RHE}$ during the first 150 cycles for the catalysts shown in (a). **(c)** Integrated anodic redox electrons (e- per Ni) and the corresponding anodic peak position ($E_{p,a}$) during the first 150 cycles of the catalysts presented in (a). All measurements were recorded in RDE setup at 1600 rpm at a scan-rate of 100 mV/s using electrochemical cells made of polypropylene (Nalgene[®]) to avoid Fe-contamination. The geometric metal loading was $\sim 5 \mu\text{g Ni+Fe cm}^{-2}$ determined by ICP-OES. All purifications were carried out according to the method reported by Trotochaud et al.⁷² This figure has been reprinted with permission from ref. 108. Copyright (2016) American Chemical Society.

S3.2. Differential Electrochemical Mass Spectrometry (DEMS)

S3.2.1. DEMS; Voltage domain

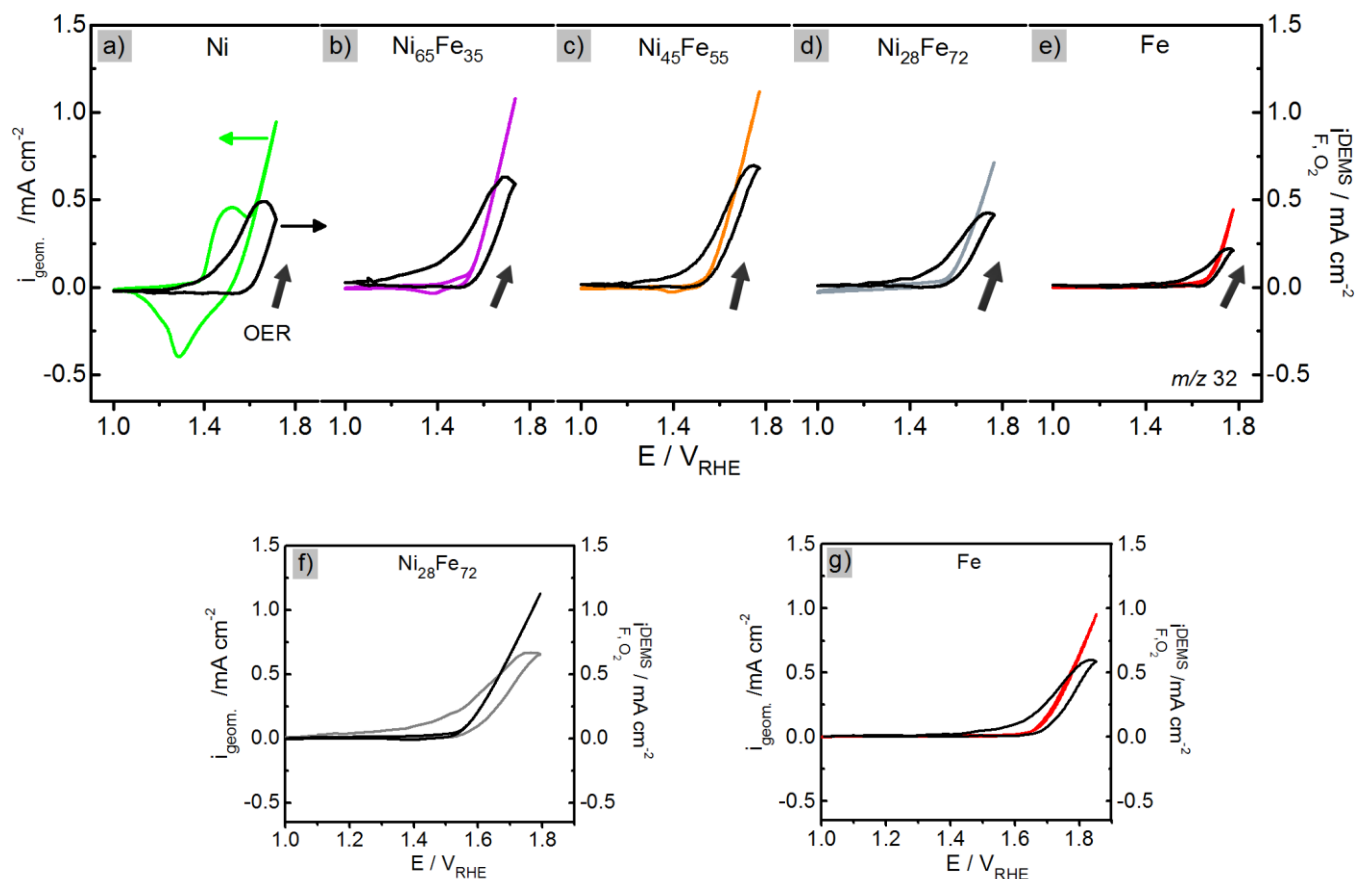


Figure S3.7. Differential electrochemical mass spectrometry (DEMS) measured in 0.1 M KOH using a dual thin-layer flow-cell. CVs were recorded at 50 mV/s between 1-1.8 V_{RHE} (before iR-comp.). **(a)** Ni catalyst **(b)** $Ni_{65}Fe_{35}$ **(c)** $Ni_{45}Fe_{55}$ **(d)** $Ni_{28}Fe_{72}$ **(e)** Fe catalyst. In order to reach higher current densities for some of the less active catalysts, CVs were recorded with increased scan-limits ($\sim 2.0 V_{RHE}$ before iR-comp.) of **(f)** $Ni_{28}Fe_{72}$ and **(g)** Fe catalyst. Geometric current density from the potentiostat (CVs) are shown as *colored lines* (left axis) and the mass spectrometric faradaic ion current of O_2 (m/z 32) are shown as *black lines* (right axis). The arrows pointing upwards indicate the scan direction of the DEMS trace. A calibration constant (K^*) was used to convert the integrated ion current to faradaic current. More information is given in Experimental section 3.2.6. The catalyst composition ($Ni_{100-x}Fe_x$) is given as atomic %. *This figure has been reprinted with permission from ref. 108. Copyright (2016) American Chemical Society.*

S3.2.2. DEMS; Time domain

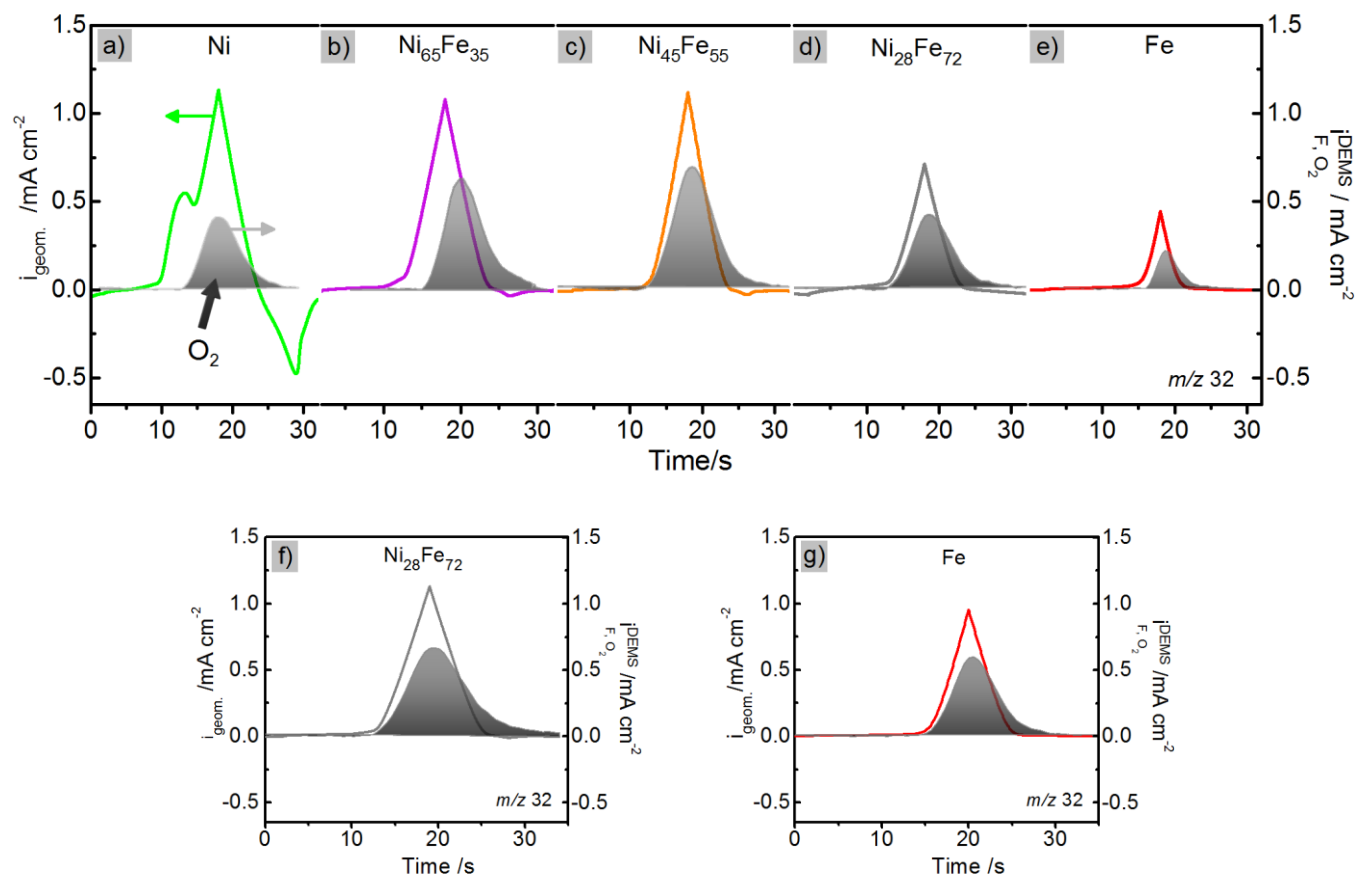


Figure S3.8. DEMS traces of the CVs in Fig. S7 shown in the time domain, measured in 0.1 M KOH using a dual thin-layer flow-cell. CVs were recorded at 50 mv/s between 1-1.8 V_{RHE} (before iR-comp.) and are shown for selected catalysts; **(a)** Ni **(b)** Ni₆₅Fe₃₅ **(c)** Ni₄₅Fe₅₅ **(d)** Ni₂₈Fe₇₂ **(e)** Fe. In order to reach higher current densities for less active catalysts CVs were recorded with increased scan-limits (~ 2.0 V_{RHE} before iR-comp.) of **(f)** Ni₂₈Fe₇₂ and **(g)** Fe catalyst. The CVs are shown as *colored lines* (left axis) and the mass spectrometric faradaic ion current of O₂ (*m/z* 32) as *black lines* (right axis). The arrows indicate the scan direction of the DEMS trace. A calibration constant (*K**) was used to convert the integrated ion current to faradaic current. More information is given in Experimental section 3.2.6. The catalyst composition (Ni_{100-x}Fe_x) is given as atomic %. *This figure has been reprinted with permission from ref. 108. Copyright (2016) American Chemical Society.*

S3.2.3. Faradaic efficiency – extended scan limits

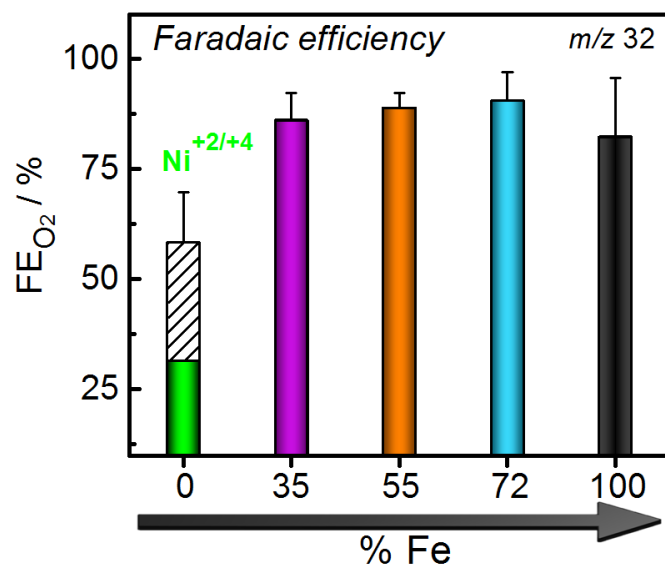


Figure 3.9. Faradaic efficiency (FE) for mixed Ni-Fe catalysts with efficiencies of the $Ni_{28}Fe_{72}$ and Fe-catalysts re-evaluated based on the measurements with extended scan-limits shown in Fig. S3.7f-g and S3.8f-g, scanned up to $\sim 2.0 V_{RHE}$ (before iR-comp.) to reach higher current densities. *This figure has been reprinted with permission from ref. 108. Copyright (2016) American Chemical Society.*

S3.2.4. Faradaic efficiency equations

These equations have been reprinted with permission from ref. 108. Copyright (2016) American Chemical Society.

$$\frac{Q_{F,jO_2}^{DEMS}}{Q_{F,O_2}^{DEMS} + Q_{F,Ni^{+3/+4}}} = 0.6 \quad (S3.1)$$

$$0.4 Q_{F,O_2}^{DEMS} = Q_{F,Ni^{+3/+4}} \quad (S3.2)$$

$$\frac{Q_{F,O_2}^{DEMS}}{Q_{F,O_2}^{DEMS} + Q_{F,Ni^{+2/+3}} + Q_{F,Ni^{+3/+4}}} = 0.33 \quad (S3.3)$$

$$1.6 Q_{F,O_2}^{DEMS} = Q_{F,Ni^{+2/+3}} \quad (S3.4)$$

$$\frac{Q_{F,Ni^{+3/+4}}}{Q_{F,Ni^{+2/+3}}} = \frac{1}{4} \quad (S3.5)$$

S3.3. X-ray diffraction

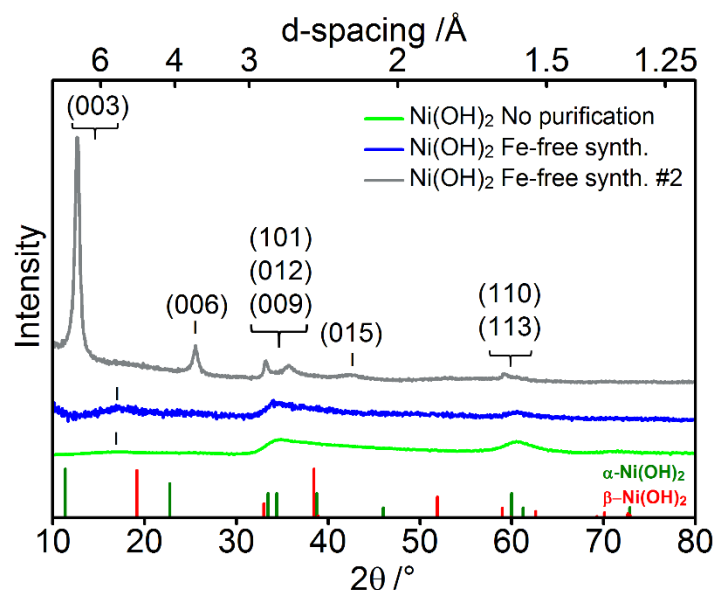


Figure S3.10. XRD of the as-prepared Ni catalyst; prepared with as-received chemicals (green curve), Fe-Free Ni catalyst prepared with purified chemicals (blue curve), and a slightly different Ni catalyst prepared with purified chemicals and a modified synthesis protocol (grey curve). Further details are given in the Experimental section 2.1. The lines at the bottom show reference patterns of α -Ni(OH)₂ (red, pdf # 00-038-0715) and β -Ni(OH)₂ (dark green, pdf # 01-074-2075). Removal of trace Fe (purification) was carried out according to the method reported by Trotochaud et al.⁷² This figure has been reprinted with permission from ref. 108. Copyright (2016) American Chemical Society.

S3.4. SEM-EDX elemental analysis

S3.4.1. SEM of Ni and Fe catalysts

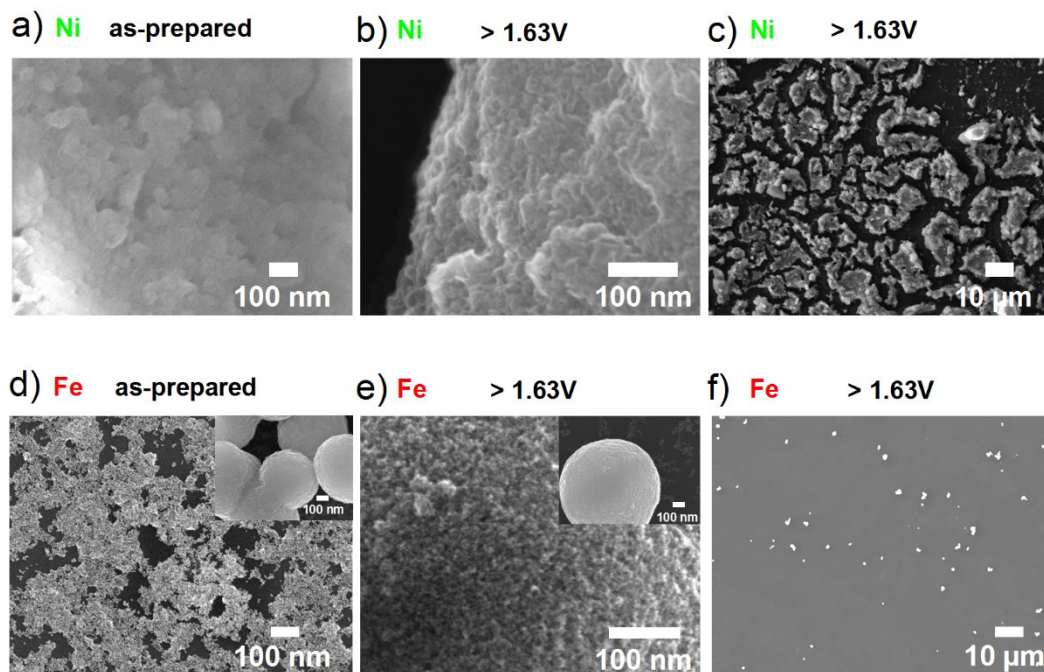


Figure S3.11. SEM images of catalysts drop-casted on glassy carbon electrodes; **(a)** as-prepared Ni catalyst **(b-c)** Ni catalyst after application of 1.63 V for 30 min in 0.1 M KOH (as received) shown at different magnifications. **(d)** As-prepared Fe catalyst. The inset shows large agglomerates of small Fe particles. **(e-f)** Fe catalyst after application of 1.63 V for 30 min in 0.1 M KOH (as received) shown at different magnifications. The inset in (d) shows a large Fe agglomerate. *This figure has been reprinted with permission from ref. 108. Copyright (2016) American Chemical Society.*

S3.4.2. EDX elemental mapping of Ni₄₅Fe₅₅

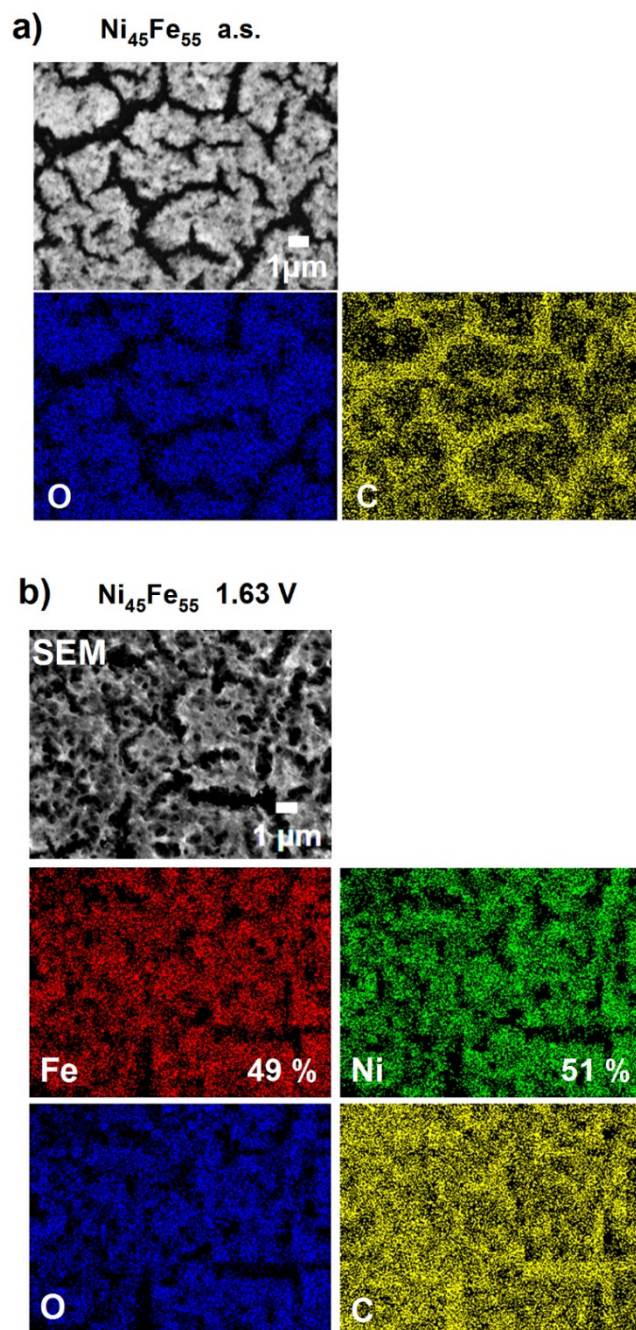


Figure S3.12. SEM images and EDX elemental mapping of the Ni₄₅Fe₅₅ catalyst drop casted on a glassy carbon electrode. **(a)** O and C content of the as-prepared catalyst **(b)** O, C, Ni, and Fe content of the catalyst shown in (a) after conditioning at 1.63 V for 30 min in 0.1 M KOH. The elements in the EDX mappings are indicated with colors; Ni (green), Fe (red), and O (blue), C (yellow). *This figure has been reprinted with permission from ref. 108. Copyright (2016) American Chemical Society.*

S3.4.3. EDX line-scan analysis of Ni₄₅Fe₅₅

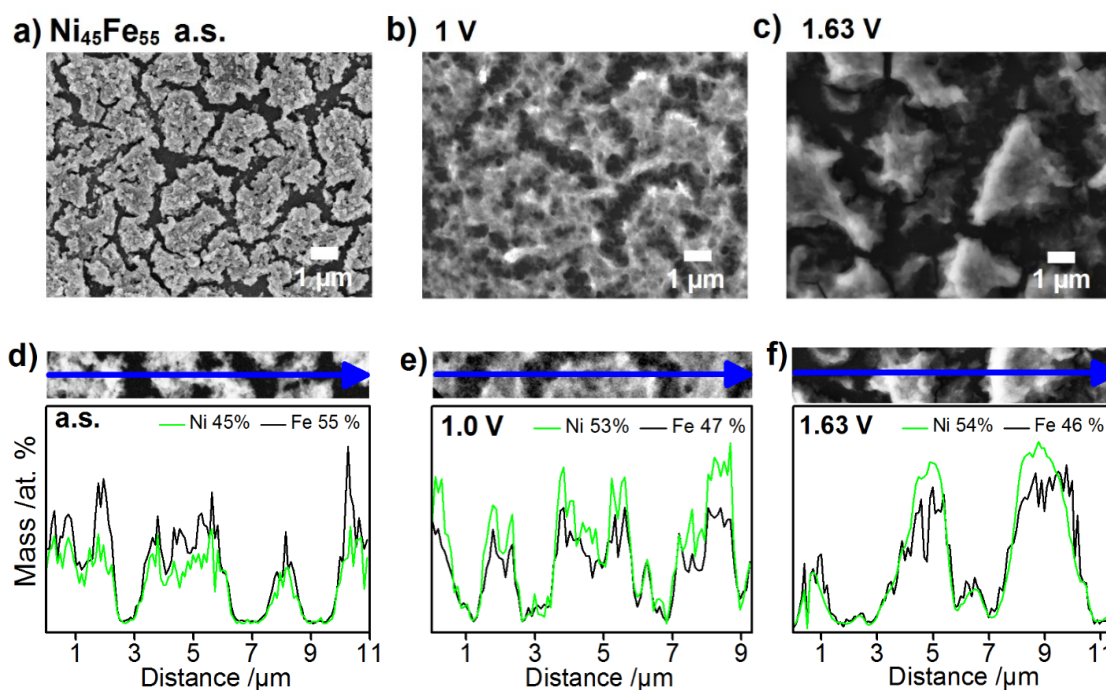


Figure S3.13. SEM images of the Ni₄₅Fe₅₅ catalysts drop-casted on glassy carbon electrodes **(a)** as-prepared catalyst (a.s.) **(b)** after application of 1.0 VRHE for 30 min in 0.1 M KOH **(c)** after application of 1.63 VRHE for 30 min in 0.1 M KOH. The catalysts in (a-c) were further analyzed using energy dispersive X-ray line-scan analysis to determine the atomic composition of Ni and Fe across a selected path (blue arrow) **(d)** as-prepared **(e)** conditioned at 1.0 V **(f)** conditioned at 1.63 V. *This figure has been reprinted with permission from ref. 108. Copyright (2016) American Chemical Society.*

S3.5. Quasi- in situ X-ray absorption spectroscopy

S3.5.1. Ni and Fe XANES

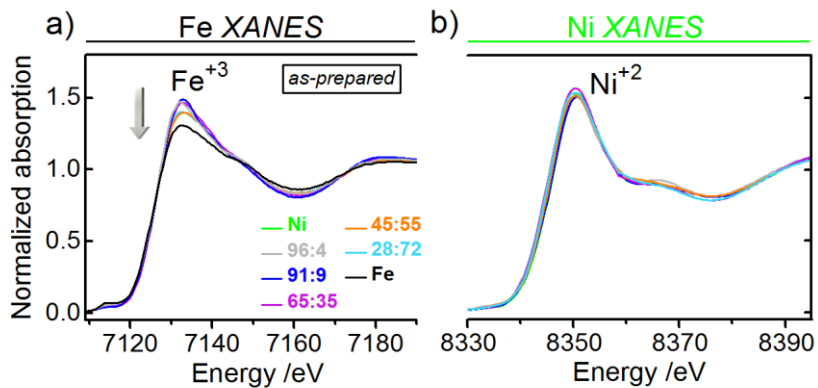


Figure S3.14. X-ray absorption near edge spectra (XANES) of as-prepared catalysts. **(a)** Fe K-edges **(b)** Ni K-edges. The catalyst composition, $\text{Ni}_{100-x}\text{Fe}_x$, is indicated as atomic % in the legend shown in (a) which applies to both Fe and Ni K-edges. *This figure has been reprinted with permission from ref. 108. Copyright (2016) American Chemical Society.*

S3.5.2. Fourier transformed EXAFS

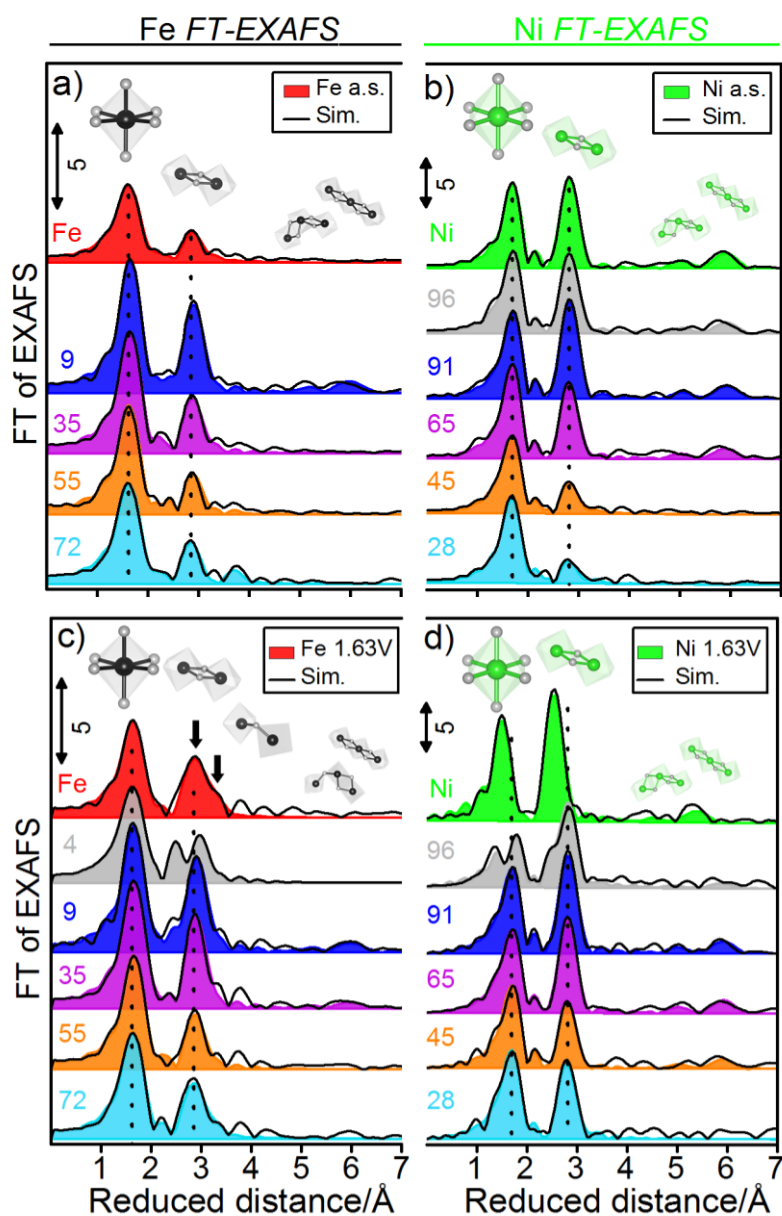
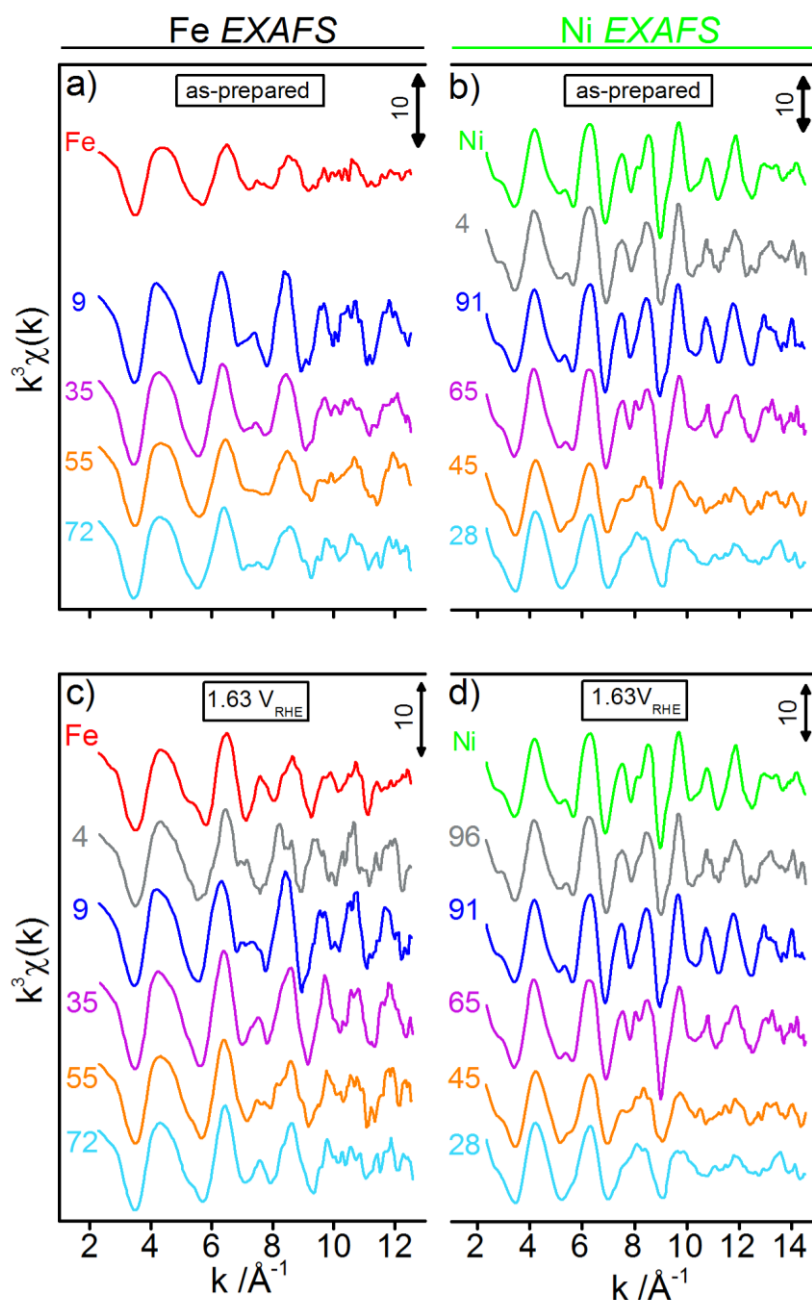


Figure S3.15. Fourier transformed k³-weighted EXAFS spectra. Experimental data (*black curves*) and simulations (*colored shaded areas*) at the **(a)** Ni K-edge of as-prepared catalysts (a.s.) **(b)** Fe K-edge of as-prepared catalysts **(c)** Ni K-edge of catalysts freeze-quenched at 1.63 V **(d)** Fe K-edge of catalysts frozen at 1.63 V. The catalyst composition, Ni_{100-x}Fe_x, is indicated as atomic % Fe or Ni for the respective edge. Catalysts were freeze quenched under applied potential after conditioning at the given potential for 30 min in 0.1 M KOH. Fit parameters are listed in Tables S3.2-S3.5. *This figure has been reprinted with permission from ref. 108. Copyright (2016) American Chemical Society.*

S3.5.3. Extended X-ray absorption spectroscopy



S3.5.4. XAS trends vs. catalyst composition

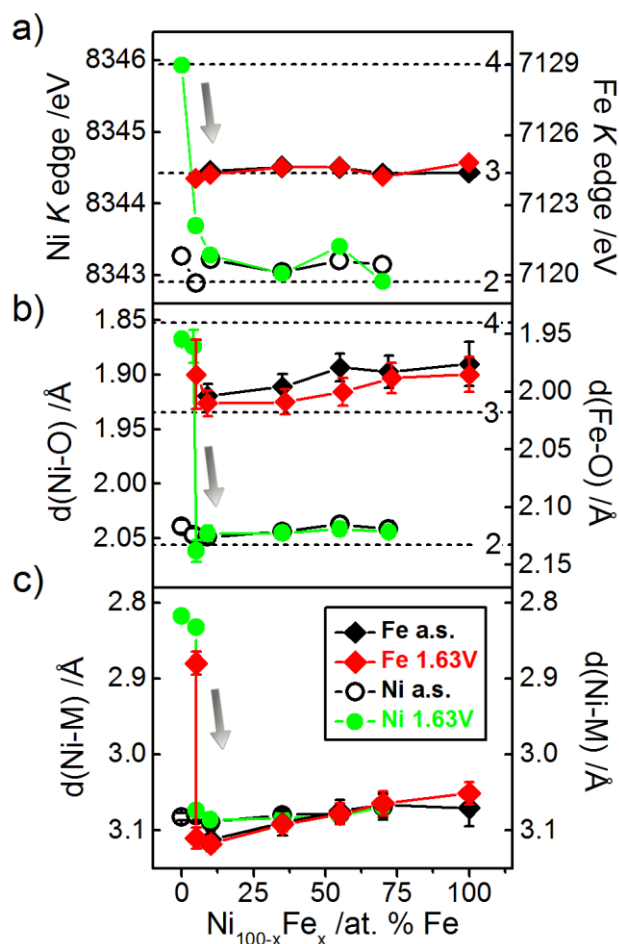


Figure S3.17. Trends obtained from the fitted XAS spectra as a function of Fe-content **(a)** Ni and Fe K-edge positions. **(b)** M-O coordination distances **(c)** M-M coordination distances. The dotted lines in (a)-(b) indicate the oxidation states determined from reference compounds presented in Tables S3.8-3.9. The values in (b-c) were obtained by the fitting k3-weighted EXAFS oscillations in k-space between 2.6-14 Å⁻¹ at the Ni K-edge and 2.6-12.5 Å⁻¹ at the Fe K-edge. Fit parameters are listed in Tables S3.2.1-S3.5. *This figure has been reprinted with permission from ref. 108. Copyright (2016) American Chemical Society.*

S3.5.5. Quasi- in situ XAS at different potentials

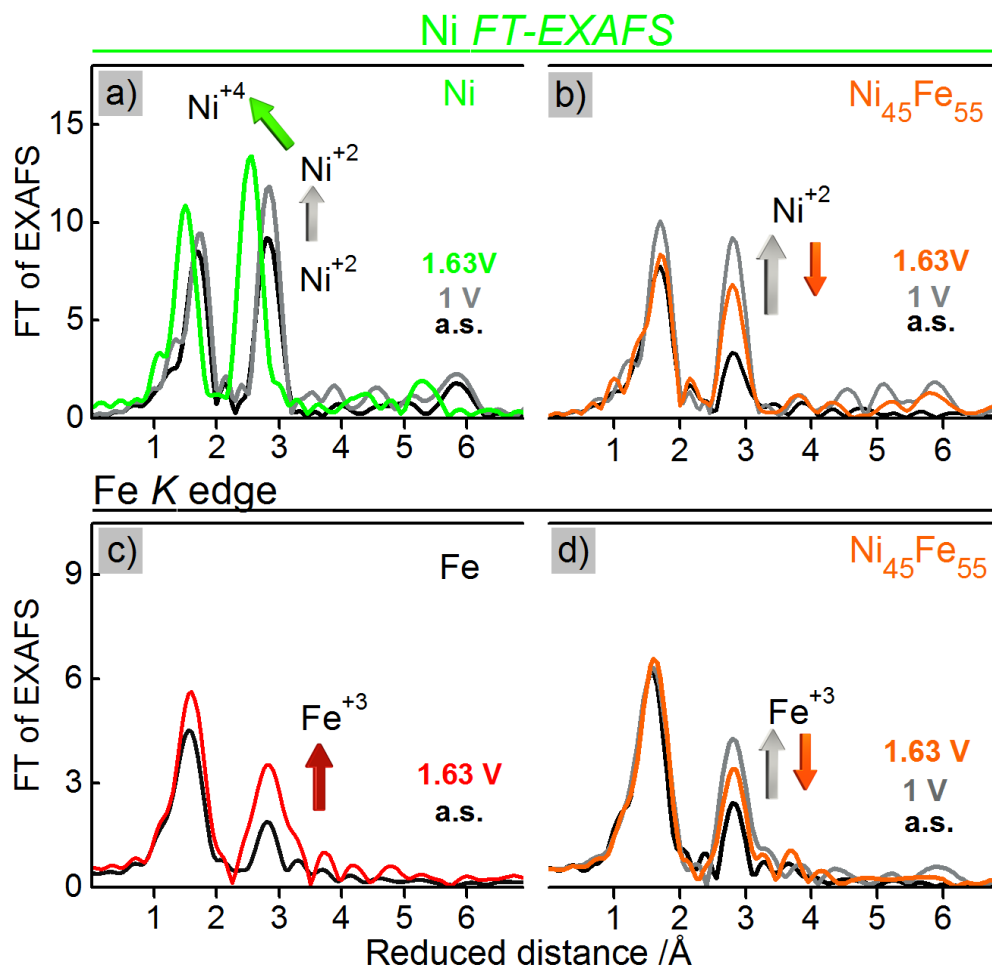


Figure S3.18. The k^3 -weighted FT-EXAFS at the Ni K -edges of the (a) Ni catalyst and (b) Ni₄₅Fe₅₅ catalyst, and at the Fe K -edges of the (c) Fe catalyst and (d) Ni₄₅Fe₅₅. Data is shown for the as-prepared catalysts (a.s., black curves), and catalysts frozen at 1.0 VRHE (grey curves), and catalysts frozen at 1.63 VRHE (colored curves). Catalysts were frozen at the given potential after conditioning for 30 min in 0.1 M KOH. This figure has been reprinted with permission from ref. 108. Copyright (2016) American Chemical Society.

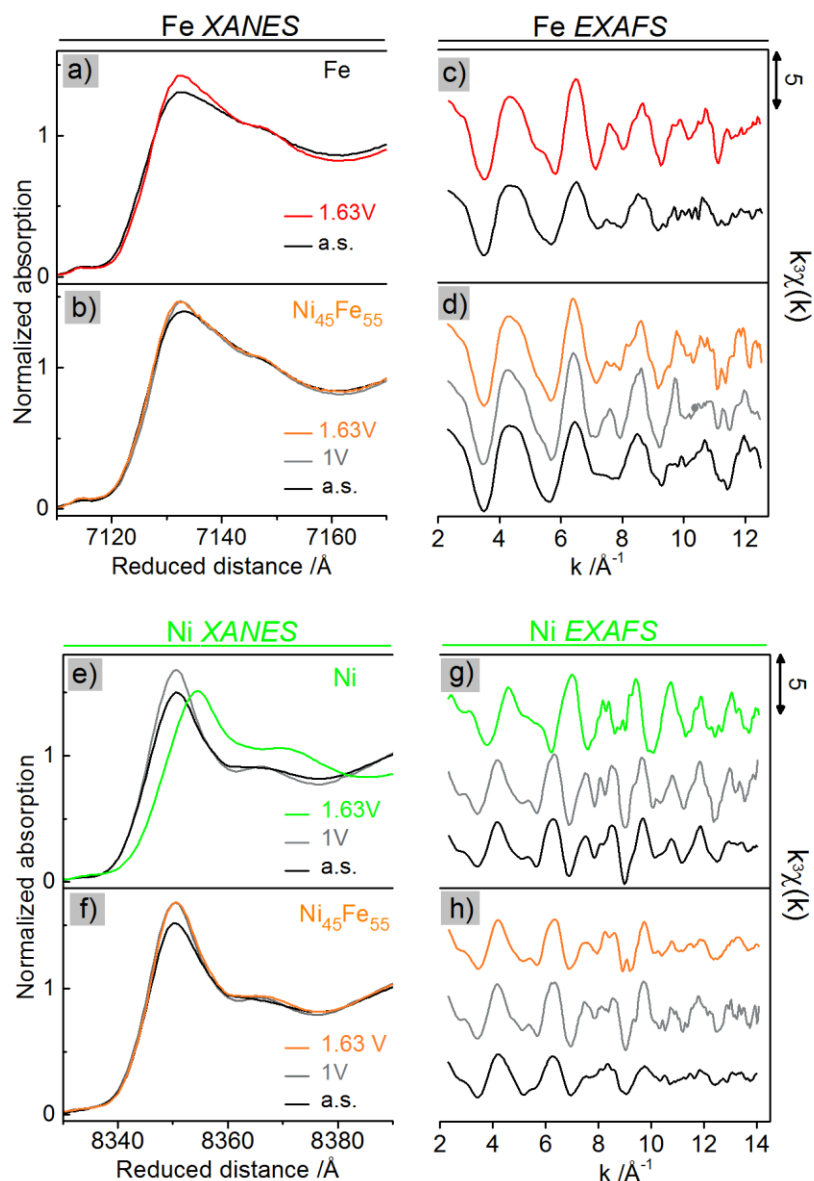


Figure S3.19. Fe K-edge XANES of (a) Fe catalyst and (b) Ni₄₅Fe₅₅, and Fe EXAFS oscillations of (c) Fe catalyst and (d) Ni₄₅Fe₅₅. Ni K-edge XANES of (e) Ni catalyst and (f) Ni₄₅Fe₅₅, and Ni EXAFS oscillations of (g) Ni catalyst and (h) Ni₄₅Fe₅₅. Shown are as-prepared catalysts (a.s., *black curves*), freeze quenched at 1.0 V_{RHE} (*grey curves*), and freeze quenched at 1.63 V_{RHE} (*colored curves*). The catalyst composition, Ni_{100-x}Fe_x is given as at. %. Catalysts were freeze-quenched under applied potential after conditioning at the given potential for 30 min in 0.1 M KOH. This figure has been reprinted with permission from ref. 108. Copyright (2016) American Chemical Society.

S3.6. XAS simulations & tables of fit parameters

The k^3 weighted EXAFS spectra were extracted using $E_0 = 8333$ eV for the Ni *K*-edge and $E_0 = 7117$ eV for the Fe *K*-edge. The simulations were carried out using in-house software (SimX) with phase functions generated from atomic coordinates of layered α -Ni(OH)₂, γ -NiOOH and γ/α -FeOOH using FEFF version 9.1 with self-consistent field option switched on^{4,5}. An amplitude reduction factor S_0^2 of 0.85 was used at both the Ni and Fe *K*-edges. The fits were carried out in *k*-space with a range of 25-750 eV above E_0 (*k*-range of 2.6 -14 \AA^{-1}) for the Ni *K*-edge and 25-600 eV (*k*-range of 2.6-12.5 \AA^{-1}) for the Fe *K*-edge. A global fit approach was used, where Debye-Waller factors of each Ni/Fe-M shell had the same value for all as-prepared catalysts and another value for all freeze-quenched catalysts. To account for variations in catalyst composition of the mixed Ni-Fe catalysts arising from variations in the phase functions associated with either Ni or Fe absorbers, each M-M shell was split into a M-Ni and M-Fe shell with a ratio between them set equal to the actual atomic Ni:Fe ratio determined by ICP-OES. To simulate the FT peaks at reduced distance 5-6 \AA , a shell corresponding to three collinearly arranged metal atoms, Ni/Fe-M-M, was added to the simulation of some of the catalysts, with a shell distance set equal to double the corresponding Ni/Fe-M distance; the shell included multiple-scattering contributions and contributions from three metal atoms arranged at an angle of 120° (see the insets of Figure S3.15 for the corresponding structural motifs). Two additional shells at 2.86 \AA and at 3.45 \AA were required in order to achieve a reasonable fit quality in the freeze-quenched catalysts and were included at both Ni and Fe *K*-edges; the two distances had the same value in all freeze-quenched catalysts in the global fit. The fit parameters were optimized by the least squares method using a Levenberg-Marquardt algorithm; parameter errors were determined from the covariance matrix of the fit and correspond to 68 % confidence intervals.

S3.6.1. Tables of XAS fit parameters

Table S3.1. Ni and Fe K-edge positions of as-prepared catalysts (a.s.) and catalysts freeze-quenched at 1.63 V after conditioning for 30 min in 0.1 M KOH, with corresponding average oxidation states determined from a comparison to reference compounds presented in Tables S3.8-3.9. *This table has been reprinted with permission from ref. 108. Copyright (2016) American Chemical Society.*

Ni_{100-x}Fe_x /at. %	Ni K-edge				Fe K-edge			
	Pos. (a.s.) /eV	Ox. state	Pos. (1.63 V) /eV	Ox. state	Pos. (a.s.) /eV	Ox. state	Pos. (1.63V) /eV	Ox. state
Ni₁₀₀Fe₀	8343.3	2.2	8345.9	4.0	-	-	-	-
Ni₉₆Fe₄	8342.9	2.0	8343.7	2.6	-	-	7124.2	2.9
Ni₉₁Fe₉	8343.2	2.2	8343.3	2.3	7124.5	3.0	7124.3	3.0
Ni₆₅Fe₃₅	8343.0	2.1	8343.0	2.1	7124.7	3.1	7124.6	3.1
Ni₄₅Fe₅₅	8343.4	2.2	8343.3	2.3	7124.6	3.1	7124.7	3.1
Ni₂₈Fe₇₂	8343.2	2.2	8342.9	2.0	7124.4	3.0	7124.2	3.0
Ni₀Fe₁₀₀	-	-	-	-	7124.4	3.0	7124.9	3.1

K-edge positions (pos.) were obtained by the integral method reported by Dau et al.¹⁷¹ The catalyst composition is given as atomic %, rounded to the nearest integer.

Table S3.2. Fe K-edge simulation parameters of the FT-EXAFS oscillations of as-prepared unconditioned catalysts (a.s.). The catalyst composition, Ni_{100-x}Fe_x, is given as atomic %. The fit k-range were 2.6-12.5 Å⁻¹. ¹. This table has been reprinted with permission from ref. 108. Copyright (2016) American Chemical Society..

Fe K-edge as-prepared						
Ni _{100-x} Fe _x	Shell	R /Å	CN	σ /Å	ΔE ₀ /eV	R _f
Ni₀Fe₁₀₀	Fe-O	1.98 ± 0.02	4.4 ± 0.9	0.10 ± 0.02	0.4	14.5
	Fe-M	3.07 ± 0.02	2.6 ± 1.1	0.09 ± 0.01*		
Ni₉₁Fe₉	Fe-O	2.00 ± 0.01	5.9 ± 0.8	0.08 ± 0.01	0.8	11.7
	Fe-M	3.11 ± 0.01	6.0 ± 1.6	0.09 ± 0.01*		
	Fe-M-M	6.22 [†]	1.5 ± 1.2	0.09 ± 0.01*		
Ni₆₅Fe₃₅	Fe-O	2.00 ± 0.01	5.6 ± 0.8	0.08 ± 0.01	0.8	12.2
	Fe-M	3.09 ± 0.02	3.5 ± 0.8	0.09 ± 0.01*		
Ni₄₅Fe₅₅	Fe-O	1.98 ± 0.01	4.8 ± 0.7	0.08 ± 0.01	0.4	15.2
	Fe-M	3.08 ± 0.02	3.8 ± 0.7	0.09 ± 0.01*		
Ni₂₈Fe₇₂	Fe-O	1.98 ± 0.01	5.3 ± 0.9	0.09 ± 0.01	0.5	16.7
	Fe-M	3.07 ± 0.02	3.0 ± 0.9	0.09 ± 0.01*		

* Debye-Waller parameters (σ) of Fe-M shells that had the same value in a global fit approach.

[†] Coordination distance of the Fe-M-M shell was set equal to double the Fe-M distance.

Debye-Waller parameters, coordination distances (R) and coordination numbers (CN) were kept unrestricted unless indicated. Catalyst composition is given as atomic %, rounded to the nearest integer.

Table S3.3. Ni K-edge EXAFS simulation parameters of as-prepared catalysts (a.s.). The fitted k-range was 2.6-14 Å⁻¹. This table has been reprinted with permission from ref. 108. Copyright (2016) American Chemical Society.

Ni K-edge as-prepared						
Ni _{100-x} Fe _x	Shell	R /Å	CN	σ /Å	ΔE ₀ /eV	R _f
Ni ₁₀₀ Fe ₀	Ni-O	2.04 ± 0.01	5.2 ± 0.5	0.07 ± 0.01	1.4	13.1
	Ni-M	3.08 ± 0.01	6.3 ± 0.4	0.07 ± 0.01*		
	Ni-M-M	6.16 [†]	2.6 ± 0.6	0.07 ± 0.01*		
Ni ₉₆ Fe ₄	Ni-O	2.05 ± 0.01	5.6 ± 0.5	0.07 ± 0.01	1.9	14.4
	Ni-M	3.08 ± 0.01	5.5 ± 0.4	0.07 ± 0.01*		
	Ni-M-M	6.16 [†]	1.9 ± 0.6	0.07 ± 0.01*		
Ni ₉₁ Fe ₉	Ni-O	2.05 ± 0.01	5.7 ± 0.5	0.07 ± 0.01	1.7	9.9
	Ni-M	3.09 ± 0.01	6.6 ± 0.4	0.07 ± 0.01*		
	Ni-M-M	6.19 [†]	2.2 ± 0.6	0.07 ± 0.01*		
Ni ₆₅ Fe ₃₅	Ni-O	2.04 ± 0.01	6.3 ± 0.5	0.07 ± 0.01	1.6	15.7
	Ni-M	3.08 ± 0.01	5.5 ± 0.3	0.07 ± 0.01*		
	Ni-M-M	6.16 [†]	1.8 ± 0.6	0.07 ± 0.01*		
Ni ₄₅ Fe ₅₅	Ni-O	2.04 ± 0.01	5.7 ± 0.5	0.08 ± 0.01	1.4	16.2
	Ni-M	3.08 ± 0.01	2.3 ± 0.2	0.07 ± 0.01*		
Ni ₂₈ Fe ₇₂	Ni-O	2.04 ± 0.01	6.4 ± 0.5	0.08 ± 0.01	1.3	20.2
	Ni-M	3.07 ± 0.02	1.8 ± 0.3	0.07 ± 0.01*		

* Debye-Waller parameters of Ni-M shells that had the same value in a global fit approach.

[†] Coordination distances of the Ni-M-M shell were set equal to double the corresponding Ni-M distance.

Debye-Waller parameters, Coordination distances (R) and coordination numbers (CN) were kept unrestricted. Catalyst composition is given as atomic %, rounded to the nearest integer.

Table S3.1. Fe K-edge EXAFS simulation parameters of catalysts freeze quenched at 1.63 V_{RHE} after conditioning at the given potential for 30 min in 0.1 M KOH. The fitted k-range was 2.6-12.5 Å⁻¹. *This table has been reprinted with permission from ref. 108. Copyright (2016) American Chemical Society.*

Fe K-edge at 1.63 V _{RHE}						
Ni _{100-x} Fe _x	Shell	R /Å	CN	σ /Å	ΔE ₀ /eV	R _f
Ni ₀ Fe ₁₀₀	Fe-O	1.98 ± 0.02	5.0 ± 0.9	0.09 ± 0.01	1.2	20.1
	Fe-M	3.05 ± 0.02	4.9 ± 1.0	0.08 ± 0.01*		
	Fe-M	2.86 ± 0.02 ^a	0.5 ± 0.7	0.08 ± 0.01*		
	Fe-M	3.45 ± 0.02 ^b	1.8 ± 0.9	0.08 ± 0.01*		
Ni ₉₆ Fe ₄	Fe-O	1.99 ± 0.03	5.8 ± 1.0	0.10 ± 0.01	0.7	23.0
	Fe-M	3.11 ± 0.01	3.7 ± 0.3	0.08 ± 0.01*		
	Fe-M	2.88 ± 0.02	2.9 ± 0.3	0.08 ± 0.01*		
	Fe-M	3.45 ± 0.02 ^b	0.0 ± 5.1	0.08 ± 0.01*		
Ni ₉₁ Fe ₉	Fe-O	2.01 ± 0.01	6.3 ± 0.8	0.09 ± 0.01	0.7	15.9
	Fe-M	3.12 ± 0.01	6.7 ± 1.0	0.08 ± 0.01*		
	Fe-M-M	6.24 [†]	1.2 ± 1.1	0.08 ± 0.01*		
	Fe-M	2.86 ± 0.02 ^a	1.2 ± 0.8	0.08 ± 0.01*		
	Fe-M	3.45 ± 0.02 ^b	0.4 ± 0.8	0.08 ± 0.01*		
Ni ₆₅ Fe ₃₅	Fe-O	2.01 ± 0.01	6.2 ± 0.8	0.09 ± 0.01	1.9	14.4
	Fe-M	3.09 ± 0.01	6.5 ± 0.8	0.08 ± 0.01*		
	Fe-M-M	6.19 [†]	0.6 ± 0.8	0.08 ± 0.01*		
	Fe-M	2.86 ± 0.02 ^a	1.1 ± 0.8	0.08 ± 0.01*		
	Fe-M	3.45 ± 0.02 ^b	0.2 ± 0.8	0.08 ± 0.01*		
Ni ₄₅ Fe ₅₅	Fe-O	2.00 ± 0.01	5.2 ± 0.8	0.08 ± 0.01	1.7	17.9
	Fe-M	3.08 ± 0.01	3.7 ± 0.5	0.08 ± 0.01*		
	Fe-M	2.86 ± 0.02 ^a	0.5 ± 0.7	0.08 ± 0.01*		
	Fe-M	3.45 ± 0.02 ^b	0.3 ± 0.8	0.08 ± 0.01*		
Ni ₂₈ Fe ₇₂	Fe-O	1.99 ± 0.01	5.4 ± 0.8	0.09 ± 0.01	0.8	19.4
	Fe-M	3.07 ± 0.02	3.5 ± 0.7	0.08 ± 0.01*		
	Fe-M	2.86 ± 0.02 ^a	0.0 ± 0.7	0.08 ± 0.01*		
	Fe-M	3.45 ± 0.02 ^b	1.2 ± 0.8	0.08 ± 0.01*		

* Debye-Waller parameters (σ) of Fe-M shells that ad the same value in a global fit approach.

[†] Coordination distances of the Fe-M-M shell were set equal to double the corresponding Fe-M distance.

The coordination distances (R) of two additional Fe-M shells, ^a and ^b, had the same value in all freeze-quenched catalysts in the global fit.

Debye-Waller parameters, coordination distances and coordination numbers (CN) were kept unrestricted unless indicated. Catalyst composition is given as atomic %, rounded to the nearest integer.

Table S3.4. Ni K-edge EXAFS simulation parameters of catalysts freeze quenched at 1.63 V_{RHE} after conditioning at the given potential for 30 min in 0.1 M KOH. The fitted k-range was 2.6-14 Å⁻¹. This table has been reprinted with permission from ref. 108. Copyright (2016) American Chemical Society.

Ni K-edge at 1.63 V _{RHE}						
Ni _{100-x} Fe _x	Shell	R / Å	CN	σ / Å	ΔE ₀ / eV	R _f
Ni ₁₀₀ Fe ₀	Ni-O	1.88 ± 0.01	4.9 ± 0.3	0.06 ± 0.01	2.6	15.2
	Ni-M	2.82 ± 0.01	6.3 ± 0.2	0.06 ± 0.02*		
	Ni-M-M	5.64 [†]	1.2 ± 0.3	0.06 ± 0.02*		
	Ni-M	3.45 ± 0.02 ^b	0.1 ± 0.3	0.06 ± 0.02*		
Ni ₉₆ Fe ₄	Ni-O	2.06 ± 0.01	4.1 ± 0.2	0.07 ± 0.01	1.4	24.4
	Ni-O	1.87 ± 0.02	1.9 ± 0.2	0.07 ± 0.01		
	Ni-M	3.07 ± 0.01	4.0 ± 0.2	0.06 ± 0.02*		
	Ni-M	2.83 ± 0.01	2.0 ± 0.2	0.06 ± 0.02*		
	Ni-M	3.45 ± 0.02 ^b	0.0 ± 0.4	0.06 ± 0.02*		
Ni ₉₁ Fe ₉	Ni-O	2.04 ± 0.01	6.6 ± 0.5	0.07 ± 0.01	1.1	15.5
	Ni-M	3.09 ± 0.01	5.4 ± 0.3	0.06 ± 0.02*		
	Ni-M-M	6.17 [†]	1.6 ± 0.5	0.06 ± 0.02*		
	Ni-M	2.86 ± 0.02 ^a	0.1 ± 0.3	0.06 ± 0.02*		
	Ni-M	3.45 ± 0.02 ^b	0.4 ± 0.4	0.06 ± 0.02*		
Ni ₆₅ Fe ₃₅	Ni-O	2.05 ± 0.01	6.6 ± 0.6	0.08 ± 0.01	1.5	16.6
	Ni-M	3.08 ± 0.01	4.9 ± 0.2	0.06 ± 0.02*		
	Ni-M-M	6.17 [†]	1.8 ± 0.5	0.06 ± 0.02*		
	Ni-M	2.86 ± 0.02 ^a	0.0 ± 0.3	0.06 ± 0.02*		
	Ni-M	3.45 ± 0.02 ^b	0.2 ± 0.4	0.06 ± 0.02*		
Ni ₄₅ Fe ₅₅	Ni-O	2.04 ± 0.01	5.6 ± 0.5	0.07 ± 0.01	2.1	24.8
	Ni-M	3.08 ± 0.01	3.3 ± 0.1	0.06 ± 0.02*		
	Ni-M-M	6.16 [†]	1.3 ± 0.5	0.06 ± 0.02*		
	Ni-M	2.86 ± 0.02 ^a	0.0 ± 0.3	0.06 ± 0.02*		
	Ni-M	3.45 ± 0.02 ^b	0.3 ± 0.4	0.06 ± 0.02*		
Ni ₂₈ Fe ₇₂	Ni-O	2.05 ± 0.01	6.7 ± 0.5	0.08 ± 0.01	0.8	23.5
	Ni-M	3.07 ± 0.01	4.4 ± 0.2	0.06 ± 0.02*		
	Ni-M	2.86 ± 0.02 ^a	0.0 ± 0.3	0.06 ± 0.02*		
	Ni-M	3.45 ± 0.02 ^b	0.8 ± 0.4	0.06 ± 0.02*		

* Debye-Waller parameters of Ni-M shells that had the same value in a global fit approach.

[†] Coordination distances of the Ni-M-M shell were set equal to double the corresponding Ni-M distance.

The distances of two additional Ni-M shells, ^a and ^b, had the same value in all freeze-quenched catalysts in the global fit. Debye-Waller parameters, coordination distances (R) and coordination numbers (CN) were kept unrestricted unless indicated. Catalyst composition is given as atomic %, rounded to the nearest integer.

Table S3.5. Fe K-edge EXAFS simulation parameters of catalysts freeze quenched at 1.0 V_{RHE} after conditioning at the given potential for 30 min in 0.1 M KOH. The fitted k-range was 2.6-12.5 Å⁻¹. *This table has been reprinted with permission from ref. 108. Copyright (2016) American Chemical Society.*

Fe K-edge at 1.0 V _{RHE}						
Ni _{100-x} Fe _x	Shell	R / Å	CN	σ / Å	ΔE ₀ / eV	R _f
Ni ₉₁ Fe ₉	Fe-O	2.01 ± 0.01	5.9 ± 0.8	0.09 ± 0.01	0.4	16.1
	Fe-M	3.12 ± 0.01	4.9 ± 0.9	0.08 ± 0.01*		
	Fe-M-M	6.24 [†]	2.1 ± 1.1	0.08 ± 0.01*		
Ni ₄₅ Fe ₅₅	Fe-O	1.99 ± 0.01	5.9 ± 0.9	0.09 ± 0.01	1.0	13.6
	Fe-M	3.08 ± 0.01	3.5 ± 0.5	0.08 ± 0.01*		
	Fe-M-M	6.16 [†]	0.9 ± 0.7	0.08 ± 0.01*		

* Debye-Waller parameters of Fe-M shells that had the same value in a global fit approach.

[†] Coordination distances of the Fe-M-M shell were set equal to double the **corresponding** Fe-M distance.

Debye-Waller parameters, coordination distances (R) and coordination **numbers** (CN) were kept unrestricted unless indicated. Catalyst composition is given as atomic %, rounded to the **nearest** integer.

Table S3.6. Ni K-edge EXAFS simulation parameters of catalysts freeze quenched at 1.0 V_{RHE} after conditioning at the given potential for 30 min in 0.1 M KOH. The fitted k-range was 2.6-14 Å⁻¹. *This table has been reprinted with permission from ref. 108. Copyright (2016) American Chemical Society.*

Ni K-edge at 1.0 V _{RHE}						
Ni _{100-x} Fe _x	Shell	R / Å	CN	σ / Å	ΔE ₀ / eV	R _f
Ni ₁₀₀ Fe ₀	Ni-O	2.06 ± 0.01	6.0 ± 0.4	0.07 ± 0.01	3.2	19.5
	Ni-M	3.09 ± 0.01	6.0 ± 0.4	0.06 ± 0.01*		
	Ni-M-M	6.18 [†]	2.5 ± 0.5	0.06 ± 0.01*		
Ni ₉₁ Fe ₉	Ni-O	2.04 ± 0.01	6.2 ± 0.5	0.07 ± 0.01	1.5	16.3
	Ni-M	3.09 ± 0.01	5.1 ± 0.3	0.06 ± 0.01*		
	Ni-M-M	6.17 [†]	1.7 ± 0.5	0.06 ± 0.01*		
Ni ₄₅ Fe ₅₅	Ni-O	2.05 ± 0.01	6.2 ± 0.4	0.07 ± 0.01	2.5	20.7
	Ni-M	3.08 ± 0.01	6.2 ± 0.7	0.06 ± 0.01*		
	Ni-M-M	6.17 [†]	2.6 ± 0.4	0.06 ± 0.01*		

* Debye-Waller parameters of Ni-M shells that had the same value in a global fit approach.

[†] Coordination distances of the Ni-M-M shell were set equal to double the **corresponding** Ni-M distance.

Debye-Waller parameters, coordination distances (R) and coordination **numbers** (CN) were kept unrestricted unless indicated. Catalyst composition is given as atomic %, rounded to the nearest integer.

S3.6.2. Structural models

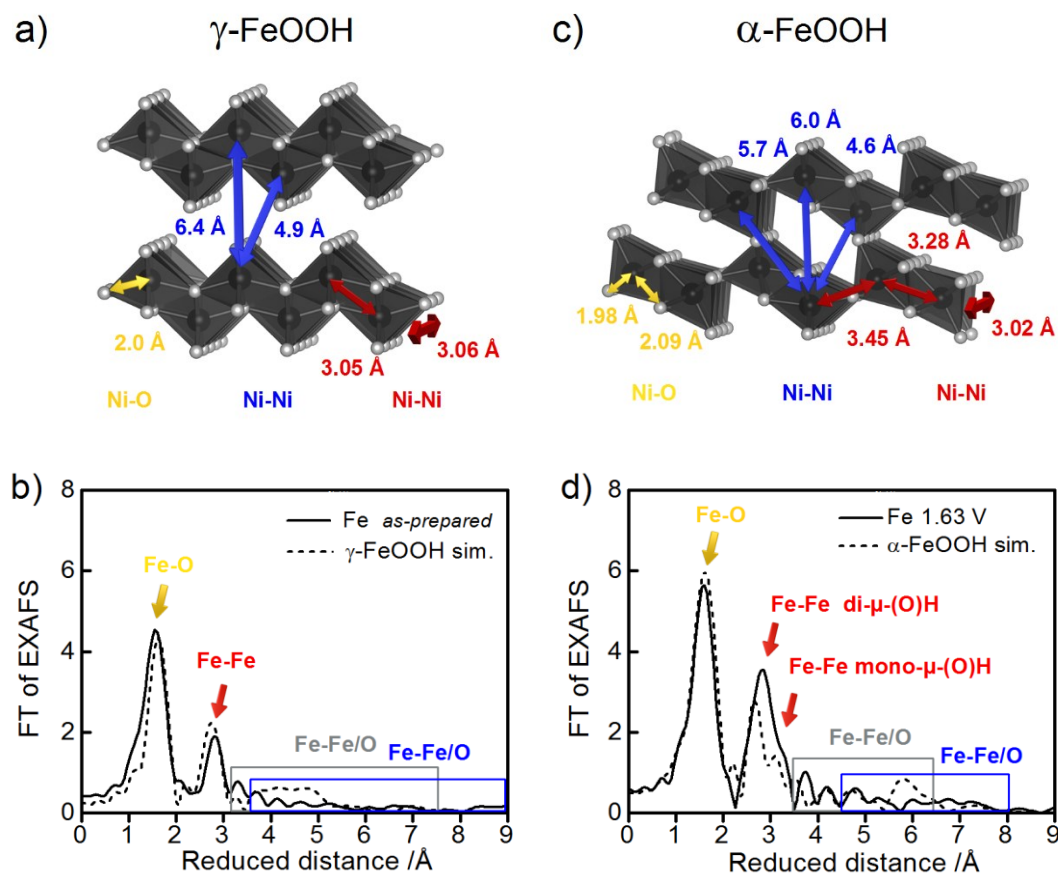


Figure S3.20. Structural models compared to experimental data at the Fe K-edge. **(a)** Structure of γ -FeOOH (cif 9011314) **(b)** FT-EXAFS of the as-prepared Fe catalyst (solid black line) and the simulated spectrum of γ -FeOOH shown in (a) (dashed black line) **(c)** Structure of α -FeOOH (cif 1008766) **(d)** FT-EXAFS of the Fe catalyst at 1.63 V; experimental data (solid black line) and the simulated spectrum of α -FeOOH shown in (c) (dashed black line). The arrows indicate the coordination distances for Fe-O (yellow), Fe-Fe (red), and interlayer distances (blue). The boxes show regions associated with double or multiple scattering. The FT amplitudes of the simulated spectrum of γ/α -FeOOH presented in (b) and (d) have been scaled to fit the experimental. *This figure has been reprinted with permission from ref. 108. Copyright (2016) American Chemical Society.*

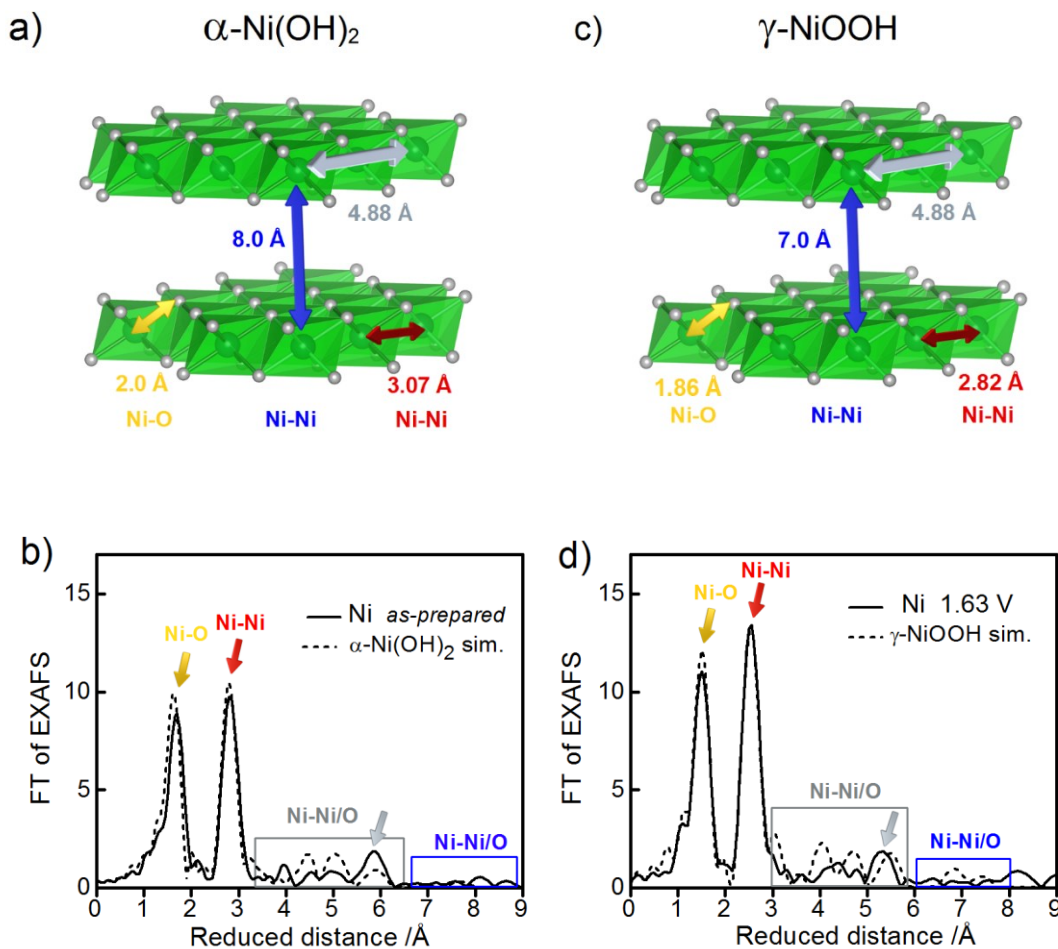


Figure S3.21. Structural models compared to experimental data at the Ni K-edge. **(a)** Structure of α -Ni(OH)₂ (cif 9012316) **(b)** FT-EXAFS of the as-prepared Ni catalyst (solid black line) compared to the simulated spectrum of α -Ni(OH)₂ shown in (a) (dashed black line). **(c)** The structure γ -NiOOH (cif 9012319) **(d)** FT-EXAFS of the Ni catalyst freeze-quenched at 1.63 V (solid black line) compared to the simulated spectrum of γ -NiOOH shown in (c) (dashed black line). The arrows indicate the coordination distances for Ni-O (yellow), Ni-Ni (red), Ni-Ni double distances (grey), and interlayer distances (blue). The boxes show regions where several distances occur due to presence of double or multiple scattering. The amplitudes of the simulated spectra of α -Ni(OH)₂ and γ -NiOOH shown in (b) and (d) have been scaled to fit the experimental data. *This figure has been reprinted with permission from ref. 108. Copyright (2016) American Chemical Society.*

S3.6.3. XAS reference compounds

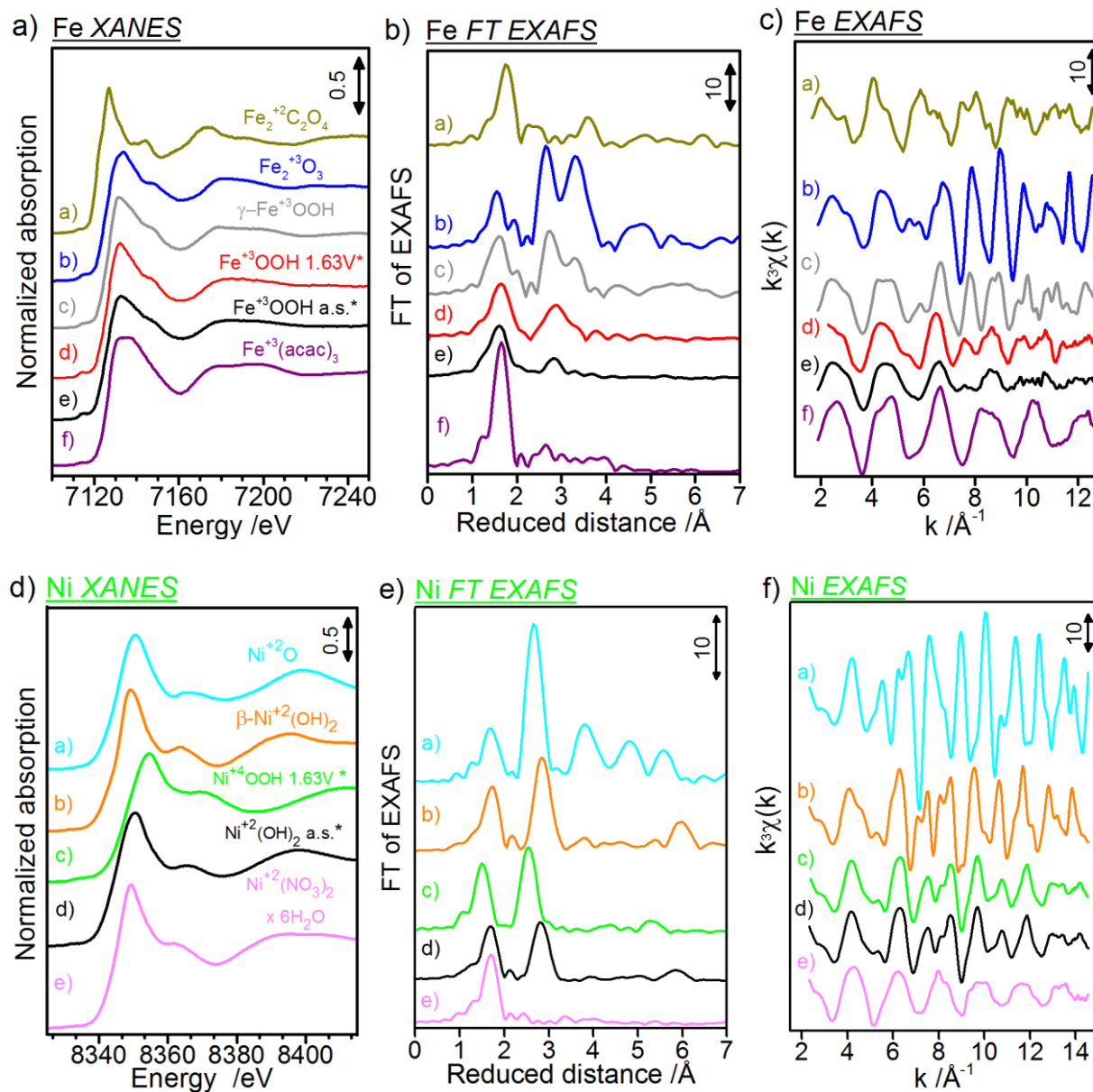


Figure 3.22. XAS spectra of reference compounds measured at the Ni and Fe K-edge. **a-b)** Ni and Fe XANES. **c-d)** Ni and Fe k^3 weighted EXAFS oscillations, $k^3\chi(k)$. **d-e)** Fourier transformed FT-EXAFS. Shown Fe compounds; $\text{Fe}_2^{(2+)}\text{C}_2\text{O}_4$ (ALDRICH), $\text{Fe}_2^{+3}\text{O}_3$, $\gamma\text{-Fe}^{+3}\text{OOH}$, Fe^{+3}OOH 1.63V (Fe catalyst at 1.63V, * this work, Fe^{+3}OOH a.s. (Fe catalyst a.s., *this work). Shown compounds are Ni^{+2}O (SIGMA-ALDRICH), $\beta\text{-Ni}^{+2}(\text{OH})_2$ (SIGMA-ALDRICH), Ni^{+4}OOH 1.63V* (Ni catalyst at 1.63V, *this work), and Ni^{+4}OOH (Ni catalyst a.s. *this work), $\text{Ni}^{+2}(\text{NO}_3)_2$ (ALDRICH). This figure has been reprinted with permission from ref. 108. Copyright (2016) American Chemical Society.

Table S3.7. Summary of literature reported EXAFS parameters for the Fe *K*-edge. *This table has been reprinted with permission from ref. 108. Copyright (2016) American Chemical Society.*

Compound	Ox. state	N	R Fe-O (Å)	K-edge pos. /eV	Method	Ref
FeC2O4	+2	6	2.12	7120.4	EXAFS	^b
FeO	+2	6	2.120	-	EXAFS	172
α-FeOOH	+3	6	2.020	-	EXAFS	173
α-FeOOH	+3	6	2.000 ^a	-	XRD	174
γ-FeOOH	+3	6	2.000	-	EXAFS	173
γ-FeOOH	+3	6	2.000	-	EXAFS	80
FeOOH (Fhyd 2)	+3.2	6	2.000	-	EXAFS	174
FeOOH (Fhyd 3)	+2.8	6	2.040	-	EXAFS	174
FeOOH (Fhyd 6)	+2.8	6	2.050	-	XRD	174
Fe2O3	+3	6	1.98	7124.2	EXAFS	^b
Fe2O3	+3	6	2.045	-	XRD	175
Fe2O3	+3	6	2.020 ^a	-	EXAFS	176
Fe3O4	+3	5	2.018 ^a	-	EXAFS	176
Fe(acac)3	+3	6	2.0	7125.1	EXAFS	^b
SrFeO3	+4	-	1.923	-	ND	177
FeOS	+4	-	1.670	-	EXAFS	178

^a The weighted average of the two given Fe-O shells. ^b Reported EXAFS data was measured in this work

Table S3.8. Summary of literature reported EXAFS parameters for the Ni *K*-edge. *This table has been reprinted with permission from ref. 108. Copyright (2016) American Chemical Society.*

Compound	Ox. state	N	R Ni-O (Å)	<i>K</i> -edge position (eV)	Method	Ref
α -Ni(OH) ₂	+2	6	2.050	-	EXAFS	101
α -Ni(OH) ₂	+2	6	2.050	-	EXAFS	80
α -Ni(OH) ₂	+2	6	2.037	-	EXAFS	179
α -Ni(OH) ₂	+2	6	2.050	-	EXAFS	162
α -Ni(OH) ₂	+2	6	2.040	-	EXAFS	163
β -Ni(OH) ₂	+2	6	2.06	8342.7	EXAFS	^b
β -Ni(OH) ₂	+2	6	2.063	-	EXAFS	179
β -Ni(OH) ₂	+2	6	2.070	-	EXAFS	162
β -Ni(OH) ₂	+2	6	2.060	-	EXAFS	163
β -Ni(OH) ₂	+2	6	2.074	-	EXAFS	180
Ni(OH) ₂	+2	6	2.050	8341.7	EXAFS	181
Ni(OH) ₂ ·6H ₂ O	+2	6	-	8342.9	EXAFS	130
NiO	+2	6	2.06	8342.1	EXAFS	^b
NiO	+2	6	2.090	-	EXAFS	107
NiO	+2	6	2.074	-	EXAFS	179
NiO	+2	6	2.070	8341.9	EXAFS	181
NiO	+2	6	2.070	8342.3	EXAFS	130
Ni(NO ₃) ₂	+2	6	2.05	8342.9	EXAFS	^b
β -NiOOH	+3	6	1.916	-	EXAFS	180
β -NiOOH	+3.16	6	1.920	-	EXAFS	182
β -NiOOH	+3.26	6	1.922	8343.9	EXAFS	130
β -NiOOH	+3	6	1.950	-	EXAFS	181
γ -NiOOH	+3.60	6	1.890	-	EXAFS	80
γ -NiOOH	+3.67	6	1.860	-	EXAFS	162
γ -NiOOH	+3.67	6	1.888	-	EXAFS	180
γ -NiOOH	+3.60	6	1.880	-	EXAFS	182
γ -NiOOH	+3.76	6	1.880	8345.0	EXAFS	130
KNiO ₆	+4	6	1.876	8342.9	EXAFS	179
KNiO ₆	+4	6	1.870	8345.8	EXAFS	181
KNiO ₆	+4	6	1.873	-	EXAFS	183

^a The weighted average of the two given Fe-O shells. ^b Reported EXAFS data was measured in this work

Chapter 4

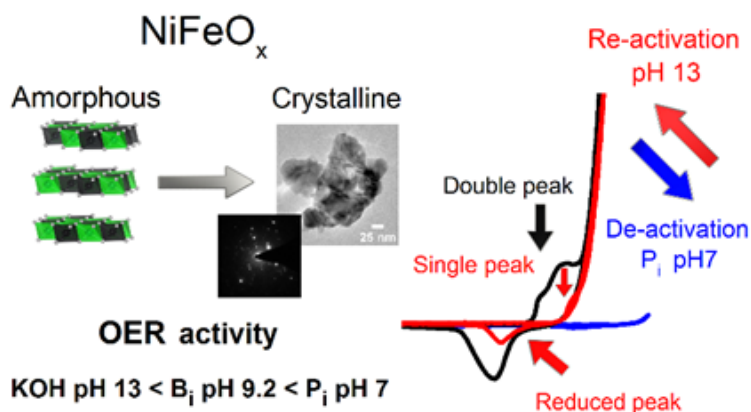
Dynamical changes of a Ni-Fe oxide water splitting catalyst investigated at different pH

This Chapter has been reprinted with permission from Elsevier as the latest version of a published Journal article (Görlin, M.; Glied, M.; Ferreira de Araújo, J.; Dresch, S.; Bergmann, A.; Strasser, P. *Catalysis Today* 2015, 262, 65).

doi:10.1016/j.cattod.2015.10.018

URL: <https://doi.org/10.1016/j.cattod.2015.10.018>

Copyright Elsevier (2016)



*Mikaela Görlin, Manuel Glied, Jorge Ferreira de Araújo, Sören Dresch, Arno Bergmann,
Peter Strasser**

¹The Electrochemical Energy, Catalysis and Materials Science Laboratory, Department of Chemistry, Chemical Engineering Division, Straße des 17. Juni 124, Technical University of Berlin, 106 23 Berlin, Germany

Abstract

Mixed Ni-Fe oxide electrocatalysts have shown high catalytic activity for the oxygen evolution reaction (OER) in alkaline electrolyte. Fundamental research on mixed Ni-Fe OER catalysts has largely focused on high pH, while the OER activity near neutral pH has remained poorly studied.

Here we review the activity of an amorphous mixed Ni-Fe oxyhydroxide catalyst supported on carbon (NiFeO_x/C) in 0.1 M KOH pH 13, in 0.1 M borate buffer (B_i) pH 9.2, and in 0.1 M phosphate buffer (P_i) pH 7.0. The OER catalytic performance was found to decrease in the order of pH 13 > pH 9.2 > pH 7. In contrast to pH 13 and 9.2, the catalyst cycled in pH 7 showed an instantaneous decrease in OER activity and a simultaneous loss of the $\text{Ni}(\text{OH})_2/\text{NiOOH}$ redox peak. Transmission electron microscopy (TEM) and selected area electron diffraction (SAED) showed the formation of crystalline areas upon CV cycling, which appeared more Ni enriched after cycling in pH 7. Deactivated electrodes cycled in pH 13 recovered the OER activity along with a partial reappearance of the Ni redox peak when subsequently cycled in pH 13. SEM-EDX spectroscopy confirmed compositional changes in the bulk during cycling at different pH, with an extensive leaching of Ni in pH 7. Our study provides new insight into the OER activity upon exposure to different electrolyte conditions, which unveils a highly dynamic Ni-Fe oxide framework.

4.1. Introduction

Conversion of energy to generate sustainable fuels such as O₂ and H₂ through electrochemical water splitting require efficient catalysts of inexpensive and abundant materials^{3-7,9,10,15,54,71,77,135,184}. Binary transition metal electrocatalysts of mixed Ni-Fe have proved amongst the most efficient catalysts for the oxygen evolution reaction (OER) in alkaline electrolyte^{10,15,69,72,76,80,81,83,87-89,185} with intrinsic activities at comparable levels to those reported for highly active noble metal based catalysts^{14,57,186} and has proven suitable for practical applications such as solar driven water splitting^{16,17,28,83}. Despite plentiful of investigations in alkaline conditions^{72,80,87,185} not much information has yet been retrieved about the OER activity of mixed Ni-Fe catalysts near neutral pH¹⁵. The fact that Ni-Fe based catalysts possess lower OER activity around neutral pH might limit their potential application. In a study by Smith et al¹⁵ a turnover frequency (TOF) of 1.4 s⁻¹ was reported for co-deposited Fe-Ni films in 0.5 M borate buffer pH 9.2 at 400 mV OER overpotential. Incidental Fe incorporation from remaining impurities in alkaline electrolyte first highlighted by Corrigan et al⁷¹, was further investigated by Trotochaud et al⁷², which showed that the OER activity in conditioned NiOOH films were correlated to the incorporated Fe content. It was also shown by the same group that the OER active phase in (Fe)NiO_x catalysts is the layered oxyhydroxide, as evidenced from *in situ* transformation of a rock salt structure into the active hydrated state upon conditioning in alkaline electrolyte⁶⁹. Gong et al⁸¹ studied a Ni-Fe-LDH/CNT electrocatalyst and found that highest OER activity was achieved with carbon support, with a reported TOF of 0.56 s⁻¹ in 1 M KOH at 300 mV overpotential based on total metal loading. Investigations of Ni-Fe based catalysts thus show promising activities at moderate pH, however questions regarding the activity and stability in a wider range of ambiances yet remain open. An understanding of the differences observed in intrinsic activity and the influence on structure in Ni-Fe based catalysts due to changes in conditions such as electrolyte composition or pH could prove indispensable when designing highly active electrode materials for electrochemical water splitting near neutral pH.

We report studies of a solvothermally prepared amorphous Ni-Fe oxyhydroxide OER catalyst described as [Ni_{1-x}Fe_x(OH)₂]^{x+} [Aⁿ⁻_{x/n}]⁻·mH₂O, supported on carbon (Vulcan XC-72r) post synthesis, herein denoted as NiFeO_x/C, with a Ni:Fe composition of 62:38 at. %. Determination of the OER activities were carried out in 0.1 M KOH pH 13, in 0.1 M borate buffer (B_i) pH 9.2, and in 0.1 M phosphate buffer (P_i) pH 7 using a standard rotating ring disc electrode (RDE) setup. To obtain qualitative measurements of the voltammetric Ni(OH)₂/NiOOH redox peak at different pH, an electrolyte switching protocol was applied where the electrodes were consecutively cycled in a sequence of KOH-P_i-KOH or KOH-B_i-KOH. An initial pre-cycling of 150 cycles in 0.1 M KOH was carried out prior to the measurements to fully activate the

electrodes in terms of stabilizing the initial increase of the charge under the Ni redox peak. Physical characterization of electrodes cycled at different pH was carried post-analysis using transmission electron microscopy (TEM), energy dispersive X-ray spectroscopy (EDX), and selected area electron diffraction (SAED). In situ differential electrochemical mass spectrometry (DEMS) was used to estimate Faradaic efficiencies of O₂ and to identify volatile products released upon exposure to the different electrolytes and pH.

4.2. Experimental

4.2.1. Catalyst preparation

The Ni-Fe catalyst with a composition of 62:38 at.% Ni:Fe was synthesized by mixing 2.93 mL of 0.1 M Ni(NO₃)₂·6H₂O (99.999% trace metals basis, Aldrich) and 1.47 mL of 0.1 M Fe(acac)₃ (99.5% trace metal basis, ALDRICH) and dissolved in 20 mL of benzyl alcohol (puriss., 99–100.5%, Aldrich), with addition of 10 mM 1,2-benzenediol (>99%, Sigma–Aldrich); analogous to a reported solvothermal approach¹²¹. All chemicals were used as received without further purification. The reaction mixture was sealed in a special microwave vial (Anton Paar) and heated in a microwave-assisted autoclave (Anton Paar) to 190 °C with a heating ramp of 16.5 °C/min, and held for 15 min. The particles were supported on 80 wt.% of Vulcan® XC-72r (Cabot) which was added to the reaction mixture after cooling down to room temperature. The catalyst–carbon mixture was agitated for 30 min by sonication and left additional 24 h under stirring. The product was washed 5 times with high purity ethanol; sonicated for 5 min and collected by centrifugation at 7500 rpm for 10 min. The catalyst was finally freeze dried and the powder was stored under inert atmosphere until use.

4.2.2. Physical characterization

Inductively coupled plasma-optical emission spectroscopy (ICP-OES) was used to determine the metal content of the as-prepared catalyst powder used for calculations of total metal loadings in the catalyst ink for rotating disc electrode measurements. Data was collected using a Varian 715-ES spectrometer coupled to a CCD detector. The sample was digested in an acid mixture of HNO₃:H₂SO₄:HCl to a ratio of 1:1:3 and heated to 180 °C for 15 min using microwave irradiation. The sample probes were diluted with >20 mΩ cm milli-Q water. Standard solutions with known concentrations of Ni and Fe (Sigma–Aldrich) were co-analyzed with the samples.

Transmission electron microscopy (TEM) and selected area electron diffraction (SAED) were acquired on a FEI Tecnai G² Microscope 20 S-Twin with a LaB₆-cathode at 200 kV accelerating voltage and GATAN MS794 P a CCD detector (ZELMI Centrum, Technical University of Berlin). Catalysts were conditioned by

cycling in KOH, P_i , and KOH between the potential limits of ca. 1–1.7 V vs. RHE (herein abbreviated V_{RHE}) after iR compensation, see more details in Section 3.2.3. Catalysts were prepared by dispersion of the powder in isopropanol by sonication and drop-casted onto Cu-lacey coated TEM grids. TEM images were analyzed using software packages from ImageJ. The catalyst compositions of local spots were determined using the energy dispersive X-ray spectroscopy (EDX) unit with an (EDAX) r-TEM SUTW detector. The intensities were estimated from the *K*-lines.

Scanning electron microscopy (SEM) using a JEOL JSM-7401F high resolution field emission SEM operated at 10 kV, were acquired on an intact electrode after each step of consecutive KOH- P_i -KOH cycling; 150 cycles in KOH, 20 cycles in 0.1 M P_i pH 7, and re-activated electrodes after 20 cycles in 0.1 M KOH. The electrode had a metal loading of ca. 30 $\mu\text{g Ni} + \text{Fe cm}^{-2}$. The catalyst composition was analyzed using EDX over a larger area of the electrode. The potential limits were kept between ca 1–1.75 V_{RHE} after iR-compensation, see more details in Section 3.2.3. Energy dispersive X-ray analysis (EDX) was carried out over a larger area after each step to estimate the bulk Ni:Fe composition. EDX analysis was acquired at 16 kV using a Quantax 400 detector (BrukerAXS Microanalysis GmbH, Germany). Quantifications of the Ni and Fe content were obtained from the *K* lines, and the total metal content estimated from the integrated *K*-line area normalized to acquisition time.

Total reflection X-ray fluorescence analysis (TXRF) was carried out of acid digested electrodes collected after each step in the consecutive cycling; KOH- P_i -KOH and KOH- B_i -KOH, to obtain the total metal content and catalyst composition. The electrodes were cycled between ca 1–1.75 V_{RHE} after iR compensation. In each step, a cycled electrode initially containing $\sim 30 \mu\text{g cm}^{-2}$ catalyst, was digested in 300 μl of HCl (37%, Merck) by sonication for 10 min, and mixed with 300 μl of 1 mg/mL of Ga-standard solution (Merck). The TXRF analysis was acquired using a PicoTAX spectrometer equipped with a 40 kV using a Si-drift detector (Röntec).

4.2.3. Electrochemical characterization

The OER activity was determined using a rotating disc electrode (RDE) setup in a standard 3-electrode configuration, with a Pt-mesh as counter electrode separated by a porous glass frit, and a reversible hydrogen reference electrode (Gaskatel) connected via a Luggin capillary. All measurements were recorded using a GAMRY 600 reference potentiostat in 0.1 M KOH (semiconductor grade, 99.99% trace metals basis, Aldrich), in 0.1 M phosphate buffer (KHPO_4 , P_i , 99.99% trace metal basis), and in 0.1 M borate buffer (H_3BO_3 , B_i > 99.8%, puriss., Aldrich). Electrolytes were degassed with N_2 for 20 min prior to each measurement and a protective atmosphere was kept by purging throughout the measurement.

Catalyst inks were prepared by dispersing catalyst powders in a mixture of 150:100:1 of milli-Q:2-propanol:5 wt.% Nafion[®] and homogeneously dispersed by ultrasonication for 15 min before drop coated onto glassy carbon electrodes ($\Phi = 5$ mm, Pine Instruments). The total metal loading was varied between 1–20 $\mu\text{g Ni} + \text{Fe cm}^{-2}$. The glassy carbon electrodes were prior to drop coating polished with 0.1 μm alumina MicroPolish (Buehler) using a Nylon cloth followed by 0.05 μm alumina polishing suspension (Buehler) using a Microcloth, and rinsed with milli-Q-aceton-milli-Q using sonication for 5 min in each step, and finally carefully rinsed with milli-Q. Different catalyst loadings were achieved by dropping a different volume of ink onto the electrode. The rotation speed was set to 1600 rpm. In the pH switching experiments, the electrolyte was consecutively changed from KOH- P_i -KOH or from KOH- B_i -KOH, and each electrolyte was held in a separate electrochemical cell and the electrodes were rinsed in milli-Q water (>20 m Ω cm) in between each step to minimize cross contamination. Cyclic voltammograms were corrected afterwards for uncompensated series resistance (R_u , herein denoted $E-iR$) determined by electrochemical impedance spectroscopy by passing 0.01–150 kHz at open circuit potential. Obtained values were typically around 30 Ω in 0.1 M KOH, 50 Ω in 0.1 M P_i , and 200 Ω in 0.1 M B_i . Chronopotentiometric measurements by applying a stable current density for 120 s were used to determine the overpotential at 1 and 10 mA/cm², and were afterwards corrected for iR drop, whereas chronoamperometric measurements by applying a stable potential at 1.53 and 1.63 V_{RHE} used for turnover frequency calculations (see more details in Section 3.2.4) were carried out at iR compensated voltages.

4.2.4. Calculation of turnover frequency (TOF) and redox charge (Q)

Turnover frequencies were estimated at 1.53 V and 1.63 V_{RHE} by applying a stable potential for 90 s, and the current used was the average of the last 10 s. The TOF was calculated as the number of moles of O₂ evolved per moles of total metal (Ni + Fe) per sec assuming a 4 electron process according to the following formula; $\text{TOF} = i/z \cdot F \cdot n$. The charge (Q) under the Ni(OH)₂/NiOOH voltammetric redox peak was determined as the area between the experimental cathodic CV scan and a fit line described by the Butler–Volmer equation; $i_a = i_0(1 - \alpha)^{F\eta/RT}$. The fit was minimized by the non-linear least squares method and the Levenberg–Marquardt algorithm using in-house software. The number of electrons transferred per Ni atom was calculated by assuming a 1 electron transfer. The metal content used for the TOF calculations was determined by ICP-OES by pipetting an amount of the ink into ICP vials.

4.2.5. Differential electrochemical mass spectrometry (DEMS)

Differential electrochemical mass spectrometry (DEMS) was acquired using a home designed dual thin-layer electrochemical flow cell, partly based on a design reported elsewhere¹²⁶. The flow cell was

connected via a 150 μm thick hydrophobic PTFE microporous membrane with 20 nm pore size (Cobetter[®]) to a Prisma[™] quadrupole mass spectrometer (QMS 200, Pfeiffer-Vacuum) equipped with two turbomolecular pumps (HiPace 80) operating the MS chamber at 10^{-6} mbar. Cyclic voltammograms were recorded in the OER regime by cycling the potential between ca 1–1.8 V_{RHE} at a scan-rate of 50 mV/s, a catalyst loading of 8 $\mu\text{g Ni + Fe cm}^{-2}$, and a flow rate of 8 $\mu\text{l/s}$ with N_2 purged electrolyte. A glassy carbon electrode ($\phi = 5$ mm, HTW GmbH) was used as a working electrode, a Pt-mesh as counter electrode, and a reversible hydrogen electrode (RHE) or an Hg/HgSO₄ as reference electrode. Faradaic efficiencies were determined using a calibration constant (K^*), which describes the relationship between the mass spectrometric ion current (i_{MS}) and the Faradaic current, determined by applying quasi stationary chronopotentiometric step measurements in the linear region. The calibration constant was extracted as the slope of the integrated mass spectrometric ion current (Q_{MS}) vs. the integrated Faradaic current (Q_{F}) assuming 100% efficiency of O_2 , according to the following formula; $K^* = Q_{\text{MS}} \cdot z / Q_{\text{F}}$.

4.3. Results & Discussion

4.3.1. Catalytic OER activity in pH 13, 9.2, and 7

Catalysts of mixed Ni and Fe have been extensively investigated due to high intrinsic catalytic activities for the oxygen evolution reaction (OER) in alkaline electrolyte^{3-12,15,54,71,135,182,184,187}. We have investigated a solvothermally prepared Ni-Fe oxyhydroxide catalyst supported on Vulcan XC-72r, herein denoted NiFeO_x/C. The OER catalyst, with a composition of 62:38 at. %, was investigated for electrocatalytic activity in 0.1 M KOH pH 13 (KOH), 0.1 M H₃BO₃ pH 9.2 (B_i), and in 0.1 M KHPO₄ pH 7.0 (P_i). Electrodes were pre-cycled 150 cycles in 0.1 M KOH prior to determination of intrinsic activity in pH 7 and pH 9.2 in order to obtain qualitative measurements of the electrolyte influence after reaching a stable CV. The OER activity of the NiFeO_x/C catalyst was found to decrease in the order of pH 13 < pH 9.2 < pH 7 (Figure 4.1a). Comparable overpotentials in different electrolytes for current densities of 1 and 10 mA/cm² presented in Figure 4.1b showed that the NiFeO_x catalyst could operate at $\eta_{\text{OER}} < 300$ mV in 0.1 M KOH, which is desirable for practical applications¹⁰, however was increasing with pH (Figure 4.1b, Figure S4.1, and Figure S4.3). Measurements at various catalyst loadings showed that the overpotential could be decreased by increasing the loading, however seemed to approach saturation around 20 $\mu\text{g Ni + Fe cm}^{-2}$. The intrinsic activity in terms of turnover frequency (TOF) was estimated in 0.1 M KOH at different catalyst loadings at $\eta_{\text{OER}} = 300$ mV and 400 mV to enable comparison of the OER activity over the entire pH range (Figure S4.4 and Figure S4.5). The highest estimated TOF at $\eta_{\text{OER}} = 300$ mV was $0.45 \pm 0.14 \text{ s}^{-1}$ in 0.1 M KOH at a catalyst loading of 8 $\mu\text{g Ni + Fe cm}^{-2}$. Pre-cycled electrodes subsequently transferred to 0.1 M B_i pH 9.2 (KOH-B_i) or 0.1 M P_i pH 7 (KOH-P_i) did not show OER activities at 300 mV overpotential and were therefore compared at 400 mV overpotential (Figure S4.3a and Figure S4.4). In B_i pH 9.2 the highest TOF was estimated to $0.32 \pm 0.01 \text{ s}^{-1}$ and to $0.10 \pm 0.01 \text{ s}^{-1}$ in pH 7. Higher TOF was reported of a Ni-Fe catalyst film measured in borate buffer pH 9.2¹⁵, however measurements were carried out in 0.5 M KOH. Direct comparison of intrinsic activities are difficult due to various approaches to estimate the catalytically active material, different electrolyte concentration, catalyst composition, and geometric metal loading. Current densities extracted at 300 mV overpotential in 0.1 M KOH in this study are comparable to previous reports of mixed NiFe catalysts^{69,76,81,87}. As mentioned, the OER activity approached saturation at higher catalyst loadings, and it might be that a higher effective layer thickness results in a decreased TOF due to shielding effects from the layers in between the electrode and the electrolyte interface layers⁷².

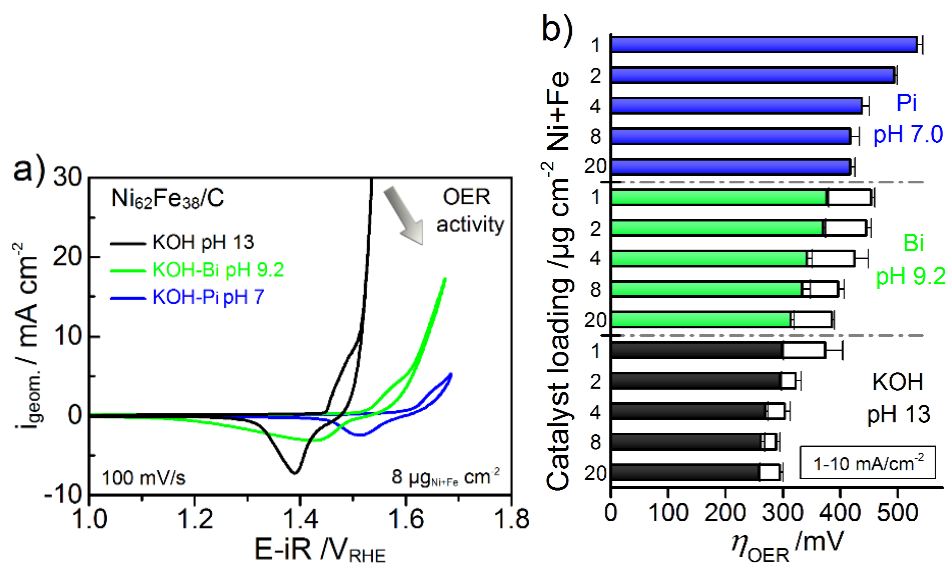


Figure 4.1. Cyclic voltammograms of $\text{Ni}_{62}\text{Fe}_{38}\text{O}_x/\text{C}$ at a catalyst loading of $8 \mu\text{g Ni+Fe cm}^{-2}$ (a) KOH pre-cycled electrode after 150 cycles in 0.1 M KOH (black), KOH pre-cycled electrode consecutively cycled 20 cycles in 0.1 M Bi pH 9.2, denoted as KOH-Bi (green), and KOH-Pi cycled electrode after 20 cycles in 0.1 M Pi pH 7 (blue). Shown is cycle 5 at a scan-rate of 100 mV/s. (b) OER overpotential (η_{OER}) extracted from chronopotentiometric measurements at a geometric current density of 1 mA/cm² (colored bars) and at 10 mA/cm² (colored + transparent bars), measured at various catalysts loading of Ni + Fe; 1, 2, 4, 8, and 20 $\mu\text{g Ni+Fe cm}^{-2}$. The catalyst loading was determined by ICP-OES. Further OER activity trends are presented in Supporting Information Figure S4.3-4.5. All measurements were carried out in RDE setup at a rotation speed of 1600 rpm in N_2 degassed electrolytes. This figure has been reprinted with permission from ref. 100. Copyright Elsevier (2016).

KOH pre-cycled electrodes subsequently transferred to pH 7 (KOH- Pi) showed a rapid loss of catalytic OER activity and a diminishing $\text{Ni(OH)}_2/\text{NiOOH}$ redox peak (Figure 4.2, Figure S4.1 and Figure S4.5). Electrodes subsequently cycled in Bi pH 9.2 after 150 cycles in 0.1 M KOH showed a stable OER activity compared to pH 7 (Figure 4.2). Deactivated electrodes transferred back to 0.1 M KOH pH 13 after 20 cycles in pH 7 remarkably recovered their OER activity substantially, however the Ni redox peak did not recover in relation to the OER activity (Figure 4.2 and Figure S4.5).

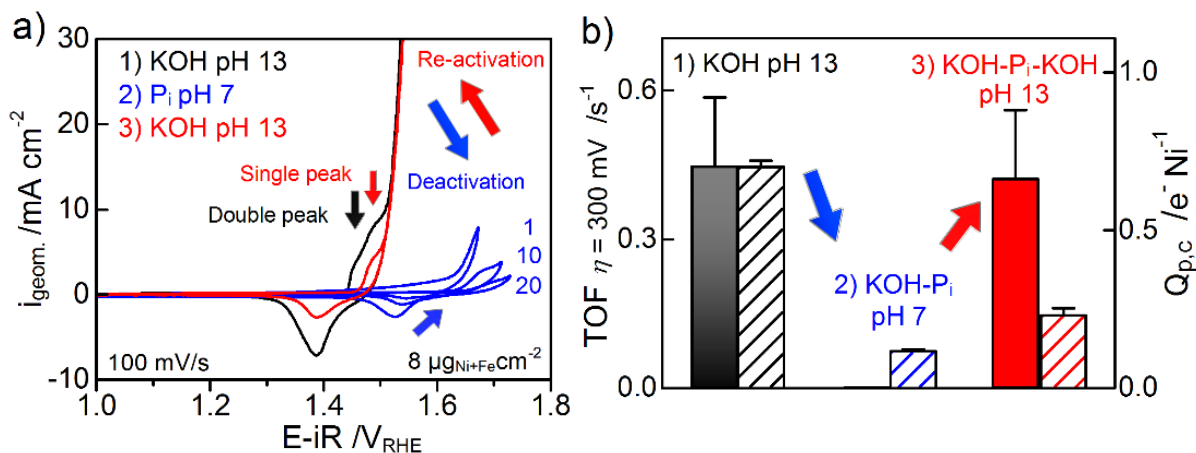


Figure 4.2. Electrolyte switching experiment of NiFeO_x/C cycled in KOH-Pi-KOH (pH 13 - pH 7 - pH 13). **(a)** Cyclic voltammograms of NiFeO_x/C at 100 mV/s at 1600 rpm and a catalyst loading of 8 μg Ni + Fe /cm² (1) KOH pre-cycled electrode after 150 cycles 0.1 M KOH. (2) KOH pre-cycled electrode from step 1 after additional 20 cycles in 0.1 M Pi (KOH-Pi). Shown are cycle 1, 10, and 20. (3) KOH-Pi cycled electrode from step 2 after additional 20 cycles in 0.1 M KOH (KOH-Pi-KOH. Shown are cycle 1, 10, and 20. The same switching experiment at different catalyst loadings is attached in Figure 4.2-S4.3). **(b)** The turnover frequency (TOF) of (1) KOH pre-cycled electrode after 150 cycles, (2) KOH-Pi deactivated electrode (3) KOH-Pi-KOH reactivated electrode. The left axis shows the turnover frequency (solid bars) and the right axis shows the integrated mass normalized charge under the Ni(OH)₂/NiOOH redox peak (hatched bars). All measurements were carried out at a geometric metal loading of 8 μg_{Ni+Fe}/cm². This figure has been reprinted with permission from ref. ¹⁰⁰ Copyright Elsevier (2016).

After switching back to KOH pH 13 after 20 cycles in pH 7, the redox peak reappeared along with the OER activity, and continued increasing slightly upon further cycling but did not reach the full initial size. The recovery of the intrinsic OER activity was much larger in comparison to the recovered mass normalized charge under the Ni(OH)₂/NiOOH redox peak (Figure S4.5a and b). A closer look at the measurements at different catalyst loadings which show a comparison of the capacitive region after prolonged cycling in pH 7 (up to 60 cycles) revealed that the activity loss might stem from a loss of active material (

Figure S4.6). The anodic redox peak hold a double peak before exposure to pH 7 which is more clearly visible at low to intermediate catalyst loadings. This might be due to that the onset of the OER overpotential shifts to higher values at lower catalyst loadings, and therefore allows the peak to be visible. However, upon reactivation in pH 13 after exposure to pH 7, the double peak feature is no longer visible, which could reflect a change in the physical state of the catalyst such as a phase or compositional change. Several peaks in Ni(OH)₂ have been observed ^{15,72,75,188}, however it is poorly understood and is thought to be due to mixtures of different types of Ni species such as α- or β-Ni(OH)₂ or the oxidized

forms β - or γ -NiOOH⁷⁶. Another observation is that the cathodic redox peak shifts up to 30 mV to more positive values by decreasing the catalyst loading 20 times. This might be caused by a larger influence from the underlying electrode at lower catalyst loadings, which is observed as a sharper peak shape.

4.3.2. Transmission electron microscopy (TEM) and selected area electron diffraction (SAED)

The morphology of Ni₆₂Fe₃₈O_x/C was investigated using transmission electron microscopy (TEM) and selected area electron diffraction (SAED) after exposure to different electrolytes; KOH pH 13, B_i pH 9.2, and P_i pH 7. TEM images and SAED patterns of the as-prepared catalyst showed only two diffraction rings which coincided with the carbon (0 0 2) and (1 0 0) indices (see Figure 4.3b). The X-ray diffractograms of the as-prepared catalyst showed similarities to those previously reported of amorphous NiFe catalysts (Figure S4.7a)^{72,89}. Catalysts cycled 150 cycles in 0.1 M KOH pH 13 between 1 and 1.75 V_{RHE} showed the presence of both amorphous and more crystalline areas which were distributed over localized spots (Figure 4.3c–f). Indexing of the SAED patterns showed common indices with that of a Ni(OH)₂ phase. Some of the crystallites resembled hexagonal shapes with corner angles close to 120° (Figure 4.3c). The distinct spots visible in the SAED pattern in Figure 4.3d could be represented by a crystalline β -Ni(OH)₂ viewed from the [0 0 1] zone axis^{178,189}. We could however not entirely rule out that the crystallites are not those of α -Ni(OH)₂ since the α - and β -structures are similar and not always simple to distinguish especially if there is influence from mixed phases⁷⁶. The presence of Fe in the host lattice might also impact on the structure, and ions in the interlayer spacing and stacking faults that result in changed interlayer distances would impact on the peak positions which would make an identification more difficult^{72,76,81,88,89,158}. Simulated XRD profiles of selected areas are attached in Figure S4.7b. According to Pourbaix diagrams of Ni, a γ -phase is likely to form during the CV cycling between the selected potential limits⁸⁰, also confirmed by in situ X-ray absorption spectroscopy⁸⁰, however mixtures of coexisting α -, β - and γ -phases of hydrated Ni species cannot entirely be excluded upon potential cycling due to different favor of these at different potentials⁷⁶.

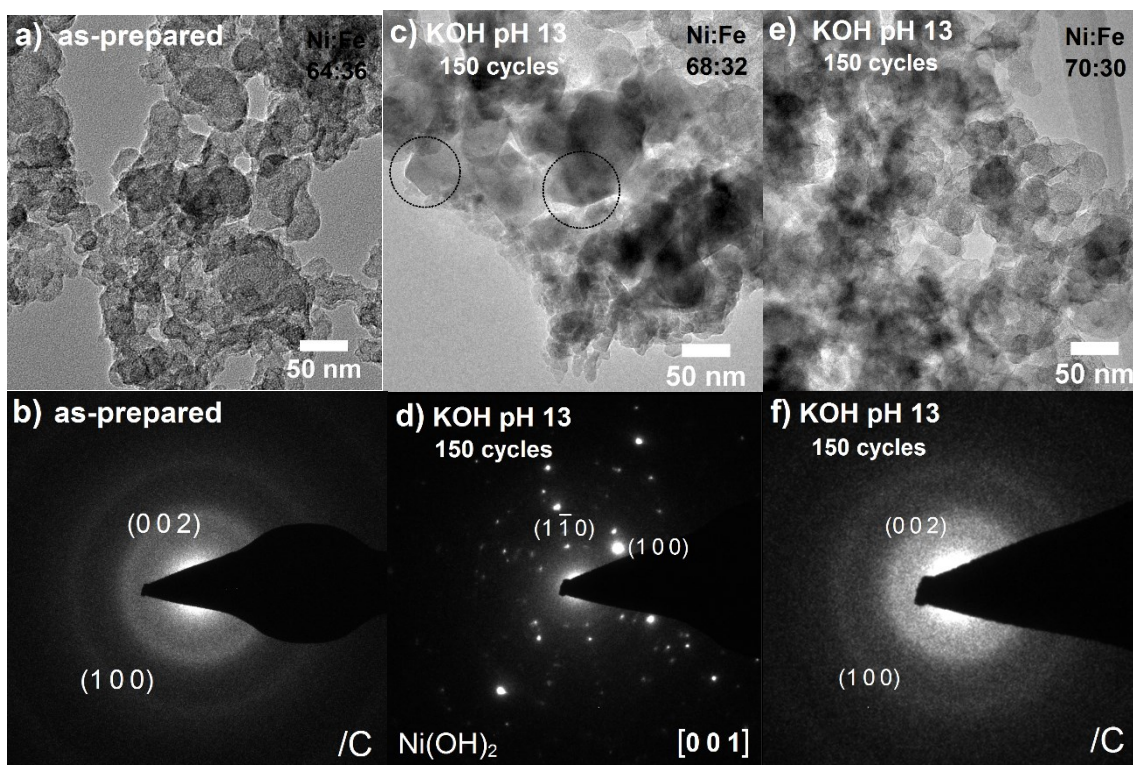


Figure 4.3. TEM images (a, c, e) and corresponding SAED patterns (b, d, f) of NiFeO_x/C. (a-b) Amorphous area of as-prepared catalyst (b-c) amorphous area after 150 cycles in 0.1 M KOH pH 13 (e-f) crystalline area after 150 cycles in 0.1 M KOH pH 13. Catalysts were cycled between 1-1.75 V_{RHE}. The Ni:Fe composition acquired by the EDX unit is indicated in the upper right corner of the TEM images. This figure has been reprinted with permission from ref. ¹⁰⁰ Copyright Elsevier (2016).

KOH-B_i cycled electrodes analyzed after 20 cycles in B_i pH 9.2 showed both amorphous areas (Figure 4.4a-b) and similar crystalline areas as observed in the as-prepared catalyst (Figure 4.4c-d and Figure S4.8b) after 150 cycles in KOH pH 13. Integrated SAED patterns revealed indices at 24°, 37°, 42°, 51°, 57°, 68° 2θ, (Figure S4.7b) which would indicate the presence of a similar phase as observed after 150 cycles in KOH. TEM images of KOH-P_i cycled electrodes analyzed after 20 cycles in P_i pH 7 also showed crystalline areas (Figure 4.4e-g), also with regularly shaped crystals with angles close to 120° (Figure S4.8c). The SAED diffraction images showed a clear spot pattern (Figure 4.4f) that could also be represented as crystalline α- or β-Ni(OH)₂. The presence of asymmetric spot intensities could be due to a mixture of crystals viewed from different crystal planes, therefore the interpretation of the SAED patterns should be taken with concern. TEM images of the KOH-P_i-KOH re-activated NiFeO_x/C catalyst with recovered the OER activity, showed an amorphous SAED pattern that was not observed prior to exposure to pH 7 (Figure 4.4g and h), with a diffraction peak at 60° (1 1 0) in addition to the carbon reflections at 24° (0 0 2) and 42° (1 0 0) 2θ.

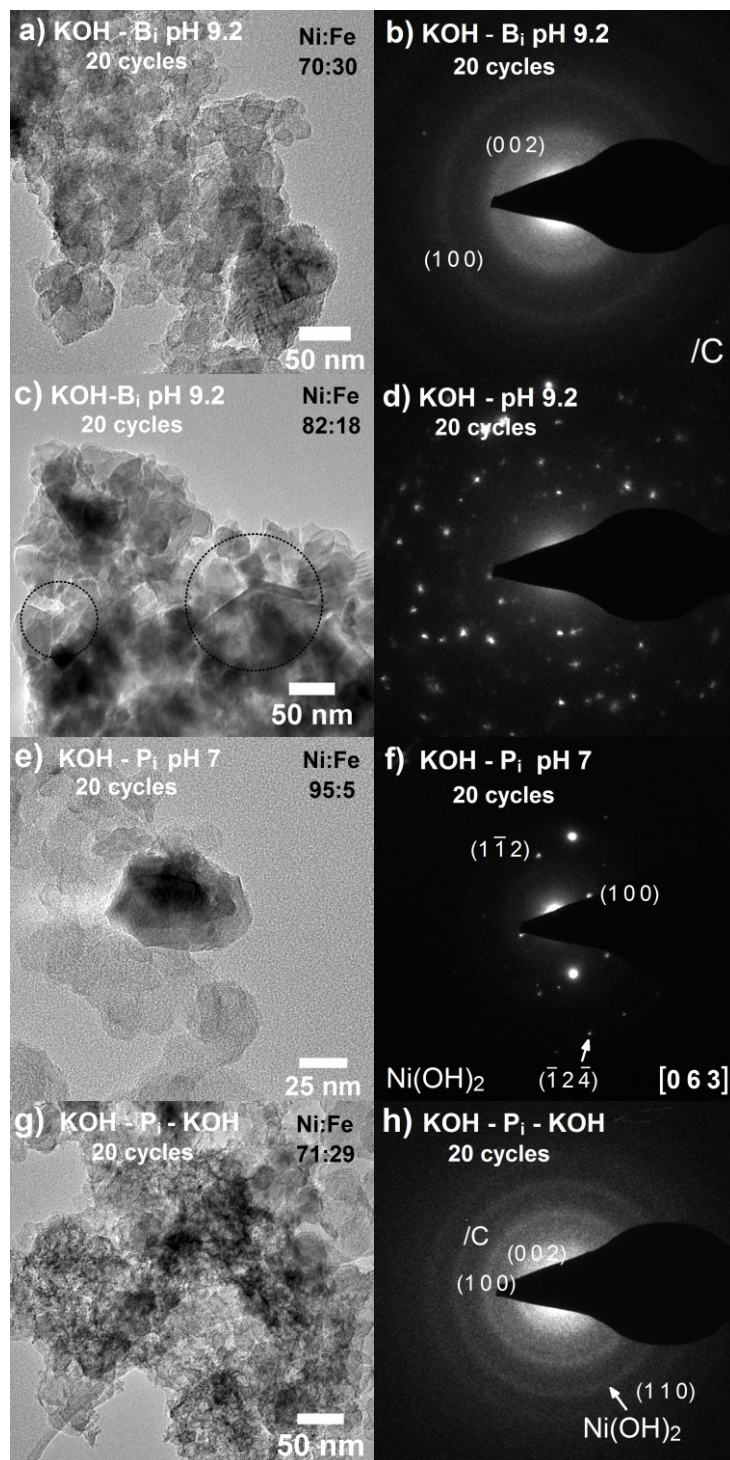


Figure 4.4. TEM images and corresponding SAED patterns of NiFeO_x/C. **(a-b)** Amorphous area of KOH-B_i cycled electrode after 20 cycles in 0.1 M B_i pH 9.2. **(c-d)** Crystalline area of KOH-B_i cycled electrode. **(e-f)** Crystalline area of KOH-P_i cycled electrode after 20 cycles in 0.1 M P_i pH 7. **(g-h)** Amorphous area of KOH-P_i-KOH reactivated electrode after 20 cycles in KOH pH 13. Catalysts were cycled between ca 1-1.75 V_{RHE}. The Ni:Fe EDX composition

is indicated in the upper right corner of the TEM images. This figure has been reprinted with permission from ref. ¹⁰⁰ Copyright Elsevier (2016).

A closer inspection of the EDX analysis of the local areas in the TEM micrographs showed that these areas on average had a higher Ni content than the average composition. This observation would support that the crystalline areas would be a more ordered form of a Ni(OH)₂/NiOOH phase. However, upon cycling in KOH pH 13, the local crystalline areas did not have an obvious higher Ni content than the amorphous areas. Since all catalysts were pre-cycled in pH 13 prior to exposure to either pH 9.2 or pH 7, the crystalline areas could not be concluded to be a cause of exposure to a specific electrolyte or pH. It is indeed interesting how dynamic the NiFeO_x catalyst structure seem upon potential cycling. Previous studies of LiCoPO₄ and LiCoO₂ battery materials showed that the less OER active LiCoO₂ cycled in 0.1 M P_i pH 7 resulted in formation of a spinel-like phase whereas the more active LiCoPO₄ also could maintain a higher degree of amorphicity in the surface regions ¹⁹⁰.

4.3.3. Catalyst composition at different pH

To address the compositional changes in the bulk upon cycling in KOH, B_i, and P_i electrolyte, the atomic composition of Ni and Fe was determined by SEM-EDX analysis and total reflection X-ray fluorescence (TXRF) analysis after each step upon cycling according to the electrolyte switching sequence KOH-B_i/P_i-KOH (Figure 4.5a). The Ni:Fe composition of the as-prepared NiFeO_x/C catalyst was estimated to 65:35 at.% according to the SEM-EDX measurements, in excellent agreement with the ICP-OES determined composition 62:38%. According to TXRF and SEM-EDX measurements, after 150 cycles in KOH pH 13, KOH-B_i (20 cycles), KOH-B_i-KOH, KOH-P_i, and KOH-P_i-KOH, the Ni:Fe compositions were determined to 69:31, 71:29, 72:28, 54:46, and 59:41, respectively. This is in contrast to what appeared as Ni rich crystallites in the TEM-EDX analysis after inspection of the local areas after cycling in pH 9.2 and 7 (Figure 4.4 and Figure 4.5 and Supplementary Information Figure S4.8). In contrary, the bulk composition after cycling in pH 7 revealed an extensive leaching of Ni, with a Ni:Fe composition that was changed to 50:50 at.%. The KOH-P_i-KOH re-activated catalyst approached the original composition, however the changes are insignificant and most likely due to stabilization of the Ni-leaching. Revised Pourbaix diagrams suggest that Ni species are more soluble around pH 7 compared to Fe species between the chosen potential limits ^{183,191}. Therefore, it was important to estimate the total loss of metal content after cycling in the different electrolytes, which was determined SEM-EDX analysis of an intact electrode analyzed after each step of KOH-P_i-KOH cycling. These measurements were confirmed using TXRF analysis of a series of acid digested electrodes after each step of KOH-P_i-KOH and KOH-B_i-KOH cycling, where electrodes were digested in HCl before analyzed. The analyses showed that cycling in KOH

pH 13 or B; pH 9.2 did not result in a significant loss of total metal content compared to cycling in P; pH 7, which resulted in a loss of nearly 50% of the total metal content after only 20 cycles (see Figure 4.5a). Upon re-activation, no additional material was gained from the electrolyte surroundings but an additional small loss was observed. This confirms that no significant amount of metal is likely to be incorporated from the electrolyte surroundings in the re-activated KOH-P_i-KOH electrode, but the compositional changes observed are more likely due to leaching of either of the metal. Since the crystalline areas are already present after 150 cycles in KOH pH 13, we could speculate that loss of OER activity in pH 7 is most likely not due to formation of crystallites but more likely due to the rapid loss of active material during each cycle.

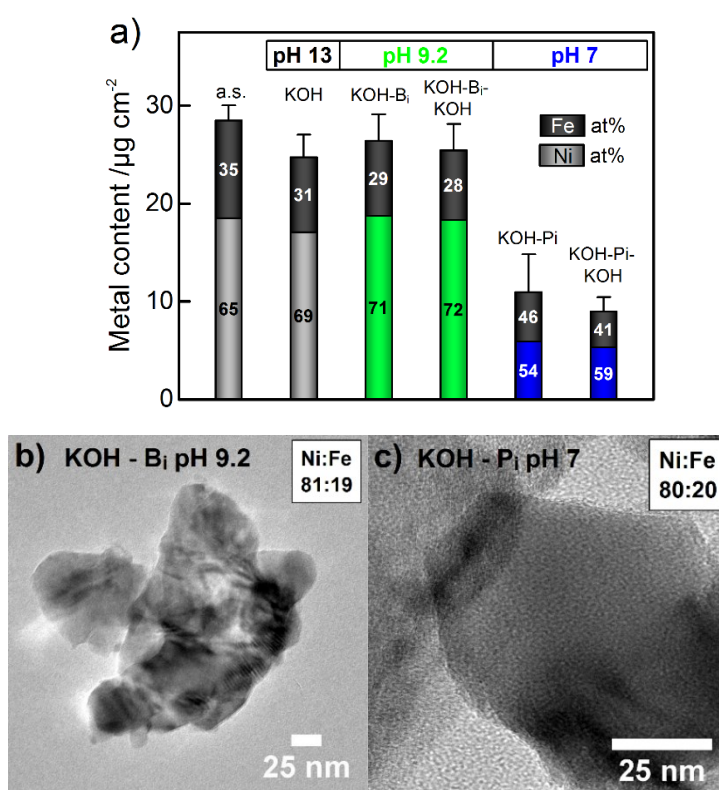


Figure 4.5. (a) Catalyst composition ($\text{Ni}_{100-x}\text{Fe}_x$) of NiFeO_x/C before and after cycling in different electrolytes and pH. Shown are the as-prepared catalyst (a.s.), after 150 cycles in KOH pH 13 (KOH), KOH-B_i cycled electrode; analyzed after 20 cycles in pH 9.2, KOH-B_i-KOH; after 20 cycles in pH 13, KOH-P_i; after 20 cycles in pH 7, and KOH-P_i-KOH re-activated; after 20 cycles in pH 13. The total bar height represent the geometric metal loading of Ni and Fe determined by TXRF analysis (left axis). The bar colors represent the atomic composition of Fe (black) and Ni (colored) given as $\text{Ni}_{100-x}\text{Fe}_x$, estimated as the average from TXRF and SEM-EDX analysis. (b) TEM image and EDX composition of selected crystallite of NiFeO_x/C after KOH-B_i cycling; 20 cycles in pH 9.2 (c) after KOH-P_i; 20 cycles in pH 7. All samples were prepared at a scan-rate of 100 mV/s between ca 1-1.75 V_{RHE} in molar concentrations of 0.1 M of the electrolytes. See more details in the Experimental section 3.2.2 and in

Supplementary Information Figure S4.8. This figure has been reprinted with permission from ref. ¹⁰⁰ Copyright Elsevier (2016).

It might be that the formation of a more crystalline phase is induced by a recrystallization process during CV cycling as a cause of mobile Ni and/or Fe species during OER catalysis. Toward lower pH values where the leaching of Ni was more extensive than the Fe species, a more Ni rich phase was formed due to an excess of mobile Ni atoms in the exposed regions. Therefore, the composition of the crystallites reflect the more mobile species which are different at different pH. The crystalline areas after 150 cycles in KOH pH 13 could not be confirmed as composed of a phase with elevated Ni content as observed after cycling in pH 9.2 or pH 7 (Figure 4.5b and c and Figure S4.8b and c). However, there is a possibility that the Ni rich areas after cycling in pH 13 might escape detection in the EDX analysis if the total amount of the Ni rich spots are fewer in number compared to the amorphous areas. TEM-EDX recorded after extensive cycling in KOH (1000 cycles) indeed showed that the crystallites appeared slightly more Ni rich than after 150 cycles (Figure S4.8a). The integrated SAED patterns after 1000 cycles also showed an additional ring which could be the (0 0 3) reflection from the interlayer distance in α -Ni(OH)₂ (insets in Figure S4.8a–c). The formation of locally observed Ni rich crystallites is not entirely understood and would need further investigations. One could argue that a Ni rich phase would enhance the redox features of the Ni(OH)₂/NiOOH redox peak ⁸⁹, however the observations of a rapid decrease of both the OER activity and the redox peak upon cycling in pH 7, is due to a larger loss of Ni atoms from the bulk as suggested by the TXRF and SEM-EDX analyses. The recovery of the OER activity and the partial recovery of the Ni redox peak upon re-activation by cycling in KOH pH 13 are more difficult to explain. The changes in the physical character of the catalyst such as phase, surface area, and crystallite size might of course impact on the Ni redox chemistry ^{74,75,192}. Reports on Fe incorporation from electrolyte impurities into the Ni(OH)₂ have been shown to enhance the OER activity ^{72,76}. We estimated that the Fe impurities present in the electrolytes were below <0.1 ppm. Since the Fe content is present in such large excess to the Ni atoms in the as-prepared NiFeO_x/C catalyst, the electrolyte impurities are neglectable to the total Fe content. Addition of Fe to a Ni(OH)₂ is known to result in a significant increase in the OER activity. The most highly active sites can be assumed to be composed of a Ni-Fe center, which has a higher TOF than a Ni or a Fe site alone ⁸⁰. When cycled at pH 7, there was a loss of ~50% Ni atoms in relative to the Fe atoms leaving a Ni:Fe composition of 50:50. This would mean that we could theoretically maintain the same number of highly active Ni-Fe sites since there was an excess of Ni atoms in the as-prepared catalyst (Ni/Fe = ~2), assuming no loss of total metal content. Therefore, the recovery of the catalytic OER activity observed after cycling in pH 7 would be feasible. Estimation of the intrinsic activity based on 50%

loss of the total metal content resulted in approximately 2 times higher intrinsic OER activity than before exposure to pH 7. The reappearance of the $\text{Ni(OH)}_2/\text{NiOOH}$ redox peak upon reactivation in pH 13 was however not proportional to the recovered OER activity. Our results would imply that the redox active Ni sites in the $\text{Ni}_{62}\text{Fe}_{38}\text{O}_x/\text{C}$ catalyst do not contribute equally to the OER current. After reactivation by cycling in KOH after exposure to pH 7, the Ni redox peak is smaller due to a loss of Ni atoms, however the OER activity is nearly preserved due to the number of highly active Ni-Fe sites could be maintained because of a smaller loss of Fe atoms in relation to Ni atoms.

4.3.4. Differential Electrochemical Mass Spectrometry (DEMS)

To further study the influence of electrolyte and pH on the OER activity of NiFeO_x/C , differential electrochemical mass spectrometry (DEMS) was acquired to probe oxygen evolution activity and detect volatile products during potential cycling in pH 13, 9.2 and 7. DEMS was carried out using a home customized dual thin-layer electrochemical flow cell, connected to a quadrupole mass spectrometer via a 150 μm thick microporous PTFE membrane (20 nm pore size) with a differential pressure generated by two turbomolecular pumps. Measurements were carried out according to the same electrolyte switching protocol as used in the RDE measurements, both in P_i pH 7 (KOH- P_i -KOH) and in B_i pH 9.2 (KOH- B_i -KOH), shown in Figure 4.6a–c. Due to the outline of the setup, CVs were recorded at a scan-rate of 50 mV/s in order give enough time for the pressure chamber to remove volatile products during completion of a CV scan. Therefore, the number of cycles was decreased to half of the cycles used in the RDE setup in order to keep the same charge passed through the catalyst. The OER activities were in good agreement with the results from the RDE setup, however due to a higher resistance in the DEMS setup, especially in B_i pH 9.2, the absolute currents could not be directly compared to RDE measurements. The Faradaic efficiencies of O_2 ($m/z = 32$) in pH 13, 9.2, and 7 are presented in Figure 4.6b.

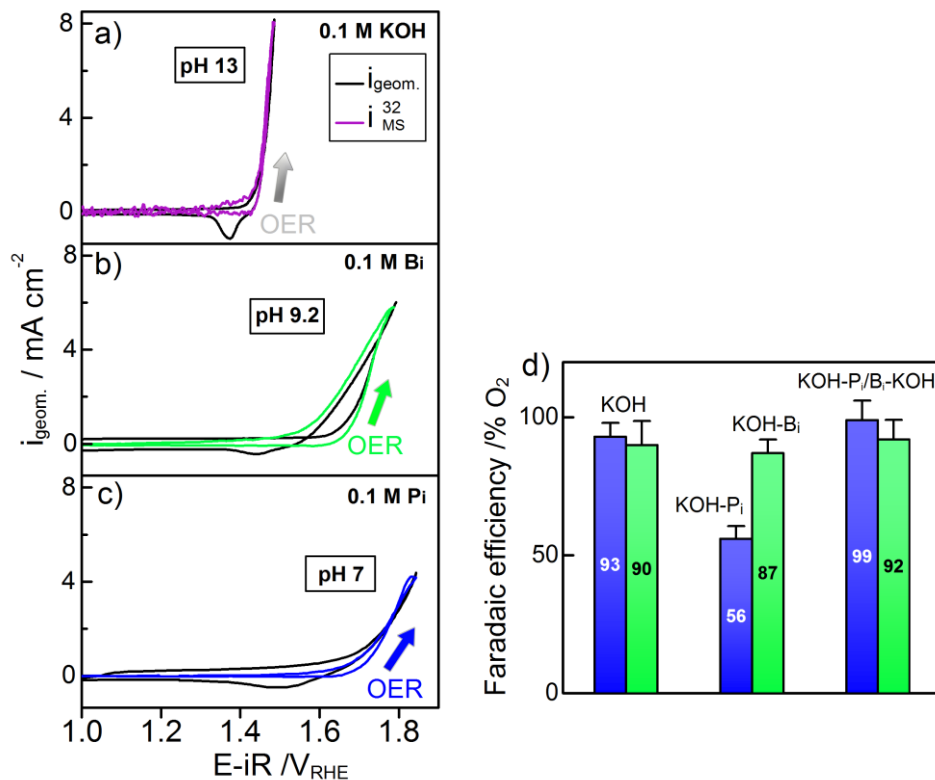


Figure 4.6. Differential Electrochemical Mass Spectrometry (DEMS) of a NiFeO_x/C electrocatalyst measured in a dual thin-layer flow cell. The Faradaic current ($i_{geom.}$) are shown as black lines and the ion current from the mass spectrometer (i_{MS}) as colored lines. **(a)** Electrode after 75 cycles in 0.1 M KOH pH 13. **(b)** KOH-B_i cycled electrode in pH 9.2. **(c)** KOH-P_i cycled electrode in pH 7. Shown are cycle 5. **(d)** Faradaic efficiency of KOH-B_i-KOH (green bars) and KOH-P_i-KOH cycled electrode (blue bars). The catalyst loading was $\sim 8 \mu\text{g cm}^{-2}$, scanned between ca 1–1.8 V_{RHE} after iR compensation. The scan-rate was kept to 50 mV/s, and the electrolyte flow 8 $\mu\text{l/min}$. This figure has been reprinted with permission from ref. ¹⁰⁰ Copyright Elsevier (2016).

The Faradaic efficiencies of O₂ ($m/z = 32$) were estimated to ~ 90 mol.% during cycling in 0.1 M KOH. In P_i pH 7, DEMS measurements confirmed a rapid loss of OER activity seen as a steadily decreasing O₂ (Figure S4.9a), and the Faradaic efficiency was estimated to only 56% by the end of the 10 cycles, and after re-activation by cycling in pH 13, the OER activity could be recovered with $\sim 95\%$ Faradaic efficiency of O₂ (Figure S4.9b). Measurements shown in the time domain (Figure S4.10a–f), revealed a contribution from CO₂ ($m/z = 44$) was slightly increasing by the end of the 10 cycles in pH 7 (Figure S4.9b), indicative of carbon corrosion. Electrodes cycled in B_i pH 9.2 did not experience a loss of OER activity, however the Faradaic efficiency was somewhat lower (87%) compared to pH 13, which might be partly caused by the higher electrolyte resistance. There was no significant formation of CO₂ in pH 13 or 9.2, however a small

contribution was observed in pH 9.2. The fact that the CO_2 was not observed in pH 13 does not exclude carbon corrosion since CO_2 is likely to form HCO_3^- ⁸⁹. DEMS measurements of re-activated electrodes in 0.1 M KOH pH 13 after cycling in pH 9.2 and pH 7, confirmed O_2 in all cases, and also showed that the O_2 release from the catalyst seemed more stable than prior to exposure to a lower pH (Figure S4.10a–f). This suggests a more efficient O_2 release from the surface to the electrolyte after cycling in pH 7 or 9.2, which together with the small increase in Faradaic efficiency supports a change at the catalytic interface. However, this would need further investigations.

4.4 Conclusions

Investigations of a mixed NiFeO_x oxyhydroxide electrocatalyst supported on Vulcan XC-72r (NiFeO_x/C) for the oxygen evolution reaction in alkaline to neutral pH range showed that OER activities were decreasing in the order of pH 13 < pH 9.2 < pH 7. The catalyst showed high intrinsic OER activity with OER overpotentials (η_{OER}) at 10 mA/cm^2 below 300 mV in 0.1 M KOH, and a turnover frequency of 0.45 s^{-1} based on total metal loading of Ni + Fe. Comparative measurements of KOH pre-cycled electrodes further investigated in 0.1 M B_i pH 9.2 and in 0.1 M P_i pH 7 showed OER activities at 400 mV overpotential with TOFs in the range of 0.32 s^{-1} and to 0.01 s^{-1} , respectively. Cycling in P_i pH 7 resulted in an instant decrease of the OER activity and a rapid loss of redox active Ni species seen as a decreased charge under the voltammetric $\text{Ni}(\text{OH})_2/\text{NiOOH}$ redox peak. Inspection of TEM images and SAED patterns after cycling in pH 13 showed formation of more crystalline areas which shared common reflections with the ordered $\text{Ni}(\text{OH})_2$. After cycling in pH 7, the crystallites appeared more Ni enriched than in pH 13 or 9.2. Deactivated electrodes cycled in pH 7 could be reactivated by subsequent cycling in pH 13, along with a partially recover of the $\text{Ni}(\text{OH})_2/\text{NiOOH}$ redox peak. SEM-EDX and TXRF measurements of electrodes cycled in KOH- P_i -KOH showed an excessive loss of Ni atoms from the bulk after only 20 cycles in P_i pH 7, which upon re-activation in pH 13 changed back to Ni:Fe compositions closer the original values. The loss of OER activity in pH 7 was confirmed as an excessive loss of Ni atoms. The recovery of the OER activity upon re-activation in pH 13 was seen as a stabilization of the Ni leaching however the composition had been changed. Differential electrochemical mass spectrometry (DEMS) confirmed both loss and recovery of the OER activity after KOH- P_i -KOH cycling, and a Faradaic contribution of $\sim 50\%$ of CO_2 in pH 7. Our study has revealed important insight into the activity and stability of mixed NiFeO_x OER catalysts at different pH, and has shown on a remarkably dynamic structure.

Acknowledgements

This work was supported by the Federal Ministry of Education and Research (BMBF) under the “energy storage” initiative, project “MEOKATS”. Partial financial support by the German Research Foundation (DFG) is gratefully acknowledged, and Unifying Concepts of Catalysis (UniCat) for financial support. We would also like to thank Prof. Dr. Holger Dau at Free University of Berlin for the TXRF analysis, and Dr.-Ing. Ralph Krähnert Technical University of Berlin for SEM-EDX measurements.

Additional Information

- Supplementary Information

Supplementary Information

Dynamical changes of a Ni-Fe oxide water splitting catalyst investigated at different pH

This material has been reprinted with permission from Elsevier as the Supplementary Information of the latest version of a published Journal article

(Görlin, M.; Gliech, M.; Ferreira de Araújo, J.; Dresp, S.; Bergmann, A.; Strasser, P. *Catalysis Today* 2015, 262, 65, DOI:10.1016/j.cattod.2015.10.018)

URL: <https://doi.org/10.1016/j.cattod.2015.10.018>

Copyright Elsevier (2016)

*Mikaela Görlin, Manuel Gliech, Jorge Ferreira de Araújo, Sören Dresp, Arno Bergmann,
Peter Strasser**

¹The Electrochemical Energy, Catalysis and Materials Science Laboratory, Department of Chemistry, Chemical Engineering Division, Straße des 17. Juni 124, Technical University of Berlin, 106 23 Berlin, Germany

S4.1. Electrochemical characterization

S4.1.1. Electrolyte switching; KOH-Pi-KOH

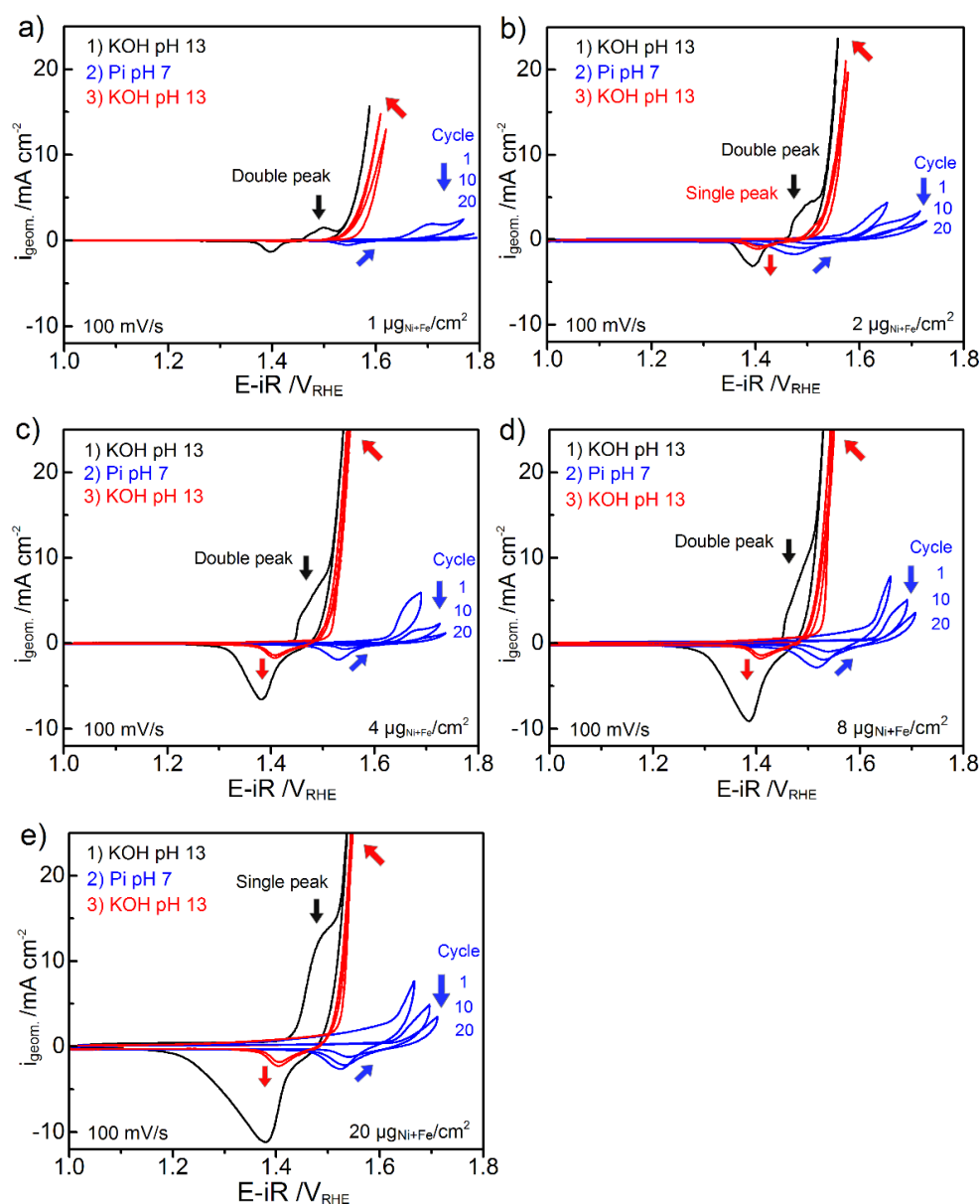


Figure S4.1. Cyclic voltammograms of NiFeO_x/C measured in RDE setup according to the electrolyte switching protocol (KOH-Pi-KOH); 150 cycles in 0.1 M KOH pH 13 (black), KOH-Pi; 20 cycles in 0.1 M Pi pH 7 (blue), KOH-Pi-KOH; re-activation by 20 cycles in KOH (red). The switching experiment was carried out at various catalyst loadings **a)** 1 $\mu g_{Ni+Fe}/cm^2$ **b)** 2 $\mu g_{Ni+Fe}/cm^2$ **c)** 4 $\mu g_{Ni+Fe}/cm^2$ **d)** 8 $\mu g_{Ni+Fe}/cm^2$, and **e)** 20 $\mu g_{Ni+Fe}/cm^2$. The rotation speed was set to 1600 rpm and the potential limits were kept between 1-1.75 V_{RHE} before iR compensation. *This figure has been reprinted with permission from ref. 100. Copyright Elsevier (2016).*

S4.1.2. Electrolyte switching; KOH-B_i-KOH

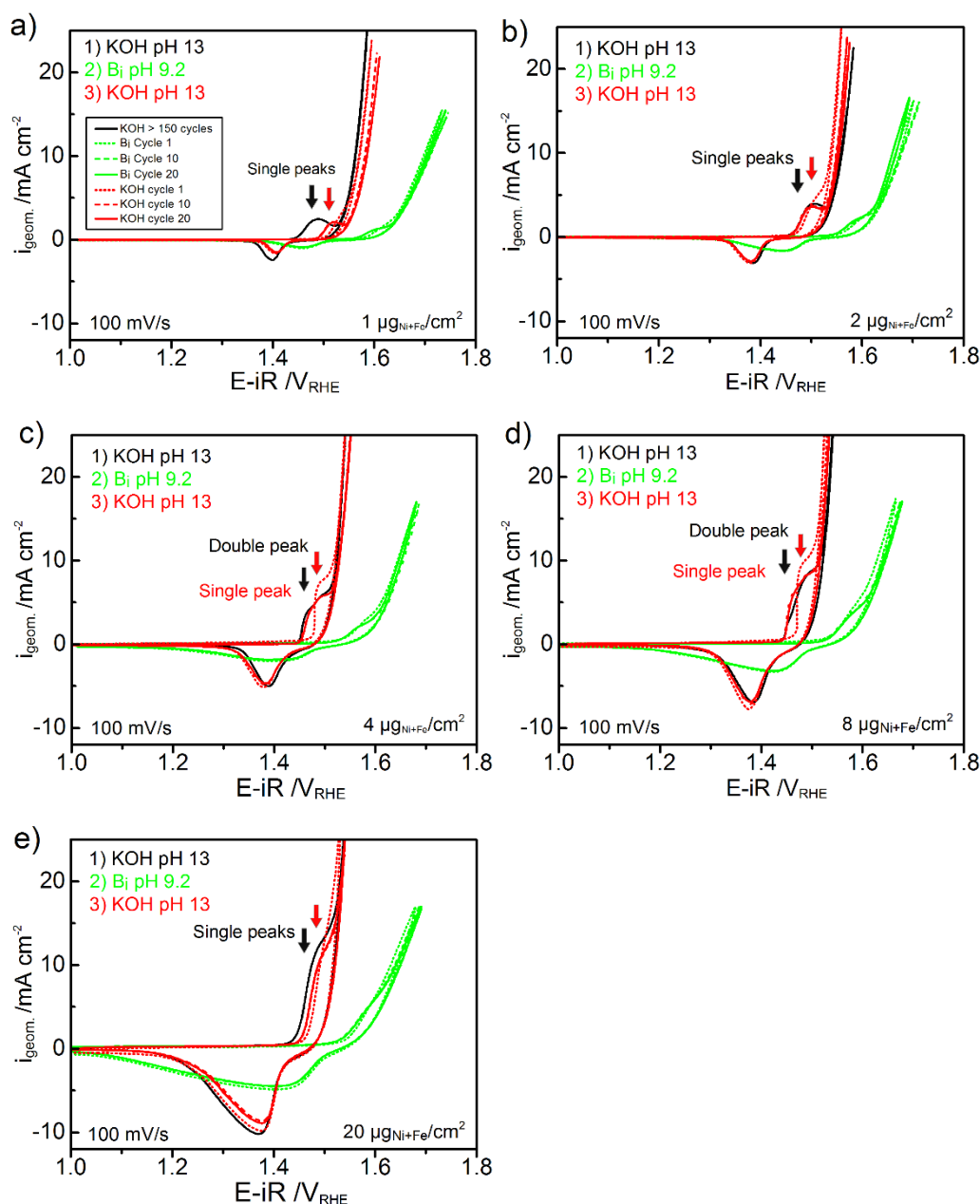


Figure 4.2. Cyclic voltammograms of NiFeO_x/C measured in RDE setup showing electrolyte switching; after 150 cycles in 0.1 M KOH pH 13 (black), after 20 cycles in 0.1 M B_i pH 9.2 (green), and after re-activation by additional 20 cycles in KOH (red). The experiment was carried out at various catalyst loadings **a)** 1 $\mu g_{Ni+Fe}/cm^2$ **b)** 2 $\mu g_{Ni+Fe}/cm^2$ **c)** 4 $\mu g_{Ni+Fe}/cm^2$ **d)** 8 $\mu g_{Ni+Fe}/cm^2$, and **e)** 20 $\mu g_{Ni+Fe}/cm^2$. The rotation speed was set to 1600 rpm and the potential limits were kept between ca 1-1.75 V_{RHE} before iR compensation. *This figure has been reprinted with permission from ref. 100. Copyright Elsevier (2016).*

S4.1.3. Oxygen evolution activity trends

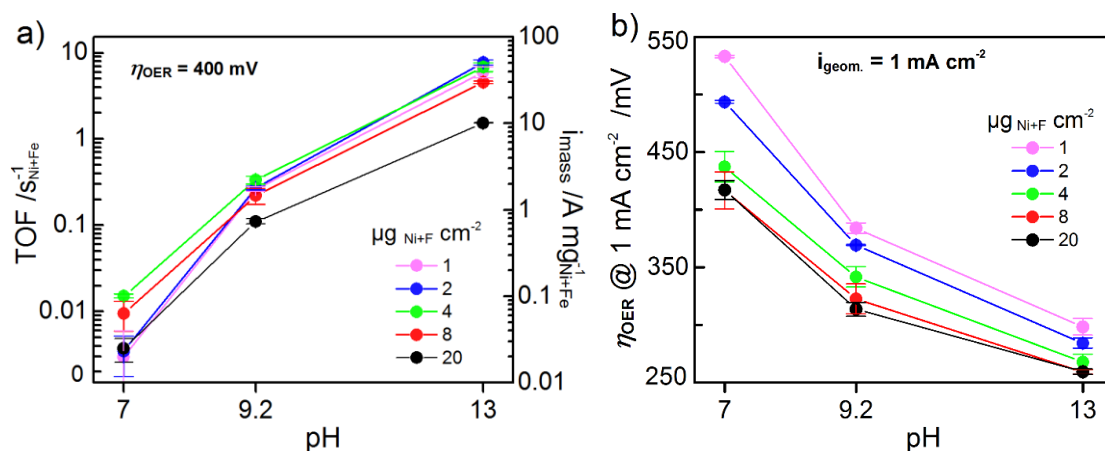


Figure S4.3. **a)** Turnover frequency (TOF) and mass activity (i_{mass}) vs. pH, measured at different geometric catalyst loadings; 1, 2, 4, 8, and 20 $\mu\text{g}_{\text{Ni+Fe}}/\text{cm}^2$. **b)** Overpotential at 1 mA cm^{-2} . Intrinsic activities are based on total geometric metal loading of Ni+Fe determined by ICP-OES. Current densities and overpotentials were extracted from chronoamperometric and chronopotentiometric measurements applying a stable potential or current for 90-120 sec, respectively. *This figure has been reprinted with permission from ref. 100. Copyright Elsevier (2016).*

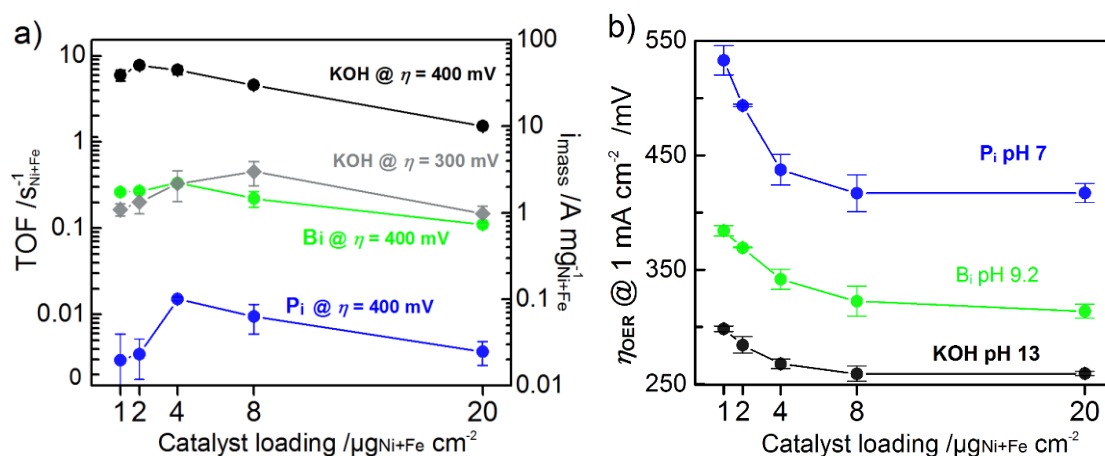


Figure S4.4. **a)** TOF and i_{mass} vs. catalyst loadings; 1, 2, 4, 8, and 20 $\mu\text{g}_{\text{Ni+Fe}}/\text{cm}^2$. Extracted at $\eta = 300$ and 400 mV in 0.1 M KOH pH 13 (grey, black) and at $\eta = 400 \text{ mV}$ in 0.1 M Bi pH 9.2 (green), and 0.1 M Pi pH 7 (blue). Intrinsic activities were based on total geometric metal loading of Ni+Fe determined by from ICP-OES. Current densities and overpotentials were extracted from chronoamperometric and chronopotentiometric measurements, respectively. *This figure has been reprinted with permission from ref. 100. Copyright Elsevier (2016).*

S4.1.4. Evaluation of the $\text{Ni}^{2+}/\text{Ni}^{3+}$ redox peak in P_i pH 7

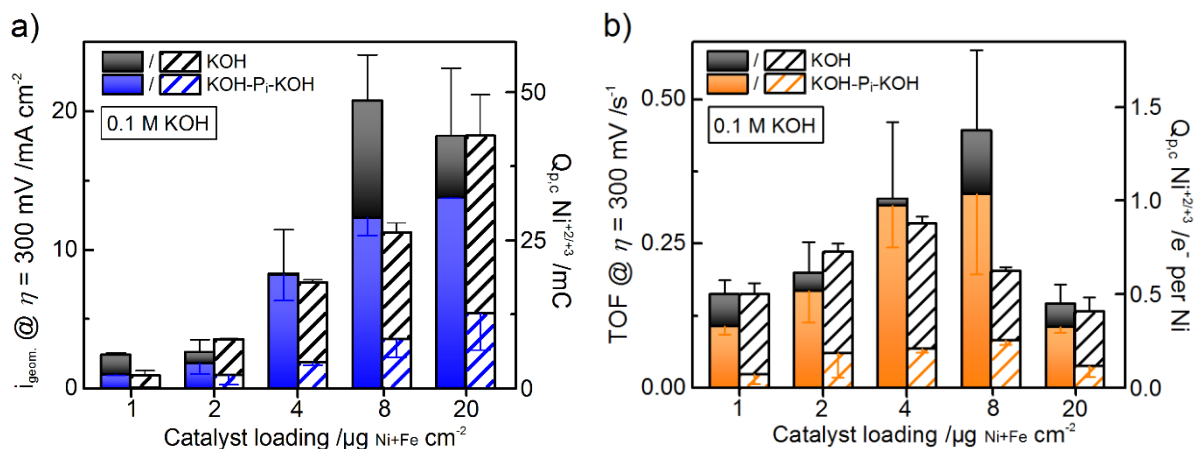


Figure S4.5. Evaluation of OER activities and the $\text{Ni}(\text{OH})_2/\text{NiOOH}$ redox peak of NiFeO_x/C in pH switching experiments (KOH-P_i-KOH) at various catalyst loadings; 1, 2, 4, 8, and 20 $\mu\text{g}_{\text{Ni+Fe}}/\text{cm}^2$. **a)** Geometric current density ($i_{\text{geom.}}$) vs. catalyst loading at $\eta_{\text{OER}} = 300 \text{ mV}$ (solid bars) in 0.1 M KOH. The right axis shows the absolute value of the integrated cathodic peak charge ($Q_{\text{p,c}}$) of the $\text{Ni}(\text{OH})_2/\text{NiOOH}$ redox peak (hatched bars). **b)** Turnover frequency vs. catalyst loading at $\eta_{\text{OER}} = 300 \text{ mV}$ in 0.1 M KOH pH 13 based on total metal loading of Ni+Fe determined by ICP-OES (left axis). The right axis shows the mass normalized Ni redox peak charge ($Q_{\text{p,c}}$) represented in (b) defined as the number of electrons transferred per Ni atoms (hatched bars). The total bar area (black + color) represent measurements of electrodes 150 cycles in 0.1 M KOH and the colored area KOH-P_i-KOH re-activated electrodes. Current densities were extracted from chronoamperometric measurements applying a stable potential for 90 sec. *This figure has been reprinted with permission from ref. 100. Copyright Elsevier (2016).*

S4.1.5. Prolonged cycling in P_i pH 7

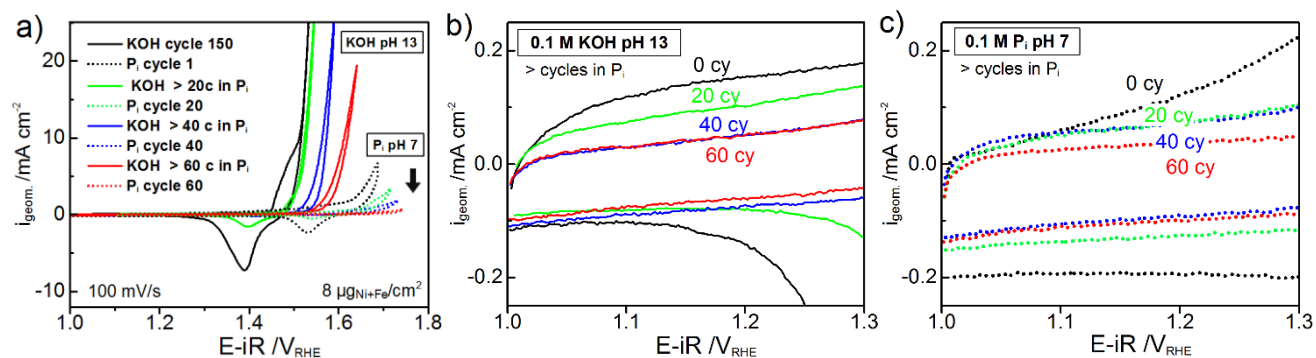


Figure S4.6. Prolonged cycling of NiFeO_x/C in 0.1 M P_i pH 7. **a)** Measurements in 0.1 M KOH pH 13 after 150 cycles in KOH (solid black), after 20 cycles in P_i (solid green), after 40 cycles in P_i (solid blue), and after 60 cycles in P_i (solid red). The corresponding cycles in P_i pH 7 are shown as dotted lines according to the same color palette. **b)** The capacitive region in KOH pH 13 **c)** The capacitive region in P_i pH 7. CVs were recorded at a scan-rate of 100 mV/s between 1-1.75 V_{RHE} before iR-compensation. The catalyst loadings were determined by ICP-OES prior to the measurements. *This figure has been reprinted with permission from ref. 100. Copyright Elsevier (2016).*

S4.2. X-ray diffraction

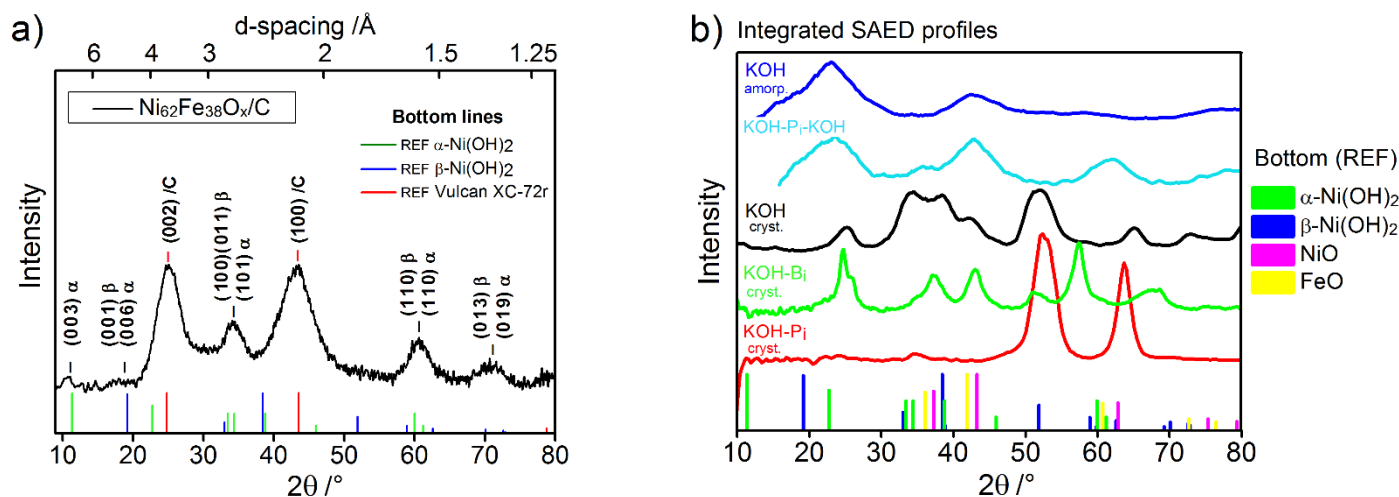


Figure S4.7. **a)** Experimental XRD pattern of the as-prepared NiFeO_x/C catalyst. **b)** Simulated XRD profiles obtained by integration of the SAED patterns from crystalline and amorphous spots presented in Fig. 3-4. Shown are the amorphous area after 150 cycles in 0.1 M KOH pH 13 (dark blue, see also Fig. 3f), re-activated amorphous spot (KOH-P_i-KOH) after 20 cycles in KOH (light blue, see also Fig. 4h), crystalline area after 150 cycles in KOH (black, see also Fig. 3d), crystalline area of KOH-B_i cycled electrode after 20 cycles in 0.1 M B_i pH 9.2 (green, see also Fig. 4d), and crystalline area of KOH-P_i cycled electrode after 20 cycles in 0.1 M P_i pH 7 (red, see also Fig. 4f). Bottom lines show reference compounds of $\alpha\text{-Ni}(\text{OH})_2$ (green), $\beta\text{-Ni}(\text{OH})_2$ (blue), NiO (pink), and FeO (yellow). *This figure has been reprinted with permission from ref. 100. Copyright Elsevier (2016).*

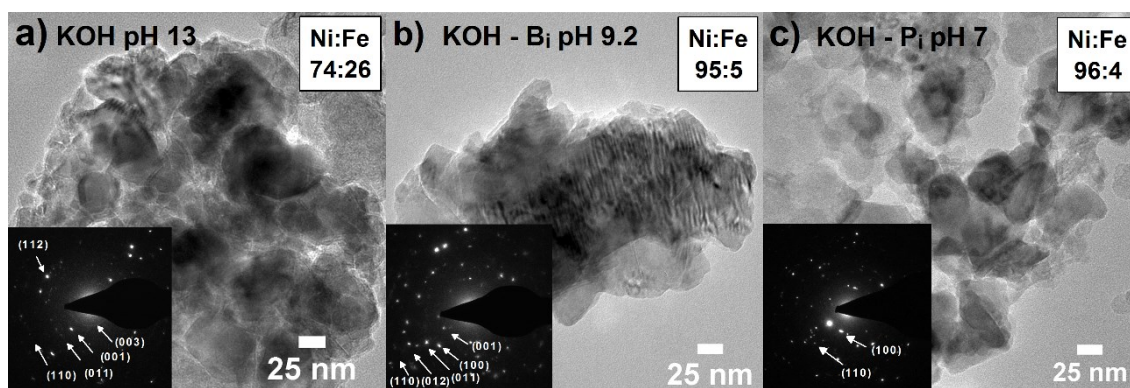


Figure S4.8. TEM images, SAED patterns, and EDX compositions of selected crystalline areas of NiFeO_x/C . **a)** Electrode extensively cycled in 0.1 M KOH pH 13 (1000 cycles) **b)** KOH-B_i after 20 cycles in pH 9.2 **c)** KOH-P_i after 20 cycles in pH 7. Insets show SAED patterns of the presented TEM area. The arrows indicate a spot lying on an indices plane assuming the $\beta\text{-Ni}(\text{OH})_2$ structure. EDX compositions are presented in the upper right corner. *This figure has been reprinted with permission from ref. 100. Copyright Elsevier (2016).*

S4.4. Differential Electrochemical mass spectrometry

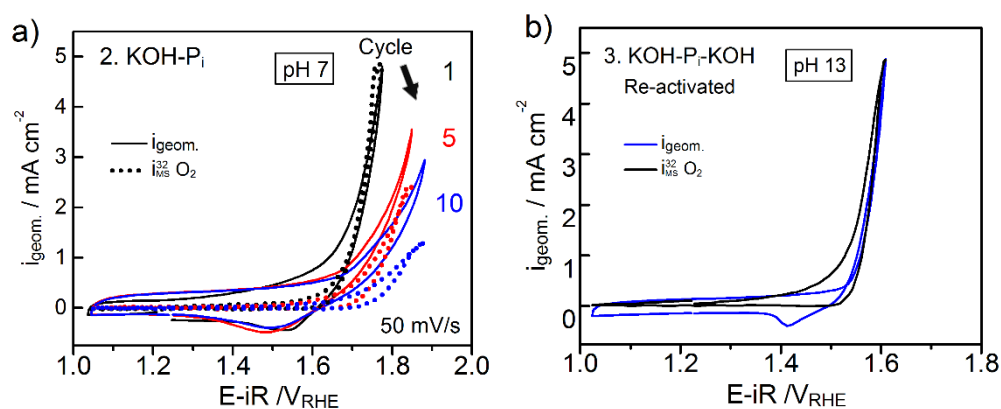


Figure S4.9. Differential electrochemical mass spectrometry (DEMS) presented in the voltage domain of NiFeOx/C measured in a dual thin-layer electrochemical flow cell. The Faradaic currents ($i_{\text{geom.}}$) from the potentiostat (solid lines) and the corresponding ion currents of $m/z = 32$ (dotted lines). **a)** Catalyst in 0.1 M P_i pH 7; after 1 cycle (black), 5 cycles (red), and 10 cycles (blue). **b)** KOH- P_i -KOH re-activated catalyst after 10 cycles in 0.1 M KOH pH 13. The scan-rate was kept to 50 mV/s, and an electrolyte flow of 8 $\mu\text{l/s}$ of N_2 -purged electrolyte. The catalyst loading was 8 $\mu\text{g Ni+Fe/cm}^2$. This figure has been reprinted with permission from ref. 100. Copyright Elsevier (2016).

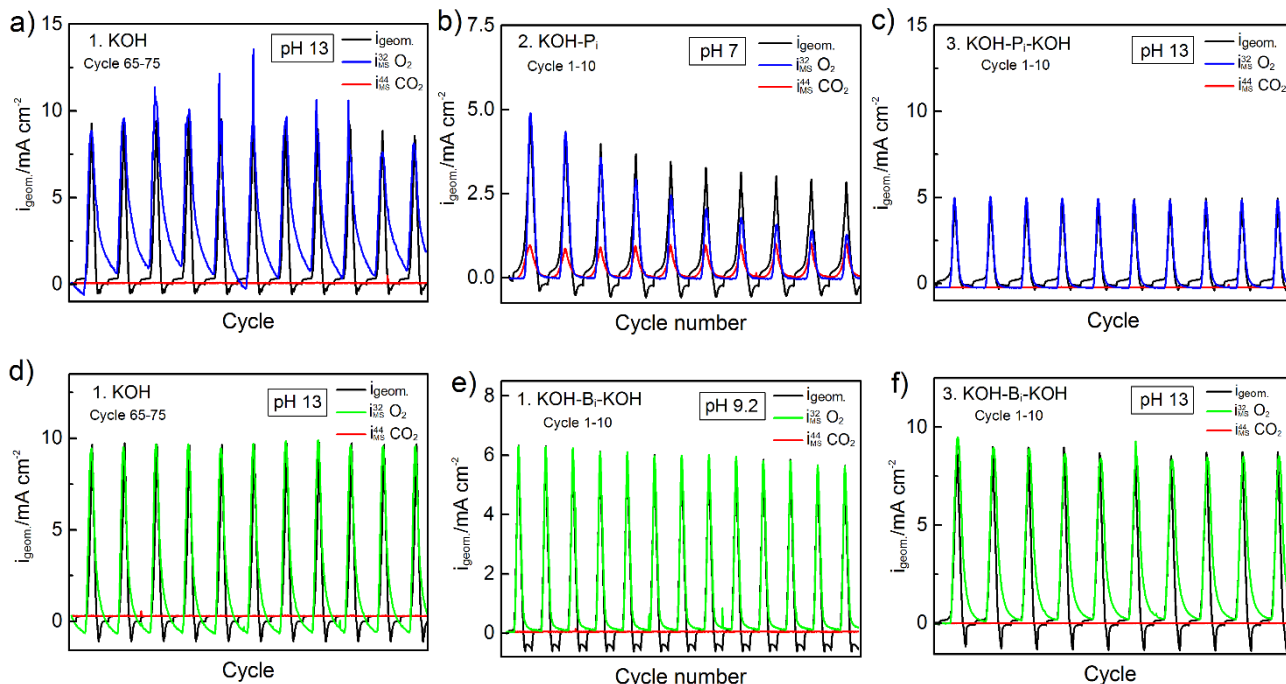
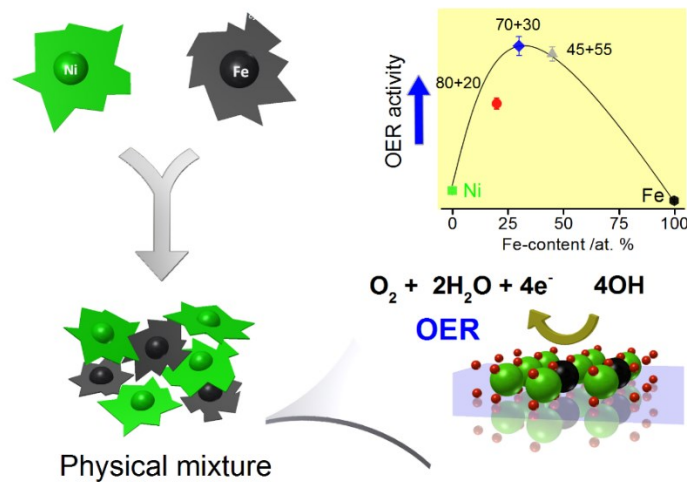


Figure S4.10. Differential electrochemical mass spectrometry presented in the time domain of NiFeOx/C. Each maximum represent the end of the scan-limit range ($\sim 1.8 V_{RHE}$). The Faradaic currents from the potentiostat (i_{geom}) are shown on the left axis (black curves), and the ion currents from the mass spectrometer (i_{MS}) for O_2 ($m/z = 32$) and CO_2 ($m/z = 44$) shown on the right axis; scaled to $m/z = 32$ to show the relative contribution of the CO_2 faradaic current. **a-c)** KOH-Pi-KOH cycling for cycle 64-75 in pH 13, cycle 1-10 in pH 7, and cycle 1-10 in pH 13. **d-f)** KOH-Bi-KOH cycling for cycle 64-75 in pH 13, cycle 1-10 in pH 9.2, and cycle 1-10 in pH 13. The potential limits were kept between ca 1-1.8 V_{RHE} , however were varying slightly in the different electrolyte depending on the resistance and different OER activities. The faradaic efficiencies of O_2 were estimated using a calibration constant (K^*) as described in the Section 2.5, see also Figure 6b. *This figure has been reprinted with permission from ref. 100. Copyright Elsevier (2016).*

Chapter 5

Formation of a highly active Ni-Fe water oxidation catalysts by physically mixing Ni and Fe oxyhydroxides

This Chapter is based on unpublished data



Mikaela Görlin¹, Petko Chernev², Tobias Reier¹, Peter Strasser¹, Holger Dau²

Contact: pstrasser@tu-berlin.de

¹Technical University of Berlin, Chemical Engineering Division, Straße des 17. Juni 124, 10623, Berlin, Germany

²Free University of Berlin, Department of Physics, Arnimallee 14, 14195 Berlin, Germany

Abstract

Catalysts for electrochemical water splitting for large-scale applications and use in solar-to-fuel conversion processes require low cost materials and simple preparation methods for both anode and cathode materials. Mixed Ni-Fe oxyhydroxides (OOH) are known as promising electrocatalysts for the oxygen evolution reaction (OER) in alkaline electrolyte. Herein we present a series of physically mixed Ni+Fe (OOH) electrocatalysts prepared by post-mixing individually prepared Ni(OH)₂ and Fe(OOH) parental catalysts. The oxygen evolution activity increased a 1000-fold in the physically mixed Ni+Fe catalysts, comparable to the activity of the solvothermally pre-synthesized Ni-Fe(OOH) catalysts investigated in Chapter 3. X-ray absorption spectroscopy identified the local atomic structure of the post-mixed Ni+Fe(OOH) catalysts under catalytic potential. The study conclude formation of an active water oxidation catalyst using this simple preparation method. To judge from the X-ray data, as a cause of partly incorporated Fe(OOH) in the physically mixed Ni+Fe(OOH) catalysts, the metal redox state of Ni was stabilized in its low-valent +2 state. This confirms the effect of Fe seen in the pre-synthesized Ni-Fe(OOH) catalysts. Our study establish a simple preparation method and contribute to further insight into the OER reaction dynamics in mixed Ni-Fe electrocatalysts under catalytic potential.

5.1. Introduction

Solving awaiting energy crisis will require efforts to develop sustainable utilization of energy which requires efforts to increase the use of alternative resources.¹ Electrochemical water splitting is a highly energy demanding process and therefore efficient catalysts are crucial to achieve this goal. Non-noble based electrocatalysts are showing promising activities towards the anode reaction, the oxygen evolution reaction (OER).^{2,5,7-9,14-18,88,109,134} Especially binary electrocatalysts of mixed Ni and Fe in alkaline electrolyte have gained attention.^{76,77,79-83,87-89,97,99,107,135,193}

Recent advances in X-ray based measurements and computational methods have contributed to a deeper insight into the metal redox states and origins of the synergism observed between Ni and Fe centers in these binary highly active electrocatalysts. The effect was earlier pointed out by Corrigan et al.⁷¹ as a drastic increase in the OER activity of electrodeposited Ni(OH)₂ based electrodes at elevated Fe content. Trotochaud et al.⁷² clearly demonstrated using X-ray photoelectron spectroscopy (XPS) that Fe in non-purified KOH electrolyte readily incorporate into Ni(OH)₂ already after a few potential cycles, therefore proposed to be the cause of the long believed activation behavior of Ni electrodes. A number of operando based X-ray and spectroscopic investigations have attempted to retrieve information of the metal oxidation states of Ni and Fe in the catalytically active state, yet deviating results have been obtained.^{77,80,101-103,161,173} Landon and coworkers were amongst the first to investigate mixed Ni-Fe oxides for OER prepared by other methods than electrodeposition, however they found an absence of redox activity at the Ni *K*-edge in the presence of Fe.⁷⁷ Due to the large bulk to surface volume, and the lack of reference materials, no absolute conclusions could be drawn by the research group in the presented study. Friebel et al.⁸⁰ more recently presented an extensive operando XAS investigation where the active site of electrodeposited Ni-Fe(OOH) catalysts on Ti/Au electrodes was identified over the full range of Ni/Fe compositions. The study concluded that only Ni atoms were redox active, with an active state described as Ni⁺⁴-Fe⁺³(OOH) regardless of composition. Wang et al.¹⁶¹ presented a study of an electrodeposited Ni-Fe(OH)_x catalyst on carbon paper which showed redox activity on both metals; the active state was proposed as Ni^{+3.6} and the Fe as highly covalent Fe⁺⁴-O bond according to operando XAS on both the Ni and Fe *K*- and *L*- edges. This was also observed in a Mössbauer spectroscopic study presented by Chen et al.¹⁰³ of solvothermally precipitated Ni-Fe(OOH) catalysts on carbon paper, where both Ni and Fe reached oxidation states close to +4. Bates et al.¹⁷³ showed that the presence of Fe resulted in a suppression of the otherwise observed strong Ni *K*-edge potential-induced shift, hence stabilizing Ni in the low-valent +2 oxidation state under OER catalytic potentials. The results by Chen et al. were also confirmed by in situ XAS results presented by our work group in Chapter 3⁶⁶, where on the

contrary to Friebe et al.⁸⁰ we observed a strong correlation between the oxidation state of Ni with the Fe composition, where Fe hindered Ni to reach the high-valent +3.6 oxidation state.

Because of past conflicting reports on the metal redox states of Ni-Fe catalysts, it is speculative whether the sensitivity of the different measurement techniques affect the outcome of the observed electronic structure. It seems likely that other external factors associated with measurement conditions such as working electrode, catalyst support, and electrolyte pH, may also have an influence. It is also not excluded that structural parameters of the catalysts such as oxide phase and particle (or layer) size, which are highly dependent on the synthesis method, also play a role in the differences observed between studies of mixed Ni-Fe(OOH) electrocatalysts.

To rule out some of these variables and to further unveil the effect of Fe on the Ni(OH)₂ in terms of local atomic structure and metal redox states under applied catalytic potential, we will in this Chapter examine physically mixed Ni+Fe(OOH) electrocatalysts with different stoichiometric compositions. These were prepared by physically mixing parental Ni(OH)₂ and Fe(OOH) catalysts prepared individually. We applied standard electrochemical measurement techniques to evaluate the oxygen evolution activity, as well as quasi- in situ X-ray absorption spectroscopy (XAS) at the Ni and Fe *K*-edges for local atomic structure, and elemental analysis. We aim to evaluate the degree of incorporated Fe, and to extend the discussion to the origins of the enhanced activity in mixed Ni-Fe electrocatalysts.

5.2. Results and Discussion

Preparation of Ni+Fe(OOH) electrocatalysts for electrochemical water oxidation was achieved by physically post-mixing parental Ni(OH)₂ and Fe(OOH) catalysts prepared individually using solvothermal synthesis (see also Chapter 3).¹³¹ The catalysts were activated by a conditioning step of 1.63 V for 30 min in 0.1 M KOH prior to further electrochemical investigations.

5.2.1 Formation of a highly active Ni+Fe catalysts

Physically mixed Ni+Fe(OOH) catalysts with different stoichiometric compositions showed a drastic increase in the catalytic OER activity (Figure 5.1a). The activities of the physically mixed Ni+Fe(OOH) catalysts were comparable to those of the solvothermally pre-synthesized Ni-Fe(OOH) catalysts presented in Chapter 3.¹³¹ An estimation of the oxygen evolution activity at 300 mV overpotential showed a near 1000-fold increase compared to the parental Fe(OOH) catalyst (Figure 5.1b), in agreement with earlier observations of mixed Ni-Fe(OOH) catalysts.^{80,87} Amongst the investigated physically mixed Ni+Fe catalysts, the highest turnover frequency based on total metal of Ni and Fe (TOF_{Ni+Fe}), was estimated to 0.16 s⁻¹, for the Ni₆₅+Fe₃₅ catalyst (see Figure 5.1c). The overpotential at a current density of 10 mA cm⁻² was estimated to 300 mV (see Figure 5.1d). The oxygen evolution activity is hence similar to the activity of pre synthesized Ni-Fe catalysts.^{14,69,87,131,193} Based on the activity increase observed when mixing parental Ni(OH)₂ and FeOOH catalysts, it appears as if the mixing results in formation of a mixed Ni-Fe(OOH) catalyst. The degree of Fe incorporated into the Ni(OH)₂ lattice in the physical mixtures would be of high interest for understanding of the origin of the interaction between Ni and Fe centers and could be applicable on a large scale where a simple preparation method is desired. Previous discussions regarding the increased OER activity between Ni and Fe have included investigations of the metal redox states under catalytic potential,^{80,103,106,108,194} the Fe solubility in Ni(OH)₂,^{15,77,80} charge-transfer effects,¹⁷³ and increased electrical conductivity.⁷² It would therefore be desirable to know if physically post-mixing Ni(OH)₂ and Fe(OOH) leads to incorporation of Fe into the Ni(OH)₂ host, or if solely the physical contact between the two separate phases can serve as an active site for oxygen evolution reaction to proceed at low overpotentials.

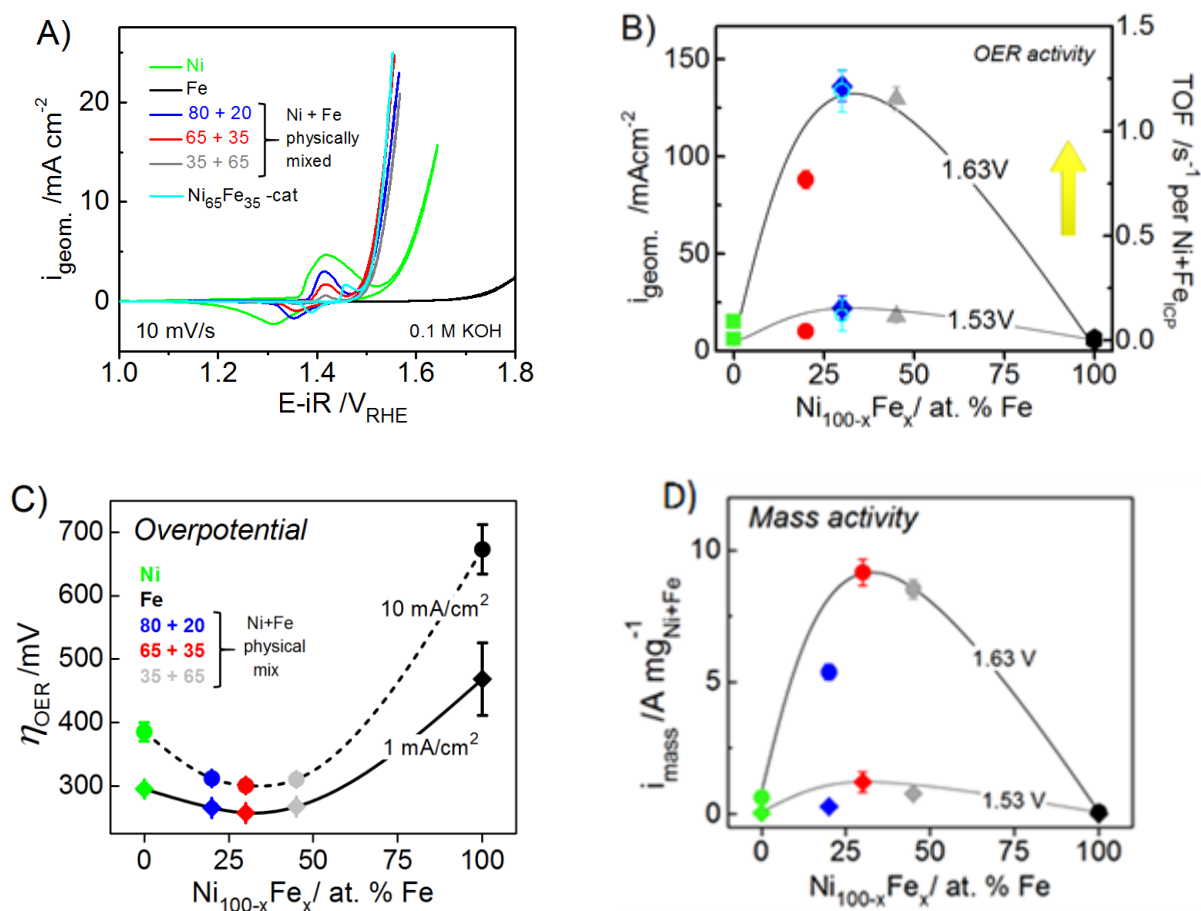


Figure 5.1. Electrochemical characterization of parental $\text{Ni}(\text{OH})_2$ and $\text{Fe}(\text{OOH})$ catalysts, physically post-mixed Ni+Fe catalysts with varying catalyst composition ($\text{Ni}_{100-x}\text{Fe}_x$) and a pre-synthesized $\text{Ni}_{65}\text{Fe}_{35}(\text{OOH})$ catalyst. **a)** CVs at a scan-rate of 10 mV/s. **b)** Geometric current density (left axis) extracted from quasi-stationary state measurements at $\eta_{\text{OER}} = 300$ mV (dots) and at 400 mV (triangles). The corresponding turnover frequency (TOF) (right axis) was estimated from on the total geometric metal loading of Ni+Fe. **(c)** Overpotential at $i_{\text{geom.}} = 1$ and 10 mA cm². **(d)** Mass based activity at $\eta=300$ mV and $\eta=400$ mV overpotential, normalized to total metal loading of Ni and Fe determined by elemental analysis. All trends were extracted from quasi-stationary state measurements. Measurements were carried out in RDE setup in 0.1 M KOH. Fe-containing catalysts were measured in KOH without further purification whereas the Ni-catalyst was measured in Fe-free KOH obtained by purification according to a reported method.⁷²

Analysis of the Tafel slopes of physical mixtures of Ni+Fe(OOH) catalysts shown that the mixing introduced a change in the Tafel slope varying with composition (Figure S5.1 and Table S5.1). Inspection of the $\text{Ni}(\text{OH})_2/\text{NiOOH}$ redox peak showed that the size of the physically mixed $\text{Ni}_{65}\text{Fe}_{35}$ catalyst was similar to that of the $\text{Ni}_{65}\text{Fe}_{35}$ catalyst (Figure S5.2). The redox peak is either significantly smaller than that of the parental $\text{Ni}(\text{OH})_2$ catalyst which should be indicative of Fe incorporated or in close contact.

Despite nearly identical OER activity of the Ni+Fe and Ni-Fe catalysts, the pre-synthesized Ni-Fe catalyst showed a noticeable more anodic peak position compared to the physically mixed Ni+Fe catalyst at comparable stoichiometric compositions. This could indicate that a difference between the post and pre mixed catalysts prevail. Estimation of redox number (electrons transferred Ni atoms) of the Ni(OH)₂ catalyst exhibited 0.9 e⁻ transferred per Ni, suggesting that all catalytic sites underwent oxidation, and hence signify that the Ni catalyst have “volume catalysis”,^{66,69} with a redox number of 1 electron per Ni, whereas both the Ni+Fe and Ni-Fe catalysts containing ~ 30 % Fe showed only 0.5 e⁻/Ni (Figure S5.3a). This would suggest as we showed in Chapter 3 , that the presence of Fe result in a much lower degree of oxidized Ni species.¹⁰⁸ Another difference between the physically mixed and pre-synthesized catalysts was that the position of the anodic redox peak. The peak did not appear affected in the Ni+Fe catalysts regardless of composition, whereas in the Ni-Fe catalysts the anodic wave shifted to anodic potentials at increased Fe-content (Figure S5.3b). Yet the cathodic wave shifted in both Ni+Fe and Ni-Fe catalysts to more anodic potentials at increased Fe content.

5.2.2. SEM and EDX elemental composition

SEM-EDX elemental mapping before and after OER catalysis of a physically mixed Ni+Fe catalyst was investigated for the degree of mixing and metal distribution. The catalyst was mixed in an Eppendorf tube prior to deposition of the catalyst film on the working electrode. The EDX elemental mapping of the as-prepared catalysts first appeared as non well-mixed Ni(OH)₂ and FeOOH (Figure 5.2a). However, because of the large difference in the stoichiometric composition of Ni and Fe in the investigated physical mixture it was difficult to discriminate how well mixed the two phases were. To distinguish the local distribution, it would be better to evaluate a catalyst film with a more similar Ni:Fe composition and at a higher resolution. Another EDX metal mapping was carried out after the electrochemical activation step (1.63 V_{RHE} for 30 min in 0.1 M KOH). The coordinates of the first EDX mapping spot was localized by marks in the working electrode. The EDX metal distribution after the OER activation step did not appear to have been changed with both Ni and Fe showing a similar distribution as the as-prepared sample (Figure 5.2b). The OER activation step was however associated with a fractional loss of Fe of ~7 at. %. This was in accordance with the findings of a pre-synthesized Ni-Fe catalyst with similar composition investigated in Chapter 3.¹³¹

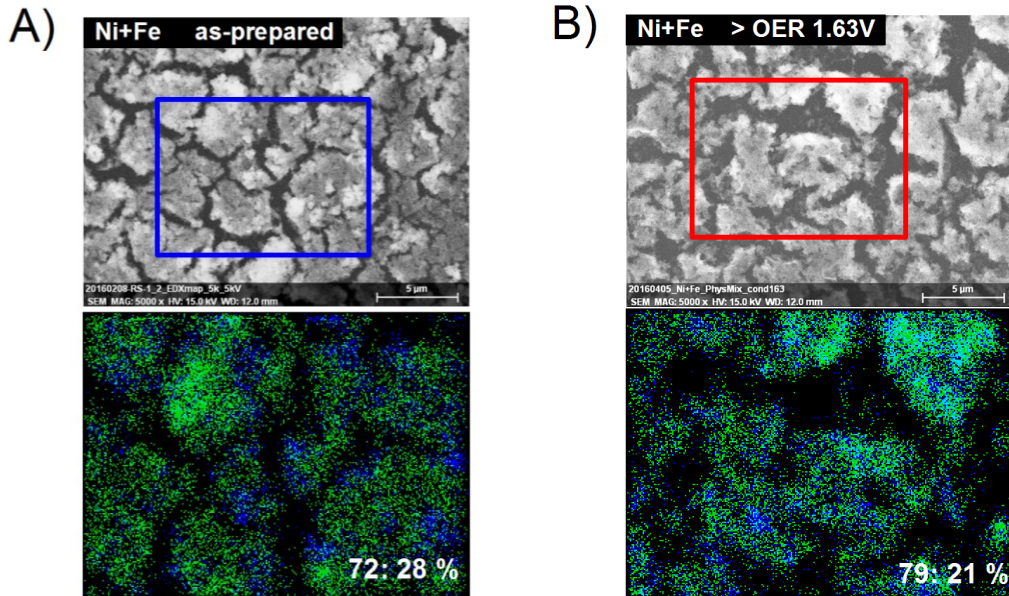


Figure 5.2. SEM-EDX elemental mapping of a physical mixture of Ni₅₀+Fe₅₀ catalyst drop-casted on a glassy carbon working electrode. The images show the (a) as-prepared catalyst (b) after the activation step of 1.63 V_{RHE} for 30 min in 0.1 M KOH. The upper images show the SEM and the lower the corresponding EDX elemental mapping. The Ni:Fe compositions are indicated in the lower right corner as atomic %.

To investigate the bulk content of Ni and Fe in the physically mixed Ni+Fe catalysts, total X-ray fluorescence (TXRF) analysis was used before and after the activation step. The catalysts were dissolved in a small volume of HCl after the measurements and Ga-standard with known concentration was added to allow for quantitative analysis. The TXRF analysis of the as-prepared Ni+Fe catalysts confirmed a geometric metal loading close to $\sim 20 \mu\text{g cm}^{-2}$ of total metal, and stoichiometric compositions close to the predicted values (see Figure 5.3, *solid bars*). After the electrochemical step of 1.63 V for 30 min in 0.1 M KOH, a portion of the total metal, especially Fe, was lost (Figure 5.3, *hatched bars*). The TXRF analysis hence evidenced that the Ni(OH)₂ catalyst was more stable than the Fe(OOH) catalyst. As a result, the physically mixed Ni+Fe electrocatalysts contained higher fractional contents of Ni than predicted. The compositions presented in Figure 5.1 based on the Ni-content before the conditioning step may be underestimated. According to investigations by Friebel et al.⁸⁰ where a series of electrodeposited Ni-Fe(OOH) catalysts were investigated using operando XAS, Fe was proposed to have limited solubility in the γ -NiOOH host above $\sim 25\%$ Fe. Their conclusions were based on deviating M-O and M-M local atomic distances, which is a proper estimate of the degree of incorporated Fe.

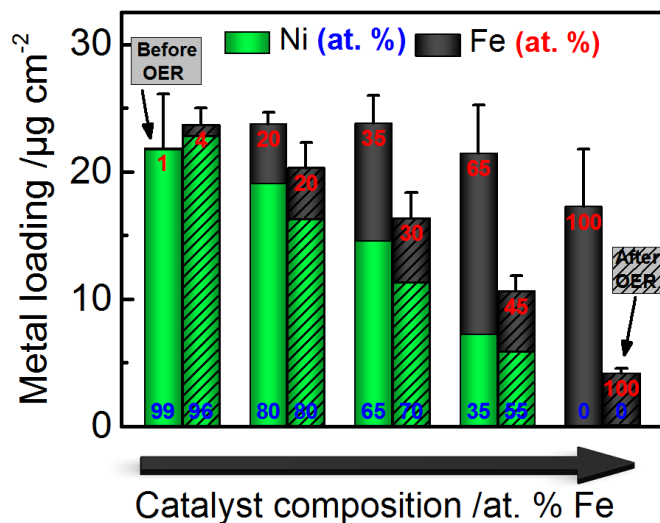


Figure 5.3. TXRF elemental analysis of physical mixtures of Ni+Fe(OOH) catalysts and the parental Ni(OH)₂ and FeOOH catalysts, with different Ni:Fe compositions. As-prepared catalysts (*solid bars*) and after application of 1.63 V_{RHE} for 30 min in 0.1 M KOH (*hatched bars*). The bar height represent the geometric total metal of Ni content (*green*) and Fe-content (*black*) given in µg cm⁻². The fractional atomic compositions (at. %) are indicated with a number for Ni (*blue*) and Fe (*red*).

The TXRF analysis reveal that a fraction of Fe is lost after exposure to catalytic potential, which leaves a nearly identical total amount of Fe in all physically mixed Ni+Fe catalysts (see Figure 5.3). Calculating TOF based on this Fe content also confirms a similar intrinsic activity. It may therefore appear as if Fe is controlling the OER activity. On the other hand, limited solubility in the Ni(OH)₂/Ni(OOH) host could also explain why a higher activity is observed at slightly higher Ni-content.

Based on the EDX metal mapping and TXRF measurements presented here, we cannot draw conclusions regarding of the degree of incorporated Fe in the physically mixed Ni+Fe catalysts. In next section, we will therefore approach the question by extending the discussion to a local atomic level.

5.2.3. Quasi- in situ X-ray absorption spectroscopy (XAS)

To answer the open question whether the increase in the catalytic activity in the physically mixed Ni+Fe catalysts leads to a rearrangement of the local atomic structure and incorporation of Fe into the Ni(OH)₂ host, we have applied quasi- in situ X-ray absorption spectroscopy to investigate the physically mixed Ni₆₅+Fe₃₅(OOH) catalyst at the metal *K*-edges. The results were compared to the pre-synthesized Ni-Fe catalyst with similar stoichiometric composition. XAS was recorded both of the as-prepared catalyst and at catalytic potential of 1.63 V_{RHE} in .1 M KOH after freeze quenching. The sample preparation method is presented in Chapter 3.^{132,133}

The Ni *K*-edge of the as-prepared catalysts revealed octahedrally coordinated Ni-centers described as [NiO₆] units with Ni-O coordinated at a distance of 2.04 Å and Ni-M at 3.07 Å (see Figure 5. 4a). The Ni atoms were mainly in oxidation state +2 in the as-prepared state (non-catalytic potential). The Ni(OH)₂ catalyst resembled that of α-Ni(OH)₂.^{80,163} The Fe *K*-edge at non-catalytic potential showed less ordered Fe-centers, with Fe-O coordination at 2.0 Å and Fe-M at 3.11 Å (see Figure 5. 4b). The atomic structure of the Fe(OOH) showed conclusively Fe atoms in oxidation state +3, and resembled that of highly distorted Fe(OOH) structures.^{80,101,173,174} Application of catalytic potential of 1.63 V resulted in a noticeable contraction of the Ni centers, ascribed to Ni atoms changing oxidation state from +2 → +3/+4. This can be described according to Ni(OH)₂ converting to NiOOH and further to a higher oxidized NiO₂ state (see Figure 5. 4c). The physically mixed Ni₆₅+Fe₃₅ catalyst did not undergo this contraction at application of 1.63 V, hence Fe seems to prohibit Ni to reach higher oxidized states. This supports the investigation in Chapter 3 with similar results of the pre-synthesized Ni₆₅Fe₃₅ catalyst,¹⁰⁸ where Fe appears to suppress or stabilize low-valent Ni centers present predominantly in the +2 oxidation state under catalytic potential (see inset in Figure 5. 4c). Stabilization of Ni⁺² atoms in the presence of Fe has recently been reported by Bates et al.¹⁰⁶ As observed in Chapter 3, a stabilization of Ni⁺² in relation to the increased OER activity is also valid for the physically mixed Ni+Fe(OOH) catalysts. Based on that work, this observation was justified by a discussion regarding a change in the equilibrium species present during OER, where an enhanced OER rate (*k*_{OER}) in relation to the metal oxidation step (*k*_{OX}) may explain the increased fraction of low-valent Ni centers in highly active Ni-Fe catalysts.¹³¹ Inspection of the Fe *K*-edge of the physically mixed Ni₆₅+Fe₃₅ catalyst showed that Fe atoms remained in oxidation state +3 at catalytic potential (see Figure 5. 4(b) and (d)), which is in agreement with the results of the pre-synthesized Ni-Fe catalysts.^{80,173}

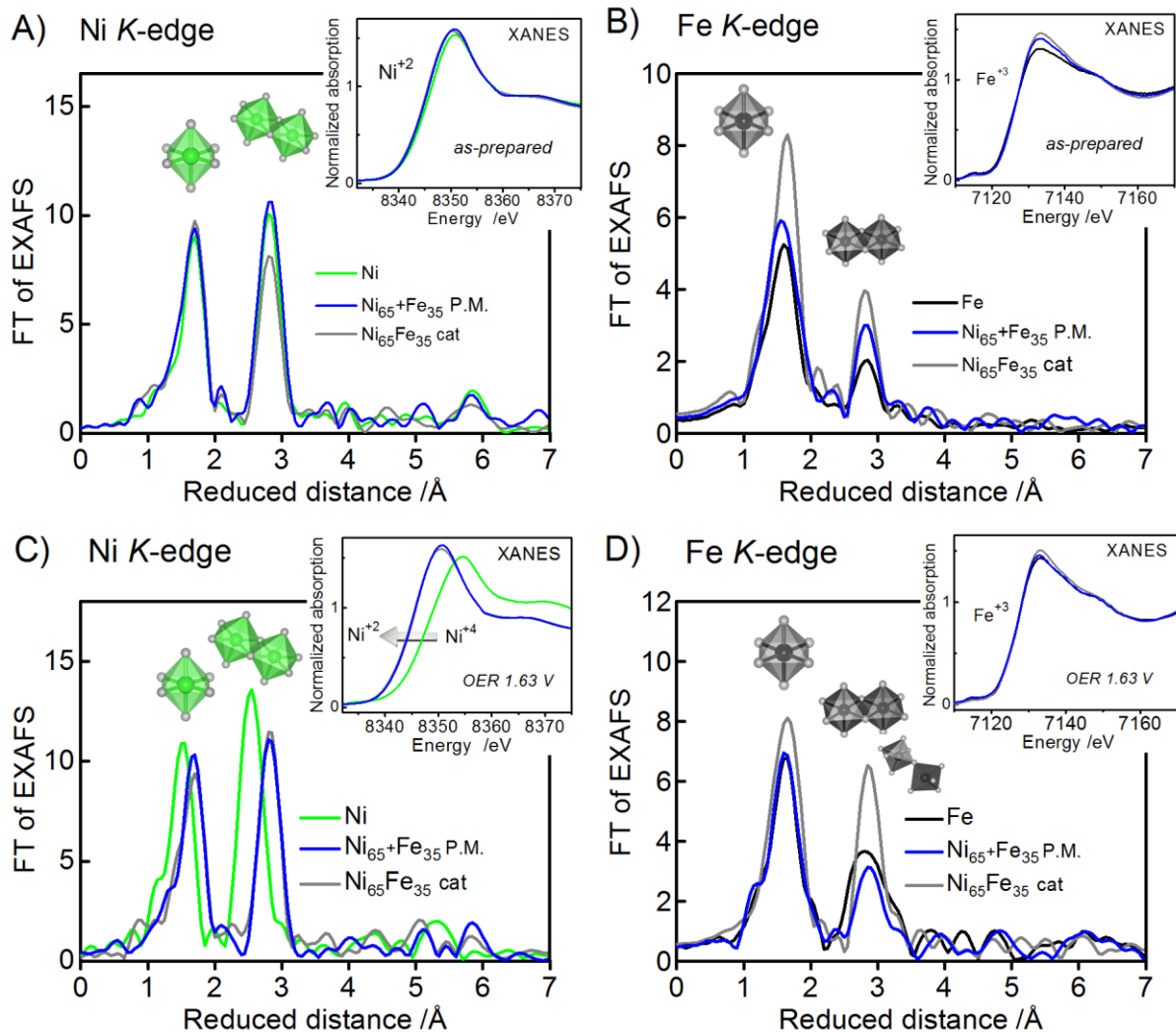


Figure 5. 4. k^3 -weighted Fourier transformed EXAFS (FT-EXAFS) of physically mixed Ni₆₅+Fe₃₅ catalyst under non-catalytic potential (as-prepared) at the **(a)** Ni K-edge **(b)** Fe K-edge. After application of 1.63 V for 30 min in 0.1 M KOH at the **(c)** Ni K-edge and **(d)** Fe K-edge. Shown are the parental Ni(OH)₂ catalyst (*green* curve), and the parental FeOOH catalyst (*black* curve), the pre-synthesized Ni₆₅Fe₃₅ catalyst (*grey* curve), and the physically mixed Ni₆₅+Fe₃₅ catalyst (*blue* curve). The catalyst composition (Ni_{100-x}Fe_x) is given as at. %.

Table 5.1. Fit parameters for quasi- in situ XAS measurements at the Ni and Fe *K*-edges at a catalytic potential of 1.63V_{RHE}, of the Ni₆₅+Fe₃₅ physical mixture (P.M.), the Ni₆₅Fe₃₅ catalyst, and the parental Ni(OH)₂ and FeOOH catalysts. Measurements were carried out in 0.1 M KOH.

Catalyst	R(M-O) /Å	CN	R(M-O) /Å	CN	Ox. state
Ni <i>K</i>-edge 1.63 V					
Ni	1.87 ± 0.01	5.2 ± 0.4	2.82 ± 0.01	5.9 ± 0.4	4 (3.7)
Ni ₆₅ + Fe ₃₅ P.M.	2.04 ± 0.01	6.3 ± 0.5	3.08 ± 0.01	7.1 ± 0.7	2
Ni ₆₅ Fe ₃₅ cat	2.04 ± 0.01	6.4 ± 0.5	3.08 ± 0.01	6.3 ± 0.7	2
Fe <i>K</i>-edge 1.63 V					
Fe	2.00 ± 0.01	3.7 ± 0.4	3.04 ± 0.02	3.4 ± 0.4	3
Ni ₆₅ + Fe ₃₅ P.M.	2.00 ± 0.01	4.0 ± 0.3	3.10 ± 0.02	2.3 ± 0.5	3
Ni ₆₅ Fe ₃₅ cat	2.01 ± 0.01	4.8 ± 0.3	3.11 ± 0.01	4.1 ± 0.4	3

Parameters were obtained from fitting in the *k*-range of 2.6-12.5 Å⁻¹ for the Fe *K*-edge and 2.6-14.5 Å⁻¹ for the Ni *K*-edge. Errors were estimated at 68 % confidence interval. Complete fit parameters and estimation of oxidation states are listed in Tables S5.2-S5.3

According to the Fe FT-EXAFS amplitudes, we noticed that the structural order of the physically mixed Ni₆₅+Fe₃₅ catalyst was lower in comparison to the FeOOH and the Ni₆₅Fe₃₅ catalyst, which suggests that Fe was only partly incorporated into the Ni(OH)₂/OOH lattice under catalytic potential. Fit parameters are listed in Table 5.1 and in Supporting Information Table S5.2-S5.3.

As suggested from XAS at the Fe *K*-edge, only a fraction of Fe seems likely to be incorporated into the Ni lattice in the physically mixed Ni+Fe(OOH) catalysts. A small fractional loss of Fe was observed in accordance with the TXRF and SEM-EDX analysis presented in previous sections (see also Figure 5.2). What then can serve as explanation of the very similar OER activities of physically mixed Ni+Fe and pre-synthesized Ni-Fe catalysts? High OER activity solely through physical contact between separate phases of NiOOH and FeOOH phases are not particularly likely however could not be ruled out in this study. The absence of a Ni *K*-edge shift in the physically mixed Ni₆₅+Fe₃₅ catalyst clearly demonstrates the effect

between Fe on Ni, also visible also in the electrochemical CV as a lower number of electrons contained within the redox wave. Our study hence supports that only a fraction of the total Fe sites are likely to contribute to the high catalytic activity. It is difficult to judge how much of the Fe that is incorporated, and therefore it is not clear how large the contribution to the high OER current from the incorporated Fe or from the physical contact may be. Based on the large effect that we see on the $\text{Ni}^{+2/+3}$ redox peak in the CV upon incorporation of Fe, we assume that there is likely a “electronic coupling” between Ni and Fe sites. In order to find out how much of the material that is actually contributing to the catalytic current, it would be necessary to deduce the electrocatalytic surface area (number of sites) contributing to the current at low overpotentials.

Our study have presented an alternative view of a less explored depth in the study of the synergism between Ni and Fe centers. We have also demonstrated a simple concept where highly active Ni+Fe electrocatalysts can be prepared simply by physically mixing the less catalytically active $\text{Ni}(\text{OH})_2$ and FeOOH parental catalyts.

5.3. Conclusions

High oxygen evolution activity was achieved by physically mixing less active $\text{Ni}(\text{OH})_2$ and FeOOH parental electrocatalysts that had been synthesized individually by solvothermal synthesis. A series of physically mixed Ni+Fe electrocatalysts showed similar trends as the pre-synthesized Ni-Fe catalyts prepared from “one-pot” synthesis.

SEM-EDX elemental mapping showed that Ni and Fe were similarly distributed over the electrode, however no conclusions regarding the atomic level of mixing of Ni and could be made. After application of 1.63 V for 30 min in 0.1 M KOH did not result in an obvious change in the metal distribution or composition. The composition derived from the EDX elemental analysis showed an indication of a fractional loss of $\sim 7\%$ Fe. TXRF analysis also confirmed a loss of Fe during exposure to catalytic potentials, which was larger Fe content. On the contrary, the associated losses of Ni was small.

Quasi-in situ X-ray absorption spectroscopy at the Ni and Fe K-edges under catalytic potential showed that physically mixing $\text{Ni}(\text{OH})_2$ and FeOOH catalyts resulted in suppression of the oxidation state change and a large fraction of Ni in oxidation +2. The OER active state could be described as $\text{Ni}^{+2}+\text{Fe}^{+3}(\text{OOH})$. The absence of a Ni K-edge shift in the presence of FeOOH confirmed s stabilization of low-valent Ni^{+2} centers. This suggests an interaction between $\text{Ni}(\text{OH})_2$ and FeOOH sites, which on the other hand is a prerequisite for the observed increased catalytic activity.

The height of the Fe FT-EXAFS amplitudes in the physically mixed Ni₆₅+Fe₃₅ catalyst suggested that only a fraction of Fe was incorporated in the Ni(OH)₂ lattice. Partly incorporated Fe could be confirmed, however determination of the exact fraction was challenging. With respect to the catalytic current, the size of the redox peak, there is obviously an effect of Fe, which likely stems from a small number of surface-confined active sites. It would however be desirable to determine the electrocatalytic surface area in order to draw conclusions about the fraction of active sites contributing to the catalytic current at low overpotentials.

Our study clearly demonstrates that highly active OER electrocatalysts can be prepared simply by mixing Ni(OH)₂ and FeOOH parental catalysts.

Supporting Information

Formation of a highly active Ni-Fe water oxidation catalyst by physically mixing Ni and Fe oxyhydroxides

This Supporting Information is based on unpublished data

Mikaela Görlin¹, Petko Chernev², Peter Strasser¹, Holger Dau²

Contact: pstrasser@tu-berlin.de

¹ *Technical University of Berlin, Chemical Engineering, Straße des 17. Juni 124, 10623, Berlin, Germany*

² *Free University of Berlin, Department of Physics, Arnimallee 14, 14195 Berlin, Germany*

5.2.1. Electrochemical characterization

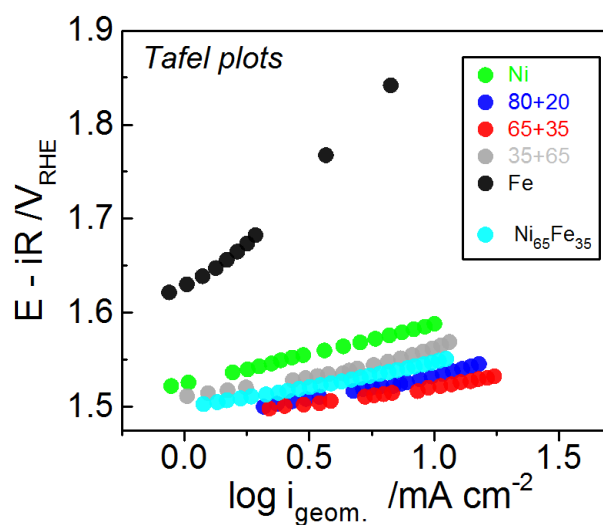


Figure S5.1. Tafel plots for physically mixed Ni+Fe(OOH) catalysts at different compositions. The slopes were extracted from quasi-stationary state measurements after conditioning at $1.63V_{RHE}$ for 30 min. Table S5.1 shows the Tafel slopes extracted by linear fit of the presented Tafel plots. The Fe-catalyst show clearly two different Tafel regions. All measurements were carried out in 0.1 M KOH.

Table S5.1. Tafel slopes of physically mixed Ni+Fe(OOH) catalysts

Catalyst [at. %]	Tafel slope [mV dec ⁻¹]
Ni	58 ± 4
Ni ₈₀ +Fe ₂₀	44 ± 3
Ni ₆₅ +Fe ₃₅	37 ± 1
Ni ₃₅ +Fe ₆₅	49 ± 4
Fe (1 st)	65 ± 20
Fe (2 nd)	280 ± 100

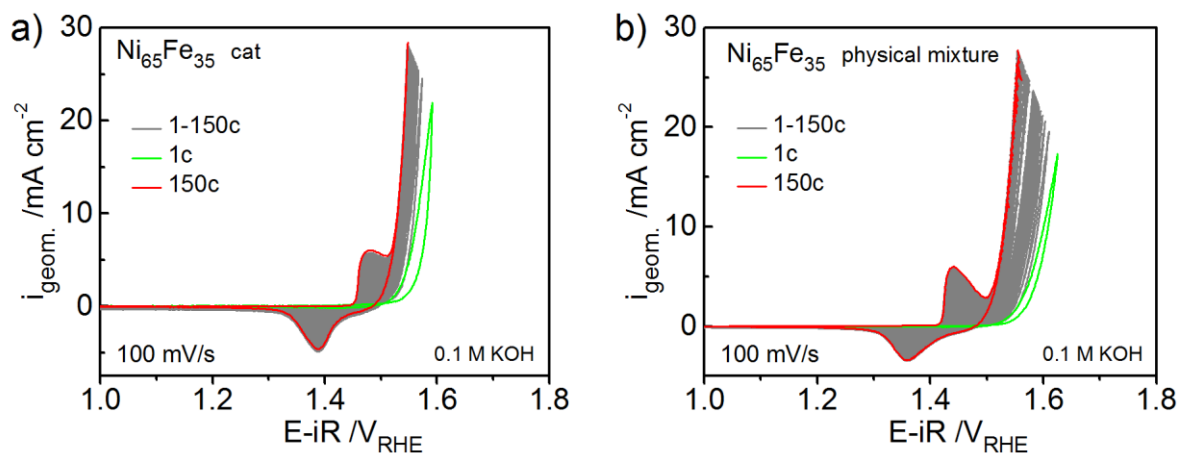


Figure S5.2. CVs cycles 1-150 of **a)** $\text{Ni}_{65}\text{Fe}_{35}$ pre-synthesized catalyst and **b)** physically mixed $\text{Ni}_{65}+\text{Fe}_{35}$ catalyst prepared by mixing the parental $\text{Ni}(\text{OH})_2$ and FeOOH catalysts post synthesis.

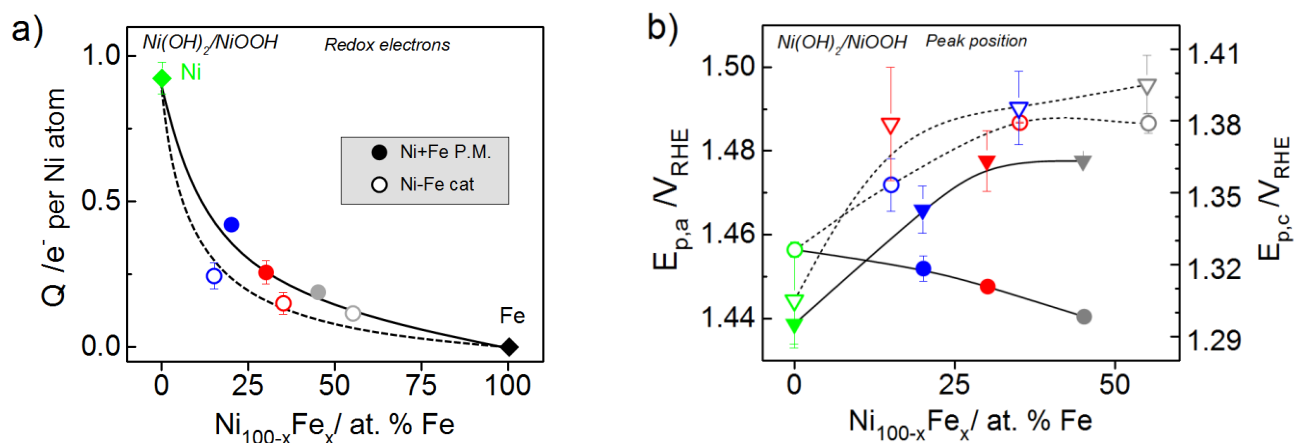


Figure S5.3. The $\text{Ni}(\text{OH})_2/\text{NiOOH}$ redox peak as a function of catalyst composition. **(a)** Number of electrons transferred per number of Ni atoms obtained by integration of the redox peak from CVs of physically mixed Ni+Fe catalysts (*filled circles*) and of pre-synthesized Ni-Fe catalysts (*open circles*). **(b)** Anodic peak position ($E_{p,a}$) (*circles*) and cathodic peak position ($E_{p,c}$) (*triangles*) of physically mixed Ni+Fe catalysts (*filled symbols*) and pre-synthesized Ni-Fe catalysts (*open symbols*). The lines are added as guideline to facilitate visualization.

5.2.3. X-ray absorption spectroscopy

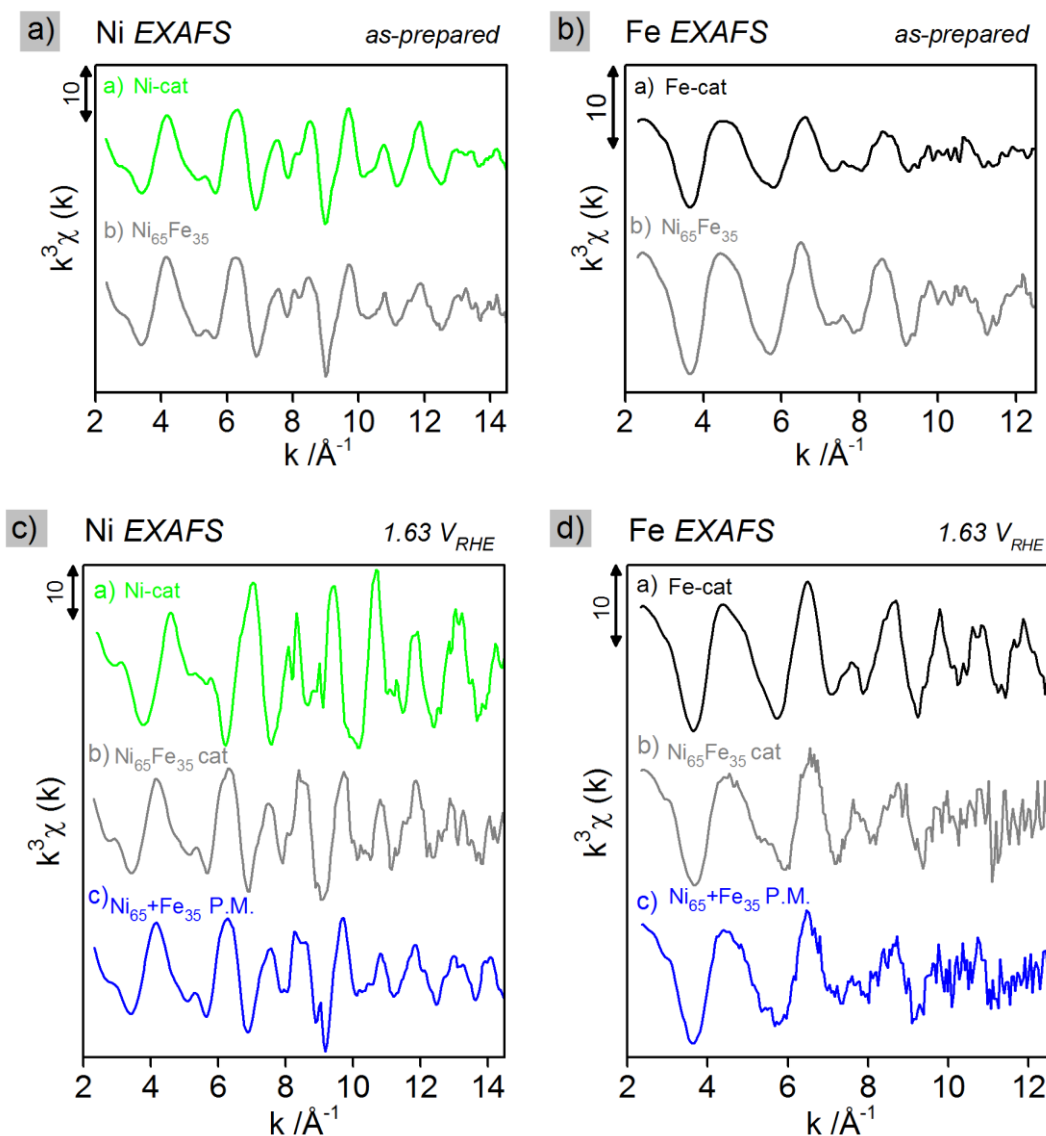


Figure S5.4. Extended X-ray absorption fine structure (EXAFS) at the (a) Ni K-edge of as-prepared catalysts (b) Fe K-edge of as-prepared catalysts (c) Ni K-edge of catalysts freeze quenched at 1.63 V in 0.1 M KOH. (d) Fe K-edge of catalysts freeze quenched at 1.63 V in 0.1 M KOH. Presented catalysts are the parental Ni(OH)₂ catalyst (green), the parental FeOOH catalyst (black), the pre-synthesized Ni₆₅Fe₃₅ catalyst (gray), and the physically mixed Ni₆₅+Fe₃₅ catalyst (blue). The catalyst composition (Ni_{100-x}Fe_x) is indicated as at. %.

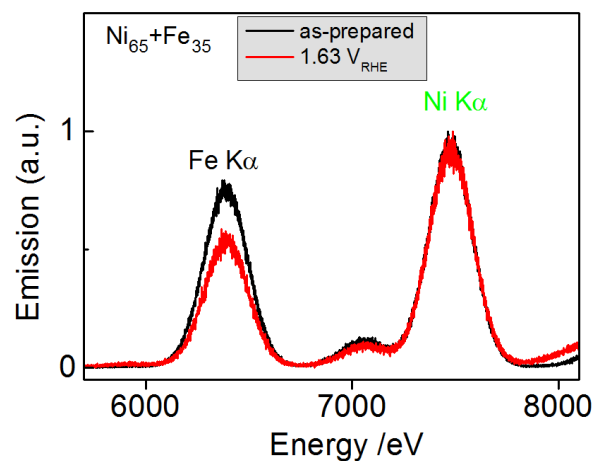


Figure S5.5. Emission spectra of the physically mixed $\text{Ni}_{65}+\text{Fe}_{35}$ catalyst recorded in the beamline setup prior to the XAS measurements; the as-prepared state (*black curve*) and of the catalyst freeze quenched after conditioning at 1.63 V for 30 min in 0.1 M KOH (*red curve*). Note that the intensities of the Ni and Fe $\text{K}\alpha$ peaks have not been weighted against its individual extinction coefficients.

Table S5.2. Fitted parameters at the Ni and Fe *K*-edges of the parental Ni(OH)₂ and FeOOH catalysts, the physically mixed Ni₆₅+Fe₃₅ catalyst, and the pre-synthesized Ni₆₅Fe₃₅ catalyst. Only the first two shells were taken into account.

Catalyst	R(M-O) /Å	CN	R(Ni-M) /Å	CN	R _f
Ni as-prepared					
Ni	2.04 ± 0.01	5.2 ± 0.4	3.08 ± 0.01	5.4 ± 0.7	16.7
Ni ₆₅ Fe ₃₅ cat	2.04 ± 0.01	6.2 ± 0.5	3.08 ± 0.01	5.2 ± 0.8	21.0
Fe as-prepared					
Fe	1.98 ± 0.02	3.0 ± 0.3	3.08 ± 0.03	1.7 ± 0.4	26.3
Ni ₆₅ Fe ₃₅ cat	2.00 ± 0.01	4.7 ± 0.3	3.10 ± 0.01	2.3 ± 0.4	27.0
Ni 1.63 V_{RHE}					
Ni	1.87 ± 0.01	5.2 ± 0.4	2.82 ± 0.01	5.9 ± 0.4	21.9
Ni ₆₅ + Fe ₃₅ P.M.	2.04 ± 0.01	6.3 ± 0.5	3.08 ± 0.01	7.1 ± 0.7	20.8
Ni ₆₅ Fe ₃₅	2.04 ± 0.01	6.4 ± 0.5	3.08 ± 0.01	6.3 ± 0.7	24.4
Fe 1.63 V_{RHE}					
Fe	2.00 ± 0.01	3.7 ± 0.4	3.04 ± 0.02	3.4 ± 0.4	26.0
Ni ₆₅ + Fe ₃₅ P.M.	2.00 ± 0.01	4.0 ± 0.3	3.10 ± 0.02	2.3 ± 0.5	29.7
Ni ₆₅ Fe ₃₅ cat	2.01 ± 0.01	4.8 ± 0.3	3.11 ± 0.01	4.1 ± 0.4	23.9

Fitting at the Fe *K*-edge was carried out in a *k*-range of 2.6-12.5 Å⁻¹ and at the Ni *K*-edge 2.6-14.5 Å⁻¹. Errors were estimated from a 68 % confidence interval. The atomic ratios are given as subscripts, estimated by TXRF analysis.

Table S5.3. Extracted edge positions and metal oxidation states, compared to oxidation states estimated from the M-O coordination distances presented in Tables S5.1-S5.2.

Catalyst	Edge position /eV	Ox. state edge pos.	Ox. state d(M-O)
Ni as-prepared			
Ni	8342.8	2.2	2.1
Ni ₆₅ Fe ₃₅ cat	8342.6	2.1	2.1
Fe as-prepared			
Fe-cat	7124.4	3.0	3.5
Ni ₆₅ Fe ₃₅ cat	7124.7	3.1	3.3
Ni 1.63 V_{RHE}			
Ni-cat	8345.9	4.0	3.7
Ni ₆₅ ⁺ Fe ₃₅ P.M.	8342.5	2.1	2.1
Ni ₆₅ Fe ₃₅ cat	8342.6	2.1	2.1
Fe 1.63 V_{RHE}			
Fe-cat	7124.9	3.1	3.4
Ni ₆₅ ⁺ Fe ₃₅ P.M.	7124.7	3.0	3.4
Ni ₆₅ Fe ₃₅ cat	7124.7	3.1	3.2

The oxidation states were extracted from calibration curves from reference compounds from Ref ^{80,130}. The edge positions were extracted using the half integral method ¹⁷¹.

Chapter 6

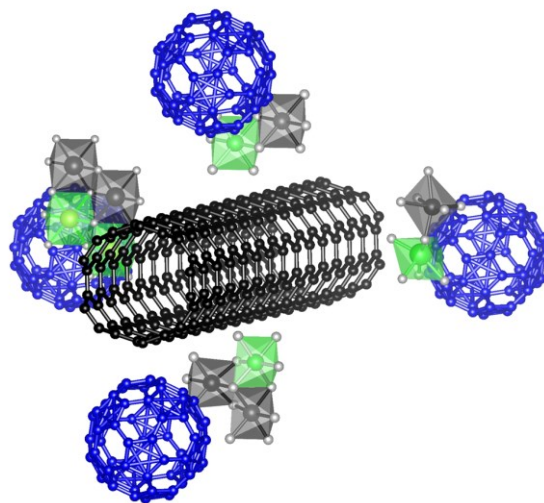
The influence of carbon support on the oxygen evolution activity in amorphous Ni-Fe electrocatalysts

Parts of this Chapter has been reprinted or adapted with permission from the American Chemical Society, as part of a published Journal article.

(Görlin, M.; Ferreira de Araújo, J.; Schmies, H.; Bernsmeier, D.; Dresp, S.; Glich, M.; Jusys, Z.; Chernev, P.; Kraehnert, R.; Dau, H.; Strasser, P. Tracking Catalyst Redox States and Reaction Dynamics in Ni–Fe Oxyhydroxide Oxygen Evolution Reaction Electrocatalysts: The Role of Catalyst Support and Electrolyte pH, *Journal of the American Chemical Society*, 2017, 139, 2070.)

DOI: 10.1021/jacs.6b12250

URL: <http://dx.doi.org/10.1021/jacs.6b12250>



Mikaela Görlin¹, Jorge Ferreira de Araújo¹, Henrike Schmies¹, Denis Bernsmeier¹, Sören Dresp¹, Manuel Glich¹, Zenonas Jusys³, Petko Chernev², Ralph Krähnert¹, Holger Dau², Peter Strasser¹

¹Department of Chemistry, Chemical Engineering Division, Technical University of Berlin, Straße des 17. June 124, 10623, Berlin, Germany

²Department of Physics, Free University of Berlin, Arnimallee 14, 14195 Berlin, Germany

³Institute of Surface Chemistry and Catalysis, Ulm University, Albert-Einstein-Allee 47, 89069 Ulm, Germany

Abstract

Solvothermally prepared Ni-Fe oxyhydroxides were investigated for electrocatalytic and stability for the oxygen evolution reaction (OER) in alkaline electrolyte. Selected catalysts were supported post synthesis on antimony doped tin oxide (ATO), oxidized carbon nanotubes (oxCNT), and Vulcan XC-72r (/C). We could confirm that highest activity was achieved with Vulcan XC-72r, seen as a 2-fold increase in activity compared to the unsupported catalysts. Further investigations at various compositions of Ni and Fe confirmed the influence of the electrolyte concentration as a further ~ 1.5 -fold increase in activity. The amount of redox active Ni on the electrode were deduced by integration of the $\text{Ni}^{+2} \rightarrow \text{Ni}^{+3/+4}$ redox peak. This confirmed an increase in the amount of redox active Ni as a result of carbon support, also visible at higher electrolyte pH.

Differential electrochemical mass spectrometry (DEMS) showed Faradaic efficiency in the range of ~ 80 % O_2 with no indications of formation of other volatile products. Short term stability test up to 1000 cycles and operation at 10 mA/cm^2 for 20 hours showed only small losses of the overall activity, however steady state polarization for 20 h resulted in higher increase of the overpotential compared to 1000 cycles. TEM images confirmed a change in morphology, which could attributed to a change in the carbon structure, and formation of crystallites.

X-ray absorption spectroscopy at the Ni and Fe *K*-edges of the Ni-Fe/C catalysts freeze quenched at catalytic potential showed an increased fraction of oxidized Ni atoms in the carbon supported catalysts. This directly relates the observed increased area under the $\text{Ni}^{+2/+3}$ redox peak to oxidized Ni species. On the other hand, the fraction of low-valent Ni atoms was higher also in the mixed Ni-Fe/C catalysts in comparison to the Ni/C catalyst, hence confirming the effect of Fe as a stabilization of low-valent Ni^{+2} .

We speculate that the higher fraction of oxidized Ni as an effect of carbon support either arise from a change in the electrical underlying conductivity, which might result in a faster metal oxidation rate (k_{ox}) in comparison to the OER rate (k_{OER}), or from improved dispersion of the catalysts on the carbon support with a higher fraction of electrocatalytically accessible sites.

6.1. Introduction

Mixed Ni-Fe catalysts for alkaline electrochemical water splitting have attracted attention due to their high activity^{15,69,71,77,81,87-89,107,146,195} which have made them prominent candidates for solar-water splitting applications.^{16-18,137}

The oxygen evolution reaction (OER) leading to formation of O₂ and protons is associated with high overpotential due to the involvement of 4 electrons being transferred in sequential steps. The reaction involves intermediates attributed to O*, OH*, and OOH*,⁵ however the nature of these intermediates are still under consideration.^{104,113,114,196}

Several studies have shown that Ni-Fe hydroxide catalysts deposited on a conductive support yield high current densities at low overpotentials. Gong et al. demonstrated the effect of the carbon support compared to unsupported Ni-Fe layered double hydroxide (LDH) catalysts supported on carbon nanotubes (CNTs).⁸¹ Qiu et al.⁸⁹ supported well defined amorphous Ni-Fe hydroxide nanoparticles (NPs) on Vulcan, which showed similar intrinsic activity to thin film Ni-Fe electrocatalysts investigated by Trotochaud et al.⁶⁹ Xunyu et al. deposited Ni-Fe LDH catalysts by electrodeposition on Ni-foam to form 3D structures,¹⁴⁷ demonstrating that high current densities could be achieved at low overpotentials with this approach. Xiaowen et al. showed that Ni-Fe nanoplates on graphene oxide (GO) electrodes resulted in high activities likely due to a large electrochemically active surface area.⁹¹ Ma et al. reported exfoliated Ni-Fe nanosheets on graphene oxide that showed high current densities.¹⁸⁵

Fundamental understanding of the origin of high OER activity in mixed Ni-Fe (oxyhydr)oxides have been addressed using in situ based techniques. X-ray absorption spectroscopy (XAS) have revealed that the oxidation state of Ni usually involves Ni atoms in an oxidized state close to +4 during OER catalysis.^{80,106,139} The result of Fe incorporation in mixed Ni-Fe oxyhydroxide catalysts have been demonstrated as a stabilization of Ni atoms in its low-valent Ni⁺² state,¹⁰⁶ opposing the classical Bode scheme of Ni-based electrodes. A hypothesis put forward by our work our group to explain the detection of low-valent Ni⁺² atoms during catalytic potential, included that Fe is likely to affect the rate constants associated with the OER cycle, leading to an accumulation of oxidized Ni⁺⁴ if the metal oxidation rate constant (k_{Mox}) exceeds that of the oxygen evolution reaction (k_{OER}).¹⁰⁸

The reported oxidation state of Fe during OER catalytic conditions have also been under debate, where both Fe⁺⁴ and Fe⁺³ have been proposed.^{80,103} Clear evidence of Fe⁺⁴ present at applied catalytic potential above 1.62 V potential was shown by Chen et al. using operando Mössbauer spectroscopy,¹⁰³ estimated to 12 % of the total Fe-content and increasing up to 21 % by further increasing the potential to 1.76 V.

Arguments were put forward that the Fe^{+4} was not directly related to the catalytic OER activity because of a slow relaxation step of the oxidized Fe^{+4} back to Fe^{+3} .

The strong pH dependence was recently investigated using Surface Enhanced Raman Spectroscopy (SERS), which showed that intermediates with superoxo character were likely to form during OER in Ni oxyhydroxide catalysts.¹¹⁴ This was proposed as a possible explanation for the strong pH dependence of the OER activity.

In this study, we compare Ni-Fe oxyhydroxide electrocatalysts supported on different catalyst supports. We address the influence of the support in order to highlight important fundamental aspects and for practical applications. We demonstrate how varying simple parameters can affect the intrinsic properties of the catalyst.

6.2. Results & Discussion

6.2.1. A comparison of different supports

Mixed Ni-Fe oxyhydroxide electrocatalysts with different compositions of Ni and Fe were synthesized according to a solvothermal method.^{100,131} Supported catalysts were prepared by immobilizing the unsupported catalysts post synthesis on either Vulcan XC-72r(/C), oxidized carbon nanotubes (oxCNT), or Antimony doped tin oxide (ATO).

Mixed Ni-Fe catalysts showed a high catalytic activity for the oxygen evolution reaction (OER) (Figure 6.1a). The carbon supported Ni₅₀Fe₅₀/C catalyst showed an overall higher activity compared to unsupported catalysts, where Ni-Fe on ATO support showed lowest activity. Elemental analysis showed that the catalyst loading was low on the ATO support, which is also a reasonable explanation for the low activity. Increasing the loading further did not increase the activity significantly on the ATO support. This may be due to the thicker catalyst layer on the electrode.

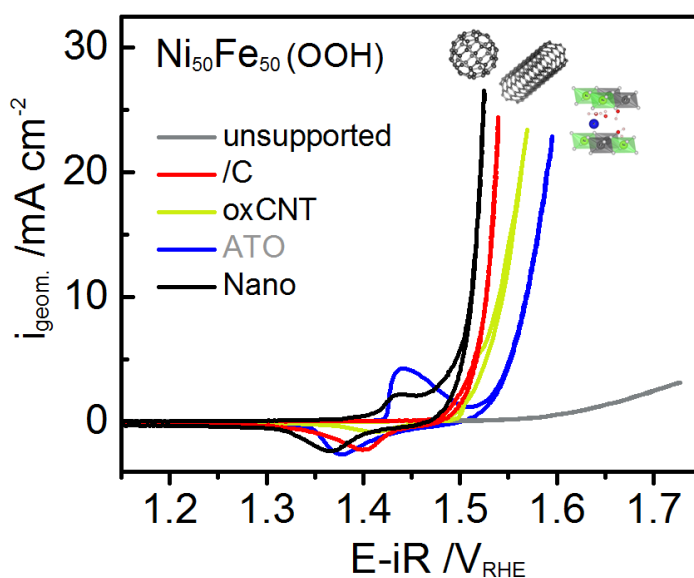


Figure 6.1. Cyclic voltammograms (CVs) of Ni-Fe(OOH) catalyst supported on different catalyst supports, unsupported (*yellow*), Vulcan XC-72r (*black*), oxidized CNTs (*red*), and ATO (*gray*). Catalyst composition, Ni_{100-x}Fe_x, is reported as mol % Fe. The measurements were recorded at 50 mV/s at 1600 rpm in 0.1M KOH.

The Ni-Fe catalyst supported on carbon nanotubes had higher activity than the unsupported catalysts, however the CVs showed a longer activation period before a stable CV was reached. This indicates an ongoing change in the Ni-Fe/oxCNTs sample. A spherically shaped Ni-FeOOH nanoparticle catalyst with a nanoparticle size of 20 nm was in addition investigated (Ni-Fe/Nano). The shape was induced by additions of surfactants during the synthesis, and as a result the Ni:Fe composition was close to 90:10.

The Ni₉₀Fe₁₀/Nano catalyst showed a lower activity than the unsupported Ni₅₀Fe₅₀ catalyst. The activity was however comparable to that of the Ni₉₀Fe₁₀ catalysts investigated in Chapter 3 with similar composition. Therefore, no conclusions could be drawn regarding the possible size effect at a defined electrocatalytic active surface area before further investigations would be needed.

TEM images of the unsupported and supported catalysts also indicated that the carbon nanotubes not appeared to have a good distribution on the nanotubes (Figure 6.2), which could suggest a lower carbon-nanoparticle interaction. To optimize the contact between the catalyst and the carbon support a preparation method such as “one-pot” synthesis demonstrated by Gong et al.⁸¹ could be applied. The morphology of the unsupported Ni₅₀Fe₅₀ and Ni₅₀Fe₅₀/C catalysts were similar to the previous morphologies in Chapter 3,¹³¹ and 4.¹⁰⁰ The catalyst in the Ni₅₀Fe₅₀/ATO sample was not visible, which could be due to the low metal loading according to ICP-OES analysis. The XRD of the Ni-Fe catalysts showed that the unsupported Ni₅₀Fe₅₀, Ni₅₀Fe₅₀/C, Ni₅₀Fe₅₀/oxCNT and Ni₅₀Fe₅₀/Nano were of amorphous character whereas the Ni₅₀Fe₅₀/ATO sample no catalyst reflections were observed (Figure S6.1a). This confirmed the amorphous structure as reported earlier for mixed Ni-Fe oxyhydroxide electrocatalysts.^{72,89} Reflections at 34° and 42° matched well with the (1 0 1) and (1 1 0) reflections of (turbostratic) α -Ni(OH)₂, which was investigated in Chapter 3 using X-ray absorption spectroscopy.¹³¹ Reflections from the interlayer distance at 15-25° was not observed for the carbon supported catalysts due to overlap with the (1 0 0) and (0 0 2) carbon reflections. The Ni₉₀Fe₁₀/Nano catalyst had slightly sharper reflections than Ni₅₀Fe₅₀ catalyst, which might also be due to the higher Ni content which has been clearly shown to result in sharper XRD reflections in Chapter 3¹³¹ and also demonstrated by Qiu et al.⁸⁹

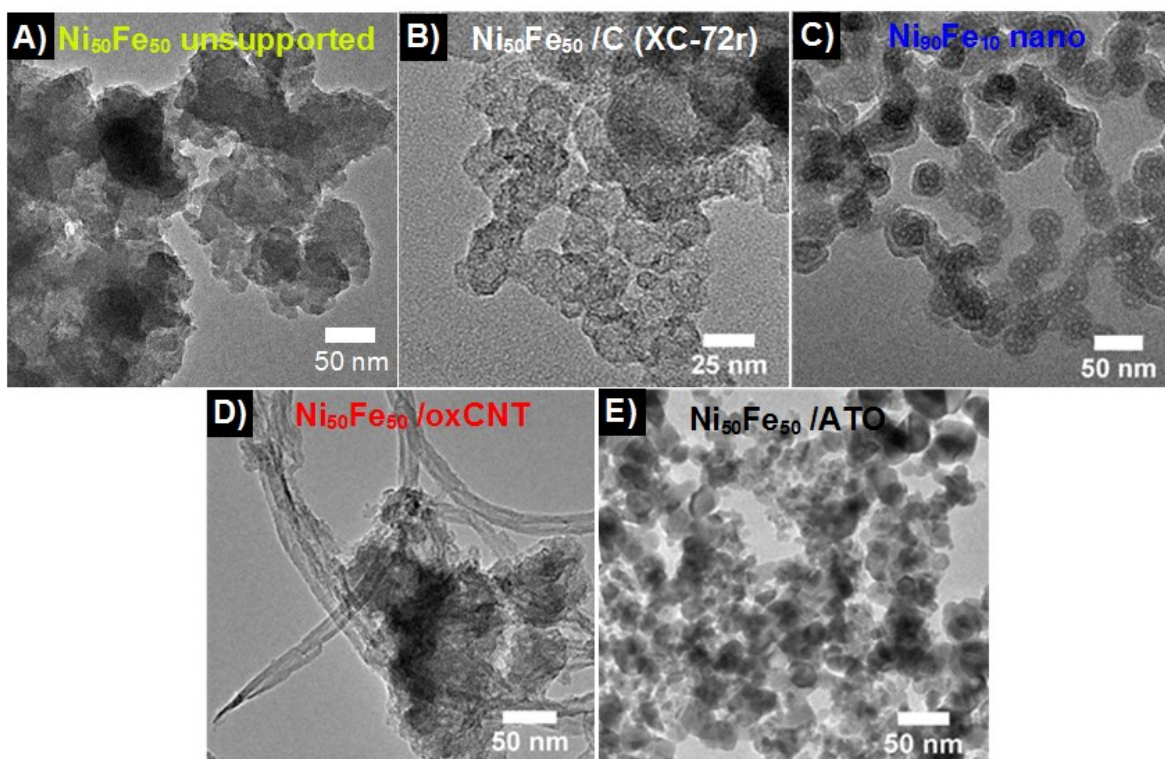


Figure 6.2. Transmission electron micrographs (TEM) images of mixed Ni-Fe(OOH) catalysts supported on different catalyst supports (a) unsupported $\text{Ni}_{50}\text{Fe}_{50}$ (b) $\text{Ni}_{50}\text{Fe}_{50}/\text{C}$ (c) $\text{Ni}_{50}\text{Fe}_{50}/\text{Nano}$ (d) $\text{Ni}_{50}\text{Fe}_{50}/\text{oxCNT}$ (e) $\text{Ni}_{50}\text{Fe}_{50}/\text{ATO}$.

6.2.2. The influence of carbon support

In previous section, we demonstrated that the OER activity increases when a catalyst support is employed. Amongst a comparison of carbon and oxide supports, we found that the carbon supports yielded higher activity, especially Vulcan XC72-r. We therefore applied Vulcan XC-72r as catalyst support for a more extensive comparison between carbon supported and unsupported catalysts with various Ni:Fe compositions.

The carbon support was seen as a 2-fold increase in the catalytic OER activity (Figure 6.4b). Whether this increase is due to an increase in the electrochemically accessible surface area or due other effects, we will further investigate. By increasing the molarity to 1 M KOH, an additional 1.5-fold increase in the OER activity was observed (Figure 6.4b). The lower limit turnover frequency based on total metal loading of

Ni and Fe ($\text{TOF}_{\text{Ni+Fe}}$) from ICP-OES measurements was estimated from CVs at a sweep-rate of 2 mV/s. These were on the other hand in good agreement with quasi-stationary state measurements (see Figure S6.2). The $\text{TOF}_{\text{Ni+Fe}}$ for the $\text{Ni}_{45}\text{Fe}_{55}$ and Fe $\text{Ni}_{45}\text{Fe}_{55}/\text{C}$ catalysts were estimated to 0.10 and 0.20 s^{-1} in 0.1 M KOH. The comparative TOFs estimated the “classical way” by integration of the area under the $\text{Ni}(\text{OH})_2/\text{NiOOH}$ redox peak yielded higher $\text{TOF}_{\text{Q,Ni}}$ of 0.67 and 0.78 s^{-1} , respectively. In 1 M KOH, the $\text{TOF}_{\text{Ni+Fe}}$ were estimated to 0.13 and 0.30 s^{-1} and the $\text{TOF}_{\text{Q,Ni}}$ to 1.45 and 1.82 s^{-1} , respectively (Figure 1c). These are amongst the high range of reported intrinsic catalytic activity up to date for mixed Ni-Fe electrocatalysts.¹⁵ Increasing the electrolyte molarity from 0.1 M to 1 M KOH also shifted the activity top towards higher Ni-contents (Figure 6.4b). It is not clear what this exactly means, however based on earlier findings about pH – OER dependence and binding energies of OER intermediates,^{80,114} it is plausible that differences in the oxide surfaces shows up as a differences in the OER activity as a function of pH when changing the catalyst composition.

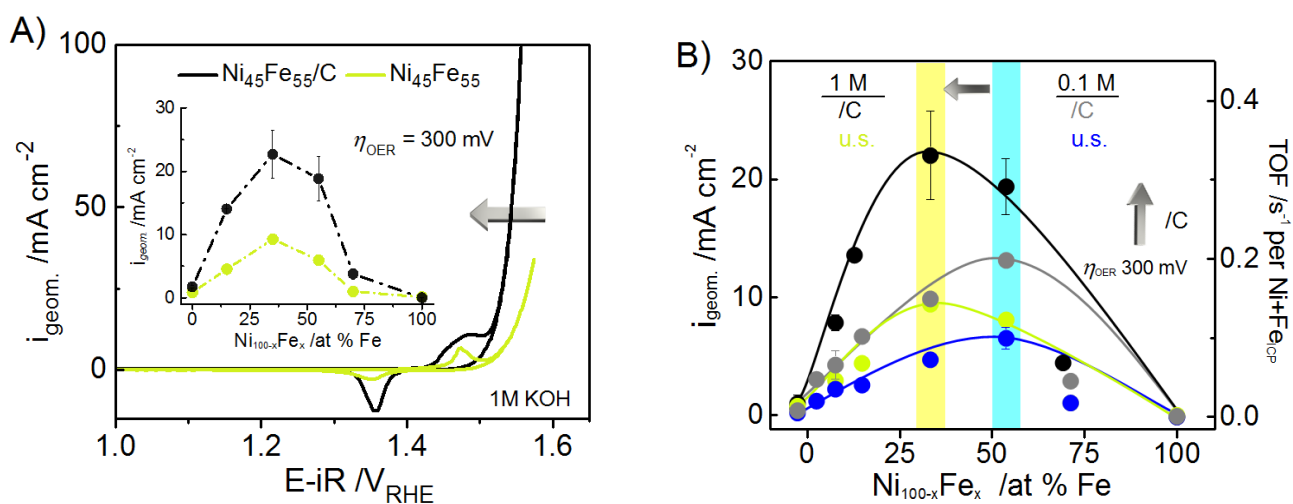


Figure 6.3. (a) Cyclic voltammograms (CVs) of unsupported Ni-Fe and carbon supported Ni-Fe/C oxyhydroxide catalysts in 1M KOH. The inset shows the geometric current density as a function of Fe-content estimated at a fixed geometric metal loading of 10 $\mu\text{g Ni+Fe}/\text{cm}^2$. (b) Mass based turnover frequency ($\text{TOF}_{\text{Ni+Fe}}$) as a function of Fe-content ($\text{Ni}_{100-x}\text{Fe}_x$), estimated at $\eta=300 \text{ mV}$ in 0.1 M and 1M KOH. *This Figure has been adapted with permission from ref. 194. Copyright (2017) American Chemical Society.*

It is so far unclear whether the redox charge is related to the number of active sites in mixed Ni-Fe catalysts. In Chapter 3 we established a correlation between the redox active Ni and the composition. Fe incorporation was shown to result in a suppression of the oxidation state change of Ni from +2 to +4¹³¹, also demonstrated by Bates et al.¹⁰⁶ This would suggest that the number of active sites are decreased

upon Fe-incorporation, assuming that the redox charge reflects the number catalytically accessible sites. We would therefore argue that somewhat an inverse scenario prevail. The redox active Ni atoms that undergo a detectable oxidation state change are the active sites that have lowest contribution to the catalytic OER current at low overpotentials. A correlation could therefore be achieved based on the activity and the redox active Ni species observed at the electrode. However, this will most likely reflect the number sites that has a lower turnover. The turnover frequency of the highly active Ni-Fe site yet appears difficult to perceive, also with respect to the extent that “bulk sites” contribute to the catalytic current since mass transport limitations and/or less structural rearrangements may be less optimal.

The response of the OER activity as a function of catalyst loading in mixed Ni-Fe catalysts were reported in a previous investigation of the Ni₆₅Fe₃₅/C catalyst in Chapter 4.¹⁰⁰ Measurements at different catalyst loadings ranging from 1-20 μg/cm² in 0.1 M and 1 M KOH revealed an activity top at lower loadings for the unsupported Ni₄₅Fe₅₅ catalyst compared to the carbon supported Ni₄₅Fe₅₅/C catalyst (Figure 6.4a).

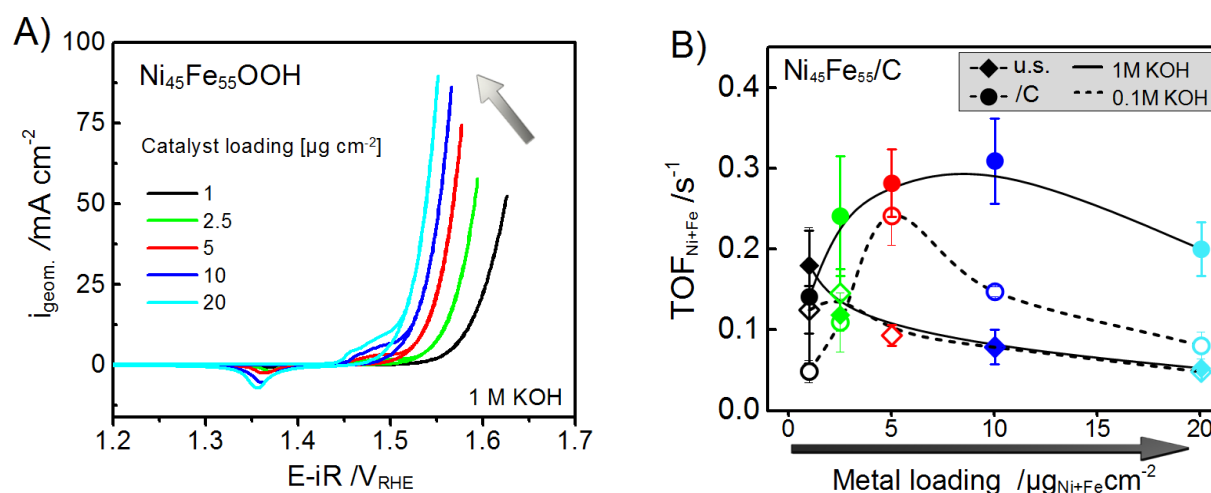


Figure 6.4. (a) CVs of Ni-Fe/C at different geometric metal loadings 1-20 μg Ni+Fe/cm² measured in 1 M KOH. (b) TOF based on the total metal as a function of metal loading for Ni₄₅Fe₅₅ and Ni₄₅Fe₅₅/C catalysts in 0.1 M and 1 M KOH. Displayed CVs in were recorded at 100 mV/s at 1600 rpm. The metal loadings were determined by ICP-OES of as-prepared catalysts. *This figure has been adapted with permission from ref. 194. Copyright (2017) American Chemical Society.*

A closer look at the integrated area under the Ni(OH)₂/NiOOH redox peak normalized to the total moles of Ni on the electrode showed that the intrinsic activity is somehow correlated to the redox active Ni on the electrode (Figure S6.3a-b). The 2-fold increase in OER activity seen as an effect of carbon support also resulted in a 2-fold increase in the oxidized Ni atoms. This could indicate that carbon support yields

more electrolyte accessible sites. It was recently shown by Batchellor et al. that pulsed electrodeposition result in a better film connectivity which shows up as an increased TOF at high catalyst loadings¹⁴⁶. It was previously shown by Trotochaud et al. that increased through film conductivity in electrodeposited Ni-Fe catalysts was correlated to the intrinsic OER activity.⁷² It therefore awakes questions if carbon support results in a higher activity due to an increased number of electrolyte accessible sites or as a cause of improved underlying electrical conductivity, or possible interactions between the support and catalyst itself.

6.2.3. The effect of electrolyte pH

In Figure 6.5, the activity of the Ni₄₅Fe₅₅ and Ni₄₅Fe₅₅/C catalysts are shown in the upper pH range (pH ~13-14) by varying the electrolyte concentration between 0.1-1 M. The measurements were carried out using a RHE reference electrode. Previous reported OER activities in mixed Ni-Fe electrocatalysts have mostly been limited to KOH electrolyte with few studies carried out in NaOH.¹⁰⁴

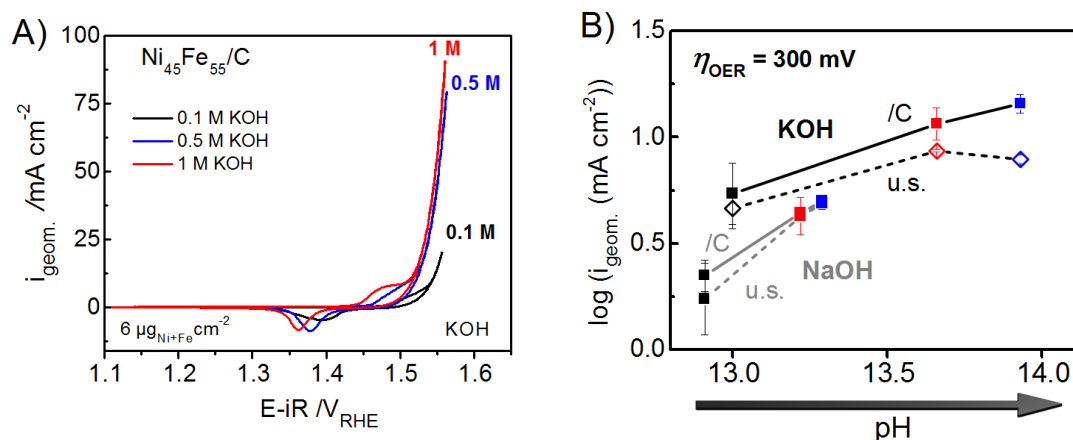


Figure 6.5. (a) CVs of Ni₄₅Fe₅₅/C in different pH obtained by varying the electrolyte concentration (b) The logarithmic current density at $\eta = 300 \text{ mV}$ as a function of electrolyte pH measured in KOH and NaOH. The measurements were carried out at a total metal loading of $\sim 6 \mu\text{g Ni+Fe/cm}^2$ determined by ICP-OES.

The OER activities showed a significant improvement by increasing the molarity from 0.1 M to 0.5 M, however increasing the molarity further did not result in significant activity increase (Figure 6.5b). The behavior in NaOH was similar to KOH, however the overall activity was consistently lower in NaOH which could be explained by a lower dissociation constant of NaOH and hence a lower effective pH. It was discussed by Klingan et al. that strong bases with a high pK_a values can act as good proton acceptor at high pH.⁶⁶ Based on the pK_a values of NaOH (pK_a 13.8) and KOH (pK_a 13.5), NaOH should be a slightly

better proton acceptor than KOH. Where the differences in activity in KOH and NaOH comes from would need further investigations in a larger pH range. The carbon supported Ni-Fe/C catalysts showed overall higher catalytic activities in comparison to the unsupported Ni-Fe catalysts in both KOH and NaOH, however a very similar pH-trend was observed. Inspection of the Ni redox peak revealed a correlation to the activity. Maximum redox charge was observed in 0.5 M KOH thus coincided with the concentration above no significant activity improvements were obtained by further increasing the electrolyte pH (Figure S6.4a). Tafel slope analysis showed similar Tafel slopes in the investigated pH range both in KOH and NaOH (Figure S6.4b-c). In the investigation presented in Chapter 3, we showed that the Ni₆₅Fe₃₅/C catalyst had a significantly lower activity in borate buffer pH 9.2 and in phosphate buffer pH 7 in comparison to KOH pH 13. This was correlated to a rapid dissolution of metals in pH 7, however in pH 9.2 there were minor losses.¹⁰⁰ Trzeźniewski et al. recently showed that active oxygen species play a pivotal role in promoting OER activity which requires pH higher than 9.2.¹⁰⁴ For our mixed Ni-Fe catalysts, we find a peak shift of ca -40 mV/pH unit on the RHE-scale for both the Ni-Fe and Ni-Fe/C catalysts in KOH and NaOH (Figure S6.5a-d). At higher Fe-content the anodic peak shift is less pronounced which might be explained by the overlap with the OER catalytic current. At higher Ni-content, it is clear that the redox peak shifts less by only ~10 mV/pH-unit for the Ni(OH)₂/OOH catalyst, see Figure S6.6a-b. The Ni catalyst was measured in Fe-free KOH purified according to the method by Trotochaud et al.⁷², however remaining Fe traces in our catalyst cannot be excluded due to a slightly higher activity than observed for complete Fe-free catalysts. Despite this, the relative peak shifts reported for the Ni(OH)₂ catalyst herein is in good agreement with the peak shifts reported by Diaz-Morales et al.¹¹⁴ In order to understand the pH dependence of the investigated catalysts, we would need further measurements.

6.2.4. BET surface area

The surface area of the carbon supported Ni-Fe/C oxyhydroxide catalysts were investigated using the BET N₂ adsorption isotherm (Figure 6.6). Independent of Ni:Fe composition, there was a low extent of mesoporosity in the mixed Ni-Fe/C catalysts, and some degree of microporosity. The surface area of the Vulcan XC-72r support without catalyst was 187 m²/g. The BET of Ni₄₅Fe₄₅/C catalyst was 182 m²/g, whereas the unsupported Ni₄₅Fe₄₅ catalyst had a surface area of 27 m²/g, which is similar to previous reports.⁷⁷

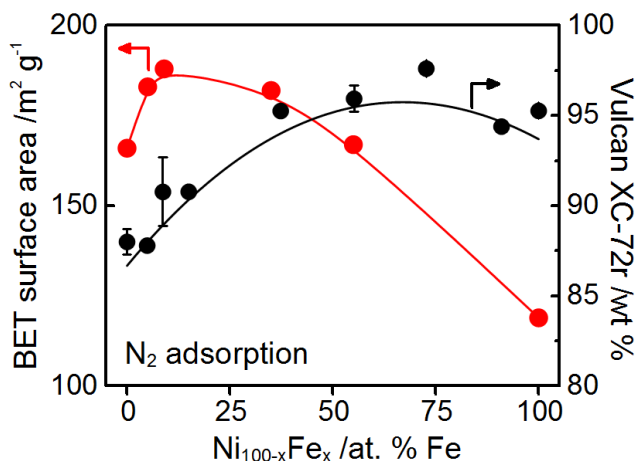


Figure 6.6. BET surface area obtained from N₂ adsorption isotherm for Ni_{100-x}Fe_x/C electrocatalysts with varying composition. The right axis shows the wt % of carbon content estimated by ICP-OES. The error bars are given as standard errors. This figure has been adapted with permission from ref. 194. Copyright (2017) American Chemical Society.

How much of the surface area that is influenced by the carbon support is not entirely clear. The tendency of a slightly higher BET surface area towards higher Ni-content is larger than the variation of the variation of carbon support ($\sim 90 \pm 6$ wt %). According to the XRD shown in Figure S6.1, increased Fe-content yields a larger amorphicity, which was also correlated to a lower local atomic degree of order around the metal center in Chapter 3,¹⁰⁸ where we also identified the FeOOH morphology as small nanoparticles < 10 nm in size. Due to agglomeration, larger particles of ~ 500 nm were also observed. This could provide an explanation why FeOOH has a low surface area in comparison with Ni(OH)₂. In a recent study of non-precious metal catalysts (Me-N-C) for the oxygen reduction reaction (ORR) by Ranjbar et al., it was shown that the ORR activity was strongly correlated to the adsorbed CO to a specific site.¹⁹⁷ Our results suggest that there is no direct correlation between BET surface area in the mixed Ni-Fe oxyhydroxides investigated here. Ni(OH)₂ has higher crystallinity according to XRD and XAS measurements, and should therefore have the lowest surface area which is contradicting to our measured surface N₂ adsorption isotherms. Therefore, we may argue that the higher surface area towards higher Ni-content favor OER activity in terms of a possible correlation to an increased number of electrolyte accessible sites.

6.2.5. Short-term stability up to 1000 c

The stability and OER performance of the Ni₄₅Fe₅₅ and Ni₄₅Fe₅₅/C electrocatalysts were investigated after 1000 cycles in 0.1 M KOH, by cycling between ~ 1 -1.75 V_{RHE} (Figure 6.7a-b). The catalysts showed

excellent stability with only a slight increase in the overpotential after 1000 cycles. The $\text{Ni}_{45}\text{Fe}_{55}$ catalyst showed a 3.5 mV increase and the $\text{Ni}_{45}\text{Fe}_{55}/\text{C}$ catalyst a 8 mV increase (see insets in Figure 6.7a-b). Chronopotentiometric curves recorded at $10 \text{ mA}/\text{cm}^2$ showed a $\sim 30 \text{ mV}$ increase in overpotential for both Ni-Fe and Ni-Fe/C catalysts after 20 h of constant operation (Figure 6.7c). A reasonable explanation for the difference is that a higher stress are introduced at constant oxygen evolution conditions in comparison to CV cycling. The carbon support did not improve the durability of the mixed Ni-Fe oxyhydroxide catalysts except for a reduced overpotential.

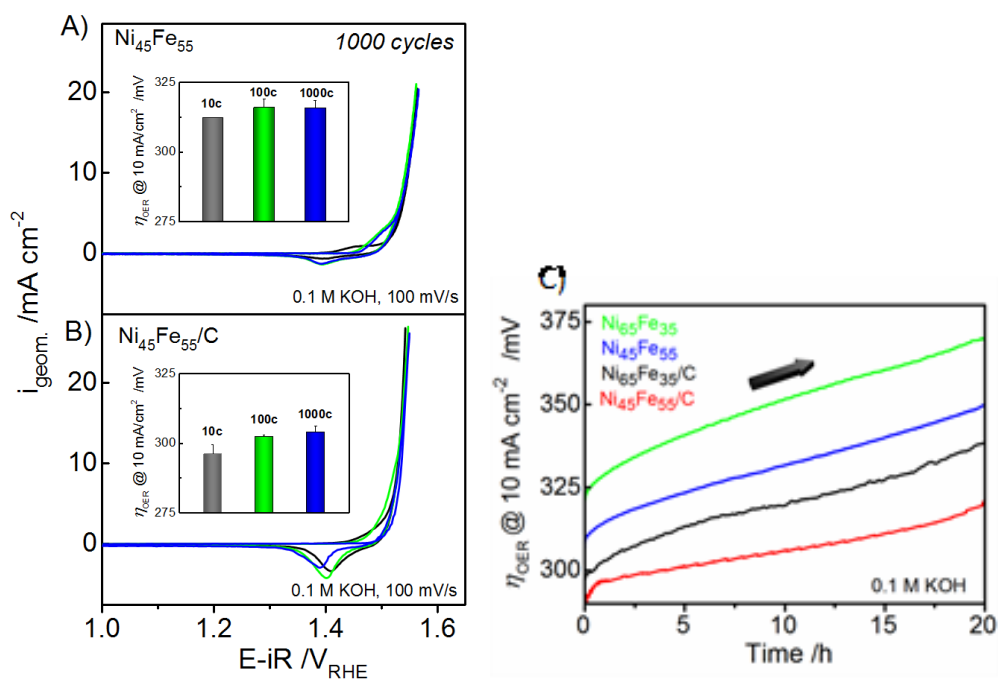


Figure 6.7. Stability test up to 1000 cycles of (a) $\text{Ni}_{45}\text{Fe}_{55}$ and (b) $\text{Ni}_{45}\text{Fe}_{55}/\text{C}$ by cycling between 1-1.75 V_{RHE} . (c) Chronopotentiometric curves at $10 \text{ mA}/\text{cm}^2$ for 20 h. Displayed CVs in (a)-(b) are cycle 10 (gray), 100 (green), and 1000 (blue). Measurements were recorded at a scan-rate of $100 \text{ mV}/\text{s}$ in RDE setup at 2200 rpm, before iR-compensation. All measurements were carried out in 0.1 M KOH. *This figure has been reprinted with permission from ref. 194. Copyright (2017) American Chemical Society.*

TEM images of unsupported Ni-Fe electrocatalysts after 1000 cycles in 0.1 M KOH showed formation of similar crystallites as signified for the $\text{Ni}_{65}\text{Fe}_{35}/\text{C}$ catalyst in the study presented in Chapter 4 (Figure 6.8).¹⁰⁰ This imply a similar crystallization process as previously observed of the $\text{Ni}_{65}\text{Fe}_{35}/\text{C}$ catalyst, and there identified as formation a more highly ordered $\text{Ni}(\text{OH})_2$ upon cycling in alkaline electrolyte.¹⁰⁰ This

was not visible for the carbon supported $\text{Ni}_{45}\text{Fe}_{55}/\text{C}$ catalyst, however there was a change in the carbon structure which could indicate carbon corrosion.

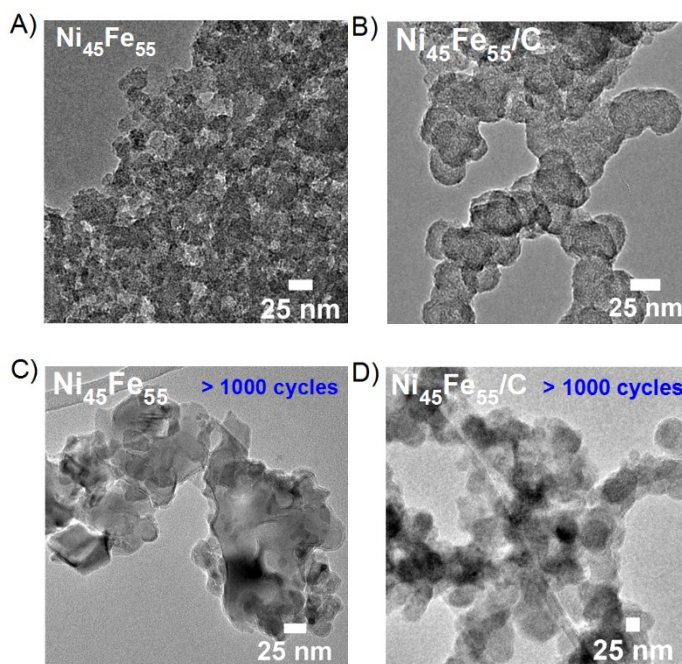


Figure 6.8. TEM images of $\text{Ni}_{45}\text{Fe}_{55}$ and $\text{Ni}_{45}\text{Fe}_{55}/\text{C}$ catalysts **(a)** as-prepared $\text{Ni}_{45}\text{Fe}_{55}$ **(b)** as-prepared $\text{Ni}_{45}\text{Fe}_{55}/\text{C}$ **(c)** $\text{Ni}_{45}\text{Fe}_{55}$ after 1000 cycles in 0.1 M KOH **(d)** $\text{Ni}_{45}\text{Fe}_{55}/\text{C}$ after 1000 cycles in 0.1 M KOH. The cycling was carried out between 1-1.75 V_{RHE} before iR-compensation, in RDE setup at a rotation speed of 2200 rpm under N_2 -protective atmosphere.

6.2.6. Mass spectrometric detection of oxygen

Differential electrochemical mass spectrometry (DEMS) was recorded in a dual thin-layer flow cell. Oxygen evolution of $\text{Ni}_{45}\text{Fe}_{55}$ and $\text{Ni}_{45}\text{Fe}_{55}/\text{C}$ (m/z 32) was monitored during CV scans in 0.1 M KOH (Figure 6.9c-d). The Faradaic efficiency of O_2 was 87 % for $\text{Ni}_{45}\text{Fe}_{55}$ and 81 % for $\text{Ni}_{45}\text{Fe}_{55}/\text{C}$, so a slightly lower efficiency of the carbon supported Ni-Fe catalyst. Due to a high resistance associated with the DEMS setup, the displayed CVs not guaranteed to be fully iR-corrected however should not affect the relative faradaic current contributions. DEMS of the $\text{Ni}_{45}\text{Fe}_{55}/\text{C}$ catalyst was also measured in 0.5 M KOH, which showed a Faradic efficiency of 80 % O_2 (Figure S6.8). No other volatile products than O_2 were detected during the CV scans, however carbon corrosion might have escaped detection due to formation of soluble carbonates in the alkaline electrolyte.

To quantify the O_2 evolved during the steady state of $Ni_{45}Fe_{55}$ and $Ni_{45}Fe_{55}/C$, online mass spectrometry was measured using a gas-tight cell setup, where O_2 was quantified in the headspace leading to the inlet of the mass spectrometer in a well-defined flow of 5 sccm N_2 (Figure 6.9c-d).

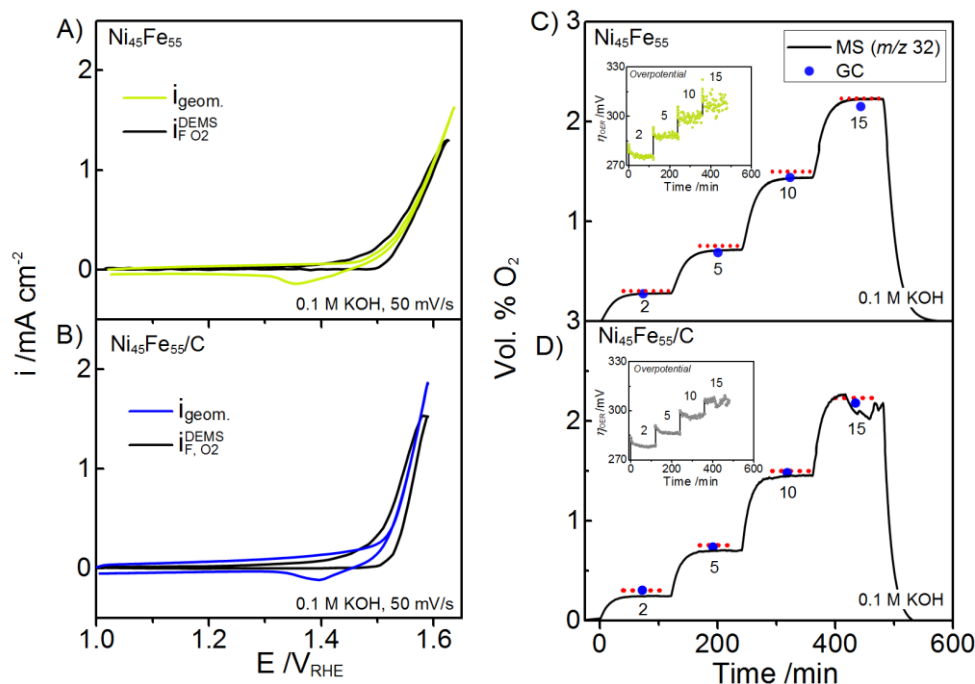


Figure 6.9. (a-b) DEMS in 0.1 M KOH of $Ni_{45}Fe_{55}$ and $Ni_{45}Fe_{55}/C$ catalysts. The geometric current density at the potentiostat, $i_{geom.}$, (colored traces), the faradaic ion current (m/z 32), i_{F,O_2}^{DEMS} (black traces), converted using a calibration sensitivity factor k^* . **(c-d)** Steady-state O_2 detection of $Ni_{45}Fe_{55}$ and $Ni_{45}Fe_{55}/C$ using online headspace mass spectrometry (MS) coupled to gas chromatography (GC). Chronopotentiometric steps were applied between 2-15 mA/cm², holding 2 hours at each step. The black curves shows the MS detected volume % of O_2 and the blue dots the % O_2 measured by GC. The insets shows the overpotential during the measurements. All measurements were carried out in 0.1 M KOH. *This figure has been adapted/reprinted with permission from ref. 194. Copyright (2017) American Chemical Society.*

Chronopotentiometric steps were applied between 0.5-15 mA/cm² with a hold time of 2 hours at each step (Figure 6.9c-d). The working electrode was a carbon fiber paper (CFP) due to a better oxygen transport. The measurements confirmed O_2 as the main product released from the $Ni_{45}Fe_{55}$ and $Ni_{45}Fe_{55}/C$ electrocatalysts in the steady state with a Faradaic efficiency of $\sim 98\%$ (see Table S6.1). Measurements of $Ni_{91}Fe_9$ and $Ni_{91}Fe_9/C$ are attached in Supporting Information Figure S6.9, which also showed faradaic efficiencies of O_2 close to $\sim 99\%$. The relative difference between the Ni-Fe and Ni-Fe/C catalysts in terms of overpotentials did not appear affected by the use of CFP (Figure S6.9a), and comparison to an empty CFP showed that the overpotential in absence of catalysts was extremely high

(Figure S6.9b). There was no detection of CO₂ (m/z 44) in the MS-GC experiments, however due to solubility of carbonates in alkaline electrolyte this does not exclude carbon corrosion, as discussed earlier.

6.2.7. The catalytically active state

Quasi-in situ X-ray absorption spectroscopy (XAS) was measured at the Ni and Fe *K*-edges of the Ni/C, Ni₄₅Fe₅₅/C and Ni₆₅Fe₃₅/C catalyst to retrieve information on the local atomic state during oxygen evolution potential. The catalysts were freeze quenched under application of 1.63V_{RHE} after being conditioned for 30 min at the given potential as an initial activation step, according to a method described elsewhere,^{132,160} also employed in Chapter 3 for investigations of the unsupported Ni-Fe catalysts.¹³¹

The Ni *K*-edges showed that the oxidation state of the Ni/C catalyst reached +3.7 (see Figure 6.10a), identical to that of the unsupported Ni catalyst investigated in Chapter 3.¹³¹ The Ni *K*-edge positions of the two Ni-Fe/C catalysts were shifted towards lower energies in comparison to the Ni/C catalyst. This would support an average lower Ni oxidation state in the mixed Ni-Fe/C catalysts in comparison to the Ni/C catalyst, in accordance with the effect of Fe of the unsupported Ni-Fe catalysts. At catalytic potential, the Ni EXAFS of the Ni/C catalyst could be well described assuming a structure of edge-sharing [NiO₆] octahedra with a Ni-O coordination distance at 1.88 Å and Ni-Ni distance at 2.82 Å, linked via di-μ-oxo-bridges, see Figure 6.10(a) and (c). In the Fe-containing catalysts, there was a fraction on Ni atoms at a longer Ni-O distance of 2.04 Å and Ni-M distance of 3.08 Å, thus showing the presence of a partly reduced state. It should be pointed out that the fraction of oxidized Ni⁺⁴ centers in the Ni-Fe/C catalysts was larger than of the unsupported catalysts. Our findings hence show that carbon support result in a higher fraction of high-valent Ni atoms in mixed Ni-Fe catalysts.

This directly establishes a correlation between oxidized Ni⁺⁴ species and an observed higher redox charge under the Ni(OH)₂/NiOOH voltammetric redox peak. It also confirms that (at minimal contributions from electrolyte inaccessible sites) Fe stabilizes Ni in a low valent state in Ni-Fe/C catalysts, in agreement with the findings in Chapter 3¹³¹ and also reported by Bates et al.¹⁰⁶

The Fe *K*-edge showed that Fe atoms was consistently in oxidation +3 under applied catalytic potentials regardless of composition (Figure 6.10b), however it is possible that the concentration of plausible Fe⁺⁴ species recently reported by Chen et al. using operando Mössbauer spectroscopy¹⁰³ is below the detection limit. Despite the absence of a *K*-edge shift and the lack of a Fe-O bond shortening, we could

see a strong contraction in the Fe-M coordination distance as a response of the oxidized Ni atoms (Figure 6.10d), which indicates that mixed Ni-Fe sites are present in the active state. The small visible edge shift in Figure 5.8b is too small to be distinguish a change in oxidation state, since oxidation state changes at the Fe K-edge is associated with a ~ 4 eV change.

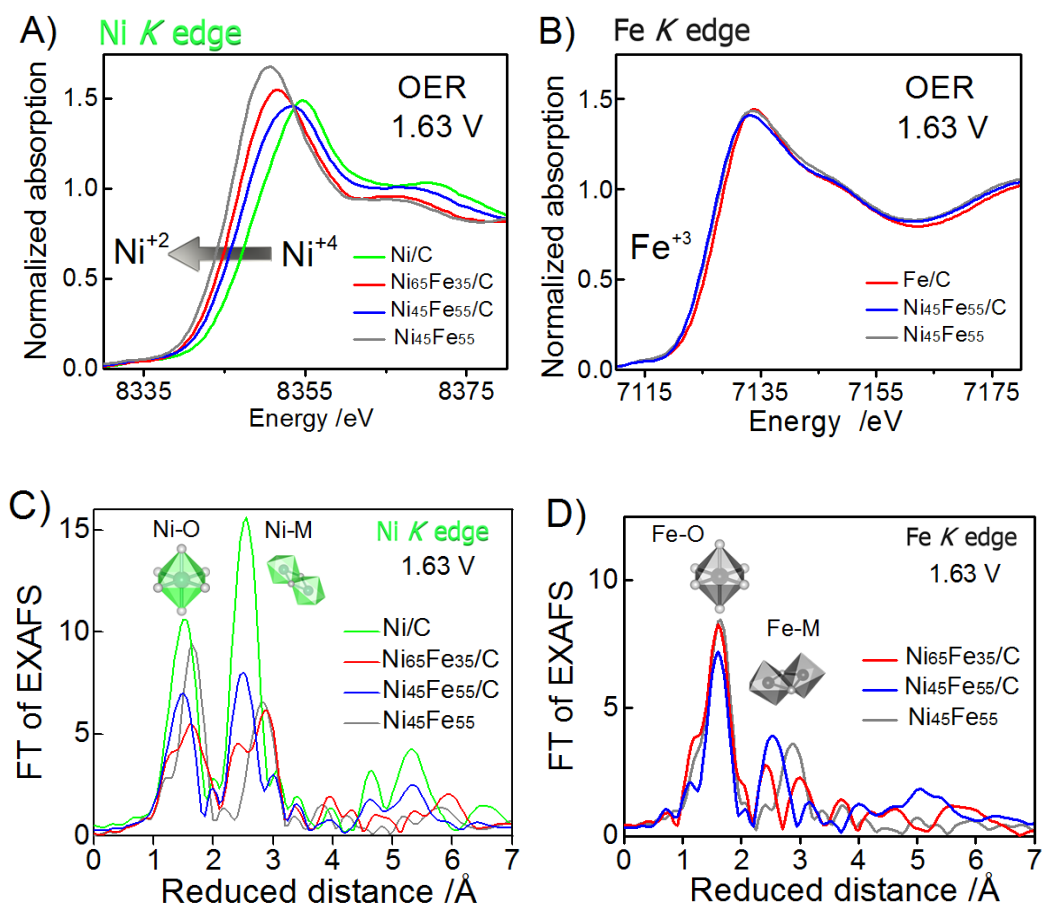


Figure 6.10. XAS measurements of carbon supported Ni₆₅Fe₃₅/C (red), Ni₄₅Fe₅₅/C (blue), and unsupported Ni₄₅Fe₅₅ catalyst (gray) under OER catalytic potential of 1.63 V_{RHE} in 0.1 M KOH. **(a)** Ni K-edges **(b)** Fe K-edges **(c)** Ni K-edge FT-EXAFS (k^3 -weighted) and **(d)** Fe K-edge FT EXAFS. The catalyst composition is given as at. %. This figure has been adapted/reprinted with permission from ref. 194. Copyright (2017) American Chemical Society.

The use of a carbon support was observed as an increase in the FT-EXAFS amplitudes, which may be a result of a more ordered structure or possibly by smaller particle size. The hypothesis put forward in the

previous study of the unsupported Ni-Fe catalysts in Chapter 3,¹³¹ showed that the fine balance of the catalytic OER rate and the rate of metal oxidation was likely to be shifted by the presence of Fe, observed as a larger fraction of Ni⁺⁴. This was correlated to a larger size of the Ni^{+2→+3/+4} redox peak. Since employing a carbon support results in an increased fraction of Ni⁺⁴ sites in mixed Ni-Fe/C catalysts, one could speculate whether carbon support either results in a larger number of electrolyte-accessible sites or an increased underlying conductivity. The latter could potentially result in a similar effect if the deprotonation step with an associated electron transfer step is facilitated. This would possibly enhance the rate associated with metal oxidation and therefore could explain a higher fraction of accumulated oxidized Ni atoms, assuming that the OER rate constant is not affected by increased conductivity. To address the possibility of a hypothetical interaction with the underlying electrode, catalyst support, and the number of electrocatalytically accessible sites leading to an increased OER catalytic activity in Ni-Fe/C catalysts would need further investigations. Adapted with permission from ref.¹⁹⁴ Copyright (2017) American Chemical Society.

6.3. Conclusions

The comparison of supported Ni-Fe catalysts showed that Vulcan XC-72r yielded highest activity amongst the investigated catalyst supports. Carbon nanotubes also resulted in high activity whereas ATO did not perform well with the investigated Ni-Fe catalysts with low metal loadings and poor activity as a result.

Ni-Fe/C catalysts supported on Vulcan XC-72r were further investigated as a function of Fe-content. It showed that carbon support promotes high catalytic oxygen evolution activity, leading to 2-fold increase. The highest OER activity was observed for the Ni₄₅Fe₅₅/C in 1 M KOH with a mass based TOF of 0.30 s⁻¹ per total metal, and a TOF of 1.82 s⁻¹ per redox active Ni site.

Measurements in different electrolyte pH was also further investigated. Higher concentration of KOH further increased the activity and induced a shift of the activity top towards higher Ni-content. Varying the catalyst loading apparently affected the mass based OER activity, with indications of a higher fraction of electrolyte accessible sites in carbon supported catalysts. A comparative study in KOH versus NaOH showed higher activities in KOH, and that increasing the molarity above 0.5 M did not further improve the activity significantly. Tafel slopes were similar for unsupported and carbon supported Ni-Fe catalysts independent of electrolyte pH, which suggest that carbon support is unlikely to affect the OER mechanistic steps.

Short-term stability test showed a good stability performance, with only ~ 5 mV increase after 1000 cycles and ~ 30 mV increase in overpotential after 20 h at 10 mA/cm². TEM images after 1000 cycles

confirmed a slight change in morphology in the Ni₄₅Fe₅₅/C catalyst, which could indicate carbon corrosion, and for the unsupported Ni₄₅Fe₅₅ there was indication of a crystallization process. BET isotherms showed that the surface area increased towards higher Ni content, which could be partly explained by the morphology, however could favor the activity towards higher Ni-content. O₂ evolution was investigated in both KOH and NaOH using DEMS, and steady-state levels confirmed using headspace MS to GC, which confirmed near ~ 90 % Faradaic efficiency for both Ni-Fe and Ni-Fe/C catalysts.

Quasi-in situ X-ray absorption spectroscopy at the metal *K*-edges at 1.63 V_{RHE} showed that carbon support increased the local atomic order around the metal center. The Ni *K*-edge showed an accumulation of low-valent Ni⁺² atoms in mixed Ni-Fe and Ni-Fe/C catalysts. There was however a comparably larger fraction of oxidized Ni⁺⁴ state in the Ni-Fe/C catalysts, hence directly relating the observed increase of the area under the Ni^{+2/+3} redox peak to a larger fraction of oxidized Ni. We speculate that the carbon support might result in a relatively faster metal oxidation step in comparison to the OER rate. It may also be an effect of improved underlying electrical conductivity or better dispersion of the carbon supported catalysts with a larger fraction of electrocatalytic accessible sites.

Supporting Information

The influence of carbon support on the oxygen evolution activity in amorphous Ni-Fe electrocatalysts

Parts of this Chapter has been reprinted or adapted with permission from the American Chemical Society, as the Supporting Information of a published Journal article.

(Görlin, M.; Ferreira de Araújo, J.; Schmies, H.; Bernsmeier, D.; Dresp, S.; Gliech, M.; Jusys, Z.; Chernev, P.; Kraehnert, R.; Dau, H.; Strasser, P. Tracking Catalyst Redox States and Reaction Dynamics in Ni–Fe Oxyhydroxide Oxygen Evolution Reaction Electrocatalysts: The Role of Catalyst Support and Electrolyte pH, *Journal of the American Chemical Society*, 2017, 139, 2070.)

10.1021/jacs.6b12250

Mikaela Görlin¹, Jorge Ferreira de Araújo¹, Henrike Schmies¹, Denis Bernsmeier¹, Sören Dresp¹, Manuel Gliech¹, Zenonas Jusys³, Petko Chernev², Ralph Krähnert¹, Holger Dau², Peter Strasser¹

¹ Department of Chemistry, Chemical Engineering Division, Technical University of Berlin, Straße des 17. June 124, 10623, Berlin, Germany

² Department of Physics, Free University of Berlin, Arnimallee 14, 14195 Berlin, Germany

³ Institute of Surface Chemistry and Catalysis, Ulm University, Albert-Einstein-Allee 47, 89069 Ulm, Germany

S6.1. X-ray diffraction

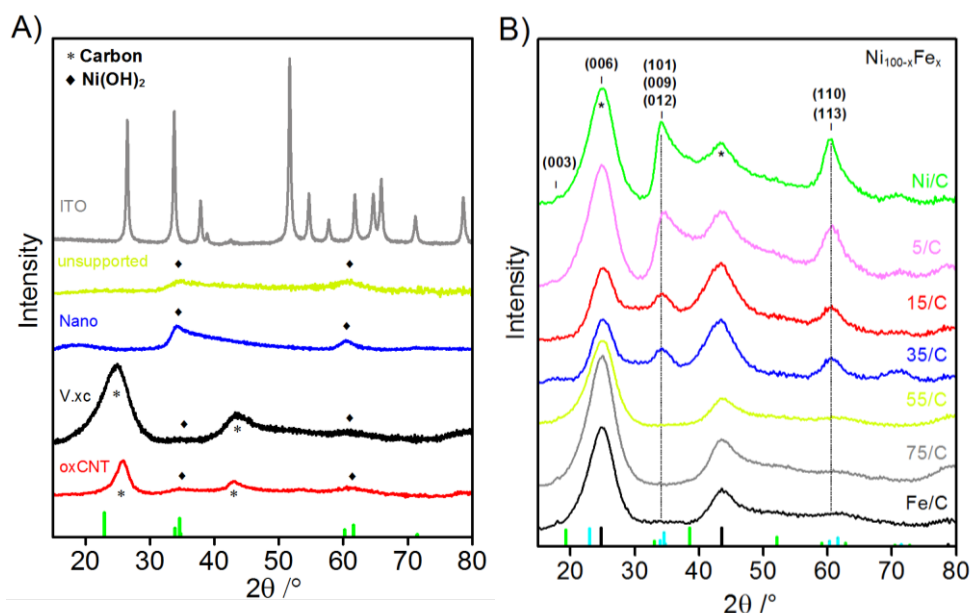


Figure S6.1. XRD diffractograms of supported Ni-Fe catalysts **(a)** $\text{Ni}_{50}\text{Fe}_{50}$ on different supports; unsupported $\text{Ni}_{50}\text{Fe}_{50}$ (yellow), $\text{Ni}_{50}\text{Fe}_{50}/\text{C}$ (V.XC-72r, black), oxidized $\text{Ni}_{50}\text{Fe}_{50}/\text{CNTs}$ (red), and $\text{Ni}_{50}\text{Fe}_{50}/\text{ATO}$ (gray), $\text{Ni}_{90}\text{Fe}_{10}/\text{Nano}$. **(b)** Ni-Fe catalysts on Vulcan XC-72r (/C) with various Ni:Fe compositions ($\text{Ni}_{100-x}\text{Fe}_x/\text{C}$). The catalyst composition is indicated as at. % Fe. The bottom lines show diffraction profiles of $\alpha\text{-Ni}(\text{OH})_2$ (green, pdf # 00-038-0715), $\beta\text{-Ni}(\text{OH})_2$ (light, pdf # 01-074-2075), and for carbon (black). Figure (b) has been reprinted with permission from ref. 194. Copyright (2017) American Chemical Society.

S6.2. Electrochemical characterization

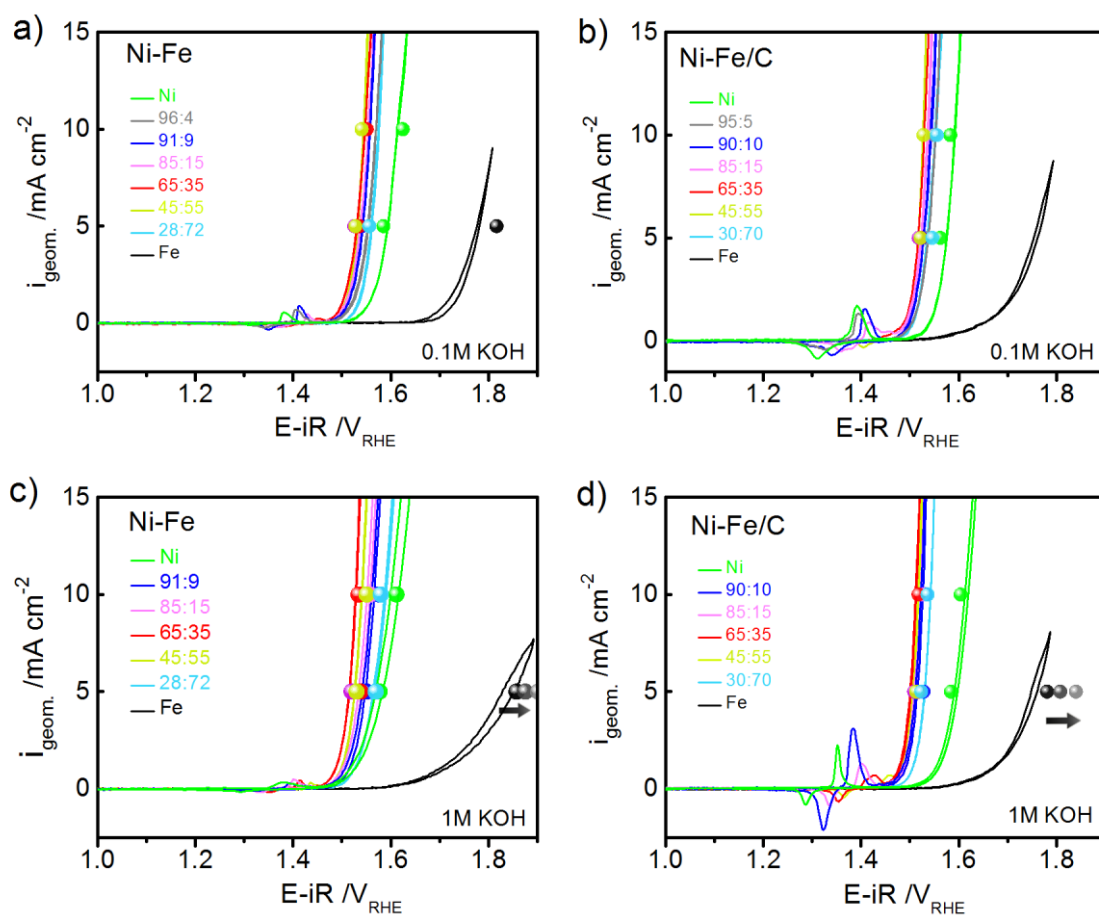


Figure S6.2. CVs measured at scan rate of 2 mV/s (curves) and steady-state chronopotentiometric measurements (circles) **(a)** unsupported Ni-Fe catalysts in 0.1 M KOH **(b)** Carbon supported Ni-Fe/C catalysts in 0.1 M KOH. **(c)** Ni-Fe catalysts in 1 M KOH **(d)** Ni-Fe/C catalysts in 1 M KOH. The CVs were recorded at a scan rate of 1600 rpm and the steady-state measurements at a rotation speed of 2200 rpm to avoid bubble blockage at the electrode surface. The metal loadings of Ni+Fe were kept at $\sim 10 \mu\text{g cm}^{-2}$, determined prior to the measurements by ICP-OES. The Ni:Fe compositions are indicated in the legends as at. %. *This Figure has been reprinted with permission from ref. 194. Copyright (2017) American Chemical Society.*

S6.2.1. Redox behavior

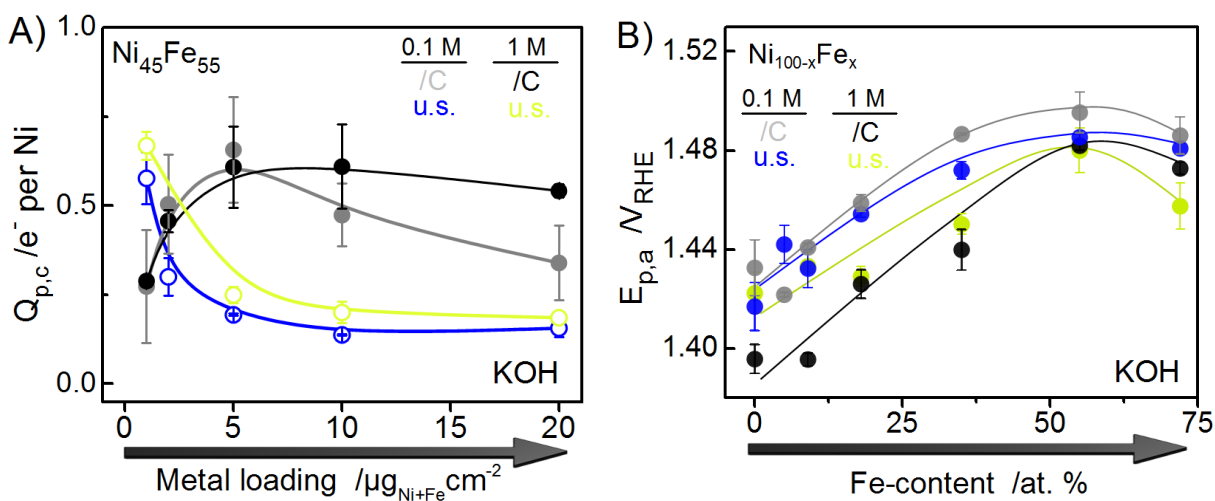


Figure S6.3. (a) The cathodic redox charge of the $\text{Ni}(\text{OH})_2/\text{NiOOH}$ redox peak of unsupported $\text{Ni}_{45}\text{Fe}_{55}$ and Vulcan XC-72r carbon supported $\text{Ni}_{45}\text{Fe}_{55}/\text{C}$, normalized to the moles of Ni on the electrode determined by ICP-OES. **(b)** The anodic peak position ($E_{p,a}$) as a function of catalyst loading in $\text{Ni}_{100-x}\text{Fe}_x$. Measurements were carried out in 0.1 and 1 M KOH at a rotation speed of 1600 rpm. Adapted with permission from ref.¹⁹⁴ Copyright (2017) American Chemical Society. *Figure (a) has been adapted with permission from ref. 194. Copyright (2017) American Chemical Society.*

S6.2.1. Activity in KOH and NaOH

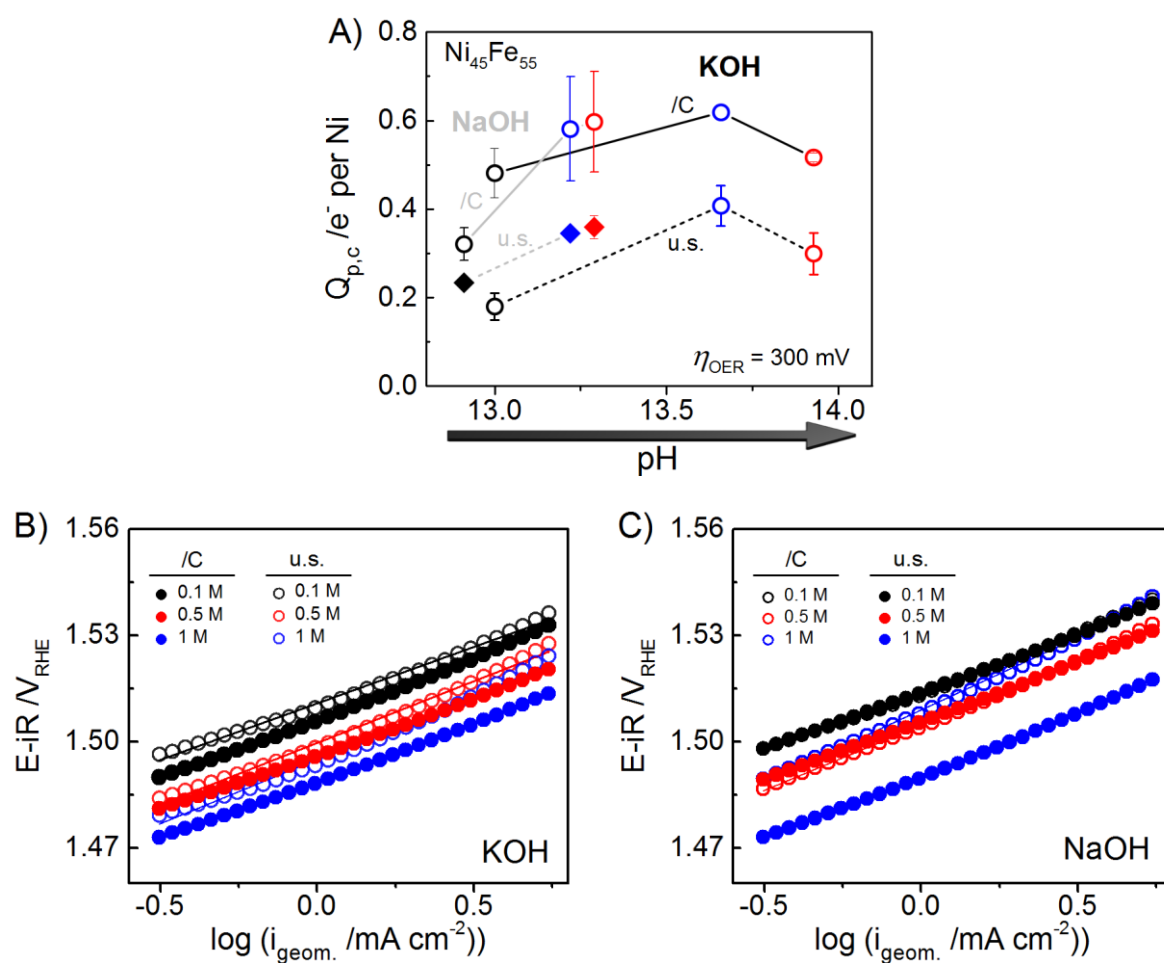


Figure S6.4. (a) Cathodic redox electrons of the $\text{Ni}(\text{OH})_2/\text{NiOOH}$ redox peak of unsupported $\text{Ni}_{45}\text{Fe}_{55}$ and Vulcan XC-72r carbon supported $\text{Ni}_{45}\text{Fe}_{55}/\text{C}$ in KOH and NaOH as a function of electrolyte pH. The moles of Ni on the electrode were determined by ICP-OES. **(b)** Tafel plots in different molarities of KOH **(c)** Tafel plots in different molarities of NaOH. Tafel data points were collected from CVs recorded at a scan-rate of 2 mV/s, between 0.5-5 mA/cm^2 .

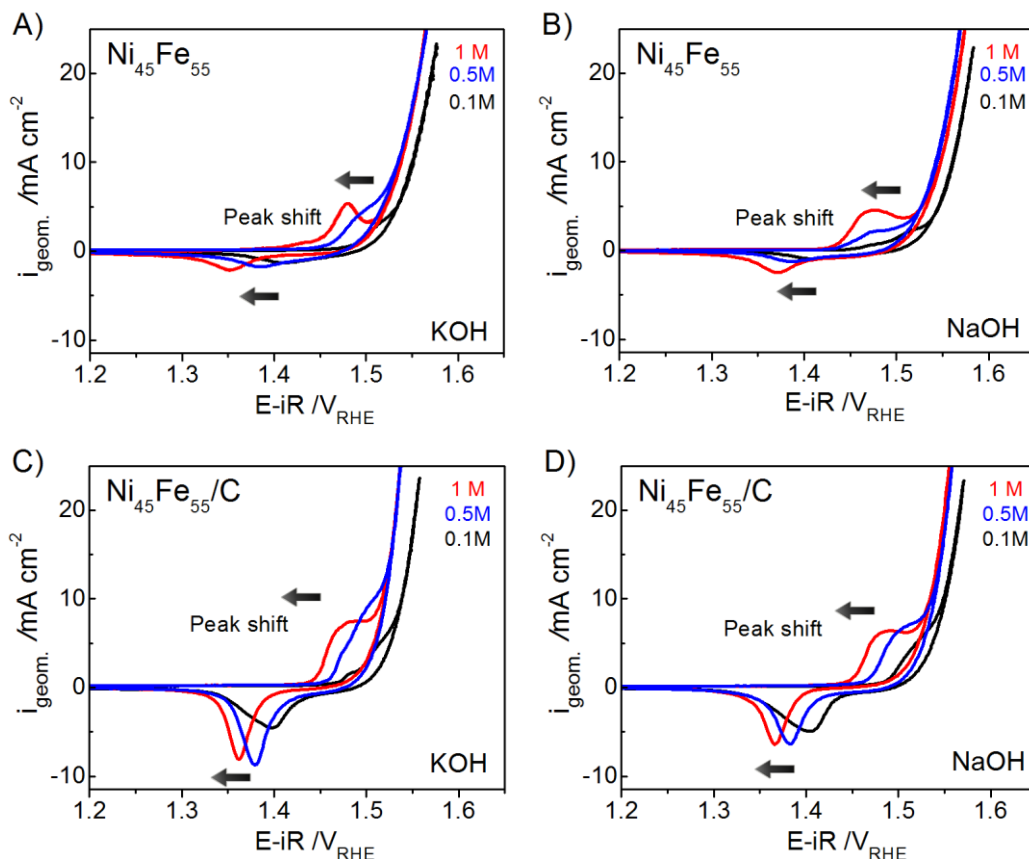


Figure S6.5. (a) Unsupported $\text{Ni}_{45}\text{Fe}_{55}$ in different concentrations of KOH (b) Unsupported $\text{Ni}_{45}\text{Fe}_{55}$ different concentrations of NaOH. (c) Carbon supported $\text{Ni}_{45}\text{Fe}_{55}/\text{C}$ in different concentrations of KOH (d) Carbon supported $\text{Ni}_{45}\text{Fe}_{55}/\text{C}$ in different concentrations of NaOH. The electrolytes were used without further purification.

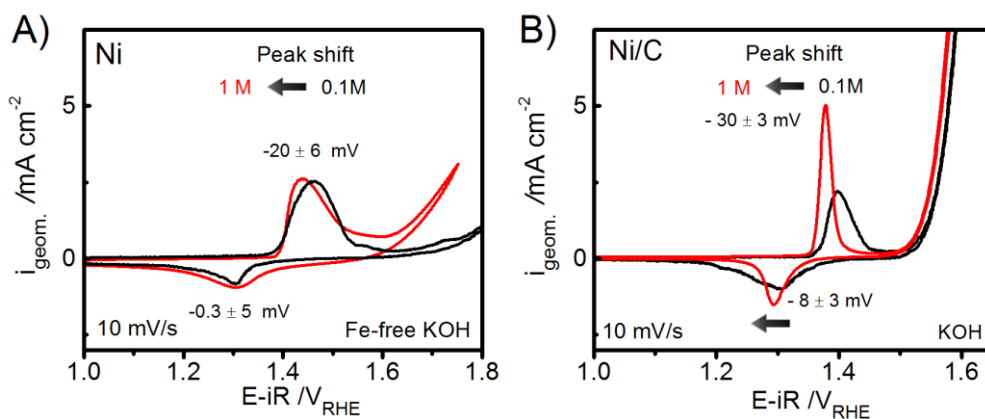


Figure S6.6. (a) Unsupported $\text{Ni}(\text{OH})_2$ catalyst in different concentrations of KOH (b) carbon supported Ni/C-catalyst in 0.1 M and 1 M KOH, at a scan-rate of 100 mV/s. The electrolyte was purified prior to the measurements according of the method reported by Trotochaud et al.⁷² This Figure has been adapted with permission from ref. 194. Copyright (2017) American Chemical Society.

S6.3. Detection of oxygen

S6.3.1. Differential Electrochemical mass spectrometry (DEMS)

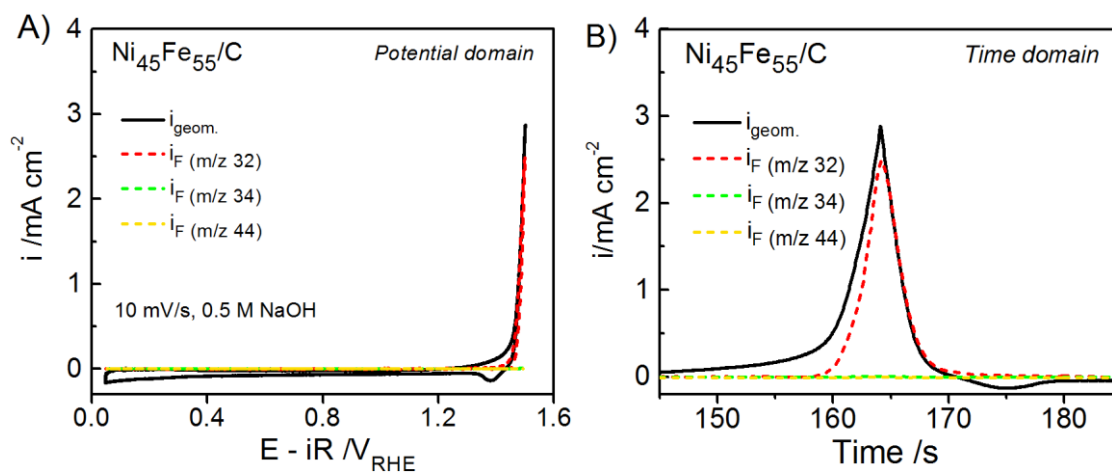


Figure S6.7. DEMS of Ni₄₅Fe₅₅/C in 0.5 M NaOH measured in a dual thin-layer double-disk electrochemical flow cell.¹²⁶ CVs are shown in **(a)** the potential domain and **(b)** the time domain. CVs were measured at 10 mV/s between 0.4-1.55 V_{RHE}. The geometric catalyst loadings were $\sim 15 \mu\text{g Ni+Fe cm}^{-2}$. Volatile gases were monitored of m/z 32, 34, 44. The working electrode was a glassy carbon disc electrode (Pine Instruments) with a geometric surface area of 0.283 cm^2 .

S6.3.2. Headspace Mass Spectrometry – Gas Chromatography

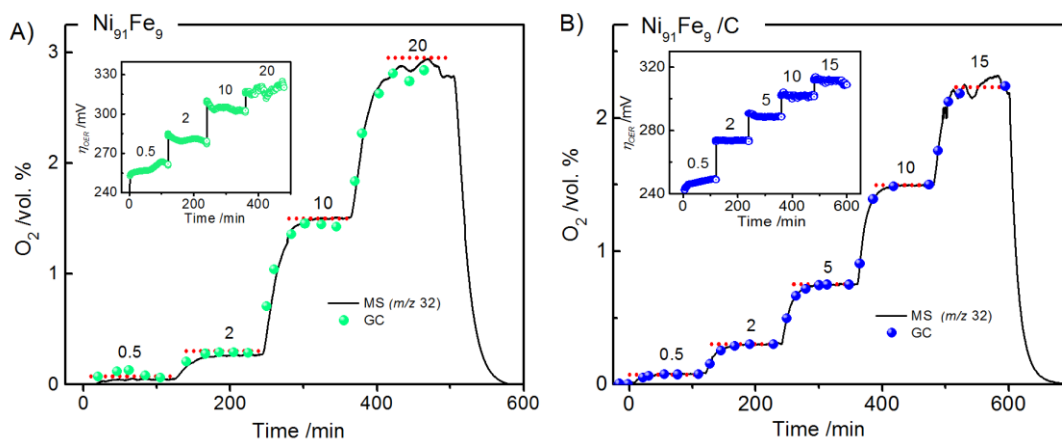


Figure S6.8. Online headspace Mass Spectrometry of (a) Ni₉₁Fe₉ and (b) Ni₉₁Fe₉/C catalysts in 0.1 M KOH. Chronoamperometric measurements were applied in a stepwise manner; 0.5, 2, 5, 10, 15 mA/cm². Each step was held for 2 h to reach a stable level of oxygen. A gas tight cell was employed with a constant flow of 5 sccm of N₂ controlled by mass flow controllers. The working electrode was a carbon fiber paper (CFP) with a geometric area of 2 cm². The insets show the OER overpotentials during the measurement.

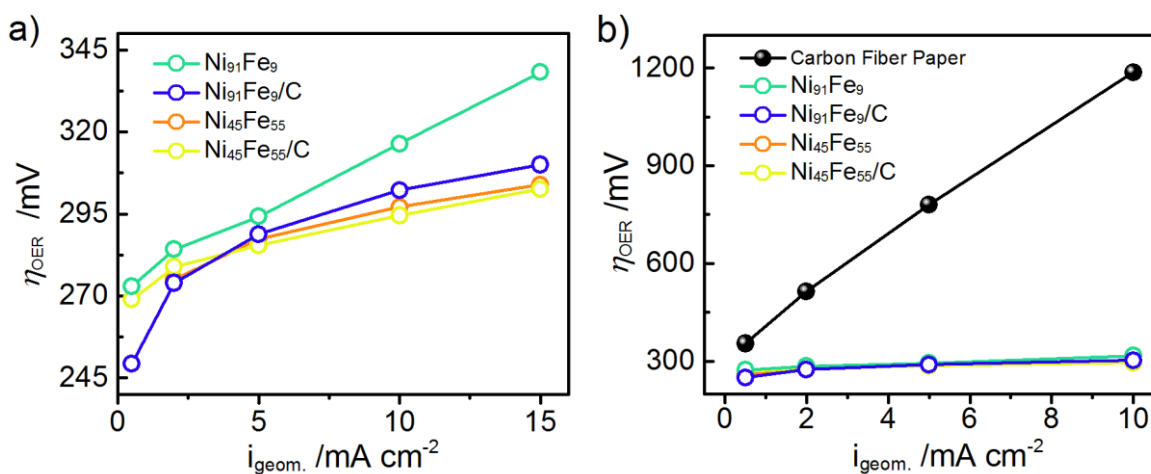


Figure S6.9. OER overpotentials monitored during headspace MS measurements for Ni₄₅Fe₅₅, Ni₄₅Fe₅₅/C, Ni₉₁Fe₉, and Ni₉₁Fe₉/C in 0.1 M KOH at a catalyst loading of 0.4 mg/cm². (a) Overpotential plotted against the geometric current density (i_{geom.}) extracted as the average of the last 1000 sec of each step (b) overpotentials for the catalysts compared to an uncoated carbon fiber paper.

Table S6.1. Faradaic efficiencies determined for O₂ (*m/z* 32) in the headspace MS-GC setup in 0.1 M KOH on carbon fiber paper. The geometric current densities were obtained by normalizing the current to the electrode area of the CFP of 2 cm². The theoretical percentage of oxygen was determined using faradays law for each applied current. *This Table has been adapted with permission from ref. 194. Copyright (2017) American Chemical Society.*

<i>i_{geom.}</i> /mA cm ⁻²	Faradaic efficiency (%)					
	Ni ₉₁ Fe ₉		Ni ₉₁ Fe ₉ /C		Ni ₄₅ Fe ₅₅	Ni ₄₅ Fe ₅₅ /C
	MS	GC	MS	GC	MS	MS
0.5	92	94	93	99	-	-
2	96	95	97	98	93	98
5	95	-	98	99	95	98
10	99	96	99	99	96	98
15	99	-	99	99	99	97
20	99	95	-	-	-	-

S6.4. X-ray absorption spectroscopy (XAS)

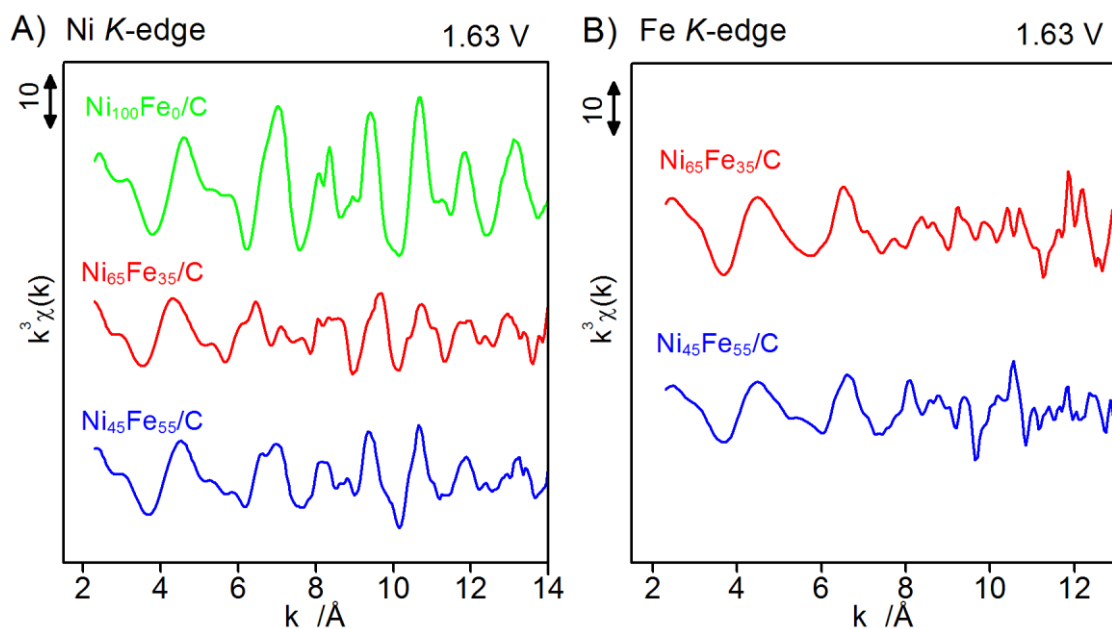


Figure 6.10. XAS measurements of unsupported catalysts (*dotted* curves) versus carbon supported catalysts $\text{Ni}_{100-x}\text{Fe}_x/\text{C}$ (*solid* curves) of catalysts freeze quenched at 1.63V after 30 min conditioning in 0.1 M. The catalyst composition is given as at. %. **(a)** Ni K-edges **(b)** Fe K-edges **(c)** Ni FT-EXAFS (k^3 -weighted) and **(d)** Fe FT-EXFAS (k^3 -weighted). *This Figure has been adapted with permission from ref. 194. Copyright (2017) American Chemical Society.*

Table S6.2. Ni K-edge simulation parameters in 0.1 M KOH. *This Table has been adapted with permission from ref. 194. Copyright (2017) American Chemical Society.*

Catalyst	Shell	R (Å)	N	σ (Å)	R _f
Ni	Ni-O (long)	2.042 ± 0.009 ^a	5.9 ± 0.9	0.07 ± 0.01	18.6
a.s.	Ni-M (long)	3.080 ± 0.006 ^b	6.1 ± 1.6	0.08 ± 0.01	
	Ni-M (double long)	6.160 ^e	1	0.09	
Ni/C	Ni-O (short)	1.876 ± 0.007 ^c	5.3 ± 0.7	0.07 ± 0.01	19.9
1.63V	Ni-M (short)	2.814 ± 0.004 ^d	6.7 ± 1.0	0.06 ± 0.01	
	Ni-M (double short)	5.629 ^e	3.1 ± 0.8	0.06	
Ni ₆₅ Fe ₃₅ /C	Ni-O (short)	1.876 ± 0.007 ^c	2.0 ± 0.6 ^f	0.08 ± 0.02 ^j	30.8
1.63V	Ni-O (long)	2.042 ± 0.009 ^a	4.0 ± 0.6 ^f	0.08 ± 0.02 ^j	
	Ni-M (short)	2.814 ± 0.004 ^d	2.2 ± 0.4 ^g	0.07 ± 0.01 ^k	
	Ni-M (long)	3.080 ± 0.006 ^b	3.8 ± 0.4 ^g	0.07 ± 0.01 ^k	
	Ni-M (double long)	6.160 ^e	1.4	0.07 ± 0.01 ^k	
Ni ₄₅ Fe ₅₅ /C	Ni-O (short)	1.876 ± 0.007 ^c	5.1 ± 1.0 ^h	0.09 ± 0.02 ^l	25.7
1.63V	Ni-O (long)	2.042 ± 0.009 ^a	0.9 ± 1.0 ^h	0.09 ± 0.02 ^l	
	Ni-M (short)	2.814 ± 0.004 ^d	4.5 ± 0.4 ⁱ	0.08 ± 0.01 ^m	
	Ni-M (long)	3.080 ± 0.006 ^b	1.5 ± 0.4 ⁱ	0.08 ± 0.01 ^m	
	Ni-M (double short)	5.629 ^e	2.8 ± 1	0.08 ± 0.01 ^m	

Values for which no fit error is shown were not fitted. Long Ni-O (^a), long Ni-M (^b), short Ni-O (^c), and short Ni-M (^d) distances had the same values in the four models in a joint-fit approach. Double Ni-M distances (^e) were set equal to the (dominating) single Ni-M distance multiplied by two. The double-distance Ni-M shells included multiple-scattering contributions. The sums of the coordination numbers of the short and long Ni-O shells in the Ni₆₄Fe₃₆/C (^f) and Ni₄₄Fe₅₆/C (^h) models were set to 6. The sums of the coordination numbers of the short and long Ni-M shells in the Ni₆₄Fe₃₆/C (^g) and Ni₄₄Fe₅₆/C (ⁱ) models were set to 6. Debye-Waller parameters of the two Ni-O and the three Ni-M shells in the Ni₆₄Fe₃₆/C (^{j,k}) and Ni₄₄Fe₅₆/C (^{l,m}) models had the same values.

Table S6.3. Fe K-edge simulation parameters in 0.1 M KOH. *This Table has been adapted with permission from ref. 194. Copyright (2017) American Chemical Society.*

Catalyst	Shell	R (Å)	N	σ (Å)	R _f
Fe	Fe-O	1.97 ± 0.02	4.6 ± 0.6	0.09 ± 0.01 ^c	18.5
a.s.	Fe-M (short)	2.93 ± 0.02 ^a	1.3 ± 1.0	0.08 ± 0.04 ^d	
	Fe-M (long)	3.11 ± 0.02 ^b	1.8 ± 1.2	0.08 ± 0.04 ^d	
Ni ₆₄ Fe ₃₆ /C	Fe-O	1.98 ± 0.01	6.4 ± 0.7	0.09 ± 0.01 ^c	18.8
1.63V	Fe-M (short)	2.93 ± 0.02 ^a	2.5 ± 1.5	0.08 ± 0.04 ^d	
	Fe-M (long)	3.11 ± 0.02 ^b	3.0 ± 1.7	0.08 ± 0.04 ^d	
Ni ₄₄ Fe ₅₆ /C	Fe-O	1.98 ± 0.02	5.1 ± 0.6	0.09 ± 0.01 ^c	18.0
1.63V	Fe-M (short)	2.93 ± 0.02 ^a	3.5 ± 1.9	0.08 ± 0.04 ^d	
	Fe-M (long)	3.11 ± 0.02 ^b	2.1 ± 1.3	0.08 ± 0.04 ^d	

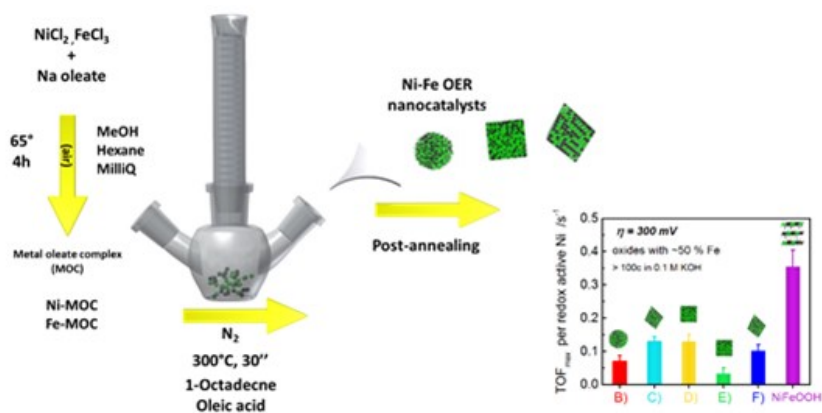
The short Fe-M (^a) and long Fe-M (^b) distances had the same values in the three models in a joint-fit approach.

Debye-Waller parameters of the Fe-O shells (^c) and the two Fe-M shells (^d) had the same values in the three models.

Chapter 7

Electrochemical water oxidation on shape-selected Ni-Fe oxide nanocrystal catalysts

This Chapter is based on unpublished data



Mikaela Görlin¹, Manuel Gliech¹, Dennis Bernsmeier¹, Fang Luo¹, Anna Loiudice², Raffaella Buonsanti², Peter Strasser¹

Contact: pstrasser@tu-berlin.de

¹Technical University of Berlin, Department of Chemistry, , Straße des 17. June 124, 10623, Berlin, Germany

²École Polytechnique Fédérale de Lausanne (EPFL), Rue de l'Industrie 17, 1950, Sion, Switzerland

Abstract

The increasing demand of renewable energy, and to reduce atmospheric levels of CO₂ levels, require efficient catalysts for energy conversion. Electrochemical water splitting to generate O₂ and H₂ or reducing equivalents to drive CO₂ electroreduction processes, offers a path to a closed energy cycle. Ni-Fe electrocatalysts have gained attention due to its high activity for the oxygen evolution reaction (OER) in alkaline electrolyte. OER activity on well-defined oxide surfaces of mixed Ni-Fe oxide nanoparticles have so far not been extensively explored. Here we present highly crystalline Ni-Fe nanocatalysts supported on Vulcan XC-72r. We used the metal-oleate-complex (MOC) route to obtain spherical nanoparticles with a narrow size distribution. The shape could be tuned into cubic and cuboctahedrally shaped particles by introducing modifications in the synthesis protocol. The nanocatalysts showed reasonable high oxygen evolution activities however did not exceed that of the Ni-FeOOH catalysts, meaning that the OER was confined to the surface. Removal of surfactants were achieved by annealing in controlled atmosphere. The catalytic activity as a function of the annealing temperature evidenced a rapid loss of activity that coincide with loss of the metallic hcp reflections in the XRD. This was in addition correlated to a rapid loss redox active Ni estimated by the integrated area of the Ni^{+2/+3} redox peak. Elemental analysis showed no significant loss of total bulk metal. Therefore, we hypothesize that the loss of activity was caused either by compositional segregation as a result of oxidizing conditions with formation of a Fe-rich surface and a Ni-rich core. Other possibilities include correlations to the underlying subsurface where the hcp structure show a significantly higher OER activity than the fcc structure. Stability test up to 1000 cycles showed clear variation in the stability despite amongst the investigated oxide nanoparticles with defined shape and size. Clear differences were visible in the Ni^{+2/+3} redox peak, which appeared as one of the most pronounced activity-controlling factors together with the appearance of hcp reflections. TEM images did not show significant morphological changes, however further investigations will be needed to establish a clear correlation between phase, shape and OER activity.

7.1. Introduction

The need of increased shares of renewable energy require efficient catalysts for electrochemical water splitting. To make the process long term sustainable it would be desirable to find catalysts of Earth abundant materials. Non-precious solid-state electrocatalysts based on Ni-Fe have shown promising activities in alkaline conditions.

The combination of Ni and Fe have shown extremely high activities compared to the parental metals.¹⁹⁸ The most widely studied Ni-Fe catalyst is the oxyhydroxide since early work by Corrigan and coworkers⁷¹ where Fe impurities in electrodeposited $\text{Ni}(\text{OH})_2$ electrodes were found to extensively improve the oxygen evolution activity. More early work has focused on achieving a profound understanding of the origins of the synergism between the Ni and Fe, where recent advances were presented by Trotochaud et al.,⁷² where Fe impurities in alkaline electrolyte could be eliminated and revised activity trends were presented. Friebel et al.⁸⁰ performed first-principles DFT calculations which showed that key OER intermediates bind more optimally to the Fe site in the Ni-Fe site which shifted the focus to Fe as the likely active site.

Despite the vast number of investigations of the Ni-FeOOH catalyst, the field of Ni-Fe oxide OER catalysts remain much less explored.^{69,77,83,107,198,199} One of the main reasons in contrary to the Ni-FeOOH catalyst have been the disadvantage because of a large bulk to surface volume ratio. This not only reduces the catalytically accessible surface sites but also makes characterizations and identification of the key intermediates in the active state reliable on surface sensitive techniques. On the other hand, it has been shown that oxide surfaces undergo hydration at the surface when exposed to alkaline conditions,⁶⁹ which render the catalysis to a confined area.

Shape-control have been immensely neglected in terms of oxygen evolution reaction on oxides.¹⁹⁹ Yet, studies for the oxygen reduction reaction (ORR) have demonstrated higher activities on the (1 1 1) facet^{58,108,200} and in CO_2 reduction the Cu (100) facet favors ethylene production, and the Cu (111) selectively produces methane.²⁰¹ Sensitivity to thickness²⁰² and particle size²⁰¹ have been investigated by a number of groups.

In this contribution, we explore synthesis of small Ni-Fe crystal nanoparticles (5-30 nm) by introducing modifications to the synthesis protocol, allowing for formation of nanoparticles with a small size distribution and defined shape. The nanoparticles were prepared by the metal-oleate route^{123,203} which takes advantage of the metal-oleate-complex (MOC), thought to act as the growth source of the nanocrystals.¹²³ In a first step, the metal salt precursors are converted to MOC at moderate temperature,

which in a second step is decomposed at high temperatures with additions of surfactant. Employing additives to the reaction can stabilize a specific shape and influence the size distribution.¹²⁴ Favoring growth of the (1 1 1) facet via the oleate route in FeO has been demonstrated by additions of tertiary ammonium salts where the Trioctylammonium ions was proposed to play a crucial role.¹²⁵ Other studies include additions of sodium oleate salt to stabilize cubic shaped nanocrystals with the (1 0 0) facet.²⁰⁴ In this study, we further explore the oleate synthesis approach with focus on the Ni-Fe system, and further evaluate the oxygen evolution activity on the different oxide surfaces, in attempt to establish correlations between surface properties and activity.

7.2. Results & Discussion

Ni-Fe nanocrystals were prepared from the metal oleate route reported previously.¹²³

7.2.1. Spherical Ni-Fe nanoparticles

Ni-Fe nanoparticles with a composition of ~50:50 atomic % obtained via the metal-oleate-complex (MOC) are shown in Figure 7.1 below.

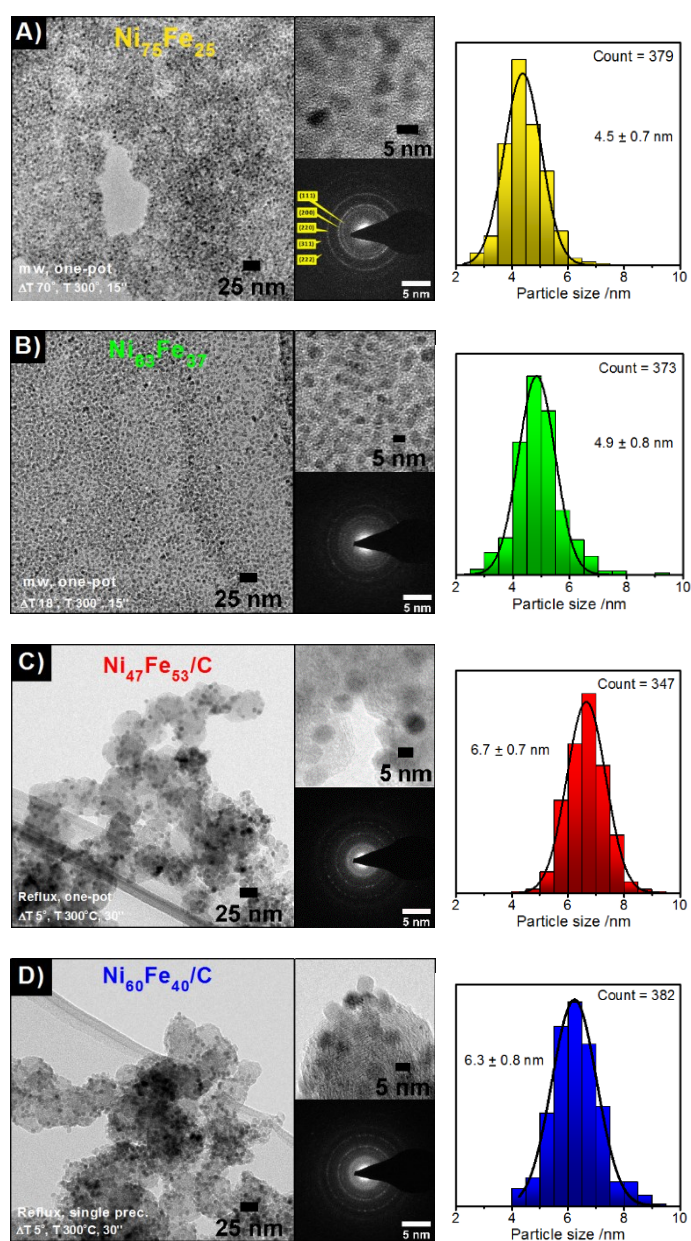


Figure 7.1. TEM images of Ni-Fe nanoparticles with ~50:50 atomic composition, and the respective selected area electron diffraction (SAED), and the particle size distribution. **(a)** unsupported $Ni_{75}Fe_{25}$ prepared from "one-pot" MOC using microwave irradiation at 300 °C for 15 min with a ramping step of 70°/min. **(b)** unsupported $Ni_{63}Fe_{37}$

prepared from "one-pot" MOC using microwave-assisted synthesis at 300 °C for 15 min with a heating ramp of 18°/min. **(c)** Carbon supported Ni₄₇Fe₅₃/C prepared from "one-pot" MOC using conventional synthesis with reflux at 300 °C for 30 min with a heating ramp of 5°/min. **(d)** Carbon supported Ni₆₀Fe₄₀/C prepared from "single precursor" MOC using conventional synthesis with reflux at 300 °C for 30 min with a heating ramp of 5°/min. The catalyst composition obtained from the ICP-OES (Ni_{100-x}Fe_x) is given as at. %.

The metal-oleate route has been reported to yield well defined Fe oxide nanocrystals with possibility to tune the size¹²³ and shape^{124,205} dependent on the synthesis conditions. In Figure 7.1a-b, we present TEM images and SAED patterns of unsupported Ni-Fe nanocrystals prepared using microwave assisted autoclave synthesis with a decomposition time of 15 min. In Figure 7.1c-d, Ni-Fe nanocrystals prepared using conventional synthesis in a 3-neck bottle under reflux conditions and N₂-protected atmosphere and a decomposition time of 30 min are presented. The size appeared smaller for the microwave-synthesized nanoparticles, which might be attributed to the shorter decomposition time. Extending the decomposition time of the conventional synthesis from 30 to 60 min on the other hand did not result in larger particles (Figure S7.1). We also noticed that increased rate of the heating ramp resulted in smaller nanoparticles (Figure 7.1a). The possibility to control the heating ramp in microwave-assisted autoclave synthesis give a more accurate estimation of the influence of changing the reaction parameters, however more investigations will be needed. The difference between the Ni-Fe nanoparticles in Fig. 7.1c and 7.1d is the preparation step of the MOCs, the nanoparticles in Figure 7.1b were prepared using "one-pot" MOC whereas the nanoparticles in Figure 7.1d were prepared using "single precursor" MOC prepared individually as Ni-MOC and Fe-MOC, and were mixed before evaporation of the hexane phase. There is not a large difference between the resulting nanoparticle size, however the "single precursor" prepared separately appear to be slightly "faceted" as visible in Figure 7.1d.

The SAED patterns is consistent with a NiO phase similar to that presented by Bau et al.¹²⁴ The crystallinity is slightly higher for the Ni-Fe nanocrystals prepared using conventional synthesis compared to the microwave synthesis, also visible in the selected area electron diffraction (SAED) pattern where more dots are visible. The microwave prepared nanoparticles also showed less well-defined edges than those prepared conventionally (see Figure 7.1d). This might be attributed to a faster heating rate, which could result in a less crystalline lattice. The incorporation of Ni and Fe in the nanoparticles followed a nearly ~ 1:1 relation, yielding the desired Ni:Fe composition. We noted however that the metal concentration of the "single precursor" oleate-complexes varied slightly for Ni and Fe. These differences could have been introduced during the washing step of the oleate complex due to a polymerization

process induced by contact with the water phase containing excess of salts. The total metal concentration was therefore determined using ICP-OES before the NP synthesis to have a better control over the nominal composition.

X-ray diffraction of the Ni-Fe nanoparticles are shown in Figure 7.2. The synthesis of the “one-pot” complexes are presented in (a-c) have a face centered cubic (fcc) phase, also reported by Bau et al. for mixed Ni-Fe nanocrystals using the oleate route.^{124,199} The Ni-Fe oxides prepared from “single precursors” shown in (d) have clearly different XRD pattern. There was an additional phase with reflections of hexagonally closed packed (hcp) Ni phase in addition to the fcc phase. The hcp phase is much less frequently reported for Ni oxides since it is a less stable phase²⁰⁵. The XRD of the pure Ni₁₀₀ and Fe₁₀₀ oxides showed that Fe crystallizes in the fcc structure and Ni in the hcp structure (Figure S7.2), which is in accordance with previous reports by Bau et al.¹²⁴. The presence of an hcp phase in the “single precursor” Ni₆₀Fe₄₀/C nanocrystal could alternatively be explained by formation of separate Ni and Fe phases during the decomposition step, and a less well-mixed Ni-Fe phase with metallic Ni contributions favored over a pure rocksalt Ni-Fe oxide phase which can be achieved with “one-pot” synthesis.

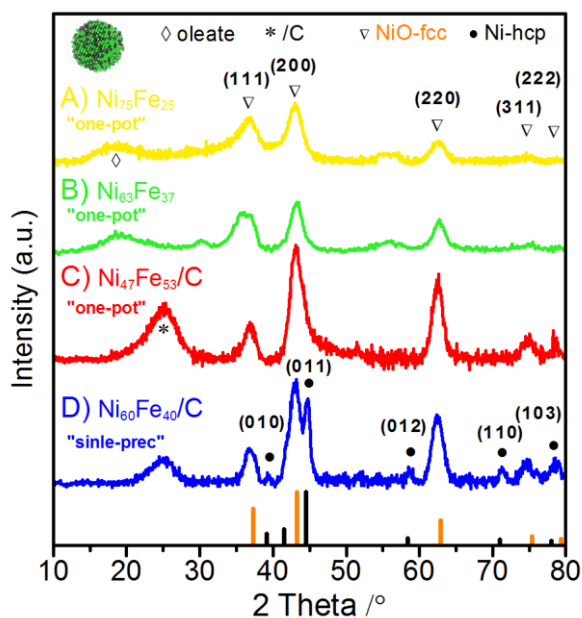
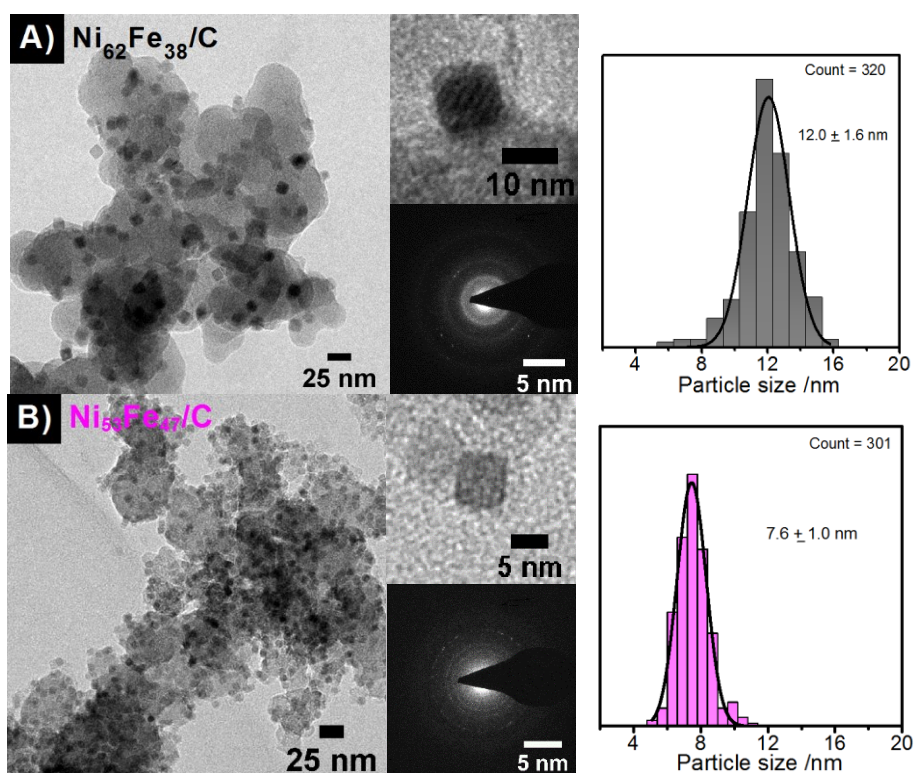


Figure 7.2. XRD of supported Ni-Fe oxide nanocrystals synthesized with the metal-oleate-complex (MOC) route. (a) unsupported Ni₇₅Fe₂₅ prepared from “one-pot” MOC using microwave-assisted synthesis at 300 °C for 15 min with a heating ramp of 18°/min. The MOC was prepared as one-pot (b) Unsupported Ni₆₃Fe₃₇ using microwave irradiation at 300 °C for 15 min with a heating ramp of 70°/min. The MOC was prepared as one-pot. (c) Carbon supported Ni₄₇Fe₅₃/C using microwave irradiation at 300 °C for 30 min with a heating ramp of 5°/min. The MOC was prepared as one-pot. d) Ni₆₀Fe₄₀/C prepared

using microwave irradiation at 300 °C for 30 min with a heating ramp of 5°/min. The bottom lines shows reference patterns of NiO-fcc (pdf#01-071-1179), and Ni-hcp (pdf#00-045-1027).

7.2.2. Shape selected Ni-Fe nanoparticles

Controlling size and shape is desirable in order to prepare model systems where chemical reactions can be studied at a well-defined surface.⁶ Previous work on Fe oxides via oleate synthesis have shown that the shape can be drastically altered by introducing small amounts of a stabilizing salt.¹²⁵ We used quaternary ammonium salts and sodium oleate to obtain nanocubes with a ~10 nm edge length and (1 1 1) faceted nanoparticles (Figure 7.3).



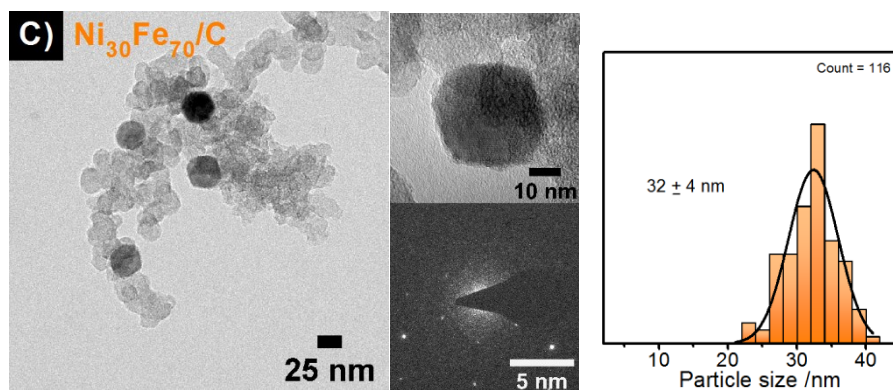


Figure 7.3. Shape selected Ni-Fe oxide nanoparticles supported in Vulcan XC-72r. a) $\text{Ni}_{62}\text{Fe}_{38}/\text{C}$ nanocube synthesized by additions of 2:1 MOC:Na-OL b) $\text{Ni}_{53}\text{Fe}_{47}/\text{C}$ nanocube synthesized by additions of 2:1 MOC:TOBr c) $\text{Ni}_{30}\text{Fe}_{70}/\text{C}$ synthesized by additions of 1:1 MOC:TOBr.

Additions of 2:1 ratio of MOC:Na-OL to the reaction and using squalene as solvent resulted in stabilization of well-defined Ni-Fe nanocubes with a size of 12 nm. Additions of quaternary ammonium salt (TOBr) in a 2:1 ratio in squalene resulted in irregularly shaped Ni-Fe oxide nanoparticles without a defined shape. Additions of 2:1 ratio of MOC:TOBr in 1-octadecene as solvent instead yielded nanocubes with an edge length of 7 nm (Figure 7.3b). According to previous reports, the shape is highly sensitive to the amount of added salt, where octahedra have been shown to form only within a narrow range. Increasing the amount of TOBr to a ratio of 1:1 indeed resulted in a change towards a (1 1 1) faceted nanoparticles accordingly.¹²⁵ However, the shape more revealed cuboctahedra with corners cut by (1 0 0) planes, described in earlier reports during growth phase of PtNi octahedra.¹⁴¹ Shavel et al. also observed a similar shape at low TOBr concentrations of shaped FeO via the oleate route.¹²⁵ XRD of the shaped Ni-Fe nanoparticles (Figure 7.4a) revealed that the shaped Ni-Fe oxides prepared with different reaction conditions also had different phases. The nanocube prepared by additions of Na-OL in squalene could be attributed to a mixture of rocksalt, Fe_2O_3 and NiFe_2O_3 (Figure 7.4a), whereas the nanocube prepared by additions of TOBr had mainly metallic hcp reflections with small contributions of Fe_2O_3 and/or and NiFe_2O_3 (Figure 7.4b). Increased amount of TOBr resulted in formation of a Fe_2O_4 phase, where traces of the rocksalt phase were no longer visible.

Attempts to further increase the TOBr concentration resulted in larger particles to judge from the XRD reflections (Figure 7.4b). Larger particles size could cause the nanoparticles not to stick well to the carbon support, and a lower metal loading was confirmed with ICP-OES.

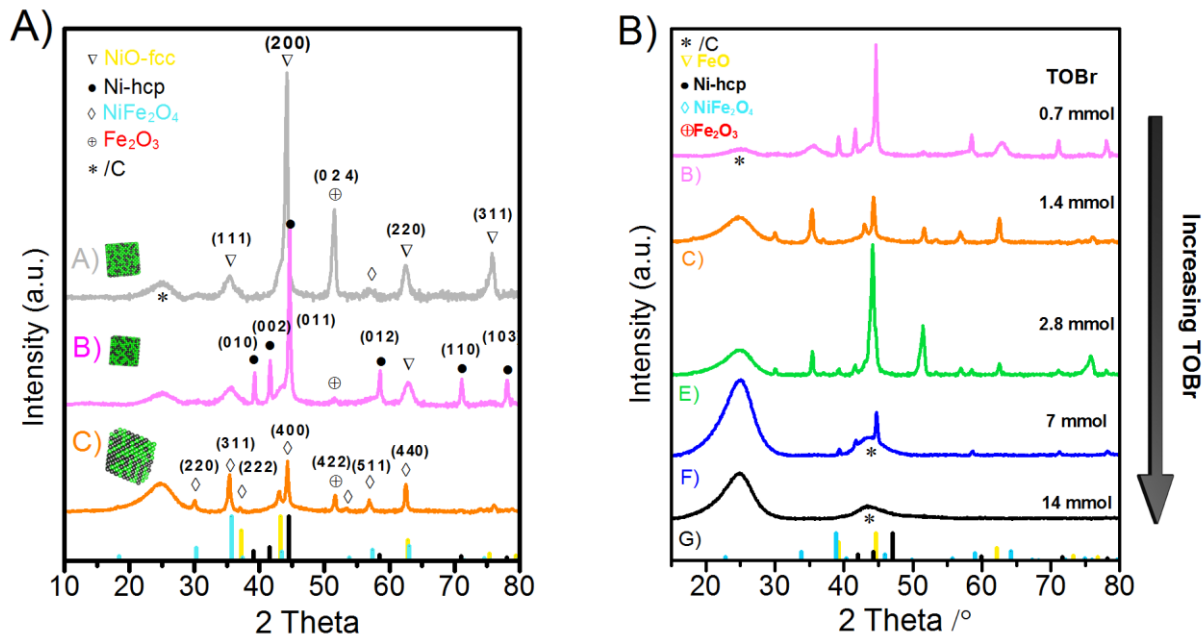


Figure 7.4. (a) XRD of shape selected Ni-Fe oxide nanoparticles supported on Vulcan XC-72r with different shapes (A) $\text{Ni}_{62}\text{Fe}_{38}/\text{C}$ nanocube prepared by 1:1 MOC:Na-OL in Squalene (B) $\text{Ni}_{53}\text{Fe}_{47}/\text{C}$ nanocube prepared by 1:1 MOC:TOBr in 1-octadecene (C) $\text{Ni}_{30}\text{Fe}_{70}/\text{C}$ cuboctahedra prepared by 1:1 MOC:TOBr in 1-octadecene. (b) The $\text{Ni}_{53}\text{Fe}_{47}/\text{C}$ nanocube shown in (A) with increasing concentration of TOBr, starting with 1:1 MOC:TOBr in 1-octadecene. (A) and (B) are repeated to facilitate view. The stars indicate the reflection of the carbon support. The bottom lines shows reference patterns of NiO-fcc (yellow, pdf#01-071-1179), Ni-hcp (black, pdf#00-045-1027), and NiFe_2O_4 (light blue, pdf#01-086-2267), Fe_2O_3 (red, #)

Hence this study shows that it is possible to obtain shape selected Ni-Fe nanocrystals, however in order to obtain high quality octahedra, the reaction conditions must be further optimized with respect to ratio of metal oleate, salt, solvent, and surfactants. The shape selected synthesis also shows that despite similar shape and Ni:Fe compositions, the phase is highly sensitive to additions of salt as well as the selection of solvent together with the salt, which did not all result in nanoparticles. Ni-Fe nanocubes with similar compositions and a narrow size distribution could on the other hand be obtained by two different approaches.

7.2.3. Optimization of annealing conditions

Annealing conditions were optimized for the carbon supported Ni-Fe nanocrystals, to remove capping oleate ligands. A few selected nanoparticles were heated to different temperatures in controlled synthetic air atmosphere and the OER activity was used as a measure to evaluate the effect of the

annealing step. Cyclic voltammograms (CVs) were measured in 0.1 M KOH by potential cycling between 1-1.75 V_{RHE} after each annealing temperature. The geometric current density at 1.53 V_{RHE} ($\eta=300$ mV) increased slightly and was highest at 200 °C (see Figure 7.5a). Increasing the annealing temperature above 250 °C resulted in a loss of OER activity (see Figure 7.5). The mass based activity showed that the difference in activity initially observed was due to small differences in geometric metal loading. The activity remained nearly identical, suggesting that annealing in air up to 250°C actually did not have a major impact on the OER activity (Fig. 2b). Inspection of the first 150 cycles comparing the as-prepared catalysts with the annealed catalysts also showed similar “activation” behavior (Figure S7.3).

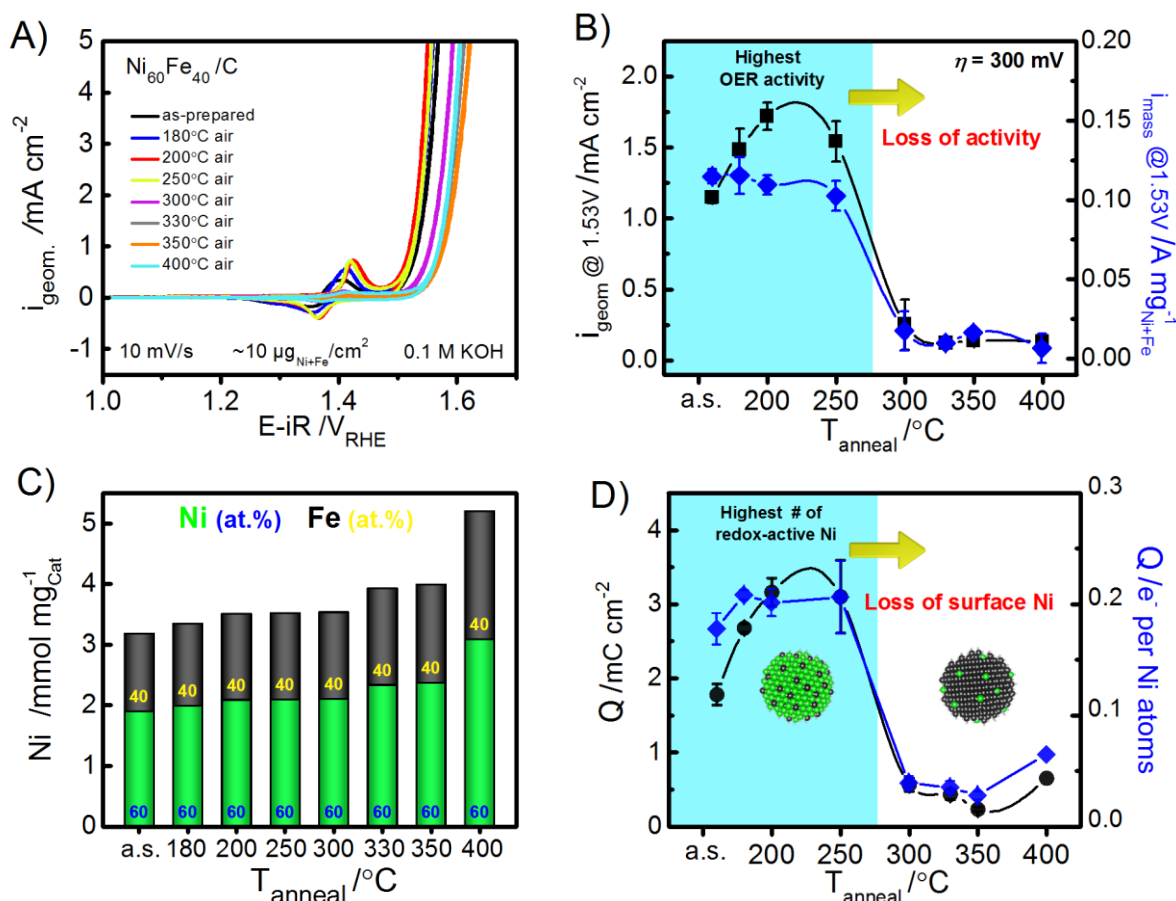


Figure 7.5. Investigation of annealing temperature on the OER activity in mixed Ni-Fe nanocatalysts, at different annealing temperatures in controlled gas atmosphere (synthetic air). **(a)** CVs recorded at 100 mV/s. **(b)** Geometric activity (*left axis*) and mass based activity (*right axis*) as a function of annealing temperature. **(c)** Elemental analysis of Ni (*green bars*) and Fe (*black bars*) in nanocatalyst powders for the different annealing temperatures determined by ICP-OES. The catalyst composition ($Ni_{100-x}Fe_x$) is indicated as atomic % at the bottom of each bar. **(d)** Redox active Ni species estimated by integration of the $Ni^{2+/+3}$ redox peak, shown as the geometric normalized

charge (*left axis*) and the mass based redox electrons (electrons transferred per Ni atoms) based on the moles of Ni on the electrode determined by ICP-OES.

We noted that the $\text{Ni}^{+2/+4}$ redox peak increased upon annealing up to $\sim 200^\circ\text{C}$ (Figure 7.5a) which indicate that surfactants may have been left at the surface below this annealing temperature. Reasonable high OER activities have been observed for mixed Ni-Fe oxides,^{69,107,199} however the generally higher overpotentials is thought to be a result of the limited catalytically accessible surface area in comparison to the Ni-FeOOH (oxyhydroxide) that show activity that likely extends to the bulk.^{66,87,109} The overall OER activity for the catalyst investigated here is lower than that of the Ni-FeOOH catalysts investigated in previous Chapters, which indicates that the catalysis is confined to the surface of the nanoparticle oxide.

ICP-OES analysis of the total metal content of the catalyst powders showed very small losses of material up to annealing temperatures of 350°C (Figure 7.5c). Annealing at 400°C showed a higher loss of metal which indicate that the structure started to decompose. The catalyst composition ($\text{Ni}_{100-x}\text{Fe}_x$) was not apparently affected by the annealing temperature, which remained $\text{Ni}_{60}\text{Fe}_{40}$ up to 400°C . The $\text{Ni}^{+2/+3}$ redox charges charge were evaluated based on integration of the area under the redox peak (Figure 7.5d). The number of electrons transferred per Ni atoms were estimated as described in Chapter 3, using the total moles of Ni on the electrode determined by elemental analysis. This clearly demonstrated that the OER activity was correlated to the redox active Ni-species at the surface, which was decreasing with increasing annealing temperature. Based on these facts, the drastic loss of the $\text{Ni}^{+2/+3}$ redox peak at annealing temperatures above 250°C , which coincide with a loss of the OER activity, might have been due to either a loss of surface concentration of Ni, or due to a loss of catalytically accessible surface sites (both Ni+Fe). It has been previously demonstrated that different annealing conditions might induce a compositional segregation of nanoparticles.²⁰⁶ Segregation of atoms as an effect of annealing conditions and temperature have been observed before in bimetallic PtNi or PtCo core shell nanoparticles,^{207,208} which is generally explained by surface energies and atomic radius, where larger atomic radius and/or a lower surface energy tend to segregate to the free surface, meaning that Ni will segregate to the surface.²⁰⁹ In order to draw more accurately conclusions about the Ni-Fe nanoparticles investigated here, further characterizations will be needed in order to determine oxidation state. Based on the electrochemical data, a Fe-rich surface would be consistent with a lower redox peak.

The XRD as a function of annealing temperature showed that the phase identified in the as-prepared catalysts (hcp) is present also up to annealing temperatures of 250°C . At higher temperatures, the hcp-reflections disappears and left are reflections from the NiO rocksalt phase (Figure 7.6). This also coincide with loss of the OER activity that occurs above 250°C . At annealing temperatures of 400°C , there was a

broadening of the NiO (1 1 1) reflection, which at higher annealing temperatures (700°C) converted into NiFe₂O₄ (Figure S7.4).

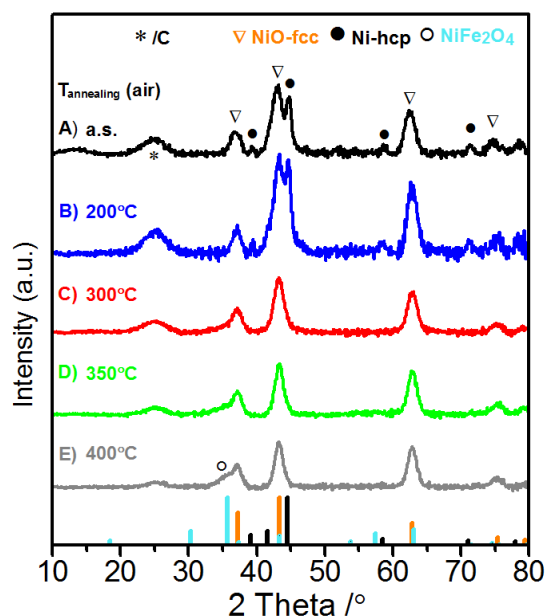


Figure 7.6. Powder XRD of the Ni₆₀Fe₄₀/C nanocatalyst at different annealing temperatures in air for 1 h. (A) as-prepared (B) annealed at 200 °C (C) annealed at 300 °C (D) annealed at 350 °C (E) annealed at 400 °C. The bottom lines show reference patterns of NiO-fcc (pdf#01-071-1179), Ni-hcp (pdf#00-045-1027), and NiFe₂O₄ (pdf#01-086-2267).

The loss of OER activity associated with the loss of redox active Ni also coincided with the loss of hcp reflections according to the XRD. Since we know from the XRD of the Ni-only catalyst (shown in Figure S7.2) that Ni nanoparticle catalysts only has hcp reflections, we could draw a parallel between these three factors; the hcp XRD reflections, the Ni^{+2/+3} redox peak, and the OER activity. It hence appear as if the activity is determined by the size of the Ni^{+2/+3} redox peak. This could either mean that the OER activity is higher when there is a higher surface concentration of Ni, or that the OER activity is higher as a cause of a larger electrolyte accessible surface area in the case of the hcp structure despite an unchanged surface composition. Which one that controls the OER activity would need further investigations in terms of determination of surface composition, surface area, and roughness.

To conclude, an annealing temperature of 200 °C was as selected as the optimal temperature to ensure removal of possible surfactants without loss of OER activity. This choice was based on the catalytic activity and redox peak. We could have chosen slightly lower annealing temperature, however the Ni redox peak was still shifted cathodically which could be an indication of remains of surfactants.

7.2.4. OER activity on shaped oxides

The OER activity was investigated for shape selected metal oxides and compared to the activity of the Ni-Fe(OOH) catalyst investigated in previous Chapters. CVs of selected Ni-Fe nanocatalysts annealed at 200 °C for 1h in air, after an initial conditioning step of 150 cycles in 0.1 M KOH are shown in Figure 7.7.

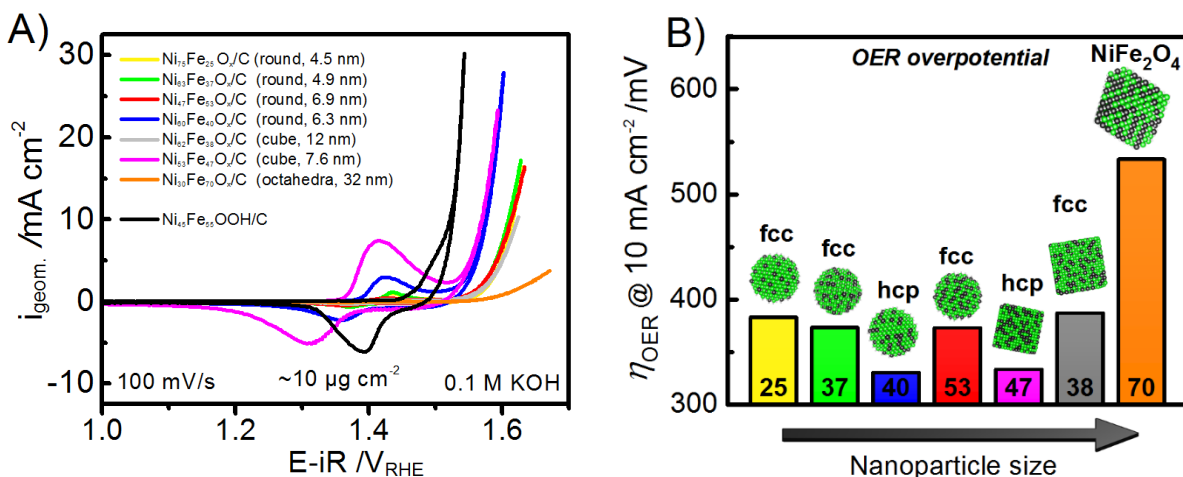


Figure 7.7. (a) CVs of selected Ni-FeOx electrocatalysts with different size, shape, and phase. (b) Overpotential at 300 mV for the catalysts shown in (a). The current density was extracted from quasi-stationary state measurements.

The Ni-Fe oxide nanocatalysts prepared by the oleate route showed lower OER activity than the Ni₄₅Fe₅₅(OOH)/C catalyst (Figure 7.7, *black curve*). To judge from the Ni^{+2/+3} redox peak, the NiFe nanocatalysts showed a large variation, however the catalysts with highest OER activity show a similar sized redox peak as the Ni₄₅Fe₅₅(OOH)/C catalyst.

Despite similar Ni-Fe composition, the OER activity varied substantially for the mixed Ni-Fe oxides. The influence of the size when comparing the OER activity on spherical nanoparticles appear to have minor influences in the investigated range. The spherical Ni₆₀Fe₄₀/C nanocatalyst prepared with “single precursor” metal oleates (previously investigated in the annealing study) however showed highest OER activity of all the spherical shaped Ni-Fe nanocatalysts. The shaped nanoparticles on the other hand showed large variation, where the smallest cube of ~7.6 nm showed highest OER activity. The cuboctahedra with a size of ~ 32 nm showed lowest OER activity. Whether this is due to size effects or other effects would need further investigations.

What is directly evident from the CVs presented in Figure 7.7a is the large variation in the size of the Ni^{+2/+4} redox peak. The redox peak is larger for the catalyst with higher OER activity, despite a similar bulk content in the nanocatalysts. What appear perhaps more interesting is that the Ni-Fe nanocatalysts with highest activity consistently show reflections in the XRD associated with hcp Ni. The catalysts with lower activity lack these reflections. As discussed above, this raises questions whether the OER activity is related to the phase or if the reflections signify a Ni-rich surface, or a surface that is more hydrated and catalysis happens in several monolayers (due to higher roughness).

To address whether the physical surface area could play a role, we measured BET N₂ adsorption isotherms, see attached values in Table 7.1 below for a summary of BET and activity. The BET surface area amongst the investigated nanocatalysts was not remarkably different. Evident was however that the Ni₄₅Fe₅₅(OOH)/C catalyst had a significantly larger BET surface area than the nanocatalysts. BET of the carbon support without catalyst revealed that the surface area was different depending on the post treatment and annealing step of the carbon support. The surface area for the nanocatalysts where subjected a more harsh treatment to remove surfactants, and the carbon showed a quite low BET area (97 m²/g) in comparison to the Vulcan XC-72r carbon support used for the Ni₄₅Fe₅₅(OOH)/C catalyst (187 m²/g).

Table 7.1. Parameters for the Ni-Fe nanocrystal electrocatalysts; OER activity, BET, size, shape.

0.1 M KOH	Catalyst	Metal loading [wt%]	Size [nm]	η_{OER} @ 10 mA cm ⁻² [mV]	BET surface area [m ² /g]	Synthesis conditions	Annealing [°C,]	Shape	Phase
A	Ni ₇₅ Fe ₂₅ /C	-	4.5	383	-	mw,300°C-15'' (dt70°), OD, one-pot	200°C-1h-air	Round	fcc
B	Ni ₆₃ Fe ₃₇ /C	-	4.9	373	-	mw,300°C-15'' (dt18°), OD, one-pot	200°C-1h-air	Round	fcc
C	Ni ₄₇ Fe ₅₃ /C	11	6.9	373	83	cv, 300°C-30'' (dt 5°), OD, one-pot	200°C-1h-air	Round	fcc
D	Ni ₆₀ Fe ₄₀ /C	20	6.3	330	-	cv, 300°C-30'' (dt 5°), OD, single prec	200°C-1h-air	Round	fcc+hcp
E	Ni ₆₂ Fe ₃₈ /C	21	12	387	114	cv, 300°C-30'' (dt 5°),Sq+ NaOL (1:1), single prec	200°C-1h-air	Cube	Fe ₂ O ₃
F	Ni ₅₃ Fe ₄₇ /C	20	7.6	333	77	300°C-30'' (dt 5°),DO, TOBr(1:1), single prec	200°C-1h-air	Cube	hcp
G	Ni ₃₀ Fe ₇₀ /C	10	32	533	-	300°C-30'' (dt 5°),OD, TOBr(2:1), single prec	200°C-1h-air	Cuboctahedra	Fe ₂ O ₃ + Fe ₃ O ₄
H	Ni ₅₅ Fe ₄₅ (OOH)/C	16	-	291	167	Solvothermal*	200°C-1h-air	Layered	oxyhydroxide

7.2.5. Stability test up to 1000 cycles

The stability was tested up to 1000 potential cycles between 1-1.75 V_{RHE} . The two cubes and one spherical oxide were selected for comparison. The measurements were carried out at similar geometric metal loading to eliminate discrepancies from mass diffusion etc. The metal loading was determined by elemental analysis. The spherical $Ni_{47}Fe_{53}/C$ nanocatalyst showed good stability up to 1000 cycles (Figure 7.8a). Of the two nanocubes, the $Ni_{62}Fe_{38}/C$ nanocube with the larger size showed lowest activity and poor stability (Figure 7.8b). The best stability and activity was observed for the smallest nanocube, which had metallic hcp XRD reflections (Figure 7.8c). Remarkable was that all catalysts showed large shifts in the position of the Ni redox peak upon cycling, hence a change in the associated $Ni^{2/+3}$ redox process. The $Ni_{53}Fe_{47}/C$ nanocube with highest activity (Figure 7.7c) also showed the highest peak shift. The anodic peak ($E_{p,a}$) shifted with 40 mV during the first 1000 cycles, whereas the cathodic peak ($E_{p,c}$) shifted 30 mV. For the spherical $Ni_{47}Fe_{53}/C$ nanocatalyst the corresponding E_a and E_c peak shifts were 20 and 0 mV. For the less active $Ni_{62}Fe_{38}/C$ nanocube the peak shift could not be accurately estimated due to the poor OER stability which may also introduce a peak shift. This could indicate that irreversible oxidation processes (phase changes or similar) happening on the anodic scan does not show the same dependence to underlying oxide surface as the reduction processes. Yet, the $Ni^{2/+3}$ redox peak appeared reversible on a short short time scale.

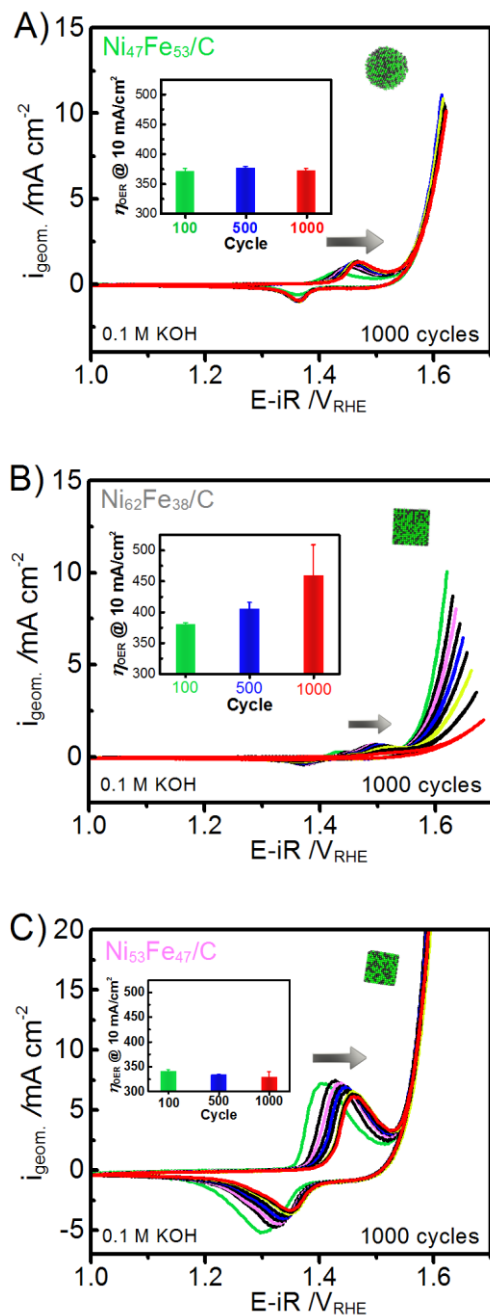


Figure 7.8. CVs up to 100 cycles of selected nanocatalysts **(a)** spherical $\text{Ni}_{47}\text{Fe}_{53}$ **(b)** $\text{Ni}_{62}\text{Fe}_{38}/\text{C}$ nanocube and **(c)** $\text{Ni}_{53}\text{Fe}_{47}/\text{C}$ nanocube. The CVs were recorded at 100 mV/s in 0.1 M KOH at a rotation speed of 1600 rpm.

Turnover frequencies were estimated both using the total metal loading and based on the integration of the $\text{Ni}^{2+/+3}$ redox peak assuming that this would be related to the catalytically accessible sites (Figure 7.9).

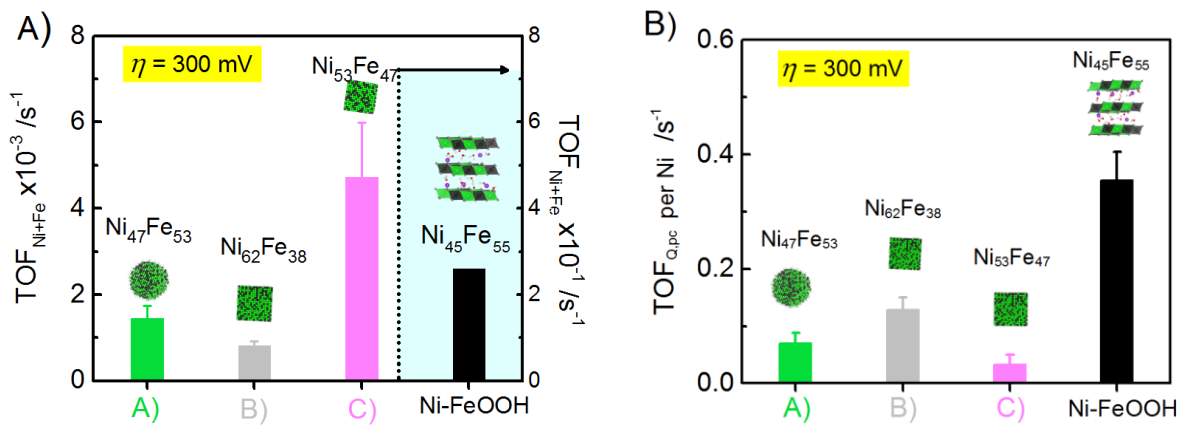


Figure 7.9. Turnover frequency of carbon supported shaped spherical and shaped oxides in comparison to a carbon supported Ni-Fe/C oxyhydroxide investigated in Chapter 6 (a) TOF normalized to total metal loading determined by TXRF analysis. The $\text{Ni}_{45}\text{Fe}_{55}/\text{C}-\text{OOH}$ catalysts had much higher TOF and is therefore located on the right axis. Notice that the left and right axis have different scaling. (b) TOF normalized to the integrated $\text{Ni}^{2+/+3}$ redox peak charge. Here the oxides are comparable to the Ni-FeOOH and are therefore located on the same axis.

It is obvious from Figure 7.9 above that the nanocatalysts have lower activity than the Ni-FeOOH catalyst. The mass based TOF differed by a factor of 100 between the $\text{Ni}_{53}\text{Fe}_{47}/\text{C}$ nanocube and the $\text{Ni}_{45}\text{Fe}_{55}\text{OOH}$ catalyst at similar metal loadings (Figure 7.9a). For the least active $\text{Ni}_{62}\text{Fe}_{38}/\text{C}$ nanocube, the TOF differed by a factor of ~ 3000 . This could indicate that the nanocatalysts not have “volume activity”⁶⁶ as the Ni-FeOOH catalyst, and therefore catalysis is likely restricted to a confined area. The TOF normalized to the integrated $\text{Ni}^{2+/+3}$ redox peak (Figure 7.9b) showed the inverse trend, i.e. that the least active catalyst actually is more active assuming that the peak corresponds to the number of active sites. This is however not entirely justified up to date (discussed in previous Chapters) and additional errors may be introduced when evaluating a small area. For the Ni-Fe(OOH) catalysts it is assumed that the catalysis extends to the bulk, and the TOF based on the redox peak is usually only slightly higher than the mass based TOF, which could indicate that all active sites are actually contributing to the catalytic current. Based on the large variation of the redox active Ni observed amongst the Ni-Fe oxide nanocatalysts, we cannot exclude that the concentration of surface Ni is also different from the bulk composition. This would need further investigations.

7.2.6. TEM and elemental composition after 1000 cycles

As discussed in previous sections, despite a stable OER performance up to 1000 cycles, the $\text{Ni}^{2+/+3}$ redox peak was shifting significantly for the Ni-Fe oxide nanocatalysts. The two nanocubes also showed very different stability and a significant difference in the size of the redox peak. To address whether this could be correlated to morphological changes, we used transmission electron microscopy (TEM) before and after 1000 cycles to compare the two nanocubes, see Figure 7.10.

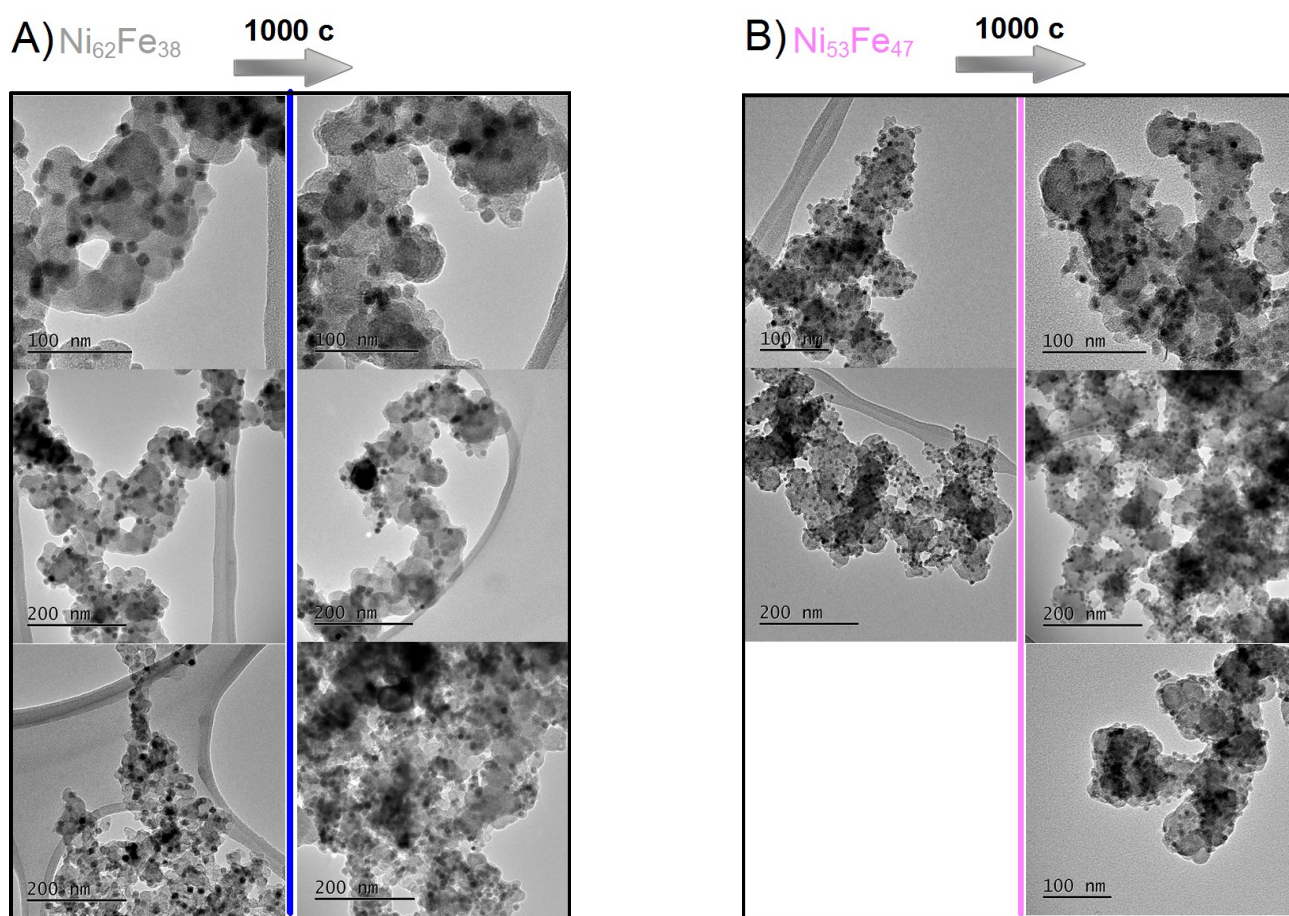


Figure 7.10. TEM images of as-prepared catalysts (*left panels*) and after 1000 cycles between ~ 1 - 1.75 V_{RHE} in 0.1 M KOH (*right panels*) **(a)** $\text{Ni}_{62}\text{Fe}_{38}/\text{C}$ nanocube catalyst **(b)** $\text{Ni}_{53}\text{Fe}_{47}/\text{C}$ nanocube catalyst.

TEM images before and after 1000 potential cycles in 0.1 M KOH did not show significant changes in size or morphology. The cubic shape was still visible, however some of the cubes appeared to have slightly

more rounded edges. A correlation between the anodic peak shift and a distinct change in shape was therefore not possible to establish.

To address the metal loading and elemental composition, TXRF analysis was measured before and after the 1000 cycle stability test. This confirmed no large loss of metal or composition (Figure 7.11), suggesting that the stability performance of the Ni-Fe nanoacatalysts up to 1000 cycles was excellent. The decrease in the OER activity observed at the Ni₆₂Fe₃₈/C nanocube is therefore not reflected in a significant loss of bulk material, and must therefore be ascribed to other changes. In order to establish clear correlations between peak shift, OER activity, and possible changes at the surface or bulk, it would be necessary to determine the surface concentration of Ni and Fe, and how these are changing upon potential cycling.

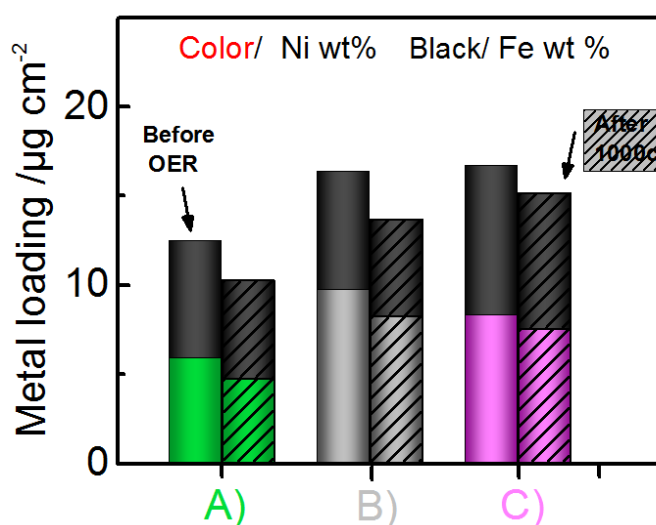


Figure 7.11. TXRF analysis of selected Ni-Fe nanocatalysts before and after 1000 cycles in 0.1M KOH. **(A)** Spherical Ni₄₇Fe₅₃ **(B)** Ni₆₂Fe₃₈/C nanocube and **(C)** Ni₅₃Fe₄₇/C nanocube catalysts.

7.3. Conclusions

Activity correlations of well-defined Ni-Fe oxide surfaces are of high interest in order to understand fundamental interaction between OER intermediates and the oxide surface. We present a series of shape selected mixed Ni-Fe oxide nanocatalysts for the oxygen evolution reaction, prepared by the metal oleate route. Nanocrystals obtained via the oleate route were supported on Vulcan XC-72r for application as nanocatalysts for the electrochemical water splitting reaction. Ni-Fe catalytic activity has been shown sensitive to composition. Therefore, we tailored the synthesis to obtain different oxide surfaces with different orientations and with similar composition for an accurate comparison between surfaces properties and the OER activity. We achieved this by addition of salts (tetraoctylammonium bromide and sodium oleate) in combination with different solvents. In this way, we obtained spherical, cubic and cuboctahedrally shaped Ni-Fe nanoparticles with similar compositions. However, the phase turned out to be highly sensitive to the reaction conditions and as a result, we obtained a mixture of different phases; fcc, hcp, and spinel Ni-Fe oxides. Surfactants were removed by annealing in controlled air atmosphere, which removed the initially present hcp-Ni phase, which however proved stable up to 400 °C.

The activity for the oxygen evolution reaction showed a clear differences for oxides with different phases, where the oxide phase and surface composition appeared to be a more strongly controlling factor than shape. We could establish a clear correlation between OER activity and the presence of Ni, where metallic Ni resulted in an overall higher OER catalytic activity. Some of the oxide surfaces showed good stability up to 1000 cycles, however there was a continuous change reflected in the Ni^{+2/+3} redox peak, which shifted upon cycling. TEM images confirmed no significant morphological changes, however the cubic particles appeared to have slightly more rounded corners. The activity was compared to the Ni-Fe oxyhydroxide catalyst, where we could conclude that the Ni-Fe oxides have inferior OER activity. This could mean a smaller number of catalytic accessible surface sites and that catalysis is likely confined to the outer boundaries of the oxide surface. An interesting observation was that a large Ni^{+2/+3} redox peak appeared to benefit the catalytic activity of the Ni-Fe oxide catalysts. This could indicate that the surface concentration of Ni play an important role in catalysis, however may reflect a larger surface roughness. More investigations will be needed in order to establish a more clear correlation between phase, shape and OER activity.

Supporting Information

Electrochemical water oxidation on shape-selected Ni-Fe oxide nanocrystal catalysts

This Chapter is based on unpublished data

Mikaela Görlin¹, Manuel Gliech¹, Anna Loiudice², Raffaella Buonsanti², Peter Strasser¹

Contact: pstrasser@tu-berlin.de

¹*Technical University of Berlin, Department of Chemistry, , Straße des 17. June 124, 10623, Berlin, Germany*

²*École Polytechnique Fédérale de Lausanne (EPFL), Rue de l'Industrie 17, Sion, 1950, Switzerland*

S7.1. Ni-Fe nanoparticle synthesis

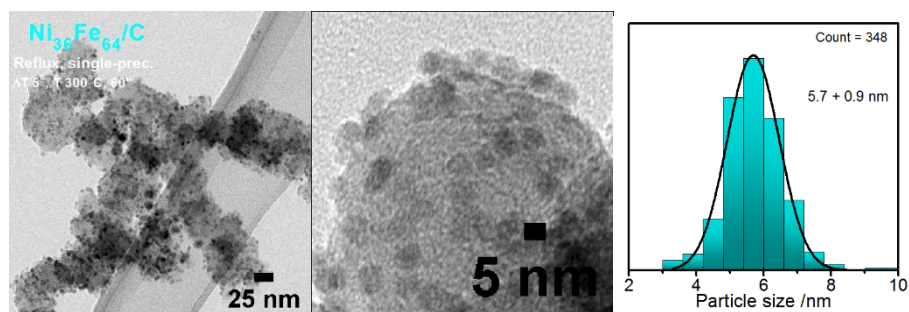


Figure S7.1. Nanoparticles synthesized with a decomposition time of 60 min, at different magnifications. The right most image shows the nanoparticle size distribution.

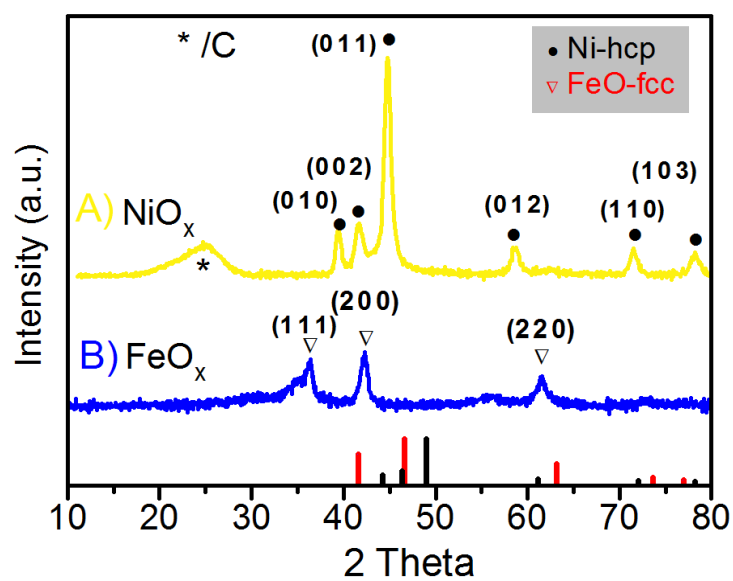


Figure S7.2. XRD of the as-prepared pure Ni/C and Fe nanoparticles.

S7.2. Annealing temperature optimization

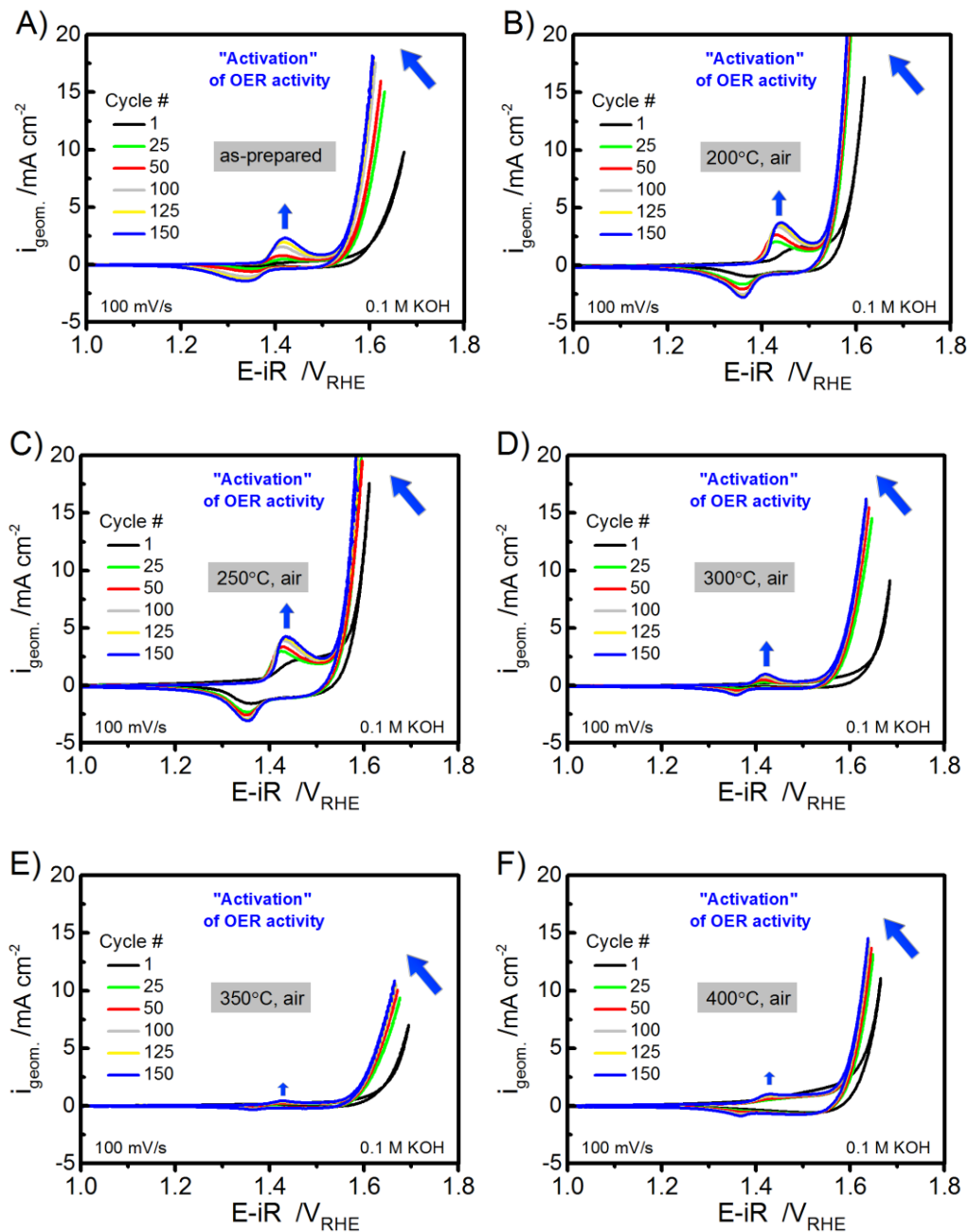


Figure S7.3. CVs at 100 mV/s shown for the first 150 cycles for $\text{Ni}_{60}\text{Fe}_{40}$ spherical nanocatalysts after annealing at different temperatures for 1 h in air. (a) as-prepared (b) annealed at 200 °C (c) annealed at 250 °C (d) annealed at 300 °C (e) annealed at 350 °C (f) annealed at 400 °C. CVs were recorded in 0.1 M KOH used without further purification, at a catalyst loading of $\sim 10 \mu\text{g cm}^{-2}$ determined by ICP-OES analysis.

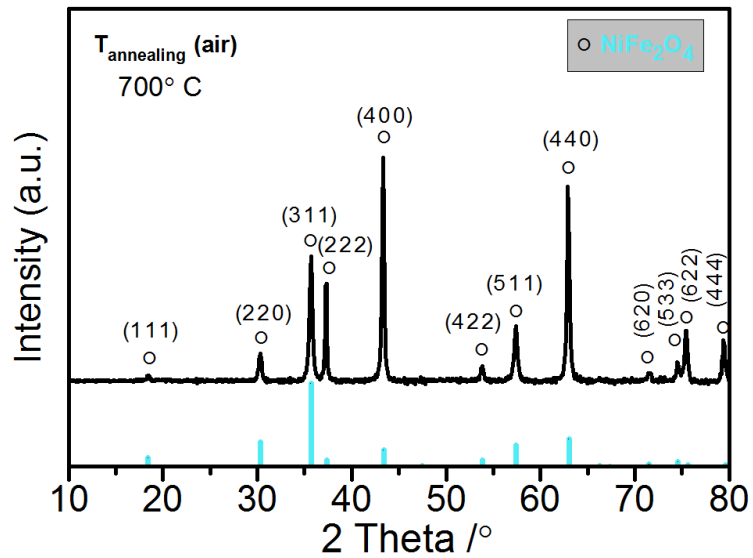


Figure S7.4. Powder XRD of the $\text{Ni}_{60}\text{Fe}_{40}/\text{C}$ nanocatalysts annealed at 700° C in air for 1h. The bottom lines show reference patterns of NiO-fcc (pdf#01-071-1179), Ni-hcp (pdf#00-045-1027), and NiFe_2O_4 (pdf#01-086-2267).

Chapter 8

SUMMARY & OUTLOOK

8.1. Summary of Chapters 3-7

In Chapter 3, we explored the interplay between the oxygen evolution reaction dynamics in mixed Ni-Fe oxyhydroxide using operando differential electrochemical mass spectrometry (DEMS). Mixed Ni-Fe catalyst with varying composition were evaluated for faradaic efficiency of O₂ and distribution of faradaic current into redox state changes versus oxygen evolution. The DEMS measurements showed that the charge contributions to redox state changes of Ni-Fe(OOH) catalysts was minimal in comparison to the charge injected into redox state changes of the Ni(OH)₂ catalyst, based on higher faradaic efficiencies for Ni-Fe. We complemented the study using in situ X-ray absorption spectroscopy (XAS) to deduce the local atomic and electronic state during catalysis. We recorded XAS both at the Ni and Fe *K*-edges and we could confirm that the Ni-catalyst showed a higher degree of oxidation state change than the mixed Ni-Fe catalysts. The XAS data hence confirmed the DEMS results; the Ni catalysts underwent oxidation state changes from +2 → +3/+4, whereas the Ni-Fe catalysts showed insignificant oxidation state changes above 4 % Fe. To reconcile the apparent low level of oxidized Ni in mixed Ni-Fe catalysts, we hypothesized that a kinetic competition between the metal oxidation process and the metal reduction step during O₂ release may lead to an insignificant accumulation of oxidized Ni⁺⁴ atoms, if the rate of the OER process (k_{OER}) exceeds that of the metal oxidation step ($k_{\text{M,OX}}$). This would reconcile many reports representing different formal charges. Here we are imagining that redox state change that are dependent on proton-coupled-electron transfer steps or the presence of non-concerted steps, might show a certain sensitivity to external influences such as electrolyte or underlying conductivity, which could enhance or slow down such processes. This might drastically change the ratio of the $K_{\text{M,OX}}/k_{\text{OER}}$ equilibrium, which becomes a measure of which reaction is dominating. Other results discussed in this Chapter was the importance of the distortion around the metal center. Based on the FT-EXAFS amplitudes, which reflect the degree of order around the metal center, we could see that high catalytic activity is associated with a highly distorted state. Whether the observed high amorphicity is a prerequisite for OER or a cause of high catalytic activity remains to explore.

In Chapter 4 we investigated a carbon supported Ni-Fe catalyst in a wider range of pH, from neutral to alkaline. Vulcan XC-72r was employed as support (denoted Ni-Fe/C or NiFeO_x/C). The oxygen evolution

activity was evaluated, which showed a decrease in the order of pH 13 < pH 9.2 < pH 7. We identified an instantaneous loss of activity when exposed to potential cycling in phosphate buffer (KPi) pH 7, which was correlated to a loss of redox active Ni species observed in the CVs. Switching forth and back from pH 13 – pH 7 - pH 13, showed that we could reactivate the activity in alkaline electrolyte after a drop to near zero activity in pH 7. The loss of OER activity in pH 7 was confirmed as an excessive loss of catalyst material, especially leaching of Ni. The recovery of the activity upon reactivation in pH 13 was confirmed as a stabilization of the metal leaching from the electrode, however resulted in a fractional change in composition. Using differential electrochemical mass spectrometry, we could confirm both loss and recovery of the OER activity in the electrolyte switching protocol pH13 - pH 7- pH13. We could confirm carbon corrosion in pH 7, with a Faradaic contribution of ~ 50 % of m/z 44 (CO_2). The same pH switching protocol was conducted in borate buffer (Bi) pH 9.2. Our study contributed to insight into loss of OER activity at lower pH to provide fundamental understanding of how the Ni-Fe catalyst performs in a wider range of electrolyte pH.

In Chapter 5, we investigated physical mixtures of Ni+Fe catalysts, which were prepared by mixing the less active parental $\text{Ni}(\text{OH})_2$ and FeOOH catalysts. We could achieve an extremely high oxygen evolution activity with this approach. We investigated local distribution of Ni and Fe using SEM-EDX elemental mapping, which confirmed a well-mixed phase. The degree of incorporation of Fe was also investigated on a local atomic level, where X-ray absorption spectroscopy was employed of physically mixed Ni+Fe catalysts. XAS measurements showed in agreement with the study in Chapter 3 that mixing FeOOH and $\text{Ni}(\text{OH})_2$ catalysts post synthesis, also resulted in a suppression of the Ni oxidation to its high-valent +4 state, confirming the findings Chapter 3 that Fe stabilizes low-valent Ni, or as hypothesized introduce a change in the $K_{\text{M,OX}}/k_{\text{OER}}$ equilibrium. By evaluating the FT-EXAFS amplitudes, we could confirm that a portion of the Fe was incorporated to the $(\text{Ni})\text{OH}_2$ catalyst, however exactly how much was difficult to accurately evaluate. Thus the study invite to a discussion about the contribution of the high catalytic current at low overpotentials of Ni-Fe site, and whether it is confined to surface sites or origins from bulk sites. Our study points towards that the high catalytic activity observed at Ni-Fe sites can be maintained at the outer boundaries of the hydroxide sheets, despite a full hydration of the film.

In Chapter 6, the influence of a catalyst support was explored, where both carbon and metal oxide supports were compared. The study showed that Vulcan XC-72r was the most compatible and easy applicable amongst the investigated supports (Vulcan XC-72r, oxCNTs, ATO). Carbon nanotubes also resulted in a reasonable high activity compared to Vulcan XC-72r, however ATO did not perform well with the Ni-Fe catalysts where difficulties occurred already in the early stage of immobilization of the

catalyst on the support. Ni-Fe/C catalysts supported on Vulcan XC-72r were further investigated with various compositions, and the influences of various parameters such as catalyst loading, electrolyte pH, and faradaic efficiency were explored. Carbon support were found to promote higher catalytic activity in comparison to unsupported catalysts. Measurements in higher pH also showed increased activity, which was correlated to a high fraction of redox active Ni visible in the voltammetric redox peak. By increasing the catalyst loading, we could reach a higher activity on carbon support in comparison to the unsupported catalysts. A nearly linear response between the catalyst loading and the amount of redox active Ni species were observed for the Ni-Fe/C catalysts, indicating a relation to the accessible surface area. Studies in different electrolyte pH showed that a relation existed between the OER activity and the redox active Ni species. In situ X-ray absorption spectroscopy measured of catalysts at a catalytic potential of 1.63 V_{RHE}, showed that carbon support resulted in a larger fraction of oxidized Ni^{+3/+4} atoms. A direct correlation could therefore be established between the observed increased area under the redox peak, oxidized Ni^{+3/+4} atoms, and increased catalytic activity. Despite a higher fraction of oxidized Ni^{+3/+4} in the Ni-Fe/C catalysts, the Ni *K*-edge shift was suppressed in comparison to the Ni/C catalyst, which confirmed the results presented in Chapter 3 and 5. This study demonstrated that external conditions may alter the equilibrium between the oxygen evolution rate and the metal oxidation rate; $K_{M,OX}/k_{OER}$. Whether this effect is due to a change in the underlying electrical conductivity introduced by the carbon support, or an effect of a larger number of electrolyte accessible sites, requires further investigations.

In Chapter 7, we presented shaped-selected Ni-Fe oxide nanocatalysts for the oxygen evolution reaction. These were prepared by the metal-oleate-complex (MOC) route, which yields highly crystalline nanoparticles with a narrow size distribution. By varying the reactions conditions, we could obtain spherical, cubic and cuboctahedrally shaped Ni-Fe oxide nanoparticles in the size range of 5-30 nm. The phase turned out to be highly sensitive to the selected synthesis conditions and a mixture of different phases were obtained; fcc, hcp, and spinel Ni-Fe oxides. The oxygen evolution activity showed a distinct difference for different oxides surfaces, which according to elemental analysis had similar bulk compositions. The oxide phase appeared to be a strongly associated with the catalytic activity, however whether the presence of a specific facet also influenced the catalytic activity would need further investigations. A correlation was established between the OER activity and the presence of hcp XRD reflections, which may be indicative of a high surface concentration (or electrolyte exposed number) of Ni^{+3/+4} species. The parental NiO catalyst were found to be stabilized in the hcp phase whereas the FeO in the fcc phase, hence it is likely that the hcp reflections are correlated to a higher surface concentration

of Ni species, and not directly to the specific phase. Optimization of the annealing step showed that exposure to more than 250 ° in air, most of the OER activity was lost, which coincided with a loss of hcp reflections. We speculate that the annealing temperatures above 250 °C induce a compositional segregation to form a Fe rich surface and a Ni rich core. It is also plausible that the surface area decreases, or that the new phase does not favor the OER activity. Some of the oxide surfaces showed good stability up to 1000 potential cycles between 1-1.75 V_{RHE}, however there was an observable change in the Ni^{+2/+3} redox peak, which underwent a significant peak shift upon cycling. TEM images confirmed no significant morphological changes; the cubes were still cubic shaped, however the edges appeared slightly more rounded after 1000 cycles. The activity was compared to the Ni-Fe(OOH) catalyst investigated in Chapter 3, and we could conclude that the Ni-Fe oxide nanocatalysts had inferior OER activity. This point towards that catalysis is confined to the surface of the crystal nanoparticles, which would lower the catalytic accessible area and the overall activity as a result. More investigations will be needed in order to establish clear correlations between phase, shape, and OER activity.

8.2. Outlook

The investigations of Ni-Fe electrocatalysts for electrochemical water oxidation is steadily increasing, yet many areas remain unexplored. This work provide contributions and insight into the catalytic site and structure of the Ni-Fe electrocatalyst. The origins of the synergisms between the Ni and Fe sites have been touched in this work, however remain still unresolved. We could contribute to a deeper understanding of the catalytic activity the Ni-Fe catalyst in terms of local atomic structure and metal redox states under catalytic conditions, which we investigated using in situ spectroscopic methods. We could also recognize underlying factors that influenced the activity and stability of Ni-Fe electrocatalyst in a wider range of pH. We have looked at various parameters such as coordination environments; redox charge transferred across the catalytic interface, and evaluated faradaic efficiencies for O₂ as a function of catalyst composition and under various reaction conditions. To reach a complete understanding the Ni-Fe catalyst, different perspectives needs to be considered. We started to look at shape-selected oxide nanoparticle catalysts and established synthesis methods to prepare defined oxide surfaces. With this, we have realized that many factors play a role in defining the catalytic activity, and a deeper insight into catalyst structure and redox states is needed before clear conclusions can be made regarding factors that defines the activity. The Ni-Fe catalyst system offers great advantages for alkaline applications, and fundamental understanding of what promotes the extremely high catalytic rate would be of interest for tailoring efficient anodes to be realized in technological applications.

List of Figures

Figure 1.1. The hydrogen cycle versus the short-lifetime carbon cycle to produce carbon fuels. Water (H ₂ O) acts as the “key” source to provide the energy in the form of electrons (e ⁻), and carbon dioxide (CO ₂) is recaptured from the atmosphere, necessary to achieve net zero emissions. Integrated photovoltaics or photocatalysts could be used to drive the energy conversion at lowest possible overpotential, powered by solar energy.	2
Figure 1.2. The catalytic water oxidation complex in photosystem II, a Mn ₄ O ₅ Ca cluster. Shown are Mn atoms labeled Mn 1-4 (<i>purple</i>), ligand-bounded oxygen (O) (<i>gray</i>), water-bound O (<i>red</i>), Ca (<i>yellow</i>), and N (<i>green</i>). The atomic coordinates are taken from the structure provided by Suga et al. ³⁶	4
Figure 1.3. “Donor-sensitizer-acceptor” triad concept where the donor (D) represents an integrated oxygen evolution reaction (OER) catalyst and the acceptor (A) an integrated hydrogen evolution reaction (HER) catalyst. The OER releases protons (H ⁺) and electrons (e ⁻) which are directed via covalently linked π ligands to the HER acceptor side. The protons are there reduced to H ₂ , which should ideally be separated from the O ₂ for instance via a membrane. The image is based on the concept presented in reference ³⁰	5
Figure 1.4. The structure of a layered Ni-Fe(OOH). The <i>left hand</i> image represent a small fragment demonstrating the interlayer spacing separating two sheets, with intercalated H ₂ O and K ⁺ . The <i>right hand</i> image demonstrate oxygen evolution reaction on a layer of Ni-Fe(OOH). Atomic coordinates are taken from α-Ni(OH) ₂ (cif 9012316).....	8
Figure 1.5. (a) Gibbs free energy diagram for electrochemical water oxidation at different electrode potentials ¹¹⁹ . The associated OER intermediates (HO _{ads} , O _{ads} , HOO _{ads}) shown for alkaline conditions. The solid lines represent the Gibbs Free reaction energies at different electrode potentials indicated on the <i>right axis</i> (b) Universal scaling relation between the OER intermediates ¹¹⁹ . The solid lines represented the Gibbs free reaction energies and the dotted lines an example of the ideal and the real case in terms of overpotential.	11
Figure 2.1. Microwave synthesis; <i>left hand</i> microwave vial, and <i>right hand</i> Anton Paar Monowave 300.	18
Figure 2.2. The synthesis setup for the metal-oleate-complex (MOC) route to highly crystalline Ni-Fe oxide nanoparticles.	20
Figure 2.3. Standard 3-compartment electrochemical cell for rotating disk electrode measurements (RDE). Switchable gas inlets/outlets for degassing electrolyte and keep N ₂ protective atmosphere (a),(e) and (d). Reference electrode compartment (b), working electrode with a Luggin capillary connection (c). Counter electrode separated by a glass frit (f). Working electrode separated by a glass frit (g).....	25
Figure 2.4. Example CV demonstrating how the integrated anodic vs. cathodic charges were determined for calculation of the redox number of the Ni ^{+2/+3} redox transition.	27
Figure 2.5. Differential electrochemical Mass Spectrometric Dual thin layer flow cell. The drawing demonstrate the real cell and were designed and made by Jorge Ferreira de Araújo, and schematical drawings in Autodesk® Inventor® Professional.....	28
Figure 2.6. Online Mass Spectrometric cells (a) initial design in glass (b) improved design of in Kel-F (PTCFE). More images of cell (b) are attached in Appendix I. Schematic drawings were prepared in Autodesk Inventor Professional.	29

Figure 2. 7. XAS sample preparation for freeze quenching (a) Schematic drawing of the working electrode (b) and of the assembly (c). Schematic drawings were prepared in Autodesk Inventor Professional. 30

Figure 3.1. Electrochemical characterization of mixed Ni–Fe catalysts with varying catalyst composition ($\text{Ni}_{100-x}\text{Fe}_x$) measured in RDE setup in 0.1 M KOH. (a) Cyclic voltammograms (CVs) recorded at a scan-rate of 100 mV/s after conditioning at 1.63 V_{RHE} for 30 min (see also Figure S3.1a for CVs at 10 mV/s). (b) Geometric current density (i_{geom}) and turnover frequency (TOF) of Ni–Fe catalysts based on the total metal loading of Ni+Fe (chosen identical for all samples) extracted from stationary measurements at $\eta_{\text{OER}} = 300$ mV (black curve) and 400 mV (blue curve). TOF is defined as moles of O_2 evolved per total moles of metal (Ni+Fe) per second. (c) Number of electrons transferred per Ni atoms ($e^- \text{Ni}^{-1}$) obtained by integration of the area under the $\text{Ni}(\text{OH})_2/\text{NiOOH}$ redox peak obtained by integration of the area under the redox peak, obtained from the maximum average value of anodic and cathodic redox wave during the first 150 cycles, $Q_{p,a} + Q_{p,c}$ (d) Midpeak potential, $E_{p,a} + E_{p,c}$ (e) Tafel slopes obtained from quasi-stationary state measurements (see also Figure S3.1d). Catalyst loadings were determined by ICP-OES analysis. Additional electrochemical measurements are presented in Supporting Information S3.1. *This figure has been reprinted with permission from ref. 108. Copyright (2016) American Chemical Society.* 41

Figure 3.2. Operando DEMS during CVs in the OER region between 1 and 1.8 V_{RHE} (before iR -comp.) in 0.1 M KOH (a) In situ cyclic voltammetric scan (green curve) and the corresponding faradaic ion current of O_2 (m/z 32) (black curve) of the Ni-catalyst. $Q_{\text{F}}^{\text{tot}}$ represents the total anodic charge under the green trace, and $Q_{\text{F},\text{O}_2}^{\text{DEMS}}$ is derived from the charge under the black ion current trace. (b) Faradaic O_2 efficiencies of Ni–Fe oxyhydroxide catalysts as a function of Fe-content ($\text{Ni}_{100-x}\text{Fe}_x$) given as atomic %. The hatched bar represent the O_2 efficiency excluding the charge associated with $Q_{\text{F},\text{Ni}^{2/+3}}$, corresponding to the $\text{Ni}(\text{OH})_2/\text{NiOOH}$ redox process. The Faradaic O_2 efficiency was derived from $\text{FE}_{\text{O}_2} (\%) = Q_{\text{F},\text{O}_2}^{\text{DEMS}} / Q_{\text{F}}^{\text{tot}}$ (c) Absolute faradaic charge ($Q_{\text{F}}^{\text{tot}} - Q_{\text{F},\text{O}_2}^{\text{DEMS}}$) injected into catalyst layer for changing metal oxidation states. The catalyst composition ($\text{Ni}_{100-x}\text{Fe}_x$) is given as atomic % Fe on x-axis. The catalyst loading was $\sim 10 \mu\text{g}/\text{cm}^2$. Error bars are derived as the standard deviation from 3 independent measurements. Additional measurements are presented in Supporting Information S3.2 (Figure S3.7–S9). *This figure has been reprinted with permission from ref. 108. Copyright (2016) American Chemical Society.* 44

Figure 3.3. (a) Powder XRD diffractograms of as-prepared Ni–Fe(OOH) catalysts with varying Ni:Fe compositions ($\text{Ni}_{100-x}\text{Fe}_x$). The inset shows the structural motif of $\alpha\text{-Ni}(\text{OH})_2$ with the arrow indicating the (003) interlayer spacing. The Fe content is indicated as atomic % Fe determined by ICP-OES. The bottom green vertical lines show the diffraction peaks of $\alpha\text{-Ni}(\text{OH})_2$ (pdf # 00–038–0715) and of FeOOH (0015441¹⁵⁹). (b) SEM image (top left and middle) and EDX elemental mapping (bottom) of the $\text{Ni}_{45}\text{Fe}_{55}$ catalyst; as-prepared catalyst. A line-scan analysis with the relative change of the Ni and Fe content across a selected path of the as-prepared catalyst is shown in the upper right corner. Atomic compositions are reported as atomic %. See also Figure S3.12 for additional SEM-EDX elemental mapping after exposure to OER catalytic conditions. *This figure has been reprinted with permission from ref. 108. Copyright (2016) American Chemical Society.* 47

Figure 3.4. X-ray absorption spectra of the Ni–Fe catalysts with varying catalyst composition ($\text{Ni}_{100-x}\text{Fe}_x$) freeze-quenched under application of catalytic potential after conditioning at 1.63 V for 30 min in 0.1 M KOH. (a) Fe K-edges and (b) Ni K-edges. Fourier transformed k^3 -weighted EXAFS oscillations (FT-EXAFS) of as-prepared (a.s.) catalysts (black

lines) and catalysts frozen under applied catalytic potential after conditioning at 1.63 V_{RHE} for 30 min in 0.1 M KOH (colored lines) measured at the (c) Ni K-edge and (d) Fe K-edge. The catalyst composition is indicated as atomic % Fe. Fit parameters are listed in Table 3.1 and Supporting Information S6, Tables S3.1-S3.7. *This figure has been reprinted with permission from ref. 108. Copyright (2016) American Chemical Society.* 49

Figure 3.5. a) XAS-derived structural motifs prevalent during OER catalysis at high and intermediate Ni-content. At high Ni-content the dominating host is the layered γ -NiOOH (a “NiO₂” phase) with octahedrally coordinated edge-sharing Ni⁴⁺. In the presence of Fe there is a mixture of edge- and corner sharing octahedra.¹⁶⁸⁻¹⁷⁰ Above 4% Fe, the dominant host is the Ni(OH)₂ with Ni²⁺. (b) Simplified scheme of the electrochemical water splitting cycle with metal oxidation rate constant, $k_{M,OX}$, and the catalytic OER rate constant, k_{OER} . *This figure has been reprinted with permission from ref. 108. Copyright (2016) American Chemical Society.* 54

Figure S3.1 (a) CVs measured at 10 mV/s in rotating disk electrode (RDE) setup after an initial pre-conditioning step of 1.63 VRHE for 30 min in 0.1 M KOH. (b) Overpotential (η_{OER}) at 1, 5, and 10 mA cm⁻², extracted from chronopotentiometric measurements. (c) Mass activity (i_{mass}) based on the total metal loading obtained by ICP-OES. (d) Tafel plots obtained from quasi-stationary state measurements by applying a stable potential for 90 s in 0.1 M KOH. The catalyst composition, Ni_{100-x}Fe_x, is indicated as atomic %. The total geometric metal loading was determined by ICP-OES prior to the measurements, kept at ~10 μ g Ni+Fe cm⁻² in the presented measurements. The rotation speed was set to 1600 rpm. *This figure has been reprinted with permission from ref. 108. Copyright (2016) American Chemical Society.* 59

Figure S3.2. CVs measured before and after application of a reducing potential (0 VRHE) for 20 min to make sure all Ni centers were in the reduced state, according to the principle presented by Batchellor et al.¹⁴⁶ (a) The Ni catalyst (b) Ni₉₆Fe₄ (c) Ni₉₁Fe₉ (d) Ni₆₅Fe₃₅ (e) Ni₄₅Fe₅₅. CVs were recorded in RDE setup at a scan-rate of 10 mV/s, a rotation speed of 1600 rpm, and a metal loading of ~6 μ g Ni+Fe cm⁻². The catalyst composition (Ni_{100-x}Fe_x) is given as atomic %. *This figure has been reprinted with permission from ref. 108. Copyright (2016) American Chemical Society.* 60

Figure S3.3. Evaluation of the OER activity during potentiodynamic and potentiostatic conditioning. (a) Geometric current densities (i_{geom}) extracted at 1.53 VRHE during the first 150 cycles, collected at a scan-rate of 100 mV/s. (b) Application of 1.63 VRHE for 30 min according to the conditioning protocol for the quasi-in situ XAS measurements. The measurements in (b) were carried out at iR-corrected potentials. Measurements were carried out in RDE setup in 0.1 M KOH. The metal loading was ~10 μ g Ni+Fe cm⁻². The catalyst composition (Ni_{100-x}Fe_x) is given as atomic %. *This figure has been reprinted with permission from ref. 108. Copyright (2016) American Chemical Society.* 61

Figure S3.4. Evaluation of the Ni(OH)₂/NiOOH redox peak during the first 150 cycles; a) Anodic redox electrons (Q_p ,a) defined as electrons transferred per Ni atoms (e- Ni-1) (b) Cathodic redox electrons (Q_p ,c) (c) Anodic peak potential (E_p ,a) (d) Cathodic peak potential (E_p ,c). The value of Q was estimated based on the moles of Ni on the electrode determined prior to the measurement using ICP-OES. Measurements were carried out in RDE setup in 0.1 M KOH, at a scan-rate 100 mV/s at a rotation speed of 1600 rpm, and a metal loading of ~10 μ g Ni+Fe cm⁻². The catalyst composition (Ni_{100-x}Fe_x) is indicated as atomic %. *This figure has been reprinted with permission from ref. 108. Copyright (2016) American Chemical Society.* 62

Figure S3.5. Evaluation of redox electrons (e- Ni-1) for the cathodic Ni(OH)₂/NiOOH redox peak estimated after application of 1.63VRHE for 30 min in 0.1 M KOH. The integration was done at different scan-rates (100, 10, and 2

mV/s). The values of Q were estimated based on the total moles of Ni on the electrodes determined of as-prepared catalysts prior to the measurements using ICP-OES (< OER), and based on the total moles of Ni on the electrodes after the conditioning step determined using TXRF analysis (> OER). *This figure has been reprinted with permission from ref. 108. Copyright (2016) American Chemical Society.* 63

Figure S3.6. The Ni-catalyst (α -Ni(OH)₂) measured in 0.1 M KOH at different levels of Fe-impurities. (a) CVs of the Ni catalyst prepared without further purification measured in non-purified KOH (1.) Ni catalyst measured in Fe-free 0.1 M KOH (2.) Ni-catalyst prepared with purified chemicals measured in Fe-free 0.1 M KOH (3.). Displayed CVs are cycle 5, 25 and 150. The inset shows an additional redox peak visible at ~1.56 V at cycle 25 (b) Geometric current density at 1.63 VRHE during the first 150 cycles for the catalysts shown in (a). (c) Integrated anodic redox electrons (e- per Ni) and the corresponding anodic peak position (E_{p,a}) during the first 150 cycles of the catalysts presented in (a). All measurements were recorded in RDE setup at 1600 rpm at a scan-rate of 100 mV/s using electrochemical cells made of polypropylene (Nalgene®) to avoid Fe-contamination. The geometric metal loading was ~ 5 μ g Ni+Fe cm⁻² determined by ICP-OES. All purifications were carried out according to the method reported by Trotochaud et al.⁷² *This figure has been reprinted with permission from ref. 108. Copyright (2016) American Chemical Society.* ... 64

Figure S3.7. Differential electrochemical mass spectrometry (DEMS) measured in 0.1 M KOH using a dual thin-layer flow-cell. CVs were recorded at 50 mV/s between 1-1.8 VRHE (before iR-comp.). (a) Ni catalyst (b) Ni₆₅Fe₃₅ (c) Ni₄₅Fe₅₅ (d) Ni₂₈Fe₇₂ (e) Fe catalyst. In order to reach higher current densities for some of the less active catalysts, CVs were recorded with increased scan-limits (~ 2.0 VRHE before iR-comp.) of (f) Ni₂₈Fe₇₂ and (g) Fe catalyst. Geometric current density from the potentiostat (CVs) are shown as *colored lines* (left axis) and the mass spectrometric faradaic ion current of O₂ (*m/z* 32) are shown as *black lines* (right axis). The arrows pointing upwards indicate the scan direction of the DEMS trace. A calibration constant (*K**) was used to convert the integrated ion current to faradic current. More information is given in Experimental section 3.2.6. The catalyst composition (Ni_{100-x}Fe_x) is given as atomic %. *This figure has been reprinted with permission from ref. 108. Copyright (2016) American Chemical Society.* 65

Figure S3.8. DEMS traces of the CVs in Fig. S7 shown in the time domain, measured in 0.1 M KOH using a dual thin-layer flow-cell. CVs were recorded at 50 mV/s between 1-1.8 VRHE (before iR-comp.) and are shown for selected catalysts; (a) Ni (b) Ni₆₅Fe₃₅ (c) Ni₄₅Fe₅₅ (d) Ni₂₈Fe₇₂ (e) Fe. In order to reach higher current densities for less active catalysts CVs were recorded with increased scan-limits (~ 2.0 VRHE before iR-comp.) of (f) Ni₂₈Fe₇₂ and (g) Fe catalyst. The CVs are shown as *colored lines* (left axis) and the mass spectrometric faradaic ion current of O₂ (*m/z* 32) as *black lines* (right axis). The arrows indicate the scan direction of the DEMS trace. A calibration constant (*K**) was used to convert the integrated ion current to faradic current. More information is given in Experimental section 3.2.6. The catalyst composition (Ni_{100-x}Fe_x) is given as atomic %. *This figure has been reprinted with permission from ref. 108. Copyright (2016) American Chemical Society.* 66

Figure 3.9. Faradaic efficiency (FE) for mixed Ni-Fe catalysts with efficiencies of the Ni₂₈Fe₇₂ and Fe-catalysts re-evaluated based on the measurements with extended scan-limits shown in Fig. S3.7f-g and S3.8f-g, scanned up to ~ 2.0 VRHE (before iR-comp.) to reach higher current densities. *This figure has been reprinted with permission from ref. 108. Copyright (2016) American Chemical Society.* 67

Figure S3.10. XRD of the as-prepared Ni catalyst; prepared with as-received chemicals (green curve), Fe-Free Ni catalyst prepared with purified chemicals (blue curve), and a slightly different Ni catalyst prepared with purified chemicals

and a modified synthesis protocol (grey curve). Further details are given in the Experimental section 2.1. The lines at the bottom show reference patterns of α -Ni(OH)₂ (red, pdf # 00-038-0715) and β -Ni(OH)₂ (dark green, pdf # 01-074-2075). Removal of trace Fe (purification) was carried out according to the method reported by Trotochaud et al.⁷² *This figure has been reprinted with permission from ref. 108. Copyright (2016) American Chemical Society. ... 69*

Figure S3.11. SEM images of catalysts drop-casted on glassy carbon electrodes; (a) as-prepared Ni catalyst (b-c) Ni catalyst after application of 1.63 V for 30 min in 0.1 M KOH (as received) shown at different magnifications. (d) As-prepared Fe catalyst. The inset shows large agglomerates of small Fe particles. (e-f) Fe catalyst after application of 1.63 V for 30 min in 0.1 M KOH (as received) shown at different magnifications. The inset in (d) shows a large Fe agglomerate. *This figure has been reprinted with permission from ref. 108. Copyright (2016) American Chemical Society. 70*

Figure S3.12. SEM images and EDX elemental mapping of the Ni₄₅Fe₅₅ catalyst drop casted on a glassy carbon electrode. (a) O and C content of the as-prepared catalyst (b) O, C, Ni, and Fe content of the catalyst shown in (a) after conditioning at 1.63 V for 30 min in 0.1 M KOH. The elements in the EDX mappings are indicated with colors; Ni (green), Fe (red), and O (blue), C (yellow). *This figure has been reprinted with permission from ref. 108. Copyright (2016) American Chemical Society. 71*

Figure S3.13. SEM images of the Ni₄₅Fe₅₅ catalysts drop-casted on glassy carbon electrodes (a) as-prepared catalyst (a.s.) (b) after application of 1.0 VRHE for 30 min in 0.1 M KOH (c) after application of 1.63 VRHE for 30 min in 0.1 M KOH. The catalysts in (a-c) were further analyzed using energy dispersive X-ray line-scan analysis to determine the atomic composition of Ni and Fe across a selected path (blue arrow) (d) as-prepared (e) conditioned at 1.0 V (f) conditioned at 1.63 V. *This figure has been reprinted with permission from ref. 108. Copyright (2016) American Chemical Society. 72*

Figure S3.14. X-ray absorption near edge spectra (XANES) of as-prepared catalysts. (a) Fe K-edges (b) Ni K-edges. The catalyst composition, Ni_{100-x}Fe_x, is indicated as atomic % in the legend shown in (a) which applies to both Fe and Ni K-edges. *This figure has been reprinted with permission from ref. 108. Copyright (2016) American Chemical Society. 73*

Figure S3.15. Fourier transformed k³-weighted EXAFS spectra. Experimental data (*black curves*) and simulations (*colored shaded areas*) at the (a) Ni K-edge of as-prepared catalysts (a.s.) (b) Fe K-edge of as-prepared catalysts (c) Ni K-edge of catalysts freeze-quenched at 1.63 V (d) Fe K-edge of catalysts frozen at 1.63 V. The catalyst composition, Ni_{100-x}Fe_x, is indicated as atomic % Fe or Ni for the respective edge. Catalysts were freeze quenched under applied potential after conditioning at the given potential for 30 min in 0.1 M KOH. Fit parameters are listed in Tables S3.2-S3.5. *This figure has been reprinted with permission from ref. 108. Copyright (2016) American Chemical Society. .. 74*

Figure S3.16. Extended X-ray absorption fine structure (EXAFS) (a) Fe K-edge of as-prepared catalysts (b) Ni K-edge of as-prepared catalysts (c) Fe K-edge of catalysts freeze quenched at 1.63 V. (d) Ni K-edge of catalysts freeze quenched at 1.63 V. The catalyst composition (Ni_{100-x}Fe_x) is indicated as atomic % Fe or Ni for the respective K-edges. Catalysts were frozen under applied potential after conditioning at the given potential for 30 min in 0.1 M KOH. *This figure has been reprinted with permission from ref. 108. Copyright (2016) American Chemical Society. 75*

Figure S3.17. Trends obtained from the fitted XAS spectra as a function of Fe-content (a) Ni and Fe K-edge positions. (b) M-O coordination distances (c) M-M coordination distances. The dotted lines in (a)-(b) indicate the oxidation states determined from reference compounds presented in Tables S3.8-3.9. The values in (b-c) were obtained by the

fitting k^3 -weighted EXAFS oscillations in k -space between 2.6-14 \AA^{-1} at the Ni K -edge and 2.6-12.5 \AA^{-1} at the Fe K -edge. Fit parameters are listed in Tables S3.2.1-S3.5. *This figure has been reprinted with permission from ref. 108.*

Copyright (2016) American Chemical Society...... 76

Figure S3.18. The k^3 -weighted FT-EXAFS at the Ni K -edges of the (a) Ni catalyst and (b) Ni₄₅Fe₅₅ catalyst, and at the Fe K -edges of the (c) Fe catalyst and (d) Ni₄₅Fe₅₅. Data is shown for the as-prepared catalysts (a.s., *black curves*), and catalysts frozen at 1.0 VRHE (*grey curves*), and catalysts frozen at 1.63 VRHE (*colored curves*). Catalysts were frozen at the given potential after conditioning for 30 min in 0.1 M KOH. *This figure has been reprinted with permission from ref. 108. Copyright (2016) American Chemical Society.* 77

Figure S3.19. Fe K -edge XANES of (a) Fe catalyst and (b) Ni₄₅Fe₅₅, and Fe EXAFS oscillations of (c) Fe catalyst and (d) Ni₄₅Fe₅₅. Ni K -edge XANES of (e) Ni catalyst and (f) Ni₄₅Fe₅₅, and Ni EXAFS oscillations of (g) Ni catalyst and (h) Ni₄₅Fe₅₅. Shown are as-prepared catalysts (a.s., *black curves*), freeze quenched at 1.0 VRHE (*grey curves*), and freeze quenched at 1.63 VRHE (*colored curves*). The catalyst composition, Ni_{100-x}Fe_x is given as at. %. Catalysts were freeze-quenched under applied potential after conditioning at the given potential for 30 min in 0.1 M KOH. *This figure has been reprinted with permission from ref. 108. Copyright (2016) American Chemical Society.* 78

Figure S3.20. Structural models compared to experimental data at the Fe K -edge. (a) Structure of γ -FeOOH (cif 9011314) (b) FT-EXAFS of the as-prepared Fe catalyst (solid black line) and the simulated spectrum of γ -FeOOH shown in (a) (dashed black line) (c) Structure of α -FeOOH (cif 1008766) (d) FT-EXAFS of the Fe catalyst at 1.63 V; experimental data (solid black line) and the simulated spectrum of α -FeOOH shown in (c) (dashed black line). The arrows indicate the coordination distances for Fe-O (yellow), Fe-Fe (red), and interlayer distances (blue). The boxes show regions associated with double or multiple scattering. The FT amplitudes of the simulated spectrum of γ/α -FeOOH presented in (b) and (d) have been scaled to fit the experimental. *This figure has been reprinted with permission from ref. 108. Copyright (2016) American Chemical Society.* 86

Figure S3.21. Structural models compared to experimental data at the Ni K -edge. (a) Structure of α -Ni(OH)₂ (cif 9012316) (b) FT-EXAFS of the as-prepared Ni catalyst (solid black line) compared to the simulated spectrum of α -Ni(OH)₂ shown in (a) (dashed black line). (c) The structure γ -NiOOH (cif 9012319) (d) FT-EXAFS of the Ni catalyst freeze-quenched at 1.63 V (solid black line) compared to the simulated spectrum of γ -NiOOH shown in (c) (dashed black line). The arrows indicate the coordination distances for Ni-O (yellow), Ni-Ni (red), Ni-Ni double distances (grey), and interlayer distances (blue). The boxes show regions where several distances occur due to presence of double or multiple scattering. The amplitudes of the simulated spectra of α -Ni(OH)₂ and γ -NiOOH shown in (b) and (d) have been scaled to fit the experimental data. *This figure has been reprinted with permission from ref. 108. Copyright (2016) American Chemical Society.* 87

Figure 3.22. XAS spectra of reference compounds measured at the Ni and Fe K -edge. (a-b) Ni and Fe XANES. (c-d) Ni and Fe k^3 weighted EXAFS oscillations, $k^3\chi(k)$. (d-e) Fourier transformed FT-EXAFS. Shown Fe compounds; Fe₂⁽⁺²⁾C₂O₄ (ALDRICH), Fe₂⁺³O₃, γ -Fe⁺³OOH, Fe⁺³OOH 1.63V (Fe catalyst at 1.63V, * this work, Fe⁺³OOH a.s. (Fe catalyst a.s., *this work). Shown compounds are Ni⁺²O (SIGMA-ALDRICH), β -Ni⁺²(OH)₂ (SIGMA-ALDRICH), Ni⁺⁴OOH 1.63V* (Ni catalyst at 1.63V, *this work), and Ni⁺⁴OOH (Ni catalyst a.s. *this work), Ni⁺²(NO₃)₂ (ALDRICH). *This figure has been reprinted with permission from ref. 108. Copyright (2016) American Chemical Society.* 88

Figure 4.1. Cyclic voltammograms of $\text{Ni}_{62}\text{Fe}_{38}\text{O}_x/\text{C}$ at a catalyst loading of $8 \mu\text{g Ni+Fe cm}^{-2}$ (a) KOH pre-cycled electrode after 150 cycles in 0.1 M KOH (black), KOH pre-cycled electrode consecutively cycled 20 cycles in 0.1 M B_i pH 9.2, denoted as KOH- B_i (green), and KOH- P_i cycled electrode after 20 cycles in 0.1 M P_i pH 7 (blue). Shown is cycle 5 at a scan-rate of 100 mV/s. (b) OER overpotential (η_{OER}) extracted from chronopotentiometric measurements at a geometric current density of 1 mA/cm^2 (colored bars) and at 10 mA/cm^2 (colored + transparent bars), measured at various catalysts loading of Ni + Fe; 1, 2, 4, 8, and $20 \mu\text{g Ni+Fe cm}^{-2}$. The catalyst loading was determined by ICP-OES. Further OER activity trends are presented in Supporting Information Figure S4.3-4.5. All measurements were carried out in RDE setup at a rotation speed of 1600 rpm in N_2 degassed electrolytes. This figure has been reprinted with permission from ref. 100. Copyright Elsevier (2016). 99

Figure 4.2. Electrolyte switching experiment of NiFeO_x/C cycled in KOH- P_i -KOH (pH 13 - pH 7 - pH 13). (a) Cyclic voltammograms of NiFeO_x/C at 100 mV/s at 1600 rpm and a catalyst loading of $8 \mu\text{g Ni + Fe /cm}^2$ (1) KOH pre-cycled electrode after 150 cycles 0.1 M KOH. (2) KOH pre-cycled electrode from step 1 after additional 20 cycles in 0.1 M P_i (KOH- P_i). Shown are cycle 1, 10, and 20. (3) KOH- P_i cycled electrode from step 2 after additional 20 cycles in 0.1 M KOH (KOH- P_i -KOH. Shown are cycle 1, 10, and 20. The same switching experiment at different catalyst loadings is attached in Figure 4.2-S4.3). (b) The turnover frequency (TOF) of (1) KOH pre-cycled electrode after 150 cycles, (2) KOH- P_i deactivated electrode (3) KOH- P_i -KOH reactivated electrode. The left axis shows the turnover frequency (solid bars) and the right axis shows the integrated mass normalized charge under the $\text{Ni(OH)}_2/\text{NiOOH}$ redox peak (hatched bars). All measurements were carried out at a geometric metal loading of $8 \mu\text{g}_{\text{Ni+Fe}}/\text{cm}^2$. This figure has been reprinted with permission from ref. 100 Copyright Elsevier (2016). 100

Figure 4.3. TEM images (a, c, e) and corresponding SAED patterns (b, d, f) of NiFeO_x/C . (a-b) Amorphous area of as-prepared catalyst (b-c) amorphous area after 150 cycles in 0.1 M KOH pH 13 (e-f) crystalline area after 150 cycles in 0.1 M KOH pH 13. Catalysts were cycled between $1-1.75 V_{\text{RHE}}$. The Ni:Fe composition acquired by the EDX unit is indicated in the upper right corner of the TEM images. This figure has been reprinted with permission from ref. 100 Copyright Elsevier (2016). 102

Figure 4.4. TEM images and corresponding SAED patterns of NiFeO_x/C . (a-b) Amorphous area of KOH- B_i cycled electrode after 20 cycles in 0.1 M B_i pH 9.2. (c-d) Crystalline area of KOH- B_i cycled electrode. (e-f) Crystalline area of KOH- P_i cycled electrode after 20 cycles in 0.1 M P_i pH 7. (g-h) Amorphous area of KOH- P_i -KOH reactivated electrode after 20 cycles in KOH pH 13. Catalysts were cycled between ca $1-1.75 V_{\text{RHE}}$. The Ni:Fe EDX composition is indicated in the upper right corner of the TEM images. This figure has been reprinted with permission from ref. 100 Copyright Elsevier (2016). 103

Figure 4.5. (a) Catalyst composition ($\text{Ni}_{100-x}\text{Fe}_x$) of NiFeO_x/C before and after cycling in different electrolytes and pH. Shown are the as-prepared catalyst (a.s.), after 150 cycles in KOH pH 13 (KOH), KOH- B_i cycled electrode; analyzed after 20 cycles in pH 9.2, KOH- B_i -KOH; after 20 cycles in pH 13, KOH- P_i ; after 20 cycles in pH 7, and KOH- P_i -KOH reactivated; after 20 cycles in pH 13. The total bar height represent the geometric metal loading of Ni and Fe determined by TXRF analysis (left axis). The bar colors represent the atomic composition of Fe (black) and Ni (colored) given as $\text{Ni}_{100-x}\text{Fe}_x$, estimated as the average from TXRF and SEM-EDX analysis. (b) TEM image and EDX composition of selected crystallite of NiFeO_x/C after KOH- B_i cycling; 20 cycles in pH 9.2 (c) after KOH- P_i ; 20 cycles in pH 7. All samples were prepared at a scan-rate of 100 mV/s between ca $1-1.75 V_{\text{RHE}}$ in molar concentrations of 0.1

- M of the electrolytes. See more details in the Experimental section 3.2.2 and in Supplementary Information Figure S4.8. This figure has been reprinted with permission from ref. ¹⁰⁰ Copyright Elsevier (2016)..... 105
- Figure 4.6. Differential Electrochemical Mass Spectrometry (DEMS) of a NiFeO_x/C electrocatalyst measured in a dual thin-layer flow cell. The Faradaic current (*i_{geom.}*) are shown as black lines and the ion current from the mass spectrometer (*i_{MS}*) as colored lines. (a) Electrode after 75 cycles in 0.1 M KOH pH 13. (b) KOH-B_i cycled electrode in pH 9.2. (c) KOH-P_i cycled electrode in pH 7. Shown are cycle 5. (d) Faradaic efficiency of KOH-B_i-KOH (green bars) and KOH-P_i-KOH cycled electrode (blue bars). The catalyst loading was ~8 μg cm⁻², scanned between ca 1–1.8 V_{RHE} after iR compensation. The scan-rate was kept to 50 mV/s, and the electrolyte flow 8 μl/min. This figure has been reprinted with permission from ref. ¹⁰⁰ Copyright Elsevier (2016). 108**
- Figure S4.1. Cyclic voltammograms of NiFeO_x/C measured in RDE setup according to the electrolyte switching protocol (KOH-P_i-KOH); 150 cycles in 0.1 M KOH pH 13 (black), KOH-P_i; 20 cycles in 0.1 M P_i pH 7 (blue), KOH-P_i-KOH; re-activation by 20 cycles in KOH (red). The switching experiment was carried out at various catalyst loadings a) 1 μg_{Ni+Fe}/cm² b) 2 μg_{Ni+Fe}/cm² c) 4 μg_{Ni+Fe}/cm² d) 8 μg_{Ni+Fe}/cm², and e) 20 μg_{Ni+Fe}/cm². The rotation speed was set to 1600 rpm and the potential limits were kept between 1-1.75 V_{RHE} before iR compensation. This figure has been reprinted with permission from ref. ¹⁰⁰ Copyright Elsevier (2016). 112**
- Figure 4.2. Cyclic voltammograms of NiFeO_x/C measured in RDE setup showing electrolyte switching; after 150 cycles in 0.1 M KOH pH 13 (black), after 20 cycles in 0.1 M B_i pH 9.2 (green), and after re-activation by additional 20 cycles in KOH (red). The experiment was carried out at various catalyst loadings a) 1 μg_{Ni+Fe}/cm² b) 2 μg_{Ni+Fe}/cm² c) 4 μg_{Ni+Fe}/cm² d) 8 μg_{Ni+Fe}/cm², and e) 20 μg_{Ni+Fe}/cm². The rotation speed was set to 1600 rpm and the potential limits were kept between ca 1-1.75 V_{RHE} before iR compensation. This figure has been reprinted with permission from ref. ¹⁰⁰ Copyright Elsevier (2016). 113**
- Figure S4.3. a) Turnover frequency (TOF) and mass activity (*i_{mass}*) vs. pH, measured at different geometric catalyst loadings; 1, 2, 4, 8, and 20 μg_{Ni+Fe}/cm². b) Overpotential at 1 mA cm⁻². Intrinsic activities are based on total geometric metal loading of Ni+Fe determined by ICP-OES. Current densities and overpotentials were extracted from chronoamperometric and chronopotentiometric measurements applying a stable potential or current for 90-120 sec, respectively. This figure has been reprinted with permission from ref. ¹⁰⁰ Copyright Elsevier (2016)..... 114**
- Figure S4.4. a) TOF and *i_{mass}* vs. catalyst loadings; 1, 2, 4, 8, and 20 μg_{Ni+Fe}/cm². Extracted at η = 300 and 400 mV in 0.1 M KOH pH 13 (grey, black) and at η = 400 mV in 0.1 M B_i pH 9.2 (green), and 0.1 M P_i pH 7 (blue). Intrinsic activities were based on total geometric metal loading of Ni+Fe determined by from ICP-OES. Current densities and overpotentials were extracted from chronoamperometric and chronopotentiometric measurements, respectively. This figure has been reprinted with permission from ref. ¹⁰⁰ Copyright Elsevier (2016). 114**
- Figure S4.5. Evaluation of OER activities and the Ni(OH)₂/NiOOH redox peak of NiFeO_x/C in pH switching experiments (KOH-P_i-KOH) at various catalyst loadings; 1, 2, 4, 8, and 20 μg_{Ni+Fe}/cm². a) Geometric current density (*i_{geom.}*) vs. catalyst loading at η_{OER} = 300 mV (solid bars) in 0.1 M KOH. The right axis shows the absolute value of the integrated cathodic peak charge (*Q_{p,c}*) of the Ni(OH)₂/NiOOH redox peak (hatched bars). b) Turnover frequency vs. catalyst loading at η_{OER} = 300 mV in 0.1 M KOH pH 13 based on total metal loading of Ni+Fe determined by ICP-OES (left axis). The right axis shows the mass normalized Ni redox peak charge (*Q_{p,c}*) represented in (b) defined as the number of electrons transferred per Ni atoms (hatched bars). The total bar area (black + color) represent**

measurements of electrodes 150 cycles in 0.1 M KOH and the colored area KOH-P_i-KOH re-activated electrodes. Current densities were extracted from chronoamperometric measurements applying a stable potential for 90 sec.

This figure has been reprinted with permission from ref. ¹⁰⁰ Copyright Elsevier (2016). 115

Figure S4.6. Prolonged cycling of NiFeO_x/C in 0.1 M P_i pH 7. a) Measurements in 0.1 M KOH pH 13 after 150 cycles in KOH (solid black), after 20 cycles in P_i (solid green), after 40 cycles in P_i (solid blue), and after 60 cycles in P_i (solid red). The corresponding cycles in P_i pH 7 are shown as dotted lines according to the same color palette. b) The capacitive region in KOH pH 13 c) The capacitive region in P_i pH 7. CVs were recorded at a scan-rate of 100 mV/s between 1-1.75 V_{RHE} before iR-compensation. The catalyst loadings were determined by ICP-OES prior to the measurements. This figure has been reprinted with permission from ref. ¹⁰⁰ Copyright Elsevier (2016). 116

Figure S4.7. a) Experimental XRD pattern of the as-prepared NiFeO_x/C catalyst. b) Simulated XRD profiles obtained by integration of the SAED patterns from crystalline and amorphous spots presented in Fig. 3-4. Shown are the amorphous area after 150 cycles in 0.1 M KOH pH 13 (dark blue, see also Fig. 3f), re-activated amorphous spot (KOH-P_i-KOH) after 20 cycles in KOH (light blue, see also Fig. 4h), crystalline area after 150 cycles in KOH (black, see also Fig. 3d), crystalline area of KOH-B_i cycled electrode after 20 cycles in 0.1 M B_i pH 9.2 (green, see also Fig. 4d), and crystalline area of KOH-P_i cycled electrode after 20 cycles in 0.1 M P_i pH 7 (red, see also Fig. 4f). Bottom lines show reference compounds of α-Ni(OH)₂ (green), β-Ni(OH)₂ (blue), NiO (pink), and FeO (yellow). This figure has been reprinted with permission from ref. ¹⁰⁰ Copyright Elsevier (2016). 117

Figure S4.8. TEM images, SAED patterns, and EDX compositions of selected crystalline areas of NiFeO_x/C. a) Electrode extensively cycled in 0.1 M KOH pH 13 (1000 cycles) b) KOH-B_i; after 20 cycles in pH 9.2 c) KOH-P_i; after 20 cycles in pH 7. Insets show SAED patterns of the presented TEM area. The arrows indicate a spot lying on an indices plane assuming the β-Ni(OH)₂ structure. EDX compositions are presented in the upper right corner. This figure has been reprinted with permission from ref. ¹⁰⁰ Copyright Elsevier (2016). 117

Figure S4.9. Differential electrochemical mass spectrometry (DEMS) presented in the voltage domain of NiFeO_x/C measured in a dual thin-layer electrochemical flow cell. The Faradaic currents (*i*_{geom.}) from the potentiostat (solid lines) and the corresponding ion currents of *m/z* = 32 (dotted lines). a) Catalyst in 0.1 M P_i pH 7; after 1 cycle (black), 5 cycles (red), and 10 cycles (blue). b) KOH-P_i-KOH re-activated catalyst after 10 cycles in 0.1 M KOH pH 13. The scan-rate was kept to 50 mV/s, and an electrolyte flow of 8 μl/s of N₂-purged electrolyte. The catalyst loading was 8 μg Ni+Fe/cm². This figure has been reprinted with permission from ref. ¹⁰⁰ Copyright Elsevier (2016). 118

Figure S4.10. Differential electrochemical mass spectrometry presented in the time domain of NiFeO_x/C. Each maximum represent the end of the scan-limit range (~ 1.8 V_{RHE}). The Faradaic currents from the potentiostat (*i*_{geom.}) are shown on the left axis (black curves), and the ion currents from the mass spectrometer (*i*_{MS}) for O₂ (*m/z* = 32) and CO₂ (*m/z* = 44) shown on the right axis; scaled to *m/z* = 32 to show the relative contribution of the CO₂ faradaic current. a-c) KOH-P_i-KOH cycling for cycle 64-75 in pH 13, cycle 1-10 in pH 7, and cycle 1-10 in pH 13. d-f) KOH-B_i-KOH cycling for cycle 64-75 in pH 13, cycle 1-10 in pH 9.2, and cycle 1-10 in pH 13. The potential limits were kept between ca 1-1.8 V_{RHE}, however were varying slightly in the different electrolyte depending on the resistance and different OER activities. The faradaic efficiencies of O₂ were estimated using a calibration constant (*K*^{*}) as described in the Section 2.5, see also Figure 6b. This figure has been reprinted with permission from ref. ¹⁰⁰ Copyright Elsevier (2016). 119

Figure 5.1. Electrochemical characterization of parental Ni(OH)₂ and Fe(OOH) catalysts, physically post-mixed Ni+Fe catalysts with varying catalyst composition (Ni_{100-x}Fe_x) and a pre-synthesized Ni₆₅Fe₃₅(OOH) catalyst. a) CVs at a scan-rate of 10 mV/s. b) Geometric current density (left axis) extracted from quasi-stationary state measurements at $\eta_{\text{OER}} = 300$ mV (dots) and at 400 mV (triangles). The corresponding turnover frequency (TOF) (right axis) was estimated from on the total geometric metal loading of Ni+Fe. (c) Overpotential at $i_{\text{geom.}} = 1$ and 10 mA cm⁻². (d) Mass based activity at $\eta=300$ mV and $\eta=400$ mV overpotential, normalized to total metal loading of Ni and Fe determined by elemental analysis. All trends were extracted from quasi-stationary state measurements. Measurements were carried out in RDE setup in 0.1 M KOH. Fe-containing catalysts were measured in KOH without further purification whereas the Ni-catalyst was measured in Fe-free KOH obtained by purification according to a reported method.⁷² 125

Figure 5.2. SEM-EDX elemental mapping of a physical mixture of Ni₅₀+Fe₅₀ catalyst drop-casted on a glassy carbon working electrode. The images shows the (a) as-prepared catalyst (b) after the activation step of 1.63 V_{RHE} for 30 min in 0.1 M KOH. The upper images show the SEM and the lower the corresponding EDX elemental mapping. The Ni:Fe compositions are indicated in the lower right corner as atomic %..... 127

Figure 5.3. TXRF elemental analysis of physical mixtures of Ni+Fe(OOH) catalysts and the parental Ni(OH)₂ and FeOOH catalysts, with different Ni:Fe compositions. As-prepared catalysts (*solid bars*) and after application of 1.63 V_{RHE} for 30 min in 0.1 M KOH (*hatched bars*). The bar height represent the geometric total metal of Ni content (*green*) and Fe-content (*black*) given in $\mu\text{g cm}^{-2}$. The fractional atomic compositions (at. %) are indicated with a number for Ni (*blue*) and Fe (*red*). 128

Figure 5. 4. k³-weighted Fourier transformed EXAFS (FT-EXAFS) of physically mixed Ni₆₅+Fe₃₅ catalyst under non-catalytic potential (as-prepared) at the (a) Ni K-edge (b) Fe K-edge. After application of 1.63 V for 30 min in 0.1 M KOH at the (c) Ni K-edge and (d) Fe K-edge. Shown are the parental Ni(OH)₂ catalyst (*green curve*), and the parental FeOOH catalyst (*black curve*), the pre-synthesized Ni₆₅Fe₃₅ catalyst (*grey curve*), and the physically mixed Ni₆₅+Fe₃₅ catalyst (*blue curve*). The catalyst composition (Ni_{100-x}Fe_x) is given as at. %..... 130

Figure S5.1. Tafel plots for physically mixed Ni+Fe(OOH) catalysts at different compositions. The slopes were extracted from quasi-stationary state measurements after conditioning at 1.63V_{RHE} for 30 min. Table S5.1 shows the Tafel slopes extracted by linear fit of the presented Tafel plots. The Fe-catalyst show clearly two different Tafel regions. All measurements were carried out in 0.1 M KOH. 135

Figure S5.2. CVs cycles 1-150 of a) Ni₆₅Fe₃₅ pre-synthesized catalyst and b) physically mixed Ni₆₅+Fe₃₅ catalyst prepared by mixing the parental Ni(OH)₂ and FeOOH catalysts post synthesis. 136

Figure S5.3. The Ni(OH)₂/NiOOH redox peak as a function of catalyst composition. (a) Number of electrons transferred per number of Ni atoms obtained by integration of the redox peak from CVs of physically mixed Ni+Fe catalysts (*filled circles*) and of pre-synthesized Ni-Fe catalysts (*open circles*). (b) Anodic peak position ($E_{\text{p,a}}$) (*circles*) and cathodic peak position ($E_{\text{p,c}}$) (*triangles*) of physically mixed Ni+Fe catalysts (*filled symbols*) and pre-synthesized Ni-Fe catalysts (*open symbols*). The lines are added as guideline to facilitate visualization. 136

Figure S5.4. Extended X-ray absorption fine structure (EXAFS) at the (a) Ni <i>K</i> -edge of as-prepared catalysts (b) Fe <i>K</i> -edge of as-prepared catalysts (c) Ni <i>K</i> -edge of catalysts freeze quenched at 1.63 V in 0.1 M KOH. (d) Fe <i>K</i> -edge of catalysts freeze quenched at 1.63 V in 0.1 M KOH. Presented catalysts are the parental Ni(OH) ₂ catalyst (<i>green</i>), the parental FeOOH catalyst (<i>black</i>), the pre-synthesized Ni ₆₅ Fe ₃₅ catalyst (<i>gray</i>), and the physically mixed Ni ₆₅ +Fe ₃₅ catalyst (<i>blue</i>). The catalyst composition (Ni _{100-x} Fe _x) is indicated as at. %.	137
Figure S5.5. Emission spectra of the physically mixed Ni ₆₅ +Fe ₃₅ catalyst recorded in the beamline setup prior to the XAS measurements; the as-prepared state (<i>black curve</i>) and of the catalyst freeze quenched after conditioning at 1.63 V for 30 min in 0.1 M KOH (<i>red curve</i>). Note that the intensities of the Ni and Fe K _α peaks have not been weighted against its individual extinction coefficients.	138
Figure 6.1. Cyclic voltammograms (CVs) of Ni-Fe(OOH) catalyst supported on different catalyst supports, unsupported (<i>yellow</i>), Vulcan XC-72r (<i>black</i>), oxidized CNTs (<i>red</i>), and ATO (<i>gray</i>). Catalyst composition, Ni _{100-x} Fe _x , is reported as mol % Fe. The measurements were recorded at 50 mV/s at 1600 rpm in 0.1M KOH.	145
Figure 6.2. Transmission electron micrographs (TEM) images of mixed Ni-Fe(OOH) catalysts supported on different catalyst supports (a) unsupported Ni ₅₀ Fe ₅₀ (b) Ni ₅₀ Fe ₅₀ /C (c) Ni ₅₀ Fe ₅₀ /Nano (d) Ni ₅₀ Fe ₅₀ /oxCNT (e) Ni ₅₀ Fe ₅₀ /ATO.	147
Figure 6.3. (a) Cyclic voltammograms (CVs) of unsupported Ni-Fe and carbon supported Ni-Fe/C oxyhydroxide catalysts in 1M KOH. The inset shows the geometric current density as a function of Fe-content estimated at a fixed geometric metal loading of 10 μg Ni+Fe/cm ² . (b) Mass based turnover frequency (TOF _{Ni+Fe}) as a function of Fe-content (Ni _{100-x} Fe _x), estimated at η=300 mV in 0.1 M and 1M KOH. <i>This Figure has been adapted with permission from ref. 194. Copyright (2017) American Chemical Society.</i>	148
Figure 6.4. (a) c) CVs of Ni-Fe/C at different geometric metal loadings 1-20 μg Ni+Fe/cm ² measured in 1 M KOH. (b) TOF based on the total metal as a function of metal loading for Ni ₄₅ Fe ₅₅ and Ni ₄₅ Fe ₅₅ /C catalysts in 0.1 M and 1 M KOH. Displayed CVs in were recorded at 100 mV/s at 1600 rpm. The metal loadings were determined by ICP-OES of as-prepared catalysts. Adapted with permission from ref. ¹⁹⁴ Copyright (2017) American Chemical Society.	149
Figure 6.5. (a) CVs of Ni ₄₅ Fe ₅₅ /C in different pH obtained by varying the electrolyte concentration (b) The logarithmic current density at η = 300 mV as a function of electrolyte pH measured in KOH and NaOH. The measurements were carried out at a total metal loading of ~6 μg Ni+Fe/cm ² determined by ICP-OES.	150
Figure 6.6. BET surface area obtained from N ₂ adsorption isotherm for Ni _{100-x} Fe _x /C electrocatalysts with varying composition. The right axis shows the wt % of carbon content estimated by ICP-OES. The error bars are given as standard errors. Adapted with permission from ref. ¹⁹⁴ Copyright (2017) American Chemical Society.	152
Figure 6.7. Stability test up to 1000 cycles of (a) Ni ₄₅ Fe ₅₅ and (b) Ni ₄₅ Fe ₅₅ /C by cycling between 1-1.75 V _{RHE} . (c) Chronopotentiometric curves at 10 mA cm ⁻² for 20 h. Displayed CVs in (a)-(b) are cycle 10 (<i>gray</i>), 100 (<i>green</i>), and 1000 (<i>blue</i>). Measurements were recorded at a scan-rate of 100 mV/s in RDE setup at 2200 rpm, before iR-compensation. All measurements were carried out in 0.1 M KOH. Adapted with permission from ref. ¹⁹⁴ Copyright (2017) American Chemical Society.	153
Figure 6.8. TEM images of Ni ₄₅ Fe ₅₅ and Ni ₄₅ Fe ₅₅ /C catalysts (a) as-prepared Ni ₄₅ Fe ₅₅ (b) as-prepared Ni ₄₅ Fe ₅₅ /C (c) Ni ₄₅ Fe ₅₅ after 1000 cycles in 0.1 M KOH (d) Ni ₄₅ Fe ₅₅ /C after 1000 cycles in 0.1 M KOH. The cycling was carried out between 1-1.75 V _{RHE} before iR-compensation, in RDE setup at a rotation speed of 2200 rpm under N ₂ -protective atmosphere.	154

Figure 6.9. (a-b) DEMS in 0.1 M KOH of Ni₄₅Fe₅₅ and Ni₄₅Fe₅₅/C catalysts. The geometric current density at the potentiostat, i_{geom} , (colored traces), the faradaic ion current (m/z 32), iF , O₂DEMS (black traces), converted using a calibration sensitivity factor k^* . (c-d) Steady-state O₂ detection of Ni₄₅Fe₅₅ and Ni₄₅Fe₅₅/C using online headspace mass spectrometry (MS) coupled to gas chromatography (GC). Chronopotentiometric steps were applied between 2-15 mA/cm², holding 2 hours at each step. The black curves shows the MS detected volume % of O₂ and the blue dots the % O₂ measured by GC. The insets shows the overpotential during the measurements. All measurements were carried out in 0.1 M KOH. Adapted with permission from ref.¹⁹⁴ Copyright (2017) American Chemical Society.

..... 155

Figure 6.10. XAS measurements of carbon supported Ni₆₅Fe₃₅/C (red), Ni₄₅Fe₅₅/C (blue), and unsupported Ni₄₅Fe₅₅ catalyst (gray) under OER catalytic potential of 1.63 V_{RHE} in 0.1 M KOH. (a) Ni K-edges (b) Fe K-edges (c) Ni K-edge FT-EXAFS (k^3 -weighted) and (d) Fe K-edge FT EXAFS. The catalyst composition is given as at. %. Adapted with permission from ref.¹⁹⁴ Copyright (2017) American Chemical Society. 157

Figure S6.1. XRD diffractograms of supported Ni-Fe catalysts (a) Ni₅₀Fe₅₀ on different supports; unsupported Ni₅₀Fe₅₀ (yellow), Ni₅₀Fe₅₀/C (V.XC-72r, black), oxidized Ni₅₀Fe₅₀/CNTs (red), and Ni₅₀Fe₅₀/ATO (gray), Ni₉₀Fe₁₀/Nano. (b) Ni-Fe catalysts on Vulcan XC-72r (/C) with various Ni:Fe compositions (Ni_{100-x}Fe_x/C). The catalyst composition is indicated as at. % Fe. The bottom lines show diffraction profiles of α -Ni(OH)₂ (green, pdf # 00-038-0715) , β -Ni(OH)₂ (light, pdf # 01-074-2075), and for carbon (black). Figure (b) has been reprinted with permission from ref. 194. Copyright (2017) American Chemical Society. 161

Figure S6.2. CVs measured at scan rate of 2 mV/s (curves) and steady-state chronopotentiometric measurements (circles) (a) unsupported Ni-Fe catalysts in 0.1 M KOH (b) Carbon supported Ni-Fe/C catalysts in 0.1 M KOH. (c) Ni-Fe catalysts in 1 M KOH (d) Ni-Fe/C catalysts in 1 M KOH. The CVs were recorded at a scan rate of 1600 rpm and the steady-state measurements at a rotation speed of 2200 rpm to avoid bubble blockage at the electrode surface. The metal loadings of Ni+Fe were kept at $\sim 10 \mu\text{g cm}^{-2}$, determined prior to the measurements by ICP-OES. The Ni:Fe compositions are indicated in the legends as at. %. This Figure has been reprinted with permission from ref. 194. Copyright (2017) American Chemical Society. 162

Figure S6.3. (a) The cathodic redox charge of the Ni(OH)₂/NiOOH redox peak of unsupported Ni₄₅Fe₅₅ and Vulcan XC-72r carbon supported Ni₄₅Fe₅₅/C, normalized to the moles of Ni on the electrode determined by ICP-OES. (b) The anodic peak position ($E_{p,a}$) as a function of catalyst loading in Ni_{100-x}Fe_x. Measurements were carried out in 0.1 and 1 M KOH at a rotation speed of 1600 rpm. Adapted with permission from ref.¹⁹⁴ Copyright (2017) American Chemical Society. Figure (a) has been adapted with permission from ref. 194. Copyright (2017) American Chemical Society. 163

Figure S6.4. (a) Cathodic redox electrons of the Ni(OH)₂/NiOOH redox peak of unsupported Ni₄₅Fe₅₅ and Vulcan XC-72r carbon supported Ni₄₅Fe₅₅/C in KOH and NaOH as a function of electrolyte pH. The moles of Ni on the electrode were determined by ICP-OES. (b) Tafel plots in different molarities of KOH (c) Tafel plots in different molarities of NaOH. Tafel data points were collected from CVs recorded at a scan-rate of 2 mV/s, between 0.5-5 mA/cm². 164

Figure S6.5. (a) Unsupported Ni₄₅Fe₅₅ in different concentrations of KOH (b) Unsupported Ni₄₅Fe₅₅ different concentrations of NaOH. (c) Carbon supported Ni₄₅Fe₅₅/C in different concentrations of KOH (d) Carbon supported Ni₄₅Fe₅₅/C in different concentrations of NaOH. The electrolytes were used without further purification. 165

Figure S6.6. (a) Unsupported Ni(OH) ₂ catalyst in different concentrations of KOH (b) carbon supported Ni/C-catalyst in 0.1 M and 1 M KOH, at a scan-rate of 100 mV/s. The electrolyte was purified prior to the measurements according of the method reported by Trotochaud et al. ⁷² <i>This Figure has been adapted with permission from ref. 194. Copyright (2017) American Chemical Society.</i>	165
Figure S6.7. DEMS of Ni ₄₅ Fe ₅₅ /C in 0.5 M NaOH measured in a dual thin-layer double-disk electrochemical flow cell. ¹²⁶ CVs are shown in (a) the potential domain and (b) the time domain. CVs were measured at 10 mV/s between 0.4-1.55 V _{RHE} . The geometric catalyst loadings were ~ 15 μg Ni+Fe cm ⁻² . Volatile gases were monitored of m/z 32, 34, 44. The working electrode was a glassy carbon disc electrode (Pine Instruments) with a geometric surface area of 0.283 cm ²	166
Figure S6.8. Online headspace Mass Spectrometry of (a) Ni ₉₁ Fe ₉ and (b) Ni ₉₁ Fe ₉ /C catalysts in 0.1 M KOH. Chronoamperometric measurements were applied in a stepwise manner; 0.5, 2, 5, 10, 15 mA/cm ² . Each step was held for 2 h to reach a stable level of oxygen. A gas tight cell was employed with a constant flow of 5 sccm of N ₂ controlled by mass flow controllers. The working electrode was a carbon fiber paper (CFP) with a geometric area of 2 cm ² . The insets show the OER overpotentials during the measurement.	167
Figure S6.9. OER overpotentials monitored during headspace MS measurements for Ni ₄₅ Fe ₅₅ , Ni ₄₅ Fe ₅₅ /C, Ni ₉₁ Fe ₉ , and Ni ₉₁ Fe ₉ /C in 0.1 M KOH at a catalyst loading of 0.4 mg/cm ² . (a) Overpotential plotted against the geometric current density (i _{geom}) extracted as the average of the last 1000 sec of each step (b) overpotentials for the catalysts compared to an uncoated carbon fiber paper.	167
Figure 6.10. XAS measurements of unsupported catalysts (<i>dotted</i> curves) versus carbon supported catalysts Ni _{100-x} Fe _x /C (<i>solid</i> curves) of catalysts freeze quenched at 1.63V after 30 min conditioning in 0.1 M. The catalyst composition is given as at. %. (a) Ni K-edges (b) Fe K-edges (c) Ni FT-EXAFS (k ³ -weighted) and (d) Fe FT-EXFAS (k ³ -weighted). <i>This Figure has been adapted with permission from ref. 194. Copyright (2017) American Chemical Society.</i>	169
Figure 7.1. TEM images of Ni-Fe nanoparticles with ~50:50 atomic composition, and the respective selected area electron diffraction (SAED), and the particle size distribution. (a) unsupported Ni ₇₅ Fe ₂₅ prepared from "one-pot" MOC using microwave irradiation at 300 °C for 15 min with a ramping step of 70°/min. (b) unsupported Ni ₆₃ Fe ₃₇ prepared from "one-pot" MOC using microwave-assisted synthesis at 300 °C for 15 min with a heating ramp of 18°/min. (c) Carbon supported Ni ₄₇ Fe ₅₃ /C prepared from "one-pot" MOC using conventional synthesis with reflux at 300 °C for 30 min with a heating ramp of 5°/min. (d) Carbon supported Ni ₆₀ Fe ₄₀ /C prepared from "single precursor" MOC using conventional synthesis with reflux at 300 °C for 30 min with a heating ramp of 5°/min. The catalyst composition obtained from the ICP-OES (Ni _{100-x} Fe _x) is given as at. %.	176
Figure 7.2. XRD of supported Ni-Fe oxide nanocrystals synthesized with the metal-oleate-complex (MOC) route. (a) unsupported Ni ₇₅ Fe ₂₅ prepared from "one-pot" MOC using microwave-assisted synthesis at 300 °C for 15 min with a heating ramp of 18°/min. The MOC was prepared as one-pot (b) Unsupported Ni ₆₃ Fe ₃₇ using microwave irradiation at 300 °C for 15 min with a heating ramp of 70°/min. The MOC was prepared as one-pot. (c) Carbon supported Ni ₄₇ Fe ₅₃ /C using microwave irradiation at 300 °C for 30 min with a heating ramp of 5°/min. The MOC was prepared as one-pot. d) Ni ₆₀ Fe ₄₀ /C prepared using microwave irradiation at 300 °C for 30 min with a heating ramp of 5°/min. The bottom lines shows reference patterns of NiO-fcc (pdf#01-071-1179), and Ni-hcp (pdf#00-045-1027).	178

Figure 7.3. Shape selected Ni-Fe oxide nanoparticles supported in Vulcan XC-72r. a) Ni₆₂Fe₃₈/C nanocube synthesized by additions of 2:1 MOC:Na-OL b) Ni₅₃Fe₄₇/C nanocube synthesized by additions of 2:1 MOC:TOBr c) Ni₃₀Fe₇₀/C synthesized by additions of 1:1 MOC:TOBr. 180

Figure 7.4. (a) XRD of shape selected Ni-Fe oxide nanoparticles supported on Vulcan XC-72r with different shapes (A) Ni₆₂Fe₃₈/C nanocube prepared by 1:1 MOC:Na-OL in Squalene (B) Ni₅₃Fe₄₇/C nanocube prepared by 1:1 MOC:TOBr in 1-octadecene (C) Ni₃₀Fe₇₀/ cuboctahedra prepared by 1:1 MOC:TOBr in 1-octadecene. (b) The Ni₅₃Fe₄₇/C nanocube shown in (A) with increasing concentration of TOBr, starting with 1:1 MOC:TOBr in 1-octadecene. (A) and (B) are repeated to facilitate view. The stars indicate the reflection of the carbon support. The bottom lines shows reference patterns of NiO-fcc (yellow, pdf#01-071-1179), Ni-hcp (black, pdf#00-045-1027), and NiFe₂O₄ (light blue, pdf#01-086-2267), Fe₂O₃ (red, #) 181

Figure 7.5. Investigation of annealing temperature on the OER activity in mixed Ni-Fe nanocatalysts, at different annealing temperatures in controlled gas atmosphere (synthetic air). (a) CVs recorded at 100 mV/s. (b) Geometric activity (*left axis*) and mass based activity (*right axis*) as a function of annealing temperature. (c) Elemental analysis of Ni (*green bars*) and Fe (*black bars*) in nanocatalyst powders for the different annealing temperatures determined by ICP-OES. The catalyst composition (Ni_{100-x}Fe_x) is indicated as atomic % at the bottom of each bar. (d) Redox active Ni species estimated by integration of the Ni^{+2/+3} redox peak, shown as the geometric normalized charge (*left axis*) and the mass based redox electrons (electrons transferred per Ni atoms) based on the moles of Ni on the electrode determined by ICP-OES. 182

Figure 7.6. Powder XRD of the Ni₆₀Fe₄₀/C nanocatalyst at different annealing temperatures in air for 1 h. (A) as-prepared (B) annealed at 200 °C (C) annealed at 300 °C (D) annealed at 350 °C (E) annealed at 400 °C. The bottom lines show reference patterns of NiO-fcc (pdf#01-071-1179), Ni-hcp (pdf#00-045-1027), and NiFe₂O₄ (pdf#01-086-2267). 184

Figure 7.7. (a) CVs of selected Ni-FeOx electrocatalysts with different size, shape, and phase. (b) Overpotential at 300 mV for the catalysts shown in (a). The current density was extracted from quasi-stationary state measurements. 185

Figure 7.8. CVs up to 100 cycles of selected nanocatalysts (a) spherical Ni₄₇Fe₅₃ (b) Ni₆₂Fe₃₈/C nanocube and (c) Ni₅₃Fe₄₇/C nanocube. The CVs were recorded at 100 mV/s in 0.1 M KOH at a rotation speed of 1600 rpm. 188

Figure 7.9. Turnover frequency of carbon supported shaped spherical and shaped oxides in comparison to a carbon supported Ni-Fe/C oxyhydroxide investigated in Chapter 6 (a) TOF normalized to total metal loading determined by TXRF analysis. The Ni₄₅Fe₅₅/C-OOH catalysts had much higher TOF and is therefore located on the right axis. Notice that the left and right axis have different scaling. (b) TOF normalized to the integrated Ni^{+2/+3} redox peak charge. Here the oxides are comparable to the Ni-FeOOH and are therefore located on the same axis. 189

Figure 7.10. TEM images of as-prepared catalysts (*left panels*) and after 1000 cycles between ~ 1-1.75 V_{RHE} in 0.1 M KOH (*right panels*) (a) Ni₆₂Fe₃₈/C nanocube catalyst (b) Ni₅₃Fe₄₇/C nanocube catalyst. 190

Figure 7.11. TXRF analysis of selected Ni-Fe nanocatalysts before and after 1000 cycles in 0.1M KOH. (A) Spherical Ni₄₇Fe₅₃ (B) Ni₆₂Fe₃₈/C nanocube and (C) Ni₅₃Fe₄₇/C nanocube catalysts. 191

Figure S7.1. Nanoparticles synthesized with a decomposition time of 60 min, at different magnifications. The right most image shows the nanoparticle size distribution. 194

Figure S7.2. XRD of the as-prepared pure Ni/C and Fe nanoparticles. 194

Figure S7.3. CVs at 100 mV/s shown for the first 150 cycles for Ni₆₀Fe₄₀ spherical nanocatalysts after annealing at different temperatures for 1 h in air. (a) as-prepared (b) annealed at 200 °C (c) annealed at 250 °C (d) annealed at 300 °C (e) annealed at 350 °C (f) annealed at 400 °C. CVs were recorded in 0.1 M KOH used without further purification, at a catalyst loading of ~10 μg cm⁻² determined by ICP-OES analysis. 195

Figure S7.4. Powder XRD of the Ni₆₀Fe₄₀/C nanocatalysts annealed at 700 °C in air for 1h. The bottom lines show reference patterns of NiO-fcc (pdf#01-071-1179), Ni-hcp (pdf#00-045-1027), and NiFe₂O₄ (pdf#01-086-2267). 196

List of Tables

Table 3.1. Fit Parameters Obtained from EXAFS Ni and Fe <i>K</i> -Edges of Selected Catalysts Freeze-Quenched under Applied Catalytic Potential of 1.63 V _{RHE} . <i>This table has been reprinted with permission from ref. 108. Copyright (2016) American Chemical Society.</i>	50
Table S3.1. Ni and Fe <i>K</i> -edge positions of as-prepared catalysts (a.s.) and catalysts freeze-quenched at 1.63 V after conditioning for 30 min in 0.1 M KOH, with corresponding average oxidation states determined from a comparison to reference compounds presented in Tables S3.8-3.9. <i>This table has been reprinted with permission from ref. 108. Copyright (2016) American Chemical Society.</i>	80
Table S3.2. Fe <i>K</i> -edge simulation parameters of the FT-EXAFS oscillations of as-prepared unconditioned catalysts (a.s.). The catalyst composition, Ni _{100-x} Fe _x , is given as atomic %. The fit <i>k</i> -range were 2.6-12.5 Å ⁻¹ . <i>This table has been reprinted with permission from ref. 108. Copyright (2016) American Chemical Society.</i>	81
Table S3.3. Ni <i>K</i> -edge EXAFS simulation parameters of as-prepared catalysts (a.s.). The fitted <i>k</i> -range was 2.6-14 Å ⁻¹ . <i>This table has been reprinted with permission from ref. 108. Copyright (2016) American Chemical Society.</i>	82
Table S3.4. Ni <i>K</i> -edge EXAFS simulation parameters of catalysts freeze quenched at 1.63 V _{RHE} after conditioning at the given potential for 30 min in 0.1 M KOH. The fitted <i>k</i> -range was 2.6-14 Å ⁻¹ . <i>This table has been reprinted with permission from ref. 108. Copyright (2016) American Chemical Society.</i>	84
Table S3.5. Fe <i>K</i> -edge EXAFS simulation parameters of catalysts freeze quenched at 1.0 V _{RHE} after conditioning at the given potential for 30 min in 0.1 M KOH. The fitted <i>k</i> -range was 2.6-12.5 Å ⁻¹ . <i>This table has been reprinted with permission from ref. 108. Copyright (2016) American Chemical Society.</i>	85
Table S3.6. Ni <i>K</i> -edge EXAFS simulation parameters of catalysts freeze quenched at 1.0 V _{RHE} after conditioning at the given potential for 30 min in 0.1 M KOH. The fitted <i>k</i> -range was 2.6-14 Å ⁻¹ . <i>This table has been reprinted with permission from ref. 108. Copyright (2016) American Chemical Society.</i>	85
Table S3.7. Summary of literature reported EXAFS parameters for the Fe <i>K</i> -edge. <i>This table has been reprinted with permission from ref. 108. Copyright (2016) American Chemical Society.</i>	89
Table S3.8. Summary of literature reported EXAFS parameters for the Ni <i>K</i> -edge. <i>This table has been reprinted with permission from ref. 108. Copyright (2016) American Chemical Society.</i>	90
Table 5.1. Fit parameters for quasi- in situ XAS measurements at the Ni and Fe <i>K</i> -edges at a catalytic potential of 1.63V _{RHE} , of the Ni ₆₅ +Fe ₃₅ physical mixture (P.M.), the Ni ₆₅ Fe ₃₅ catalyst, and the parental Ni(OH) ₂ and FeOOH catalysts. Measurements were carried out in 0.1 M KOH.	131
Table S5.1. Tafel slopes of physically mixed Ni+Fe(OOH) catalysts	135
Table S5.2. Fitted parameters at the Ni and Fe <i>K</i> -edges of the parental Ni(OH) ₂ and FeOOH catalysts, the physically mixed Ni ₆₅ +Fe ₃₅ catalyst, and the pre-synthesized Ni ₆₅ Fe ₃₅ catalyst. Only the first two shells were taken into account. ...	139
Table S5.3. Extracted edge positions and metal oxidation states, compared to oxidation states estimated from the M-O coordination distances presented in Tables S5.1-S5.2.	140

Table S6.1. Faradaic efficiencies determined for O ₂ (m/z 32) in the headspace MS-GC setup in 0.1 M KOH on carbon fiber paper. The geometric current densities were obtained by normalizing the current to the electrode area of the CFP of 2 cm ² . The theoretical percentage of oxygen was determined using faradays law for each applied current. This Table has been adapted with permission from ref. 194. Copyright (2017) American Chemical Society.	168
Table S6.2. Ni K-edge simulation parameters in 0.1 M KOH. This Table has been adapted with permission from ref. 194. Copyright (2017) American Chemical Society.	170
Table S6.3. Fe K-edge simulation parameters in 0.1 M KOH. <i>This Table has been adapted with permission from ref. 194. Copyright (2017) American Chemical Society.</i>	171
Table 7.1. Parameters for the Ni-Fe nanocrystal electrocatalysts; OER activity, BET, size, shape.	186

APPENDIX I

Gas-tight cell assembly for online headspace Mass Spectrometry

Mass spectrometric oxygen detection experiments presented in Chapter 6 were carried out using online headspace MS in a gas tight cell setup. This included construction of a gas tight cell for low flow rates (~ 5 sccm). The cell parts were designed in PCTFE, PEEK, and Teflon in order to provide flexibility and options to custom made already existing parts, and to eliminate contaminations from alkaline glass etching.

** Drawings have been made using software from Autodesk® Inventor® Professional 2015*

Specifications Headspace cell

Material: PCTFE, Teflon, PEEK

Height: 53 mm

Outer Diameter (OD): 50 mm

Inner Diameter (ID): 30 mm

MS Headspace cell

Mikaela Görlin
AK Strasser

FRONT



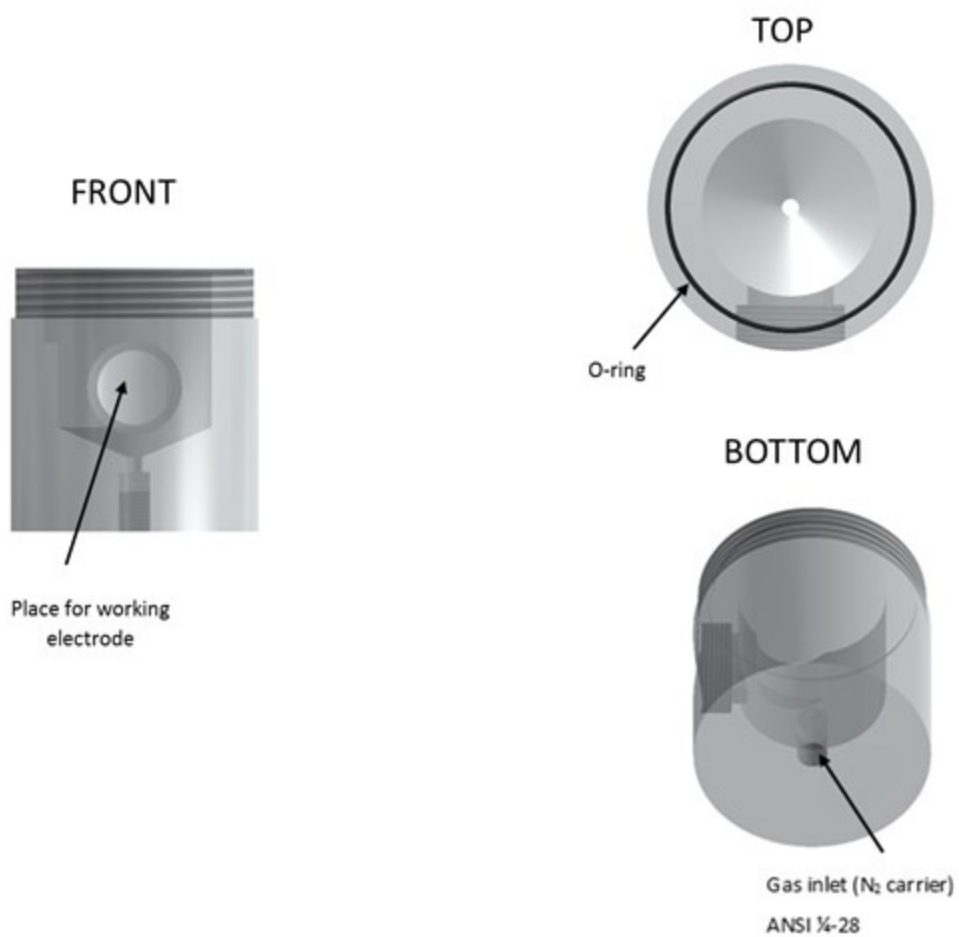
TOP



BOTTOM



1.1. Body

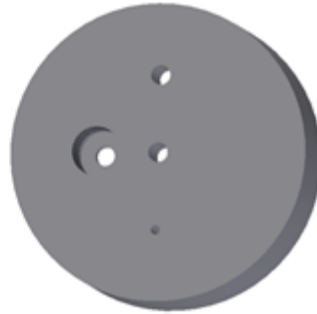


1.2. Disc

TOP

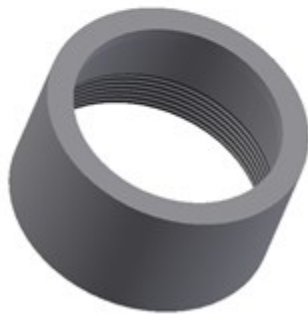


BOTTOM

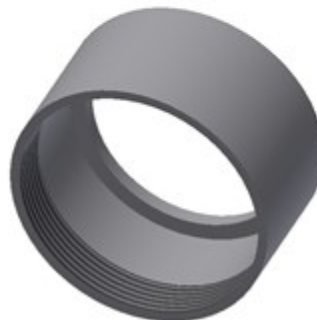


1.3 CAP

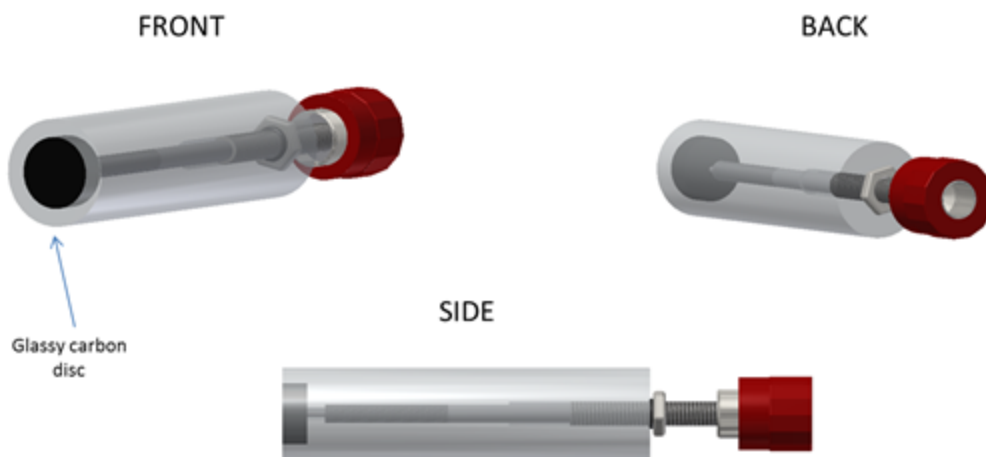
TOP



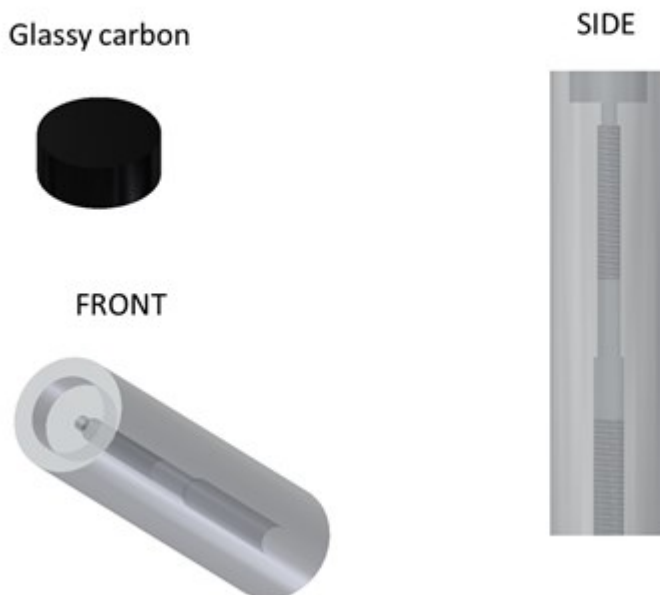
BOTTOM



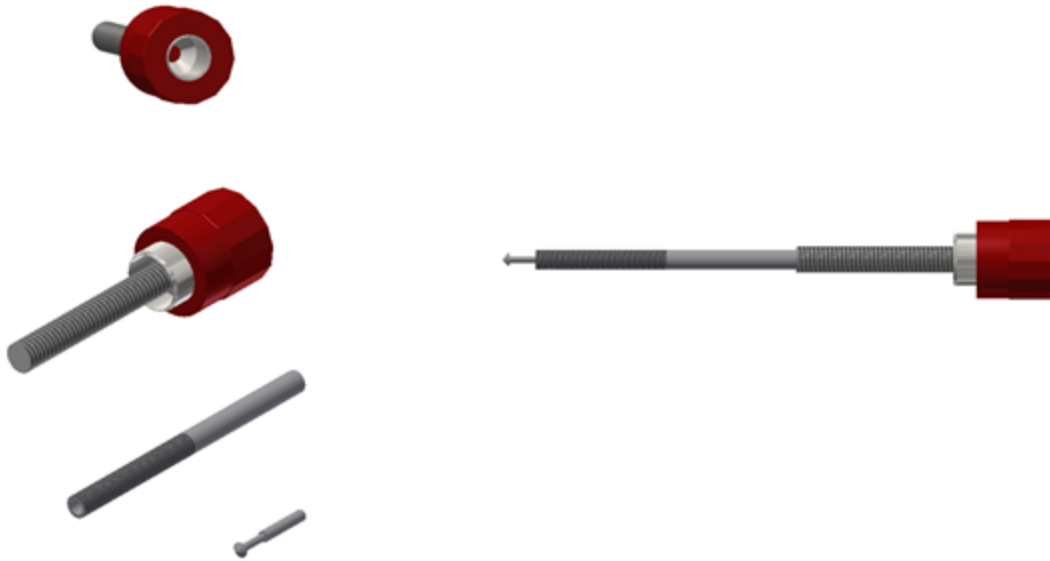
2. Working electrode (WE)



2.1. WE - holder



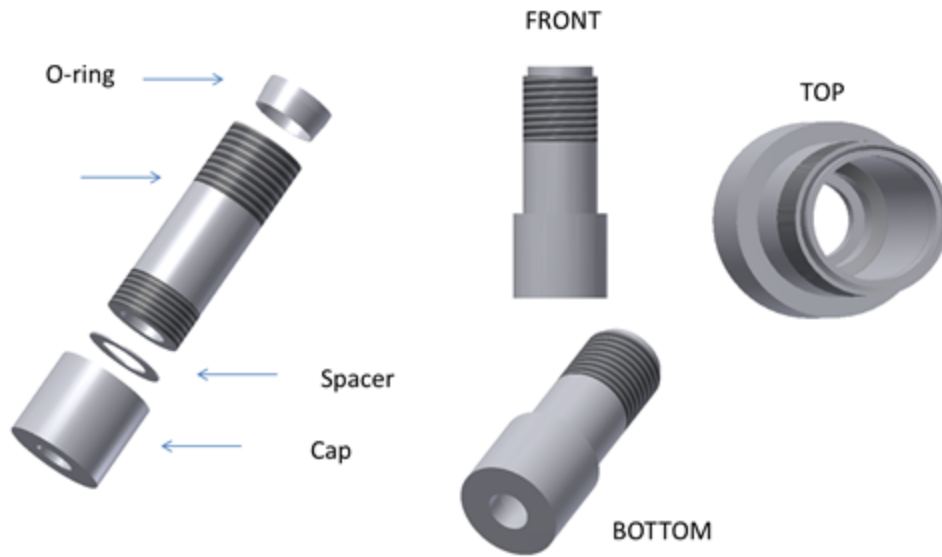
2.2. WE - connector



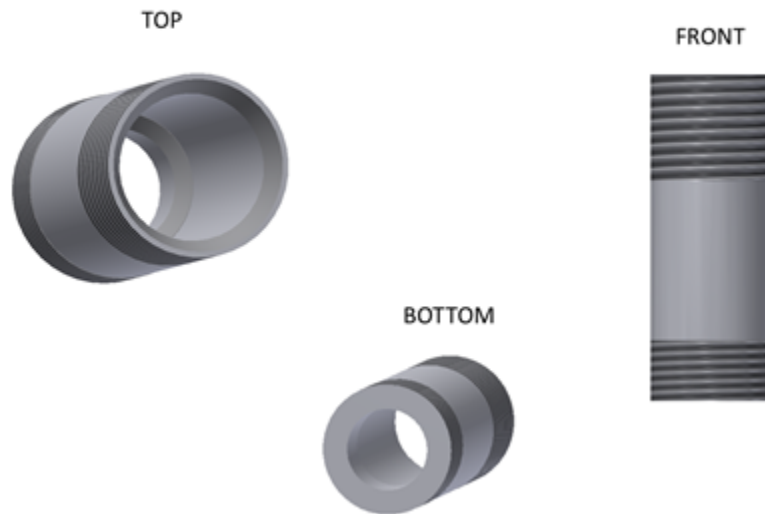
2.3. WE - Screw



3. Counter Electrode (CE)

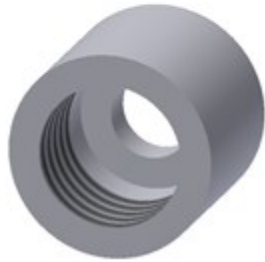


3.1. Membrane holder



3.2. Cap

BOTTOM



TOP



3.3. O-ring + Spacer

O-ring



Spacer



List of publications

Görlin, M.; Ferreira de Araújo, J.; Schmies, H.; Bernsmeier, D.; Dresch, S.; Gliech, M.; Jusys, Z.; Chernev, P.; Kraehnert, R.; Dau, H.; Strasser, P. *Journal of the American Chemical Society*, 2017, 139, 2070.

Görlin, M.; Chernev, P.; Ferreira de Araújo, J.; Reier, T.; Dresch, S.; Paul, B.; Krähnert, R.; Dau, H.; Strasser, P. *Journal of the American Chemical Society*, 2016, 138, 5603.

Görlin, M.; Gliech, M.; Ferreira de Araújo, J.; Dresch, S.; Bergmann, A.; Strasser, P. *Catalysis Today*, 2015, 262, 65.

References

- (1) Nocera, D. G. *Inorganic Chemistry* **2009**, *48*, 10001.
- (2) Trasatti, S. *Journal of Electroanalytical Chemistry and Interfacial Electrochemistry* **1980**, *111*, 125.
- (3) Kanan, M. W.; Nocera, D. G. *Science* **2008**, *321*, 1072.
- (4) Walter, M. G.; Warren, E. L.; McKone, J. R.; Boettcher, S. W.; Mi, Q.; Santori, E. A.; Lewis, N. S. *Chemical Reviews* **2010**, *110*, 6446.
- (5) Dau, H.; Limberg, C.; Reier, T.; Risch, M.; Roggan, S.; Strasser, P. *Chemcatchem* **2010**, *2*, 724.
- (6) Man, I. C.; Su, H. Y.; Calle-Vallejo, F.; Hansen, H. A.; Martinez, J. I.; Inoglu, N. G.; Kitchin, J.; Jaramillo, T. F.; Norskov, J. K.; Rossmeisl, J. *Chemcatchem* **2011**, *3*, 1159.
- (7) Subbaraman, R.; Tripkovic, D.; Chang, K. C.; Strmcnik, D.; Paulikas, A. P.; Hirunsit, P.; Chan, M.; Greeley, J.; Stamenkovic, V.; Markovic, N. M. *Nature Materials* **2012**, *11*, 550.
- (8) Liao, P.; Keith, J. A.; Carter, E. A. *Journal of the American Chemical Society* **2012**, *134*, 13296.
- (9) Singh, A.; Spiccia, L. *Coordination Chemistry Reviews* **2013**, *257*, 2607.
- (10) McCrory, C. C. L.; Jung, S.; Peters, J. C.; Jaramillo, T. F. *Journal of the American Chemical Society* **2013**, *135*, 16977.
- (11) Hu, S.; Xiang, C.; Haussener, S.; Berger, A. D.; Lewis, N. S. *Energy & Environmental Science* **2013**, *6*, 2984.
- (12) Jin, J.; Walczak, K.; Singh, M. R.; Karp, C.; Lewis, N. S.; Xiang, C. *Energy & Environmental Science* **2014**, *7*, 3371.
- (13) Trasatti, S. *Journal of Electroanalytical Chemistry* **1999**, *476*, 90.
- (14) de Levie, R. *Journal of Electroanalytical Chemistry* **1999**, *476*, 92.
- (15) Smith, A. M.; Trotochaud, L.; Burke, M. S.; Boettcher, S. W. *Chemical Communications* **2015**, *51*, 5261.
- (16) Luo, J.; Im, J.-H.; Mayer, M. T.; Schreier, M.; Nazeeruddin, M. K.; Park, N.-G.; Tilley, S. D.; Fan, H. J.; Grätzel, M. *Science* **2014**, *345*, 1593.
- (17) Wang, L.; Dionigi, F.; Nguyen, N. T.; Kirchgeorg, R.; Gliech, M.; Grigorescu, S.; Strasser, P.; Schmuki, P. *Chemistry of Materials* **2015**, *27*, 2360.
- (18) Trotochaud, L.; Mills, T. J.; Boettcher, S. W. *Journal of Physical Chemistry Letters* **2013**, *4*, 931.
- (19) Agency, I. E. *Tracking Clean Energy Progress*; OECD/IEA: Paris, 2015.
- (20) Agency, I. E. *Key World Energy Statistics*; OECD/IEA: Paris, 2015.
- (21) Davis, S. J.; Caldeira, K.; Matthews, H. D. *Science* **2010**, *329*, 1330.
- (22) Luthi, D.; Le Floch, M.; Bereiter, B.; Blunier, T.; Barnola, J.-M.; Siegenthaler, U.; Raynaud, D.; Jouzel, J.; Fischer, H.; Kawamura, K.; Stocker, T. F. *Nature* **2008**, *453*, 379.
- (23) Loulergue, L.; Schilt, A.; Spahni, R.; Masson-Delmotte, V.; Blunier, T.; Lemieux, B.; Barnola, J.-M.; Raynaud, D.; Stocker, T. F.; Chappellaz, J. *Nature* **2008**, *453*, 383.
- (24) Agency, I. E. *Technology Roadmap, Solar Photovoltaic Energy*; OECD/IEA: Paris, 2014.

- (25) Ashford, D. L.; Gish, M. K.; Vannucci, A. K.; Brennaman, M. K.; Templeton, J. L.; Papanikolas, J. M.; Meyer, T. *J. Chemical Reviews* **2015**, *115*, 13006.
- (26) Varela, A. S.; Schlaup, C.; Jovanov, Z. P.; Malacrida, P.; Horch, S.; Stephens, I. E. L.; Chorkendorff, I. *The Journal of Physical Chemistry C* **2013**, *117*, 20500.
- (27) Kortlever, R.; Shen, J.; Schouten, K. J. P.; Calle-Vallejo, F.; Koper, M. T. M. *The Journal of Physical Chemistry Letters* **2015**, *6*, 4073.
- (28) Lee, R.-L.; Tran, P. D.; Pramana, S. S.; Chiam, S. Y.; Ren, Y.; Meng, S.; Wong, L. H.; Barber, J. *Catalysis Science & Technology* **2013**, *3*, 1694.
- (29) Mathew, S.; Yella, A.; Gao, P.; Humphry-Baker, R.; CurchodBasile, F. E.; Ashari-Astani, N.; Tavernelli, I.; Rothlisberger, U.; NazeeruddinMd, K.; Grätzel, M. *Nat Chem* **2014**, *6*, 242.
- (30) Magnuson, A.; Anderlund, M.; Johansson, O.; Lindblad, P.; Lomoth, R.; Polivka, T.; Ott, S.; Stensjö, K.; Styring, S.; Sundström, V.; Hammarström, L. *Accounts of Chemical Research* **2009**, *42*, 1899.
- (31) Umena, Y.; Kawakami, K.; Shen, J.-R.; Kamiya, N. *Nature* **2011**, *473*, 55.
- (32) Zouni, A.; Witt, H.-T.; Kern, J.; Fromme, P.; Krauss, N.; Saenger, W.; Orth, P. *Nature* **2001**, *409*, 739.
- (33) Guskov, A.; Kern, J.; Gabdulkhakov, A.; Broser, M.; Zouni, A.; Saenger, W. *Nat Struct Mol Biol* **2009**, *16*, 334.
- (34) Ferreira, K. N.; Iverson, T. M.; Maghlaoui, K.; Barber, J.; Iwata, S. *Science* **2004**, *303*, 1831.
- (35) Kamiya, N.; Shen, J.-R. *Proceedings of the National Academy of Sciences* **2003**, *100*, 98.
- (36) Suga, M.; Akita, F.; Hirata, K.; Ueno, G.; Murakami, H.; Nakajima, Y.; Shimizu, T.; Yamashita, K.; Yamamoto, M.; Ago, H.; Shen, J.-R. *Nature* **2015**, *517*, 99.
- (37) Nelson, N.; Ben-Shem, A. *Nat Rev Mol Cell Biol* **2004**, *5*, 971.
- (38) Bozoglian, F.; Romain, S.; Ertem, M. Z.; Todorova, T. K.; Sens, C.; Mola, J.; Rodríguez, M.; Romero, I.; Benet-Buchholz, J.; Fontrodona, X.; Cramer, C. J.; Gagliardi, L.; Llobet, A. *Journal of the American Chemical Society* **2009**, *131*, 15176.
- (39) Tseng, H.-W.; Zong, R.; Muckerman, J. T.; Thummel, R. *Inorganic chemistry* **2008**, *47*, 11763.
- (40) Concepcion, J. J.; Jurss, J. W.; Hoertz, P. G.; Meyer, T. J. *Angewandte Chemie International Edition* **2009**, *48*, 9473.
- (41) Gust, D.; Moore, T. A.; Moore, A. L. *Accounts of Chemical Research* **2001**, *34*, 40.
- (42) Gärtner, F.; Sundararaju, B.; Surkus, A.-E.; Boddien, A.; Loges, B.; Junge, H.; Dixneuf, P. H.; Beller, M. *Angewandte Chemie* **2009**, *121*, 10147.
- (43) Borgström, M.; Shaikh, N.; Johansson, O.; Anderlund, M. F.; Styring, S.; Åkermark, B.; Magnuson, A.; Hammarström, L. *Journal of the American Chemical Society* **2005**, *127*, 17504.
- (44) Gust, D.; Moore, T. A.; Moore, A. L. *Accounts of Chemical Research* **2009**, *42*, 1890.
- (45) Zhang, C.; Chen, C.; Dong, H.; Shen, J.-R.; Dau, H.; Zhao, J. *Science* **2015**, *348*, 690.
- (46) Fujishima, A.; Honda, K. *Nature* **1972**, *238*, 37.
- (47) O'Regan, B.; Gratzel, M. *Nature* **1991**, *353*, 737.
- (48) Hickling, A.; Hill, S. *Discussions of the Faraday Society* **1947**, *1*, 236.
- (49) Beer, H. B. US Patent classification 710551 **1958**.

- (50) Millet, P.; Andolfatto, F.; Durand, R. *International Journal of Hydrogen Energy* **1996**, *21*, 87.
- (51) Carmo, M.; Fritz, D. L.; Mergel, J.; Stolten, D. *International Journal of Hydrogen Energy* **2013**, *38*, 4901.
- (52) Bockris, J. O. *The Journal of Chemical Physics* **1956**, *24*, 817.
- (53) Trasatti, S. *Electrochimica Acta* **2000**, *45*, 2377.
- (54) Trasatti, S. *Electrochimica Acta* **1984**, *29*, 1503.
- (55) Matsumoto, Y.; Sato, E. *Materials Chemistry and Physics* **1986**, *14*, 397.
- (56) Reier, T.; Weidinger, I.; Hildebrandt, P.; Kraehnert, R.; Strasser, P. In *Electrochemical Synthesis of Fuels 2* 2013; Vol. 58, p 39.
- (57) Nong, H. N.; Gan, L.; Willinger, E.; Teschner, D.; Strasser, P. *Chemical Science* **2014**, *5*, 2955.
- (58) Dionigi, F.; Reier, T.; Pawolek, Z.; Gliech, M.; Strasser, P. *ChemSusChem* **2016**, *9*, 1.
- (59) Zeradjanin, A. R.; Menzel, N.; Schuhmann, W.; Strasser, P. *Physical Chemistry Chemical Physics* **2014**, *16*, 13741.
- (60) Cui, C.; Ahmadi, M.; Behafarid, F.; Gan, L.; Neumann, M.; Heggen, M.; Cuenya, B. R.; Strasser, P. *Faraday Discussions* **2013**, *162*, 91.
- (61) El Wakkad, S. E. S.; Hickling, A. *Transactions of the Faraday Society* **1950**, *46*, 820.
- (62) Risch, M.; Khare, V.; Zaharieva, I.; Gerencser, L.; Chernev, P.; Dau, H. *Journal of the American Chemical Society* **2009**, *131*, 6936.
- (63) Kanan, M. W.; Yano, J.; Surendranath, Y.; Dincă, M.; Yachandra, V. K.; Nocera, D. G. *Journal of the American Chemical Society* **2010**, *132*, 13692.
- (64) Zaharieva, I.; Chernev, P.; Risch, M.; Klingan, K.; Kohlhoff, M.; Fischer, A.; Dau, H. *Energy & Environmental Science* **2012**, *5*, 7081.
- (65) Dinca, M.; Surendranath, Y.; Nocera, D. G. *Proceedings of the National Academy of Sciences of the United States of America* **2010**, *107*, 10337.
- (66) Klingan, K.; Ringleb, F.; Zaharieva, I.; Heidkamp, J.; Chernev, P.; Gonzalez-Flores, D.; Risch, M.; Fischer, A.; Dau, H. *ChemSusChem* **2014**, *7*, 1301.
- (67) Bergmann, A.; Martinez-Moreno, E.; Teschner, D.; Chernev, P.; Gliech, M.; de Araujo, J. F.; Reier, T.; Dau, H.; Strasser, P. *Nat Commun* **2015**, *6*.
- (68) Reier, T.; Pawolek, Z.; Cherevko, S.; Bruns, M.; Jones, T.; Teschner, D.; Selve, S.; Bergmann, A.; Nong, H. N.; Schlögl, R.; Mayrhofer, K. J. J.; Strasser, P. *Journal of the American Chemical Society* **2015**, *137*, 13031.
- (69) Trotochaud, L.; Ranney, J. K.; Williams, K. N.; Boettcher, S. W. *Journal of the American Chemical Society* **2012**, *134*, 17253.
- (70) Ali-Löyty, H.; Louie, M. W.; Singh, M. R.; Li, L.; Sanchez Casalongue, H. G.; Ogasawara, H.; Crumlin, E. J.; Liu, Z.; Bell, A. T.; Nilsson, A.; Friebel, D. *The Journal of Physical Chemistry C* **2016**, *120*, 2247.
- (71) Corrigan, D. A. *Journal of the Electrochemical Society* **1987**, *134*, 377.
- (72) Trotochaud, L.; Young, S. L.; Ranney, J. K.; Boettcher, S. W. *Journal of the American Chemical Society* **2014**, *136*, 6744.
- (73) Bode, H.; Dehmelt, K.; Witte, J. *Electrochimica Acta* **1966**, *11*, 1079.

- (74) Barnard, R.; Randell, C. F. *Journal of Applied Electrochemistry* **1983**, *13*, 97.
- (75) Lyons, M. E. G.; Cakara, A.; O'Brien, P.; Godwin, I.; Doyle, R. L. *International Journal of Electrochemical Science* **2012**, *7*, 11768.
- (76) Klaus, S.; Cai, Y.; Louie, M. W.; Trotochaud, L.; Bell, A. T. *The Journal of Physical Chemistry C* **2015**, *119*, 7243.
- (77) Landon, J.; Demeter, E.; Inoglu, N.; Keturakis, C.; Wachs, I. E.; Vasic, R.; Frenkel, A. I.; Kitchin, J. R. *Acs Catalysis* **2012**, *2*, 1793.
- (78) An, X.; Shin, D.; Ocon, J. D.; Lee, J. K.; Son, Y.-i.; Lee, J. *Chinese Journal of Catalysis* **2014**, *35*, 891.
- (79) Corrigan, D. A.; Bendert, R. M. *Journal of the Electrochemical Society* **1989**, *136*, 723.
- (80) Friebel, D.; Louie, M. W.; Bajdich, M.; Sanwald, K. E.; Cai, Y.; Wise, A. M.; Cheng, M.-J.; Sokaras, D.; Weng, T.-C.; Alonso-Mori, R.; Davis, R. C.; Bargar, J. R.; Nørskov, J. K.; Nilsson, A.; Bell, A. T. *Journal of the American Chemical Society* **2015**, *137*, 1306.
- (81) Gong, M.; Li, Y.; Wang, H.; Liang, Y.; Wu, J. Z.; Zhou, J.; Wang, J.; Regier, T.; Wei, F.; Dai, H. *Journal of the American Chemical Society* **2013**, *135*, 8452.
- (82) Hunter, B. M.; Blakemore, J. D.; Deimund, M.; Gray, H. B.; Winkler, J. R.; Müller, A. M. *Journal of the American Chemical Society* **2014**, *136*, 13118.
- (83) Kleiman-Shwarsstein, A.; Hu, Y. S.; Stucky, G. D.; McFarland, E. W. *Electrochemistry Communications* **2009**, *11*, 1150.
- (84) Galán-Mascarós, J. R. *ChemElectroChem* **2015**, *2*, 37.
- (85) Li, X. H.; Walsh, F. C.; Pletcher, D. *Physical Chemistry Chemical Physics* **2011**, *13*, 1162.
- (86) Li, Y.-F.; Selloni, A. *ACS Catalysis* **2014**, *4*, 1148.
- (87) Louie, M. W.; Bell, A. T. *Journal of the American Chemical Society* **2013**, *135*, 12329.
- (88) Oliver-Tolentino, M. A.; Vázquez-Samperio, J.; Manzo-Robledo, A.; González-Huerta, R. d. G.; Flores-Moreno, J. L.; Ramírez-Rosales, D.; Guzmán-Vargas, A. *The Journal of Physical Chemistry C* **2014**, *118*, 22432.
- (89) Qiu, Y.; Xin, L.; Li, W. *Langmuir* **2014**, *30*, 7893.
- (90) Pérez-Alonso, F. J.; Adán, C.; Rojas, S.; Peña, M. A.; Fierro, J. L. G. *International Journal of Hydrogen Energy* **2014**, *39*, 5204.
- (91) Yu, X.; Zhang, M.; Yuan, W.; Shi, G. *Journal of Materials Chemistry A* **2015**, *3*, 6921.
- (92) Fabbri, E.; Haberer, A.; Waltar, K.; Kotz, R.; Schmidt, T. J. *Catalysis Science & Technology* **2014**, *4*, 3800.
- (93) Gerken, J. B.; Shaner, S. E.; Masse, R. C.; Porubsky, N. J.; Stahl, S. S. *Energy & Environmental Science* **2014**, *7*, 2376.
- (94) Hong, D. C.; Yamada, Y.; Nagatomi, T.; Takai, Y.; Fukuzumi, S. *Journal of the American Chemical Society* **2012**, *134*, 19572.
- (95) Hu, C.-C.; Wu, Y.-R. *Materials Chemistry and Physics* **2003**, *82*, 588.
- (96) Chen, J. Y. C.; Miller, J. T.; Gerken, J. B.; Stahl, S. S. *Energy & Environmental Science* **2014**, *7*, 1382.
- (97) Miller, E. L.; Rocheleau, R. E. *Journal of the Electrochemical Society* **1997**, *144*, 3072.
- (98) Li, X.; Walsh, F. C.; Pletcher, D. *Physical Chemistry Chemical Physics* **2011**, *13*, 1162.

- (99) Feng, Y.; Zhang, H.; Zhang, Y.; Li, X.; Wang, Y. *ACS Applied Materials & Interfaces* **2015**, *7*, 9203.
- (100) Görlin, M.; Glied, M.; Ferreira de Araújo, J.; Dresch, S.; Bergmann, A.; Strasser, P. *Catalysis Today* **2015**, *262*, 65.
- (101) Balasubramanian, M.; Melendres, C. A.; Mini, S. *The Journal of Physical Chemistry B* **2000**, *104*, 4300.
- (102) Kim, S.; Tryk, D. A.; Antonio, M. R.; Carr, R.; Scherson, D. *Journal of physical chemistry (1952)* **1994**, *98*, 10269.
- (103) Chen, J. Y. C.; Dang, L.; Liang, H.; Bi, W.; Gerken, J. B.; Jin, S.; Alp, E. E.; Stahl, S. S. *Journal of the American Chemical Society* **2015**, *137*, 15090.
- (104) Trzeźniewski, B. J.; Diaz-Morales, O.; Vermaas, D. A.; Longo, A.; Bras, W.; Koper, M. T. M.; Smith, W. A. *Journal of the American Chemical Society* **2015**, *137*, 15112.
- (105) del Arco, M.; Malet, P.; Trujillano, R.; Rives, V. *Chemistry of Materials* **1999**, *11*, 624.
- (106) Bates, M. K.; Jia, Q.; Doan, H.; Liang, W.; Mukerjee, S. *ACS Catalysis* **2016**, *6*, 155.
- (107) Fominykh, K.; Chernev, P.; Zaharieva, I.; Sicklinger, J.; Stefanic, G.; Döblinger, M.; Müller, A.; Pokharel, A.; Böcklein, S.; Scheu, C.; Bein, T.; Fattakhova-Rohlfing, D. *ACS Nano* **2015**, *9*, 5180.
- (108) Görlin, M.; Chernev, P.; Ferreira de Araújo, J.; Reier, T.; Dresch, S.; Paul, B.; Krähnert, R.; Dau, H.; Strasser, P. *Journal of the American Chemical Society* **2016**, *138*, 5603.
- (109) Burke, M. S.; Enman, L. J.; Batchelor, A. S.; Zou, S.; Boettcher, S. W. *Chemistry of Materials* **2015**, *27*, 7549.
- (110) Vincent, C.; Scrosati, B. *Modern Batteries 2nd Edition*; Elsevier, 1997.
- (111) Stolten, D. *Hydrogen and Fuel Cells: Fundamentals, Technologies and Applications*; John Wiley & Sons, 2010.
- (112) Haynes, W. M. *CRC Handbook of Chemistry and Physics*; CRC Press: Boca Raton, FL., 2000, Vol. 92nd Ed.
- (113) Hong, W. T.; Risch, M.; Stoerzinger, K. A.; Grimaud, A.; Suntivich, J.; Shao-Horn, Y. *Energy & Environmental Science* **2015**, *8*, 1404.
- (114) Diaz-Morales, O.; Ferrus-Suspedra, D.; Koper, M. T. M. *Chemical Science* **2016**, 2639.
- (115) Yu, N.; Zhang, W.-B.; Wang, N.; Wang, Y.-F.; Tang, B.-Y. *The Journal of Physical Chemistry C* **2008**, *112*, 452.
- (116) Mulakaluri, N.; Pentcheva, R.; Scheffler, M. *The Journal of Physical Chemistry C* **2010**, *114*, 11148.
- (117) Rossmeisl, J.; Logadottir, A.; Nørskov, J. K. *Chemical Physics* **2005**, *319*, 178.
- (118) Ferse, A. *2012* **2012**, *4*.
- (119) Ferse, A.; Ferse, B. *Electrochimica Acta* **2016**, *192*, 497.
- (120) J., B. A.; R., F. L. *Electrochemical Methods: Fundamentals and applications*; 2nd Ed. ed.; John Wiley & Sons: New York, 2001.
- (121) Niederberger, M.; Garnweitner, G.; Buha, J.; Polleux, J.; Ba, J. H.; Pinna, N. *Journal of Sol-Gel Science and Technology* **2006**, *40*, 259.
- (122) Surendranath, Y.; Kanan, M. W.; Nocera, D. G. *Journal of the American Chemical Society* **2010**, *132*, 16501.
- (123) Park, J.; An, K.; Hwang, Y.; Park, J.-G.; Noh, H.-J.; Kim, J.-Y.; Park, J.-H.; Hwang, N.-M.; Hyeon, T. *Nat Mater* **2004**, *3*, 891.

- (124) Bau, J. A.; Li, P.; Marenco, A. J.; Trudel, S.; Olsen, B. C.; Lubber, E. J.; Buriak, J. M. *Chemistry of Materials* **2014**, *26*, 4796.
- (125) Shavel, A.; Rodríguez-González, B.; Pacifico, J.; Spasova, M.; Farle, M.; Liz-Marzán, L. M. *Chemistry of Materials* **2009**, *21*, 1326.
- (126) Jusys, Z.; Kaiser, J.; Behm, R. J. *Electrochimica Acta* **2004**, *49*, 1297.
- (127) Barra, M.; Haumann, M.; Loja, P.; Krivanek, R.; Grundmeier, A.; Dau, H. *Biochemistry* **2006**, *45*, 14523.
- (128) Ankudinov, A. L.; Ravel, B.; Rehr, J. J.; Conradson, S. D. *Physical Review B* **1998**, *58*, 7565.
- (129) Rehr, J. J.; Albers, R. C. *Reviews of Modern Physics* **2000**, *72*, 621.
- (130) Risch, M.; Klingan, K.; Heidkamp, J.; Ehrenberg, D.; Chernev, P.; Zaharieva, I.; Dau, H. *Chemical Communications* **2011**, *47*, 11912.
- (131) Petrykin, V.; Macounova, K.; Franc, J.; Shlyakhtin, O.; Klementova, M.; Mukerjee, S.; Krtil, P. *Chemistry of Materials* **2011**, *23*, 200.
- (132) Risch, M.; Ringleb, F.; Kohlhoff, M.; Bogdanoff, P.; Chernev, P.; Zaharieva, I.; Dau, H. *Energy & Environmental Science* **2015**, *8*, 661.
- (133) O'Day, P. A.; Vlassopoulos, D.; Root, R.; Rivera, N. *Proceedings of the National Academy of Sciences of the United States of America* **2004**, *101*, 13703.
- (134) Frydendal, R.; Paoli, E. A.; Knudsen, B. P.; Wickman, B.; Malacrida, P.; Stephens, I. E. L.; Chorkendorff, I. *ChemElectroChem* **2014**, *1*, 2075.
- (135) Smith, R. D. L.; Prevot, M. S.; Fagan, R. D.; Trudel, S.; Berlinguette, C. P. *Journal of the American Chemical Society* **2013**, *135*, 11580.
- (136) Gong, M.; Dai, H. *Nano Res.* **2015**, *8*, 23.
- (137) Morales-Guio, C. G.; Mayer, M. T.; Yella, A.; Tilley, S. D.; Grätzel, M.; Hu, X. *Journal of the American Chemical Society* **2015**, *137*, 9927.
- (138) Wang, D.; Zhou, J.; Hu, Y.; Yang, J.; Han, N.; Li, Y.; Sham, T.-K. *The Journal of Physical Chemistry C* **2015**, *119*, 19573.
- (139) Ogrady, W. E.; Pandya, K. I.; Swider, K. E.; Corrigan, D. A. *Journal of the Electrochemical Society* **1996**, *143*, 1613.
- (140) Pinna, N.; Niederberger, M. *Angewandte Chemie-International Edition* **2008**, *47*, 5292.
- (141) Jusys, Z.; Massong, H.; Baltruschat, H. *Journal of The Electrochemical Society* **1999**, *146*, 1093.
- (142) Wolter, O.; Heitbaum, J. *Berichte der Bunsengesellschaft für physikalische Chemie* **1984**, *88*, 2.
- (143) Baltruschat, H. *Journal of the American Society for Mass Spectrometry* **2004**, *15*, 1693.
- (144) Yeo, B. S.; Bell, A. T. *Journal of Physical Chemistry C* **2012**, *116*, 8394. (145) Trotochaud, L.; Boettcher, S. W. *Scripta materialia* **2014**, *74*, 25.
- (146) Batchellor, A. S.; Boettcher, S. W. *ACS Catalysis* **2015**, *5*, 6680.
- (147) Lu, X.; Zhao, C. *Nature Communications* **2015**, *6*, 1.
- (148) Smith, R. D. L.; Berlinguette, C. P. *Journal of the American Chemical Society* **2016**, *138*, 1561.

- (149) González-Flores, D.; Sánchez, I.; Zaharieva, I.; Klingan, K.; Heidkamp, J.; Chernev, P.; Menezes, P. W.; Driess, M.; Dau, H.; Montero, M. L. *Angewandte Chemie International Edition* **2015**, *54*, 2472.
- (150) Iwasaki, T.; Yoshii, H.; Nakamura, H.; Watano, S. *Applied Clay Science* **2012**, *58*, 120.
- (151) Kim, M. S.; Hwang, T. S.; Kim, K. B. *Journal of the Electrochemical Society* **1997**, *144*, 1537.
- (152) Wehrens-Dijksma, M.; Notten, P. H. L. *Electrochimica Acta* **2006**, *51*, 3609.
- (153) Shangguan, E.; Tang, H.; Chang, Z.; Yuan, X.-Z.; Wang, H. *International Journal of Hydrogen Energy* **2011**, *36*, 10057.
- (154) Stern, L.-A.; Hu, X. *Faraday Discussions* **2014**, *176*, 363.
- (155) Hall, D. S.; Lockwood, D. J.; Bock, C.; MacDougall, B. R. *Proceedings. Mathematical, Physical, and Engineering Sciences / The Royal Society* **2015**, *471*, 1.
- (156) Mansour, S. A. A. *Thermochimica Acta* **1993**, *228*, 173.
- (157) Rives, V.; Angeles Ulibarri, M. a. *Coordination Chemistry Reviews* **1999**, *181*, 61.
- (158) Wang, K.; He, X.; Li, X.; Jiang, J.; Sun, Y. *Rare Metals* **2009**, *28*, 500.
- (159) Michel, F. M.; Ehm, L.; Antao, S. M.; Lee, P. L.; Chupas, P. J.; Liu, G.; Strongin, D. R.; Schoonen, M. A. A.; Phillips, B. L.; Parise, J. B. *Science* **2007**, *316*, 1726.
- (160) Bergmann, A.; Martinez-Moreno, E.; Teschner, D.; Chernev, P.; Gliech, M.; de Araujo, J. F.; Reier, T.; Dau, H.; Strasser, P. *Nat Commun* **2015**, *6*, 1.
- (161) Brown, I. D.; Altermatt, D. *Acta Crystallographica Section B* **1985**, *41*, 244.
- (162) Capehart, T. W.; Corrigan, D. A.; Conell, R. S.; Pandya, K. I.; Hoffman, R. W. *Applied Physics Letters* **1991**, *58*, 865.
- (163) Pandya, K. I.; Ogrady, W. E.; Corrigan, D. A.; McBreen, J.; Hoffman, R. W. *Journal of physical chemistry (1952)* **1990**, *94*, 21.
- (164) Gorlin, Y.; Chung, C.-J.; Benck, J. D.; Nordlund, D.; Seitz, L.; Weng, T.-C.; Sokaras, D.; Clemens, B. M.; Jaramillo, T. F. *Journal of the American Chemical Society* **2014**, *136*, 4920.
- (165) Seitz, L. C.; Hersbach, T. J. P.; Nordlund, D.; Jaramillo, T. F. *The Journal of Physical Chemistry Letters* **2015**, *6*, 4178.
- (166) Doyle, R. L.; Godwin, I. J.; Brandon, M. P.; Lyons, M. E. G. *Physical Chemistry Chemical Physics* **2013**, *15*, 13737.
- (167) Cherevko, S.; Zeradjanin, A. R.; Keeley, G. P.; Mayrhofer, K. J. J. *Journal of The Electrochemical Society* **2014**, *161*, 822.
- (168) Jolivet, J.-P.; Tronc, E.; Chanéac, C. *Comptes Rendus Geoscience* **2006**, *338*, 488.
- (169) Manceau, A. *Clay Minerals* **2009**, *44*, 19.
- (170) Sadeghi, O.; Zakharov, L. N.; Nyman, M. *Science* **2015**, *347*, 1359.
- (171) Dau, H.; Liebisch, P.; Haumann, M. *Anal Bioanal Chem* **2003**, *376*, 562.
- (172) Thorat, S.; Rose, J.; Garnier, J. M.; Van Geen, A.; Refait, M. P.; Traverse, A.; Fonda, E.; Nahon, D.; Bottero, J. Y. *Environ Sci Technol* **2005**, *39*, 9478.

- (173) Suzuki, S.; Suzuki, T.; Kimura, M.; Takagi, Y.; Shinoda, K.; Tohji, K.; Waseda, Y. *Applied Surface Science* **2001**, 169–170, 109.
- (174) Manceau, A.; Schlegel, M. L.; Musso, M.; Sole, V. A.; Gauthier, C.; Petit, P. E.; Trolard, F. *Geochimica et Cosmochimica Acta* **2000**, 64, 3643.
- (175) Fleet, M. *Acta Crystallographica Section B* **1981**, 37, 917.
- (176) Corrias, A.; Ennas, G.; Mountjoy, G.; Paschina, G. *Physical Chemistry Chemical Physics* **2000**, 2, 1045.
- (177) Hodges, J. P.; Short, S.; Jorgensen, J. D.; Xiong, X.; Dabrowski, B.; Mini, S. M.; Kimball, C. W. *Journal of Solid State Chemistry* **2000**, 151, 190.
- (178) Krest, C. M.; Silakov, A.; Rittle, J.; Yosca, T. H.; Onderko, E. L.; Calixto, J. C.; Green, M. T. *Nat Chem* **2015**, 7, 696.
- (179) Mansour, A. N.; Melendres, C. A. *The Journal of Physical Chemistry A* **1998**, 102, 65.
- (180) Morishita, M.; Ochiai, S.; Kakeya, T.; Ozaki, T.; Kawabe, Y.; Watada, M.; Tanase, S.; Sakai, T. *Journal of the Electrochemical Society* **2008**, 155, 936.
- (181) Farley, N. R. S.; Gurman, S. J.; Hillman, A. R. *Electrochimica Acta* **2001**, 46, 3119.
- (182) Bediako, D. K.; Lassalle-Kaiser, B.; Surendranath, Y.; Yano, J.; Yachandra, V. K.; Nocera, D. G. *Journal of the American Chemical Society* **2012**, 134, 6801.
- (183) Currie, D. B.; Levason, W.; Oldroyd, R. D.; Weller, M. T. *Journal of the Chemical Society, Dalton Transactions* **1994**, 1483.
- (184) Smith, R. D. L.; Prévot, M. S.; Fagan, R. D.; Zhang, Z.; Sedach, P. A.; Siu, M. K. J.; Trudel, S.; Berlinguette, C. P. *Science* **2013**, 340, 60.
- (185) Ma, W.; Ma, R.; Wang, C.; Liang, J.; Liu, X.; Zhou, K.; Sasaki, T. *ACS Nano* **2015**, 1977.
- (186) Forgie, R.; Bugosh, G.; Neyerlin, K. C.; Liu, Z.; Strasser, P. *Electrochemical and Solid-State Letters* **2010**, 13, B36.
- (187) Bediako, D. K.; Nocera, D. G. *Abstracts of Papers of the American Chemical Society* **2011**, 242.
- (188) Barnard, R.; Randell, C. F. *Journal of Power Sources* **1983**, 9, 185. (189) Su, D.; Ford, M.; Wang, G. *Scientific Reports* **2012**, 2, 924.
- (190) Lee, S. W.; Carlton, C.; Risch, M.; Surendranath, Y.; Chen, S.; Furutsuki, S.; Yamada, A.; Nocera, D. G.; Shao-Horn, Y. *Journal of the American Chemical Society* **2012**, 134, 16959.
- (191) Beverskog, B.; Puigdomenech, I. *Corrosion Science* **1997**, 39, 969.
- (192) Ortel, E.; Reier, T.; Strasser, P.; Kraehnert, R. *Chemistry of Materials* **2011**, 23, 3201.
- (193) O'Day, P. A.; Vlassopoulos, D.; Root, R.; Rivera, N.; NATL ACAD SCIENCES: 2004.
- (194) Görlin, M.; Ferreira de Araújo, J.; Schmies, H.; Bernsmeier, D.; Dresch, S.; Glied, M.; Jusys, Z.; Chernev, P.; Kraehnert, R.; Dau, H.; Strasser, P. *Journal of the American Chemical Society* **2017**, 139, 2070.
- (195) McCrory, C. C. L.; Jung, S.; Ferrer, I. M.; Chatman, S. M.; Peters, J. C.; Jaramillo, T. F. *Journal of the American Chemical Society* **2015**, 137, 4347.
- (196) Bediako, D. K.; Surendranath, Y.; Nocera, D. G. *Journal of the American Chemical Society* **2013**, 135, 3662.

- (197) Ranjbar, S. N.; Kramm, U. I.; Steinberg, J.; Zhang, Y.; Thomas, A.; Reier, T.; Paraknowitsch, J.-P.; Strasser, P. *Nat Commun* **2015**, *6*.
- (198) Koper, M. T. M. *Physical Chemistry Chemical Physics* **2013**, *15*, 1399.
- (199) Bau, J. A.; Lubber, E. J.; Buriak, J. M. *ACS Applied Materials & Interfaces* **2015**, *7*, 19755.
- (200) Cukier, R. I.; Nocera, D. G. *Annual Review of Physical Chemistry* **1998**, *49*, 337.
- (201) Enman, L. J.; Burke, M. S.; Batchellor, A. S.; Boettcher, S. W. *ACS Catalysis* **2016**, *6*, 2416.
- (202) Angelinetta, C.; Falciola, M.; Trasatti, S. *Journal of Electroanalytical Chemistry and Interfacial Electrochemistry* **1986**, *205*, 347.
- (203) Katsounaros, I.; Chen, T.; Gewirth, A. A.; Markovic, N. M.; Koper, M. T. M. *The Journal of Physical Chemistry Letters* **2016**, *7*, 387.
- (204) Dresch, S.; Luo, F.; Schmack, R.; Kuhl, S.; Gliech, M.; Strasser, P. *Energy & Environmental Science* **2016**, *9*, 2020.
- (205) Kim, C.; Kim, C.; Lee, K.; Lee, H. *Chemical Communications* **2014**, *50*, 6353.
- (206) Cui, C.; Gan, L.; Heggen, M.; Rudi, S.; Strasser, P. *Nat Mater* **2013**, *12*, 765.
- (207) Ahmadi, M.; Cui, C.; Mistry, H.; Strasser, P.; Roldan Cuenya, B. *ACS Nano* **2015**, *9*, 10686.
- (208) Mayrhofer, K. J. J.; Juhart, V.; Hartl, K.; Hanzlik, M.; Arenz, M. *Angewandte Chemie International Edition* **2009**, *48*, 3529.
- (209) Göttle, A. J.; Koper, M. T. M. *Chemical Science* **2016**, *8*, 458.